Kinematics, Motion Control and Force Estimation of a Chewing Robot of 6RSS Parallel Mechanism

A thesis presented in partial fulfilment of the requirements for the degree of

Doctor of Philosophy

in

Engineering

at Massey University, Palmerston North

New Zealand

Jonathan David Torrance

2011

ABSTRACT

Parallel robots have been found in many applications where the work requirements are beyond the capabilities of serial robots. Mouth movements during the chewing of foods are ideally suited to the parallel robot due to relatively high force together with 6 degree of freedom (DOF) motion all occurring in a small workspace. The Massey Robotic Jaw (MRJ) is a life sized mastication robot of 6RSS parallel mechanism designed with human physiology in mind, and to be capable of recreating the movements and forces of human mastication. The MRJ consists of a movable mandible attached to a fixed 'skull' through 6RSS crank mechanisms enabling six degree of freedom motion. In order to perform targeted movements of the MRJ, inverse kinematics of mechanism are solved. Target movements of the lower jaw can then be translated to six individual movements of each actuator. The synchronised motion of all six actuators is implemented using appropriate motion control to create the desired motion at the lower jaw. Motion control in context of the MRJ involves position control during the non-occluding phases of the mastication cycle.

The kinematic and dynamic models of a generic 6RSS robot are discussed and are then simplified considering the special features of a practical chewing robot and the requirements of controller design. The issue of dynamic position and force control of a chewing robot with a 6RSS mechanism is addressed. An impedance control scheme is proposed to achieve the position and force control of the robot. A detailed description on the steps to implement the controller is also presented.

The application of the 6RSS parallel chewing robot to food chewing experiments was described. The force vector applied on the active molar was calculated from the measured torques applied on the six actuators using an analysis of forces through the linkage mechanism. A series of experiments were carried out using model and real foods. The work shows promise for application of the robot to characterise food texture, however a number of future developments are required. To make the robot more human-like, a tongue, cheek and mouth chamber need to be included. Furthermore, accurate force sensing and position sensing of the mandible in Cartesian space is suggested as a means to validate the impendence control method proposed and to verify the force measurement strategy implemented in chapter 6.

ACKNOWLEDGEMENT

I would like to thank the following people for their contributions:

- Firstly my supervisors Professor Peter Xu and Professor John Bronlund who have supported me throughout the PhD program and given great guidance and advice whenever called upon. Their help and patience throughout my research are greatly appreciated.
- Richard Sun, who worked with me on food chewing experiments and gave me assistance during final thesis preparation.
- Charles Chen for his work with me during force experiments.
- Sebastian Pap for his work on the mechanical design of the Massey Robotic Jaw.
- Dr Kylie Foster and Scott Hutchings for their Food Technology expertise and EMG data which was an important element needed for my research.
- Dr Oliver Rohrle and Dr Jules Kieser for their jaw trajectory data and teeth models.
- Dr Loulin Huang for his advice.
- My parents and girlfriend for their support, thesis dedicated to my father who is currently recovering in Auckland hospital 9 months after a motorcycle accident.

RELATED PUBLICATIONS

Huang, L., Xu, W. L., Torrance, J., & Bronlund, J. E. (2010). Design Of A Position And Force Control Scheme For 6RSS Parallel Robots And Its Application In Chewing Robots. *Int. J. Human. Robot., 7*(03), 477-489.

Torrance, J., Hutchings, S., Bronlund, J., & Huang, L. (2010). Human jaw motion measurement, analysis and robotic reproduction. *International Journal of Intelligent Systems Technologies and Applications, 8*(1), 288-302.

Torrance, J., Pap, J., Xu, W., Bronlund, J., & Foster, K. (2006). *Motion control of a chewing robot of 6 RSS parallel mechanism.* Paper presented at and in the Proceedings of 3rd International Conference on Autonomous Robots and Agents (ACARA), Palmerston North, New Zealand.

Xu, W., Torrance, J., Chen, B., Potgieter, J., Bronlund, J., & Pap, J. S. (2008). Kinematics and experiments of a life-sized masticatory robot for characterizing food texture. *Industrial Electronics, IEEE Transactions on, 55*(5), 2121-2132.

TABLE OF CONTENTS

LIST OF FIGURES

LIST OF TABLES

1. INTRODUCTION

1.1. Background

A large area of research revolves around the creation of new foods that are more desirable to the consumer by making them healthier while maintaining hedonic value. In order to produce better foods, there needs to be criteria for assessing the foods. In the past panels of human testers would take a sample of food and report back on certain qualities of the food such as texture, hardness and chewiness. Alternatively, food properties can be assessed using purpose built machines that compress the food and record forces to give an indication of hardness, or provide share forces to the food to give an indication of chewiness and other properties. While the first method provides real chewing behaviour to the food, the final assessment is subjective, and varies both for the individual depending on mood, and also between individuals due to differing biological make ups and personal preferences. The second outlined method using simple machines to test the mechanical properties of the foods gives truly objective data, however the testing is far removed from what is actually happening to the food once inside a human mouth. It is currently seen as a great challenge to find unequivocal relations between the objective physical food properties that can measured in vitro with current instruments and subjective perception expressed in sensory attributes (Bosman, F., Bilt, A., Abbink, J., & Glas, H. W. (2004a)).

A mixing of the two food property sensing philosophies is what is required to obtain the advantages of both methods. For this purpose we could either take the human subject, standardizing them with a fixed/known biology and fixed food property perception mechanism in order to create consistent and repeatable results, or we could take the food property analysing machines and add human like motion and sensory feedback so results can be closely aligned with specific sensory attributes. Clearly the second approach is more realistic and is what this PhD is targeted towards.

This thesis details findings relating to a 6-DOF chewing machine developed at Massey University which we call the Massey Robotic Jaw, MRJ. The MRJ was first designed and assembled as a mechatronic device during the first year of this research. Much of the practical input for the structural design came from a master student whose goal was to assemble the physical robot ready to control. The component selection and robot design was based on strict criteria with the aim to add human elements to mechanised food property assessment. Important to the MRJ's design was the ability to provide all movements seen in human mastication, and to perform them at the speeds and forces seen during real human chewing. Furthermore it was required that actuations would be analogous to the human chewing system, with actuators placed so that they mimic

the closing muscles of the biological model in humans. This meant a unique robot and a unique motion control problem.

When creating a robotic mechanism and control strategy to mimic a biological system, it is first necessary to take a close look at the biological system. In the case of human mastication it will be shown in the literature review section that there are still many mysteries as to exactly how humans chew foods. The approach taken in light of the uncertainties surrounding the human chewing process was to incorporate as many human aspects into the robot and lower level control design as possible. This philosophy allows for any unknown advantages inherited from the biological model to be made use of as the higher level control strategies are developed.

In order to make the MRJ perform the same chewing functions of a human, accurate control of all 6-DOF is required. Jaw motion must be controlled during both the non-occlusion and occlusion phases with special consideration to the forces encountered during the occlusion phases. A human will attempt to chew a hard food, but will stop if this force required becomes too large. Such an approach to the chewing of hard foods needs to be incorporated in the MRJ also. For the purpose of adding sensory feedback on the food being chewed, forces at the chewing surface need to be recorded. The unique arrangement of actuators also provides the possibility of estimating forces required by the human muscles of mastication to chew the food sample. Together this force data can provide a unique and objective measure of the experience a human is likely to have from the mastication of the food sample.

Throughout the project the mechatronic design approach is used where mechanical design, driving actuator design, and motion control are integrated and developed in parallel. The parallel approach allows close consideration of how one design approach affects the others so smooth concurrent solutions can be formed. The integration of the biological system that makes the MRJ unique is seen during the first ‘specifications’ phase which is covered in chapter 3. The specifications derived from biological findings therefore affect mechanical, actuator, and control design and are inherited into all parts of the design approach.

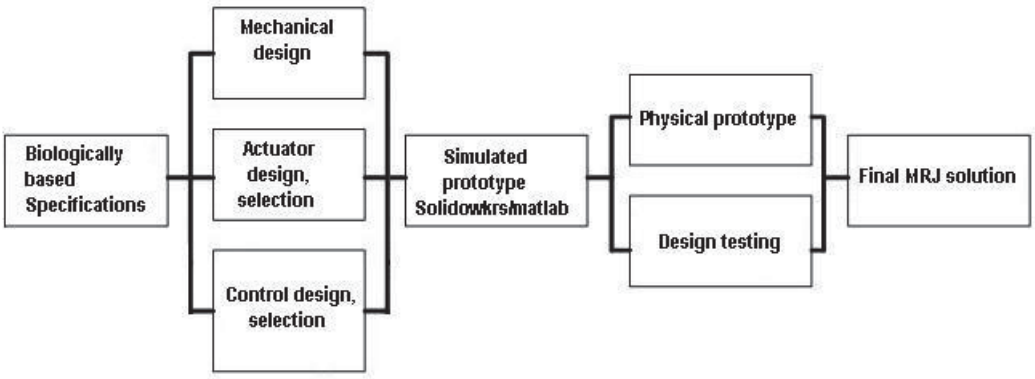

Figure 1.1 The mechatronic design approach

1.2. Scope of Research

This research looks at the selection of suitable motion control hardware and implementation of suitable motion control strategies to meet the specified requirements outlined in the next section. Design analysis and verification is to be performed to ensure requirements are met; these include singularity analysis and force capability analysis for certain crucial points.

A force measurement approach for force on the chewing surface and forces through the actuators is to be provided. Additionally, as verification that objectives outlined in chapter 6 meet, experimental testing of the functioning MRJ on various food samples are to be run.

Food properties of taste, smell, texture as perceived by the human olfactory system, taste buds, tongue and cheek systems is not to be attempted in this project. Provisions for the addition of these functions at a later date and proposed methodology for the inclusion of these functions to the MRJ will be briefly discussed.

Active human decision making during the chewing process based on sensory feedback is outside the scope of this research, however methods to control forces produced by the jaw on the food sample is to be part of this project.

Robotic dynamics will be considered in the motion control problem. The robots dynamics are to be considered and treated appropriately in order to maintain objectives outlined in chapter 4.

The human chewing process is to be researched in this PhD, and considerations given to the need for active force control during the chewing process. Active force control is to be considered part of the research only if it's found to be required in order to meet the objectives outlined chapter 7.

1.3. Objectives of Research

1. Given a novel mastication robot of 6-RSS mechanism, solve for the first time the closed form inverse kinematics, defining important co-ordinate frames on the robot and all physical parameters in the process.

2. Derive for the first time the Jacobian for the novel mastication robot of 6-RSS mechanism, and use it to find singularities of the robot.

3. By making required physical modifications to the robot, and by selecting and applying novel motion control techniques, perform six degree of freedom mastication movements with the robot.

4. By first solving for the first time the problem of dimensional differences between human and robot jaws, re-create a recorded human mastication sequence in all six degrees of freedom on the robot.

5. By experimentation and addition of force limiting features to the robot, prove the novel mastication robot can perform human mastication sequences on a variety of foods and food models.

6. By using a novel force sensing method provide for the first time a set of force data from the robot during the recreation of a recorded human mastication sequence in six degrees of freedom on real food samples. From force data collected, prove the potential of the robot as a food property analyser.

2. LITERATURE REVIEW

This chapter reviews available literature on the human mastication process, what elements are required to be replicated, and what is currently the state of the art in robotic chewing devices.

2.1. Human Mastication

This section reviews literature on the human mastication process. By finding out how humans perform mastication it may be possible to incorporate similar methods on the MRJ. It is also important to review the human process thoroughly in order to find the required specifications of the robotic jaw being designed. The following sections first outline the objective of human mastication, and then describe the individual elements that make it up. The final section details how the individual elements are combined to perform mastication in humans.

2.1.1. *Objective*

Health and Prinz (1999) described the mastication process in the three phases; ingestion (transfer of food onto the teeth surface), main sequence (food chewed to form bolus), clearance and swallowing. This thesis is concerned only with the second phase where food is mechanically manipulated to form the bolus, and for the rest of the thesis this simplified definition will be used. The objective of this main sequence phase is to begin the digestion process by breaking down the food, mixing it with saliva into a bolus that can be easily and safely swallowed. This process is essential to enable the later stages of digestion to perform their tasks where the bolus is further broken down and nutrients absorbed.

2.1.2. *Apparatus*

The main elements of the human masticatory system are the Maxilla, or upper jaw, the Mandible, or lower jaw, the teeth, the muscles that drive the Mandible and the central nervous system that controls the driving muscles. Also of note is the Temporomandibular joint (TMJ) which is unique in that it is a moving pivot point in what can be modelled as a class-3 lever. The maxilla and mandible are uniquely shaped bone structures and need no further description.

The mastication process is performed by movements of the lower mandible which is driven by several clusters of muscles.

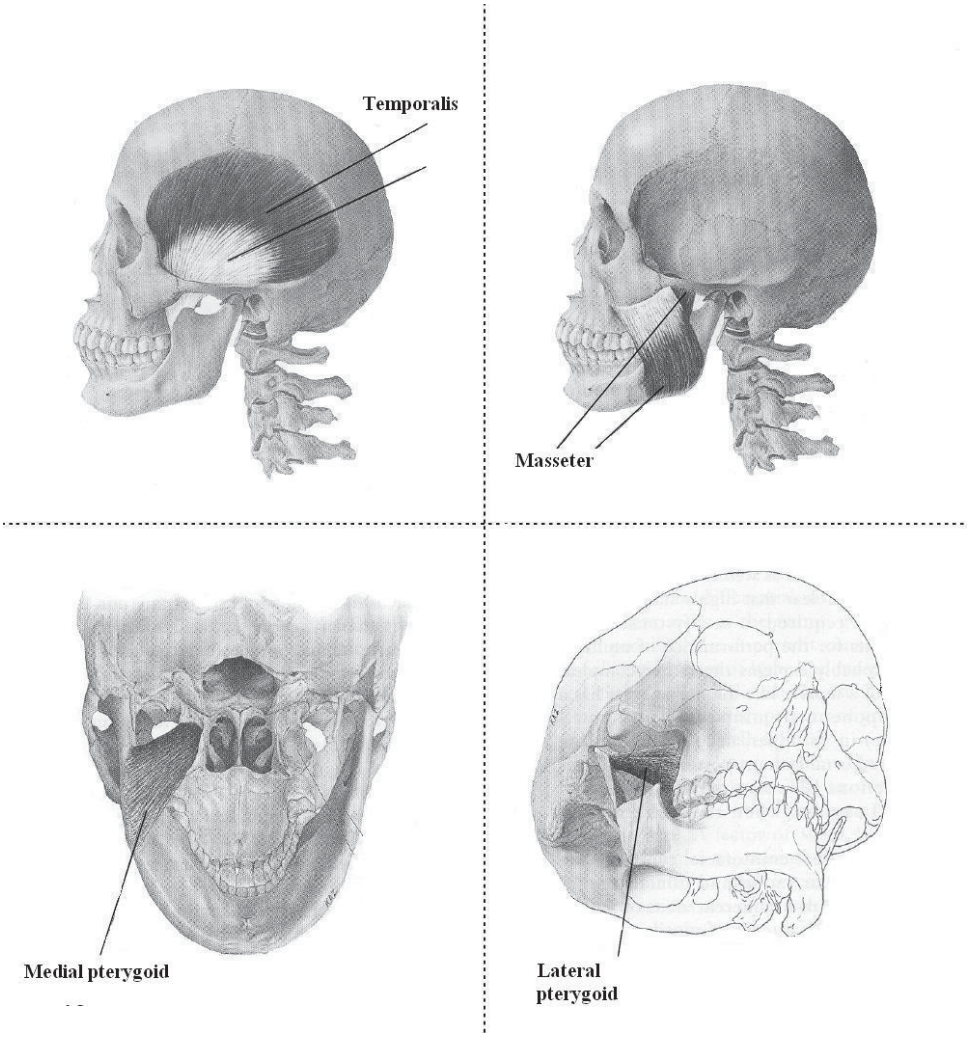

Figure 2.1 The major muscles involved in chewing (Hannam, 1997)

Because the muscles evolved in parallel with the many other biological features of the human head and face, their locations and actions are unique. Koolstra (2002) defines the human mastication system as mechanically redundant as there are an infinite number of muscle contraction patterns that can cause the same movement. The formation of mastication muscle in the human was certainly not formed analytically in order to solve a pre-defined problem, but is likely to have resulted from years of adaptation in lock step with the many other mechanisms that are involved in mastication such as the central nervous system, jaw, skull bone, teeth and tongue. By operating together under co-ordinated instruction from the central nervous system the muscles of mastication can move the mandible in six degrees of freedom.

The maxilla and mandible have teeth embedded which are responsible for the physical contact and forces that break down the food particles. Figure 2.1 shows major muscles and the layout of the different teeth, each type performing a different function which will be detailed in the next section. As with the muscles of mastication the teeth are

uniquely suited to fit in with the other elements of mastication. The teeth make a curve in both frontal and sagittal planes. The sagittal curve is called the curve of spee and its function and formation are still debated especially in the orthodontic circles. Dr. Georg Risse (2007) states prehistoric humans had no curve of spee together with vastly different jaw geometry and muscle layouts. Risse states that the curve of spee may allow the long axis of molars to align with the main force vectors from the muscles of mastication in modern humans. Another theory on the curve of spee function is that it allows the incisors and canines to contact before the molars, enabling some guidance for the high force motion involved when molars come into contact (Wynne, 2005).

Finally the central nervous system, which can be thought of as the control system, which through processes removed from the humans conscious thoughts, commands the muscles to move the mandible and teeth through precise trajectories that maximise food breakdown while at the same time preserving the delicate tissue of the inner mouth and tongue. The process in which the central nervous system (CNS) achieves this may be the least well known element of the human mastication system. Muscles have sensors called spindles which give feedback of force and displacement to the human brain. Pattern generating neurons in the brain have been seen to be active during rhythmic mastication (Nakamura & Katakura, 1995). The survival based goal of getting the food into a bolus suitable for swallowing has moulded these CNS processes, in parallel with the other elements of mastication, over many thousands of years making human mastication a unique and complex process.

2.1.3. *Method*

The mastication muscles provide motion to the mandible enabling the teeth to act on foods. Repeated rhythmical cycles of the mandible opening and closing breakdown the food particles, which with help from tongue, cheeks and salivary system, are turned into a bolus able to be swallowed.

Jaw motion during the main sequence phase has been recorded using various means. The movement involves all 6 degrees of freedom (6DOF), with the Temporal-mandibular joint allowed to move back and forth as well as act as a pivot point for the lower jaw to open.

Figure 2.2 below shows the Posselt Envelope which defines the boundary shape of the human jaws workspace. The shape of the Posselt Envelop is unique and is due to the muscles, TMJ joint and teeth shape as motion becomes limited once teeth contact or TMJ joint or muscles hit workspace limits. An individual will have their own Posselt Envelope that is similar in shape to that shown in figure 2.2 but with dimensions unique to the individual.

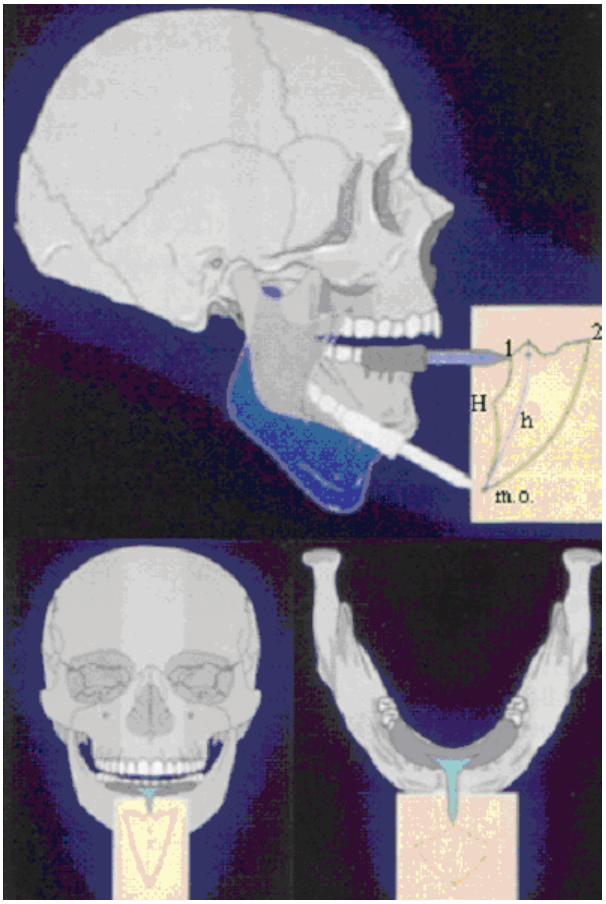

Figure 2.2 The Posselt Envelope (Douglass G.D et al 1997).

Movement of the jaw during chewing must fall within the individuals own Posselt Envelope. Figure 2.3 below shows a single chewing cycle of the incisor point, where the three distinct phases of a chewing cycle opening, closing and occlusion can be seen. Motion in the sagittal plane (a) will produce posterior and inferior displacement concurrently as rotation about the TMJ functions to lower the mandible. In the frontal plane it is possible to get mirror images about the vertical axis as food is chewed on one side then the other. The maximum intercuspation can be thought of as the jaw fully closed position, where molars are meshed together. Occlusion is considered to be mandible movement within 0.5mm from the maximum intercuspation position (MI). The occlusion phase is most important as this is where forces are likely to peak and food is broken down. During occlusion the jaw motion depends on the geometry of the molars as they come into contact and attempt to reach maximum intercuspation position (Agrawal, Lucas, & Bruce, 2000).

There is also a strong relationship between food properties and jaw movements. Anderson, Throckmorton, Buschang and Hayasaki (2002) showed that increasing levels of hardness of chewing gum resulted in increased vertical and lateral movements of the jaw during mastication. Agrawal et al. (2000) also stated that the angle of the jaw at start of the occlusion phase varied based on the hardness of the food, with more lateral movements during the occlusion phase for the harder foods. As food

breakdown also depends on the jaw motion acting on the food, interaction between food and jaw movement exists. This interaction is an important consideration when assessing food texture properties and it highlights the need to consider food specific tests as well as sensory feedback to change testing as food breaks down after each cycle.

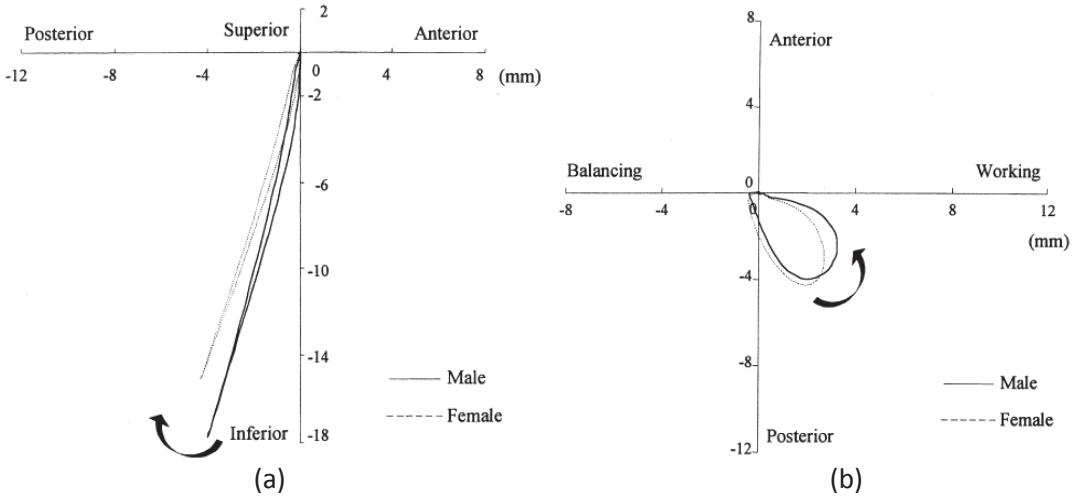

Figure 2.3 The chewing cycle trajectory in sagittal plane (a) and frontal plane (b) (Anderson et al. (2002).

As the mandible closes and in particular during the occlusion phase, forces are exerted from the mandible through the teeth and onto the foods. The mandible is capable of maximum biting forces ranging from 500N to 700N (Wood & Williams, 1981). Forces during chewing depend largely on the type of food being chewed, but in all cases are significantly less than the maximum force that the mandible is capable of in a one off bite. Foods such as biscuits and cooked meat have been seen to produce forces between 190 and 260N. As this mandible force is transmitted between several teeth on contact with the food, an estimate of force on any tooth for these foods is 70 to 150N. The much higher maximum bite force is likely to be a result of the how the human muscles in general behave, with low repetition forces always far exceeding forces seen when repetitions are larger, such as 30 repetitions for a single bite sized portion and over a hundred during the course of a meal.

Having considered jaw movement and forces a look at the resulting tooth interaction is the next logical step. Tooth interaction occurs during the occlusion phase when teeth mesh together to either break off or grind down the food depending on the teeth involved. The incisors are used for biting foods in order to remove a small manageable portion from a larger piece. The molars are shaped with spherical cusps and the alignment of upper and lower molars is such that foods tend to fracture when pressured between them (Lucas, 2004). This multiple fracturing caused by the uniquely shaped molars coming together at specific angles with sufficient force is central to food breakdown and bolus formation.

In addition to the above teeth-jaw dynamics that act on the food there are also several other important processes that occur in the mouth during mastication. Saliva is added to the food particles as they are broken down, some food components are dissolved, aroma and flavour is released, and boluses temperature is regulated. As food is broken down, the increased jaw movement and surface area of the food accelerates all these saliva based processes, which in turn alter the perceived texture of the food particles in the mouth. The interactions of the jaw/teeth dynamics that cause the mechanical breakdown of the food with the saliva based processes and perceived food texture are shown in figure 2.4 below.

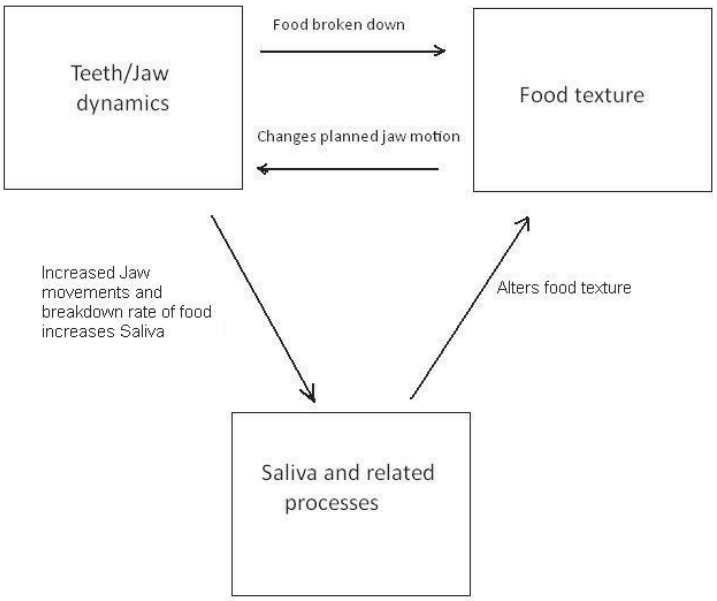

Figure 2.4 The interactions between Teeth/Jaw dynamics, food texture, saliva and related processes

The selection of food particles to be chewed each cycle is performed by the tongue and is another very complex process that occurs inside the mouth during mastication. Together with the cheeks, the tongue acts to keep larger portions of the food on the teeth surfaces, while smaller already broken down particles are allowed to accumulate near the throat or are lost into other areas of the mouth. Detailed descriptions of how the tongue performs these actions are still subject of research (Hiiemae & Palmer, 2003).

Finally we will have a brief look at how some of these individual processes are co-ordinated and controlled in the human through the CNS. While still the subject of

research, the jaw motion control is thought to be based partly on predefined chewing patterns and partly on muscle actions that respond specifically to the presence of the food particles in the mouth. The predefined patterns are handled by central pattern generators in the brain, while any extra muscle activity required to overcome foods is classified as voluntary and requires sensory feedback in order to perform properly (Iwasaki & Zheng, 2006). In control terms the research suggests motion control of the human jaw has an open-loop pattern produced part and a closed-loop force following part.

2.2. Robot Requirements

Having examined the key elements of human mastication and how they function in the human, we can now look at what is required of a mastication robot if it is to accurately replicate the core actions of the human system.

Not included in this section are the saliva based processes and action the tongue and cheeks during mastication. They have not been included in the robot requirements as they are themselves very large and complex processes requiring their own specialised research. The assumption has been made that these elements can be developed separately and included at a later stage.

2.2.1. *Motion and Forces*

In order to replicate human like chewing the robot must be able to recreate the same range of jaw movements. This means a robot of 6-DOF with workspace that exceeds the Posselt Envelope for a given individual of interest. Unlike such measures as human height, individuals Posselt Envelope dimensions are not as well documented, so emphasis has to be placed on whatever data on human jaw movement during mastication there is available. Klineberg (2005) approximated the range of jaw movement in adults with reference to the Posselt Envelope. Klineberg states jaw movement range in the sagittal plane as follows: 2-m.o. with 40-70 *mm*, 1-H with 15-20 *mm*, and 2-5 with 5-10 *mm*. While these figures give a good guideline to required robotic workspace, they are insufficient to fully describe the required range of motion in all 6-DOF's.

Pap, Xu and Bronlund (2005) described an alternative approach to finding required range of mastication motions in all 6-DOF's. Pap et al. used data obtained from (Rörle, Anderson, & Pullan, 2005) in which a custom made brace was used to track jaw motion in all 6-DOF's. The results from Pap et al. (2005) are shown in table 1 below.

Table 2-1 Maximum incisor displacements, angular movements of the mandible and chewing times for all four chewing trajectories

	Chewing trajectory			
	One	Two	Three	Four
Incisor displacement				
x (*mm*)	-	+5; -15	+3; -18	+3; -27
y (*mm*)	+7; -5	+5; -5	+11; -8	+10; -14
z (*mm*)	0; -30	+2; -23	+3; -30	+5; -38
Angular movement (mandible)				
about x (°)	-	+2; -2	+0.5; -0.7	+1; -4
about y (°)	-	+7; -13	+5; -13	+5; -18
about z (°)	-	+0.2; -0.1	+3; -4	+6; -8
Chewing time (*s*)	45.32	32.86	68.86	62.24

Some inaccuracies in the recording process may have resulted in positive z-axis displacement, such as poor zeroing at maximum intercuspation position. These have an effect on the final reference frame in which all data is reported. A more thorough look at tracking jaw motion will be examined in chapter 4 of this thesis. The final trajectories recorded in the paper (Rörle et al., 2005) do provide a border movement that was used to validate the mechanical design of the MRJ by Pap et al. (2005). It is important to note that in the robotic model there is no need to deliberately make the same physical limitation as seen in humans as these can always be formed in software if need be. The key requirement here is to ensure that any physical limitations specific to the robotic model do not limit motion in areas where there is no limitation in humans.

In addition to the workspace requirements of the robot, there are requirements on speed and acceleration of the robot also. From the previous section it can be seen that the jaw motion interacts with other processes in the mouth and with the texture of the food that is changing all the time, so the rate of mechanical breakdown needs to be same as that observed in humans. Also, the mechanical breakdown of the food is not purely a result of a set degree of compression on the food from the teeth, but effects of impact are seen as teeth move with speed through the food particles. For accurate replication of human mastication its clear both speed and acceleration seen in humans

is matched by the robotic model. Pap et al. (2005) used recorded human jaw motions to define velocity and acceleration requirements of the robotic jaw. Of specific interest to the robotic development are the associated kinematics required of the actuators that drive the system (see Table 2-2). These were found by running a simulation of the recorded human jaw motion on a Solidworks model of the human mandible, allowing kinematics of specific actuator attachment points to be found.

Table 2-2 The actuator kinematics found for the human jaw motions (Pap 2005).

	Actuator properties			Angular movement	
	Displacement (*mm*)	Velocity (*mm/s*)	Acceleration (mm/s^2)	Frontal angle (°)	Sagittal angle (°)
Masseter					
Left	7	40	500	2	4
Right	7	40	600	5	6
Temporalis					
Left	17	75	1000	4	12
Right	14	65	1000	4	8
Lt. Pterygoid					
Left	8	40	400	14	17
Right	8	40	450	10	15

In addition to matching the kinematics of the human jaw the robotic jaw must also be capable of producing the same forces as a human jaw during mastication. One dimensional forces have been recorded during human chewing and show a wide range depending on the food being chewed. A detailed look at forces in 3 dimensions acting on the teeth during human chewing is extremely difficult due to difficulties placing force sensors such that it doesn't interfere with food, so there is lack of data on this. A maximum vertical force of 700N by the human jaw has been recorded (Wood & Williams, 1981) so this is required by the robotic jaw also so that whatever forces required during mastication can be obtained. By aligning actuators in similar way to human muscles of mastication, it becomes likely that maximum forces in the other unmeasured dimensions are going to be similar so long as actuators are capable of meeting the vertical force requirement.

2.2.2. *Teeth and Jaw Geometry*

The requirement for jaw movements to be subject to teeth geometry during occlusion phase (within 0.5mm of maximum intercuspation position) highlights the need for human like teeth to be used in the robotic model. The molars and premolars are of particular interest during the occlusion phase and there accurate alignment before reaching occlusion is important. Ideally the robotic model would have jaw dimensions and teeth layouts that can be changed to match any particular subject whose chewing motion we wish to simulate. In reality this is not possible and so emphasis should be given to recreating the kinematics of the molars during grinding motions where full occlusion is present, and on recreating incisor motion when biting motion is to be recreated. There needs to be a method to align a specific subjects jaw dimensions or specifically there tooth layout, onto the standardised robotic jaw so that motions are recreated as accurately as possible despite difference in physiology. This requirement and proposed solution is explained in more detail in chapter four.

2.2.3. *Control Strategy*

Accurate closed-loop position control of the robotic jaw is required such that desired jaw kinematics is followed. It is hard to specify a desired level of accuracy for the position control as it is not clearly understood how small variations in the trajectory could impact the resulting food breakdown. A safe approach is to aim for the best possible accuracy within reason, with sub 0.5mm accuracy being a fair starting point, which also relates to the point where occlusion starts and from which position then becomes subject to tooth geometry. To become too ambitious and aim for extremely high levels of accuracy may lead to unnecessary compromises in other aspects; it makes more sense to create a complete working model from which we can then analyse functions and call for improvements in areas only when needed.

By ensuring the robot can move through a range of motions at specified speeds and accelerations is important for the open-loop pattern following sections of the mastication cycle, but further special requirements are needed for the important occlusion phase where teeth-teeth and food-teeth contact occur. From the previous section it was seen that this occlusion movement is determined by the teeth shape as they mesh together in order to reach maximum intercuspation. This indicates the need to relax position control of the jaw when contact exists and allow teeth shape to guide movements under some form of force control. From the previous section it was shown muscle spindles provide feedback on both displacement and force to the human during mastication. The robotic model will require similar feedback from encoders and force sensors in order to control both position and force.

2.2.4. *Biological Basis*

Due to the fact that the mastication robot is attempting to replicate a biological function that is only partially understood, it is of potential benefit to incorporate as many biological features as reasonably possible. Of particular importance is the motion control side of mastication, which involves the full complexity of the human brain and CNS of which many functions are unknown. By keeping in mind the biological basis we allow for the addition of future discoveries in these unknown fields of the human mastication process to be incorporated into the robotic model at a later stage. With regard to the lower level motion control, the use of similar actuator attachment points to the biological model may allow for analogies to EMG data from human muscles of mastication to be drawn, as well as making future integration of a higher level control system that operates similarly to the biological model a possibility.

2.3. Current Operational Robotic Devices

There have been several robotic devices developed that aim to replicate aspects of the human mastication system. This section reviews the most relevant and summarises their key features with reference to the requirements stated in the previous section.

2.3.1. *WY Series Robots*

The WY series of robotic jaws were developed for treating patients with jaw disorders by assisting the patient during opening and closing movements (Okino et al., 2003; H. Takanobu, Maruyama, Takanishi, Ohtsuki, & Ohnishi, 2000; HU Takanobu & Takanishi, 2003; H. Takanobu et al., 2002). The robots developed during the 1990's and through to 2004, going from a 1-DOF robot into a full 6-DOF robot capable of all movements and forces seen in the human jaw.

The 6-DOF version, named the WY-5, uses six linear ball-screw actuators arranged in parallel fashion. While the robot is capable of 6-DOF's due to its structure, control by a doctor during patient treatment is limited to the 3-DOF's.

Figure 2.5 shows the 6-DOF robot. From the figure it is clear that the robot was made with only predefined functional objectives in mind, and while it may be successful in replicating human motion and force its doesn't have many of the biological characteristics incorporated in its final design. This robot has performed well for treatment of jaw disorders, and with further modifications was able to be used to measure food texture also (www.takanishi.mech.waseda.ac.jp, 2011).

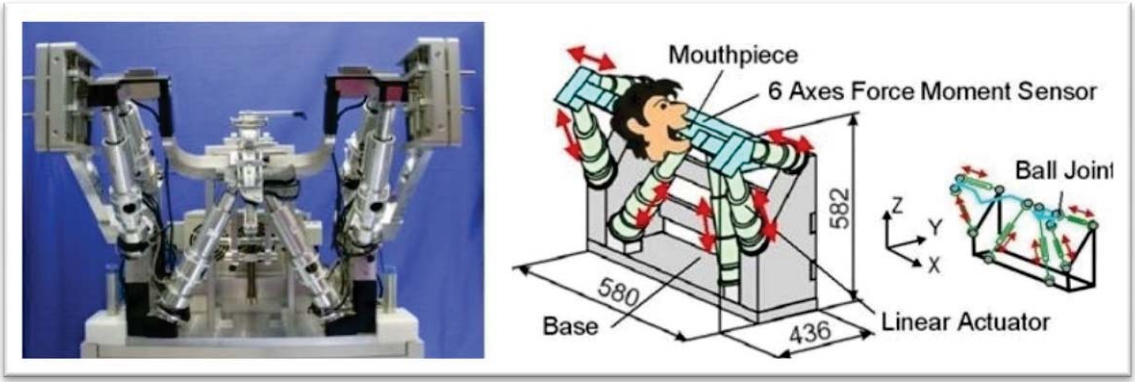

Figure 2.5 WY series of 6-DOF robot (www.takanishi.mech.waseda.ac.jp, 2011)

2.3.2. *WJ Series Robots*

This series of robots were developed in association with the WY series described in the previous section. The WJ robots were made to simulate a human on which the WY robots may operate on (HU Takanobu & Takanishi, 2003; H. Takanobu et al., 2002; H. Takanobu et al., 1998). Unlike the WY series the WJ robots were designed with biological factors considered. The robots used wires as actuators in order to replicate the unidirectional capabilities of human muscles. Separate sets of actuators were required for both closing and opening the jaw. A human like jaw and skull was used and control schemes corresponding to those seen in human chewing was used, with tension sensors on each 'muscle actuator' allowing forces to be accessed through each 'muscle'. Pressure sensors were incorporated into the upper and lower molars. During non-occluding jaw motion, the WJ robotic jaw is under position control, and during occlusion force control is used, a scheme thought to be similar to that in humans.

The 'muscle actuators' which were servo controlled DC motors applying tension to an arrangement of wires, joined the jaw in similar locations as the biological model, however they were not grounded in the same biological locations on the Maxilla. By using biological arrangement of 'muscle actuators' together with load cells, force data acting through each actuator was able to be recorded and related to the human muscles of mastication; however any stresses on the Maxilla are unable to be recorded.

Functionally, from a mastication perspective, the WJ robots were less capable than the WY series robots due to the more complex actuation system. The latest WJ robot was only capable of movements in 3-DOF and was only seen to be capable of tracking several artificial trajectories, unable to cater for more complex 6-DOF movements. While some form of force control is stated in available literature, no evidence of force profile following was seen.

2.3.3. *BITE Master II*

This robot was designed to analyse food textures, aiming to improve on correlations between instrumental texture data and perceived texture by sensory panels. The robot is controlled using stepper motors and is capable of 6-DOF movements, although it is unclear how many DOF are controlled. Force sensors were incorporated to obtain information on food properties during mastication.

Meullenet and Gandhapuneni (2006) fitted dentures modelled on human subjects such that the subjects jaw motion and teeth geometry were matched before performing a single mastication cycle on a food sample. By using the same teeth, trajectory, and food samples as used by the human subject, it was hoped better correlations between force data obtained by the robot and perceived food texture properties by the trained subject would be obtained. Results showed the robots results produced correlations no better than those previously possible with more conventional texture analysers that use 1 DOF motion (Meullenet & Gandhapuneni, 2006).

The BITE Master II attempts to accurately recreate occlusion movements via position control, and allows any forces to occur as a result. By using matched human subject's teeth and trajectory it would seem fair that this approach is taken provided position control, and recreated teeth models were both accurate enough. From the previous sections we have seen the human system to rely more on force control during the teeth guided occlusion phase, and this approach has been taken by the WJ and WY series robots also. Considering the occlusion phase begins 0.5mm from MI position, it's clear that very small movements are involved during the teeth guided phase, and it may be very difficult to rely on pure position control in order to recreate them. Small inaccuracies during the occlusion phase may be to blame for the poor correlations seen between the BITE Master II and perceived forces of human subjects.

Jaw trajectory implementation techniques used with the BITE Master II in (Wynne, 2005) also lead to possibilities of inaccuracies. A single sensor was used to trace 3D movements of the subjects jaw, so angular rotations are not able to be recorded, and true molar trajectories left unknown. It is also unclear how BITE Master II jaw and human subject jaw are aligned together when recreating the trajectory. A small error in alignment of planes could amplify position error at the molar where most forces are expected to occur.

2.4. Limitations of Current Robotic Devices

The current robotic devices outlined in this chapter all fail to produce good co-relations between robot and human assessment of foods. In order to create better co-relations, the robots must be able to re-create the entire suite of human jaw movements. The WY-5 can only be controlled in 3-DOF and the WJ series robots are

only capable of 3-DOF movements also, so replication of real human mastication sequences in 6-DOF is not possible for these devices.

The BITE Master II robot is capable of 6-DOF movements so is capable of re-creating human mastication, but also fails to create good co-relations with human subjects with regards to food property assessment. The BITE Master II does not incorporate many biological aspects into its design, with pure position control throughout the occlusion phase being the most significant difference when compared to the human model. This pure position control results in potentially very large uncontrolled forces during the occlusion phase, and is the likely cause of the poor co-relations with texture perceptions by human subjects.

2.5. Review of Work Done on Massey Robotic Jaw

Massey began research work on creating a robotic chewing device in 2004. Initial interest was from the food technology sector, where potential advantages of a robot to replace sensory panels were significant.

Daumas, Xu and Bronlund (2005) did initial work on examining the human masticatory model and developing an early mathematical model of a robotic device that could be simulated. The resulting passive platform mechanism equipped with linear spring loaded actuators that held the jaw in closed position and allowed manual manipulation to simulate chewing movements.

Daumas et al. (2005) used this initial model to add into Matlab SimMechanics allowing inverse and forward kinematics to be solved, together with results of jaw dynamics through use of existing Matlab functions without the need to specify analytical solutions to dynamic and kinematic models. Inverse kinematics was performed using a Stewart platform leg length generator function in SimMechanics.

Linear actuator locations were based on biological findings in humans, and simulations showed potential for human like jaw motion with this initial model. Control based on SimMechanics simulations using estimated values for jaw and actuator inertia was seen to be challenging.

Pap et al. (2005) attempted to create a mechanical model based on Daumas findings. Pap highlights the problem of fitting linear actuators powerful enough to obtain desired jaw speeds and forces between the locations specified by Daumas on his findings from the biological model. Several solutions were proposed by Pap, including a self designed actuator. The final actuation system was a driven revolute joint followed by two passive spherical joints. Actuator drives together with encoder arrangements were selected to fit with both the motion control system and the final actuation mechanism. More details of this actuation system are given in chapter 3.

Pap modelled the mechanical system, together with the final actuation system in SolidWorks. A lower moving plate to house artificial dentures was formed, with dimensions fitting with the biological model. Mounts for the upper teeth and actuators, analogous to the skull in the human model, were also formed. Details of the final designs are given in the following section. Simulations of the working mechanical system were performed in Solidworks including the implementation of recorded human chewing cycles in 6-DOF as a means to verify physical design. The physical robot was then created, with main structures machined from bullet aluminium. Assembly and passive manipulation of the lower jaw to verify a range of movements completed the physical design aspect.

The initial Solidworks model of the 6-RSS Massey Robotic Jaw designed in 2006 is shown in figure 2.6 below. Key elements in this model were the locations of the 6-RSS actuators such that they mimic the human muscles used in closing the human jaw. The RSS linkages allow for both required actuator speed and force requirements to be met, with each linkage length and line of action comparable to the human model. The 3D co-ordinates of the attachment points of the actuators on the lower jaw were obtained from samples of eight cadavers provided by the School of Dentistry at the University of Otago. The initial model with linkage dimensions and mounting locations allowed work to start on defining robot kinematics which will be covered in detail in chapter 4.

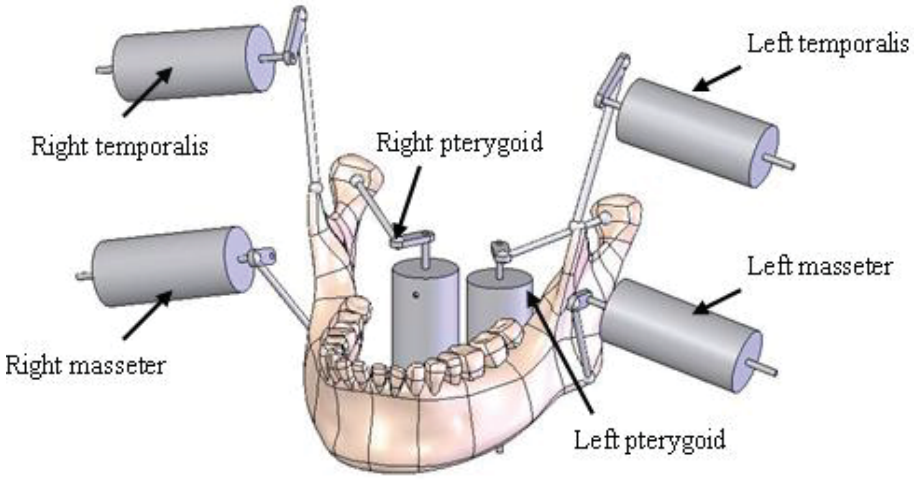

Figure 2.6 Solidworks model of the 6-RSS Massey Robotic Jaw (Pap 2005)

Initial Solidworks model in figure 2.6 above was further modified as specific elements were chosen for the framework, lower and upper jaw, RSS mechanism and driving units. Each component had its own criteria for selection which is outlined below:

2.5.1. *Framework*

Figure 2.7 shows the robot framework on which the other elements are mounted. The framework is loosely analogous to the human skull as it provides a solid stationary base to mount the elements of mastication. The assumption that any displacements of

the human skull due to forces of mastication are insignificant to the mastication process meant the complex shapes and physical properties of the human skull did not need to be considered, and focus was on providing a solid yet relatively compact and lightweight frame.

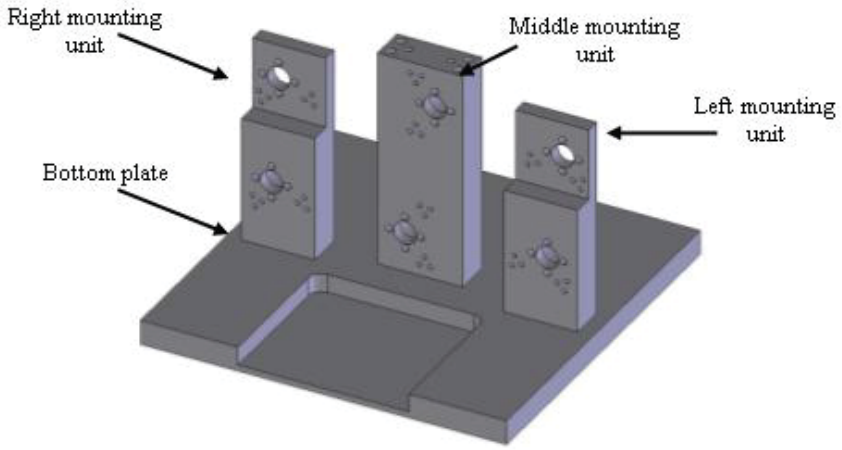

Figure 2.7 The 6-RSS robot framework (Pap 2005)

The frame consists of four main parts: a bottom plate, left, mid and right mounting units. Aluminium was chosen as a material as it provided adequate strength while not being so heavy to making moving the robot overly difficult. A cut away in the bottom plate enable greater range of mandible movement and ensured lower jaw parts could be put on and off without needing to pull entire robot apart. The three mounting units had two dowels together with four bolts to ensure accurate and repeatable alignments upon assembly. The middle mounting unit supported the left and right pterygoid actuators while the left and right units supported left and right masseter and temporalis actuators respectively. The upper jaw was also to be mounted on top of the middle mounting unit, so extra strength considerations leading to extra thickness of material was necessary for the middle mounting unit.

2.5.2. *Lower and Upper Jaw*

Section 2.2.2 outlined the importance of having teeth and jaw geometries that replicate those seen in humans. This was achieved on the MRJ by using a basic study model of teeth from Trimut Corporation, Kyoto, Japan. The basic study model of teeth ensured valid contact points which are essential for accurate occlusion action. The teeth were made from melamine plastic and strong enough for initial chewing tests.

Figure 2.8 below shows the Solidworks model and actual model of the lower jaw, where ML, MR, TL, TR, PL, and PR represent the mounting points for left masseter, right masseter, left temporalis, right temporalis, left lateral pterygoid and right lateral pterygoid respectively. The lower jaw was made from three aluminium parts; the base,

left and right ramus, all locked together using dowels for accurate and repeatable alignments.

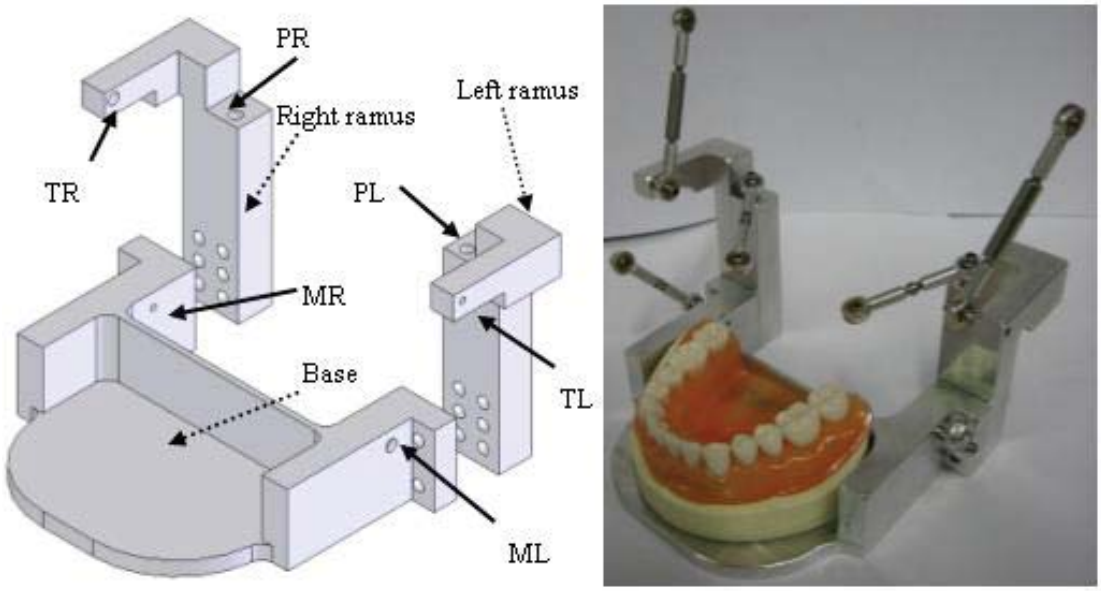

Figure 2.8 The Solidworks model and actual model of the lower jaw (Pap 2005)

The upper jaw consisted of a plate to mount the upper set of teeth via three countersunk screws. A mounting unit and connecting unit were used to mount the upper jaw to the middle mounting unit. Dowels were used for each mate to ensure accurate and repeatable alignment of all elements.

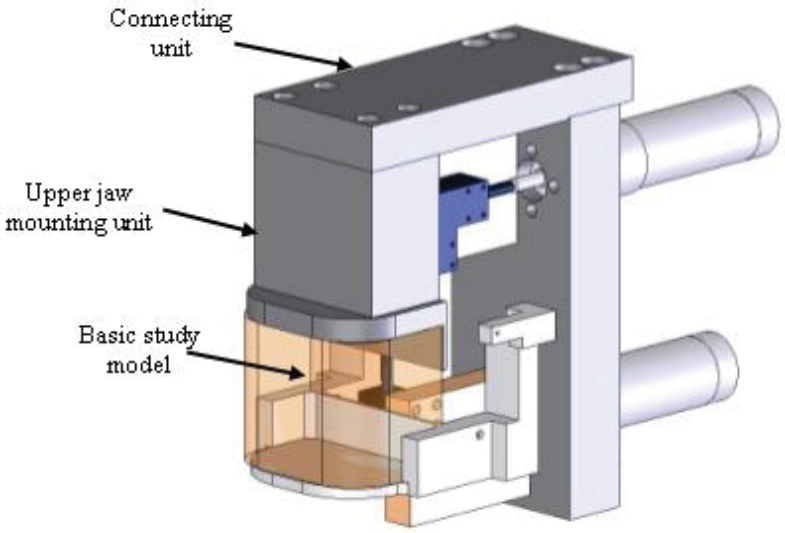

Figure 2.9 Upper jaw, mounting and connecting units (Pap 2005)

2.5.3. *RSS Mechanism*

Figure 2.10 below shows the elements that make up each individual RSS linkage. The two spherical joints are labelled S, the revolute joint labelled R. Dimensions and orientations of the elements each RSS linkage were determined by Pap et al. (2005) by using the biological findings of the human mastication system together with simulations from the earlier model that assumed linear actuators. The couple length represents the length of the linear actuators at jaw closed position. Important initial crank lengths and angles were determined to avoid singularities where the RSS mechanism reached extension or folding of 180 degrees relative to the coupler. The next chapter will look with more detail at the kinematics of the RSS linkages.

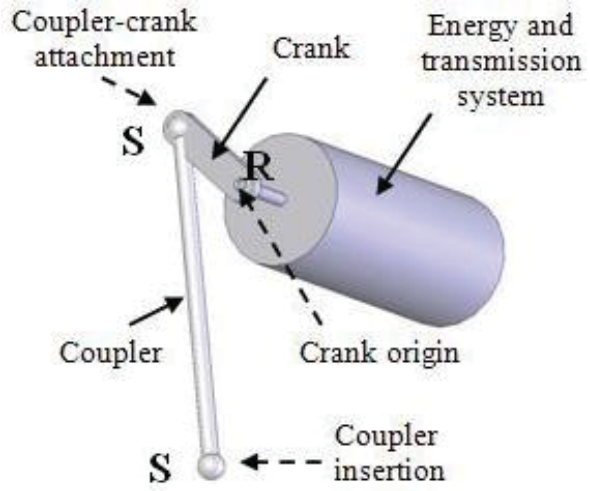

Figure 2.10 The elements that make up each individual RSS linkage (Pap 2005).

Spherical ball joints were required for each end of the couple, and custom cranks needed to be made to joint onto the driven shaft. Cranks were made of mild steel and grub screws allowed attachment to the output shaft of the gearbox. Figure 2.11 shows the coupler with spherical rod ends purchased from a model shop.

Figure 2.11 The coupler with spherical rod ends (Pap 2005)

Static load tests were performed by Pap et al. (2005) to ensure suitability of spherical joints and couplers, which showed results of failure at 988N and an extension of 0.1mm, which was seen as acceptable for this stage of robot development. Figure 2.12 shows the assembling and attachment of crank and couplers via cap screw. Bushings were embedded into the crank and provided dual roles of spacing for the coupler and support for the cap screw to prevent buckling under load. Both bush and cap screw head were bevelled to allow approximately 25 degrees of angular movement laterally.

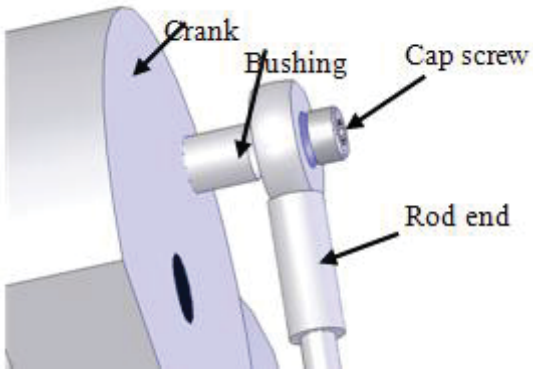

Figure 2.12 The assembling and attachment of crank and couplers via cap screw (Pap 2005)

2.5.4. *Driving Units*

Each of the 6 driving units consists of a DC motor, an encoder, and an inline reduction gearbox. Due to orientations of motors, more compact designs were possible by using bevel gears; these bevels also had the added bonus of taking the axial load off the driving unit components.

The DC motor is a Maxon 60W running off 24V. The motor torque speed curve is shown in figure 3.8 below. Together with a 66:1 inline reduction gearbox, this motor provided the required torque and speed to drive the revolute joint of the crank. The six driving units were mounted on the mounting units using four embedded M3 x 6 cap screws to ensure accurate alignment.

Encoders were available from Maxon also and were able to be installed on the end of the motor shaft. The encoder chosen was a digital MR encoder part number 228452, which had 500 quadrature cycles per rotation, which meant 2000 counts per revolution. Together with the 66:1 reduction this encoder provided maximum possible accuracy of 0.011 degrees, which is sufficient.

In addition to the inline planetary gearbox, bevel gearboxes with 1:1 ratio were fit to allow driving units to be placed neatly behind the robot. In addition to improving the aesthetics of robot, the bevel gears also provided extra protection of axial loads into the planetary gearboxes which were rated to 140N, which may be exceeded during chewing.

2.6 Conclusion

In this chapter I have reviewed the human mastication system and used them to define requirements for a mastication robot. It was seen that there are still many elements to the human mastication system that are not understood in detail, which has lead to an approach that aims to incorporate biological features where possible while still meeting functional level objectives of human mastication. The most relevant existing robotic devices were reviewed and their features compared to the outlined requirements. The balance between functionality and biological integration was seen to be fairly poor for all current robots, with each placing emphasis on one at the expense of the other.

The MRJ has been reviewed in greater detail due to its importance to this thesis. The MRJ to this point has no integrated motion control system and can not provide any functions, and so was reviewed separately to other functional mastication robots. Movements on the MRJ at this point have been simulated in solidworks only.

3. MASSEY ROBOTIC JAW MODIFICATION AND MOTION CONTROL SECLECTION

This chapter covers the modifications required to the physical robot and selection of appropriate motion control hardware.

3.1. Modifications of Physical Robot

Several problems with the initial physical model needed addressing; this section briefly outlines the changes made to the MRJ.

The teeth of the bevel gears were subject to wear and introduced excessive backlash into the robot, particularly on the temporalis and masseter actuators that provide the vertical movements of the jaw. Backlash with the bevels and without was determined experimentally by using a clamp to physically lock the crank and then commanding motion first in one direction then the other. A range of backlashes were seen depending on the degree of wear on the bevel gears. Figure 3.1 and 3.2 below shows scope readings without bevel gears and with the bevel gears respectively. The ideal case of zero backlash would see zero actual position and a position error plot identical to the commanded motion plot. Without the bevel gear, position moved 725 encoder counts or 1.97 degrees at the crank. With the bevel gear the motor shaft was able to move 2968 encoder counts or 8.09 degrees at the crank.

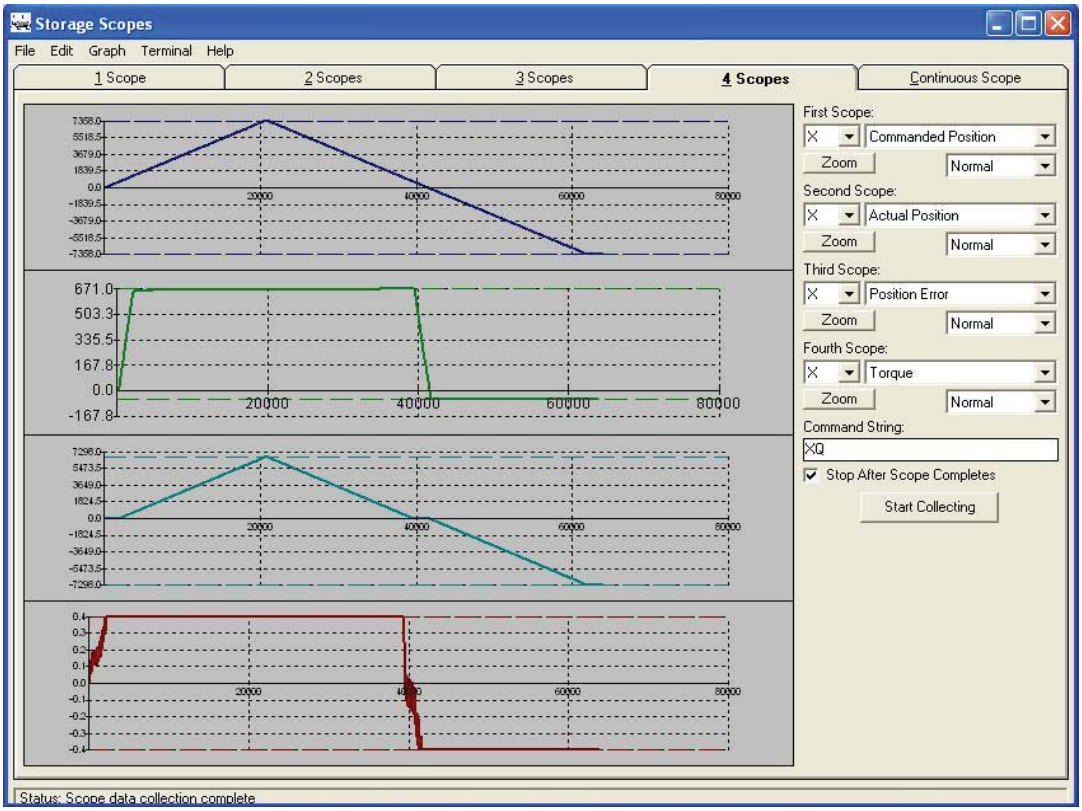

Figure 3.1 Motion scopes during backlash assessment experiment without bevel gearbox

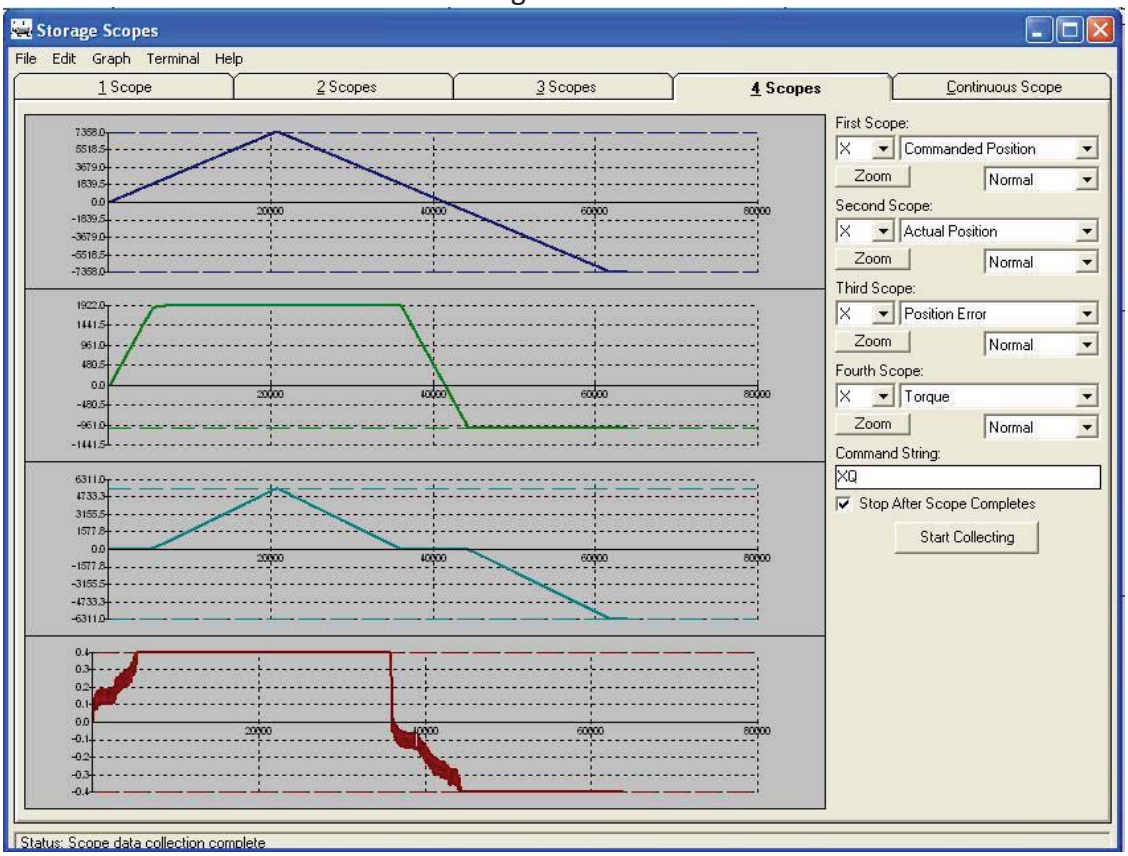

Figure 3.2 Motion scopes during backlash assessment experiment with bevel gearbox

Axial loads which the bevels help isolate against were likely to be less on the masseter and temporalis actuators compared to those on the pterygoid actuators so it was decided to remove bevels on the four masseter and temporalis actuators and mount the driving units directly to the cranks. The problem of fitting the motor and inline gearbox vertically on the pterygoid actuators also influenced the decision to keep the bevels for these two actuators.

During further experiments where real chewing trajectories were reproduced on the MRJ, workspace issues arose during certain robot poses. Initial workspace assessment was done by Pap et al. using a single 6-DOF chewing trajectory to confirm physical parameters. As more trajectories were performed, modifications were made to the lower jaw and cranks to increase workspace (See Figure 3.3). A cut out was made on the lower jaw to allow a greater jaw opening angle. The modified cranks with material were removed to reduce needless workspace restrictions. The MRJ with bevels were removed for the masseter and temporalis actuators, and temporalis cranks machined to allow greater workspace.

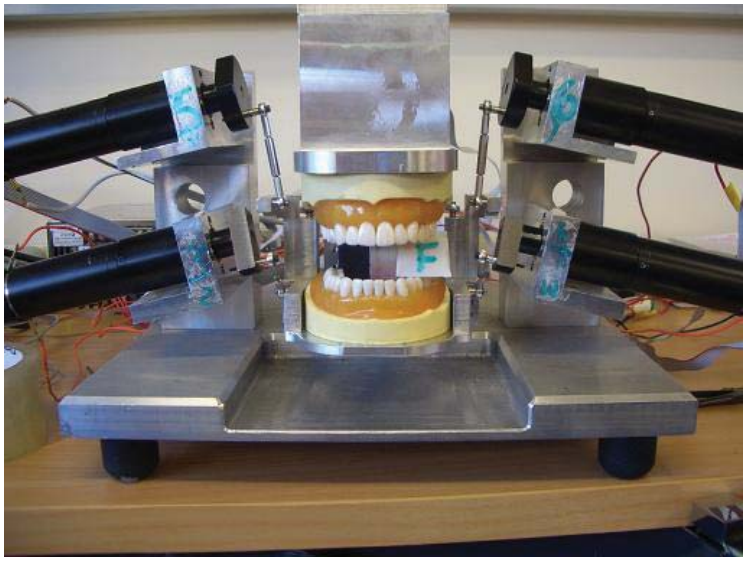

Figure 3.3 The 6RSS robot after modification

3.2. Motion Control System

Selection of a motion control system to use on the MRJ required careful consideration of desired robot functionality and the concurrently selected drive system. A system by Galil Motion Control company was available and had features which enabled all of the required functionality. Specifications of the controller are listed in appendix A. Key features relating the MRJ are listed:

- Able to run six co-ordinated motion control programs simultaneously for each of the MRJ's six actuators.
- Able to accept high frequency encoder; At max speed of 75mm/s (table 2-2) or approximately 360 degrees per second at the crank depending on robot pose, the DC motor moves through 23,760 degrees or 132,000 encoder counts per second. The Galil motion control card allows for up to 12,000,000 encoder counts per second.
- Strong PID tuning software an advantage. The Galil system has a tuning package that allows the MRJ actuators to be tuned automatically using Galil specified tuning algorithms where the whole actuator system can be tuned without need to model individual elements. Point to point tuning method is one of the algorithms provided that is particularly well suited to the MRJ where actuators are tuned to be critically damped allowing accurate tracking of contoured movements.
- Low servo loop update time to enable fast reflex to changing load, particularly important during the occlusion phase on the MRJ where teeth-food and teeth-teeth contact is made. The Galil control card update control signal every 500 µsec which at close to maximum speed of 75mm/s (table 2-2) or approximately 360 degrees per second for the temporalis actuator, the control signal gets updated every 66 encoder counts, or 0.18 degrees at the crank. This equals 0.047mm of sector length travelled for the 15mm crank on the temporalis actuator (less on all other actuators). This means that if the jaw is moving at maximum speed and hits a hard food, the temporalis actuator would travel only 0.047mm into the hard food before the control signal responded, other actuators have lower specified maximum speeds (table 2-2) so would travel an even smaller distance.

Figure 3.4 below shows the robot together with the Galil motion control system consisting of the control card in the PCI slot of the computer, two amplifiers capable of driving 4 axis each, and a 500W DC power supply. Smart terminal is Galil supplied software. All hardware specifications are included in appendix A.

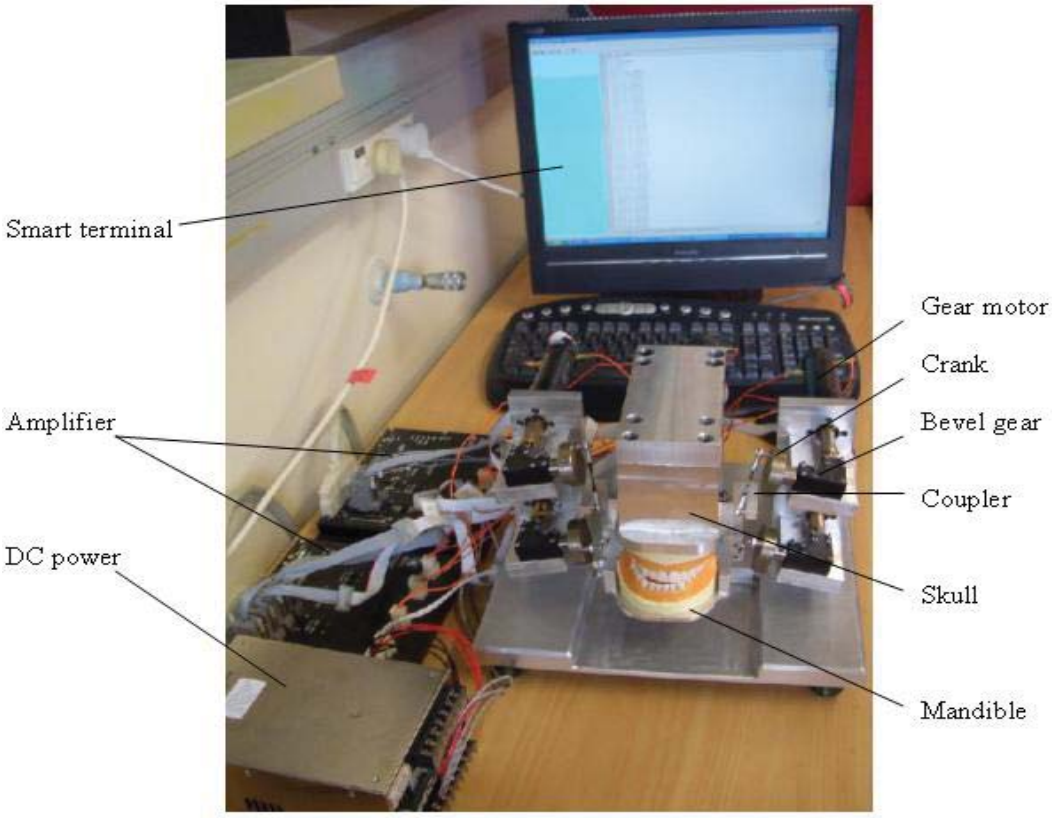

Figure 3.4 The robot with the motion control system

4. INVERSE KINEMATICS AND MOTION CONTROL OF THE MRJ

In order to perform targeted movements of the MRJ, inverse kinematics of mechanism need to be solved. Target movements of the lower jaw can then be translated to six individual movements of each actuator. The synchronised motion of all six actuators can then be implemented using appropriate motion control to create the desired motion at the lower jaw. The inverse kinematics calculation and motion control of actuators will be detailed in this chapter.

4.1. Review of Kinematics of Parallel Robots

Kinematics is the study of motion without regard to the forces creating it. Forward kinematics is the study of how movements of actuators relate to movement at the end-effector. For six limbed parallel mechanisms such at the MRJ, forward kinematics can be challenging, and no closed form analytical solution exists. Figure 4.1 below gives an illustration of how the forward kinematic problem relates to a parallel 6RSS mechanism such as the MRJ. Here we are given six fixed and known positions, S1 through to S6 in the figure below, which represent the attachment point of the spherical joints of each linkage to the cranks of the six actuators on the MRJ. The forward kinematic problem aims to find locations M1 through to M5 on each of their workspace spheres shown in grey such that alignments with fixed attachments locations on the end-effector can be obtained for all linkages. If we take the corners of the hexagon in figure 4.1 as the locations on the end-effector of attachment points, you can get a sense of how this may be done on the physical mechanism by attaching one corner, then the next, but in doing so moving the previously attached points. Poorly chosen initial position of the first attachment point can make attaching the rest impossible if singularities are met.

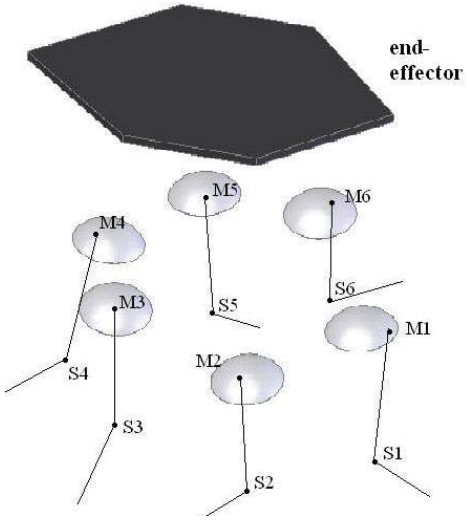

Figure 4.1 End-effector with six spherical joints of each linkage

The problem can be solved mathematically using numerical methods only. SolidWorks Cosmos motion in solidworks uses undisclosed numerical methods to solve the forward kinematics of the MRJ by allowing six trajectories of the actuators to be specified and running a simulation. By selecting trace path locations on the lower jaw, the resultant displacement-time plots of the lower jaw can be obtained. Because forward kinematics was not seen as important in motion control of the MRJ, and only to be used in offline analysis, it was decided to not attempt to form an algorithm to solve the forward kinematics numerically.

The inverse kinematics problem involves finding the six crank angles for any given lower jaw pose. Obviously the formation of inverse kinematics is essential before any defined jaw trajectory can be replicated. For parallel robots, the inverse kinematic solution is less difficult. In the case of the MRJ, the robot pose is given, and points M1 through to M6 in figure 4.1 can be directly found reducing the problem to the inverse kinematics of six individual RSS linkages.

Kinematic parameters and coordinate systems are defined and detailed inverse kinematic solutions are given in the following sections.

4.2. Co-ordinate Systems of MRJ

Before any meaningful kinematic descriptions can be given, we first must define points of interest and co-ordinate frames. Figure 4.2 below shows the MRJ moved by 6 RSS type actuators, each actuator consisting of a driver unit (Di, i = 1,2,…6), crank (Ci, i = 1,2,…6), and coupler link (Li, i = 1,2,…6). The three joints are a revolute at the actuators ground point where the driving shaft connects to the crank (Gi, i = 1,2,…6), a spherical joint where the crank joins to the coupler linkage (Si, i = 1,2,…6), and a final spherical joint where the coupler linkage joins to the mandible (Mi, i = 1,2,…6).

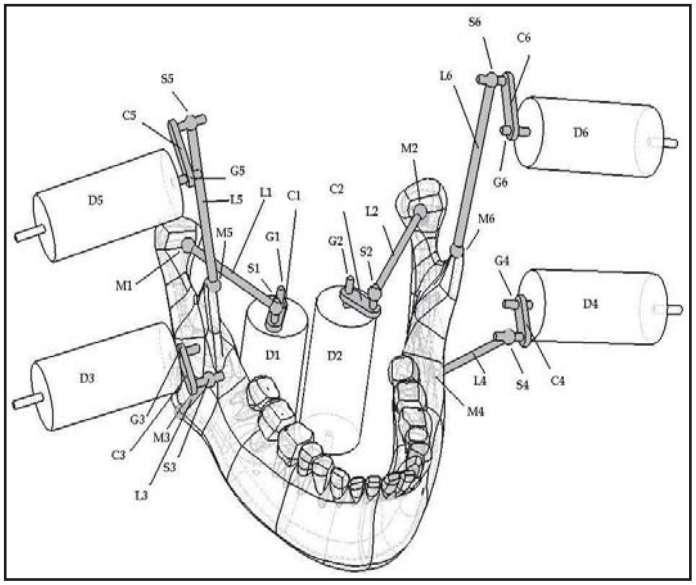

Figure 4.2 Robotic model with six actuators

Figure 4.3 shows the location and orientation of the two major frames, the skull frame $OXYZ_S$ fixed to the skull and the mandible frame $OXYZ_M$ fixed to the mandible.

The mandible frame is placed at the bottom of the mandibular incisor and has a sagittal plane (X-Z plane), a frontal plane (Y-Z plane) and a horizontal plane (X-Y plane). The mandible relative to the skull can be defined by a homogenous transform ${}^{S}_{M}T$.

$$ {}^{S}_{M}T = \begin{bmatrix} c\alpha c\beta & c\alpha c\beta s\gamma - s\alpha c\gamma & c\alpha s\beta c\gamma + s\alpha s\gamma & {}^{s}O_{mx} \\ s\alpha c\beta & s\alpha s\beta s\gamma + c\alpha c\gamma & s\alpha s\beta c\gamma - c\alpha s\gamma & {}^{s}O_{my} \\ -s\beta & c\beta s\gamma & c\beta c\gamma & {}^{s}O_{my} \\ 0 & 0 & 0 & 1 \end{bmatrix} \quad (1) $$

in which ${}^{s}O_{m} = ({}^{s}O_{mx}\ {}^{s}O_{my}\ {}^{s}O_{mz})^{T}$ is the origin of {M} with respect to {S} and (γ, β, α) are roll-pitch-yaw rotational angles about skull's x-, y- and z- axis, respectively. They represent three-dimensional motion of the mandible depicted in {S}. When the mouth is at the closed configuration, $({}^{s}O_{mx}\ {}^{s}O_{my}\ {}^{s}O_{mz})^{T} = (-6.09\ -0.07\ -20.17)^{T}$ and ($\gamma, \beta,$ α)=($0^{o}, 3^{o}, 1.5^{o}$) for the built robot.

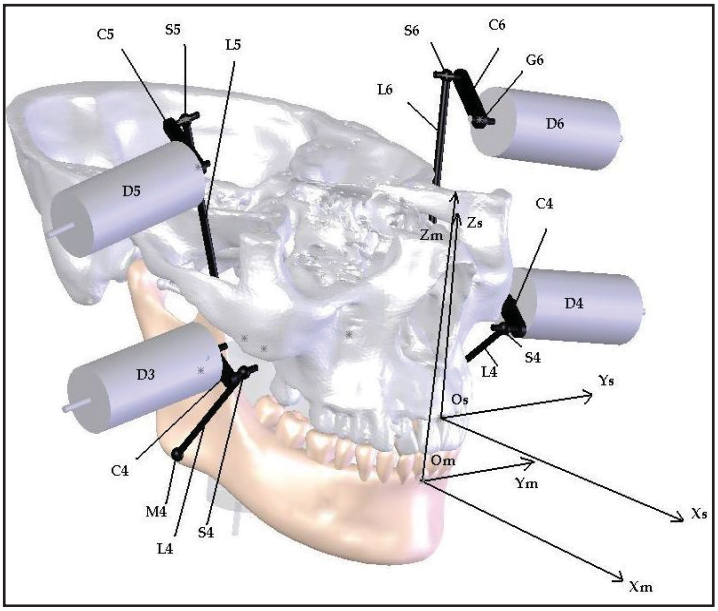

Figure 4.3 The two major co-ordinate systems, skull and mandible.

In addition to the two main frames seen in figure 1.2 above, I also have 6 frames {Ci}, $i = 1,2,...6$ for the 6 RSS actuators. The crank frames are fixed on the crank, with origin being at the point G_i, point S_i lying on the $X_{C.i}$ axis, and axis Z_i running through the centre of the driver unit.

Each RSS linkage is described in its own frame, or crank frame. Figure 3 illustrates crank frame 5, or {*C*5} for linkage 5, with the origin being at the pivotal point G_5, *x*-axis being along $G_5\ S_5$, *z*-axis running through the rotational axis of the crank and *y*-axis completing the system. A crank frame {Ci} is expressed in relation to the skull frame {S},

$$ {}^{S}_{Ci}T = \begin{bmatrix} c\alpha_i c\beta_i c\theta_i - s\alpha_i s\theta_i & -c\alpha_i c\beta_i s\theta_i - s\alpha_i c\theta_i & c\alpha_i s\beta_i & {}^{s}G_{xi} \\ s\alpha_i c\beta_i c\theta_i + c\alpha_i s\theta_i & -s\alpha_i c\beta_i s\theta_i + c\alpha_i c\theta_i & s\alpha_i s\beta_i & {}^{s}G_{yi} \\ -s\beta_i c\theta_i & s\beta_i s\theta_i & c\beta_i & {}^{s}G_{zi} \\ 0 & 0 & 0 & 1 \end{bmatrix} \qquad (2) $$

where the upper left 3x3 matrix is a Z-Y-Z Euler rotational matrix with angles in order α_i, β_i, and θ_i measured in frame {Ci} and ${}^{s}G_i = ({}^{s}G_{xi}\ {}^{s}G_{yi}\ {}^{s}G_{zi})^T$ is the origin of frame {Ci} in the frame {S}. The parameters α_i, β_i and ${}^{s}G_i$ are determined by the built robot and the angle θ_i is the only variable for actuation. The valuType equation here.es of all the deterministic parameters for the built robot are given in Table 4-1. The initial crank angles of zero values, as the reference, are defined at the mouth closed configuration. Figure 1.3 shows how the crank frames are located and orientated on the crank.

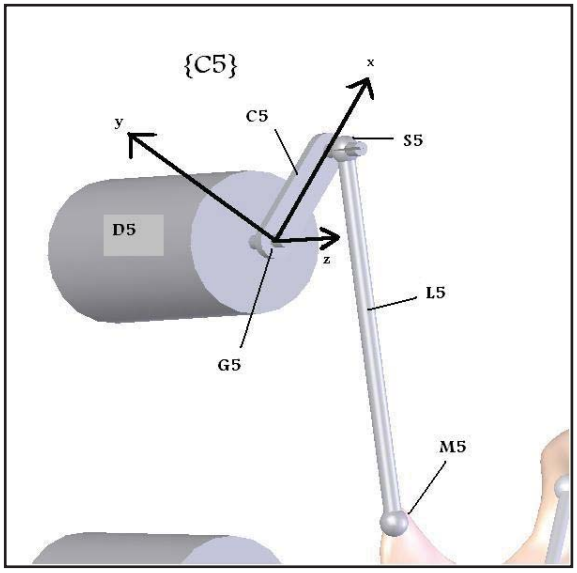

Figure 4.4 Location and orientation of crank frame 1

4.3. Kinematic Parameters of MRJ

Having defined points of interest and co-ordinate systems, we can now define the kinematic parameters of the MRJ in the aforementioned co-ordinate systems.

The parameters of the six RSS linkages are given in Table 4-1. The initial crank angles of zero values are defined at the mouth closed configuration. The coordinates of coupler point M_i (i=1,2,…, 6) in the mandible frame {M}, the coordinates of the other couple point S_i (i=1,2,…, 6) in its linkage frame $\{C_i\}$, and the length of each coupler S_iM_i (i=1,2,…, 6) are given in Table 4-2.

Table 4-1 Parameters for six linkage frames defined in CAD drawings

	Frame {C1}	**Frame {C2}**	**Frame {C3}**	**Frame {C4}**	**Frame {C5}**	**Frame {C6}**
Gx	-70.28	-70.92	-38.50	-41.63	-53.36	-56.36
Gy	-14.04	10.42	-60.91	58.89	-58.69	55.74
Gz	6.72	6.75	16.31	16.47	66.31	66.46
α	0.00	1.97	90.18	-87.99	89.14	-87.86
β	2.99	2.50	80.09	80.21	75.03	77.81
θ	θ_1	θ_2	θ_3	θ_4	θ_5	θ_6

Table 4-2 Other kinematic parameters for the built robot

	M_1	M_2	M_3	M_4	M_5	M_6	S_1	S_2	S_3	S_4	S_5	S_6
x	-79.75	-79.75	-60.85	-60.85	-53.25	-53.25	10.00	10.00	10.00	10.00	15.00	15.00
y	-41.10	41.10	-44.70	44.70	-43.00	43.00	0.00	0.00	0.00	0.00	0.00	0.00
z	38.77	38.77	-5.83	-5.83	43.87	43.87	0.00	0.00	0.00	0.00	0.00	0.00
Coupler	l_1=33.90		l_2=33.90		l_3=49.90		l_4=49.90		l_5=52.26		l_6=52.26	
Crank	c_1=10		c_2=10		c_3=10		c_4=10		c_5=15		c_6=15	

4.4. Closed Form Solution to Inverse Kinematics of MRJ

The inverse solution is to find a set of actuation angles, θ_i (i=1,2, .., 6), given the mandible movement in relation to the skull, i.e., ${}^{S}_{M}T$ in Eq. (1). The inverse solution for the robot can be derived as follows. On one hand, the vector G_iM_i can be found explicitly (Figure 3),

$$G_iM_i = G_iO_s + O_sO_m + O_mM_i \tag{3}$$

where the first term is determined by the location coordinates of G_i on the skull (Table 4-1); the second term is given by the prescribed mandible movement with respect to the skull, Eq.(1); and the third term is determined by the location of M_i on the mandible (Table 4-2). On the other hand, the vector G_iM_i can also be expressed by,

$$G_iM_i = G_iS_i + S_iM_i \tag{4}$$

in which G_iS_i is the crank vector and S_iM_i is the couple vector.

Substituting Eq. (3) into (4) yields,

$$S_iM_i = G_iM_i - G_iS_i \tag{5}$$

and further squaring the norm of the above vector equation gives,

$$\|S_iM_i\|^2 = \|G_iM_i\|^2 - 2G_iM_i \bullet G_iS_i + \|G_iS_i\|^2 \tag{6}$$

in which $||S_iM_i||=l_i$ is the coupler length (Table 4-2), $||G_iS_i||=c_i$ is the crank length (Table2), and $||G_iM_i||$ is calculated by Eq. (3).

Letting $r_i = -(l_i^2 - c_i^2 - \|G_iM_i\|^2)/2$, which is known up to this point, Eq. (6) can be re-arranged as,

$$G_iM_i \bullet G_iS_i = r_i \tag{7}$$

According to Eq. (3), the vector G_iM_i is calculated in {S},

$$G_iM_i = \begin{bmatrix} GM_{xi} \\ GM_{yi} \\ GM_{zi} \end{bmatrix} = -{}^{S}\begin{bmatrix} G_{xi} \\ G_{yi} \\ G_{zi} \end{bmatrix} + {}^{S}\begin{bmatrix} O_{mx} \\ O_{my} \\ O_{mz} \end{bmatrix} + {}^{S}_{M}R \; {}^{M}\begin{bmatrix} M_{xi} \\ M_{yi} \\ M_{zi} \end{bmatrix} \tag{8}$$

in which all the terms are known according to Table 4-1, 4-2 and Eq. (3).

The vector G_iS_i is expressed in {S},

$$G_iS_i = \begin{bmatrix} GS_{xi} \\ GS_{yi} \\ GS_{zi} \end{bmatrix} = {}^{S}_{C_i}R \; {}^{C_i}\begin{bmatrix} S_{xi} \\ 0 \\ 0 \end{bmatrix} = S_{xi}\begin{bmatrix} c\alpha_i c\beta_i c\theta_i - s\alpha_i s\theta_i \\ s\alpha_i c\beta_i c\theta_i + c\alpha_i s\theta_i \\ -s\beta_i c\theta_i \end{bmatrix} \tag{9}$$

in which S_{xi}, α and β are the known robotic parameter in Table 4-1 and 4-2.

Putting Eq. (8) and (9) onto Eq. (7) results in,

$$a\cos\theta_i + b\sin\theta_i = c \tag{10}$$

in which

$$a = GM_{xi}c\alpha_i c\beta_i + GM_{yi}s\alpha_i c\beta_i - GM_{zi}s\beta_i$$

$$b = -GM_{xi}s\alpha_i + GM_{yi}c\alpha_i$$

$$c = r_i / S_{xi}$$

Eventually, the two inverse solutions are found,

$$\theta = \tan^{-1}(b/a) \pm \tan^{-1}(\sqrt{a^2 + b^2 - c^2}/c) \tag{11}$$

4.5. Solving for a Chewing Trajectory in Matlab

Equation 11 gives the solution to the inverse kinematics of the MRJ. For a series of jaw movements in 6DOF over time, the inverse kinematic solution needs to be found at every time step.

Matlab was used to implement each of the six inverse kinematic solutions for the each of the six actuators. Six m-files, solvey*i.m* (i=1,2..6) were formed using eq. (11) with kinematic parameters that corresponded to the actuator being solved. Another m-file, inversesolve.m, was formed to solve a series of robot poses in 6DOF.

'Inversesolve.m' takes a CSV file containing a jaw trajectory in terms of three position elements (x, y, z) and three angular elements (roll, pitch, yaw), and returns the 6 individual trajectories for the 6 crank mechanisms. The input CSV file must contain only numbers and the data listed from columns 1 to 6 respectively as roll, pitch, yaw, translation x, y, and z. All input data must be with respect to the mandible frame at the jaw closed position. The next chapter illustrates methods of obtaining jaw trajectory data and converting it into forms that can be easily implemented on the MRJ. An overview of inversesolve.m is given below. All m-files are included in appendix CD.

INPUT:

- User defined CSV file containing the jaw trajectory.

PROCESSING:

1. csvread.m is called to put trajectory data into a matrix in Matlab.
2. Starting at first point, convertTM.m is called to change the 6 input elements of the trajectory into a 4 by 4 transformation matrix so can be used by solvey.m.
3. solvey1.m through to solvey6.m are called to return the 6 crank angles.
4. Increment to next point in trajectory and loop back to step 2 until all points have been processed.
5. Solutions are saved in a matrix of 6 columns, one for each crank trajectory, and written to a CSV file.

OUTPUT:

- 6 individual trajectories for the 6 crank mechanisms in the form of a 6 column matrix (length determined by number of points in trajectory).

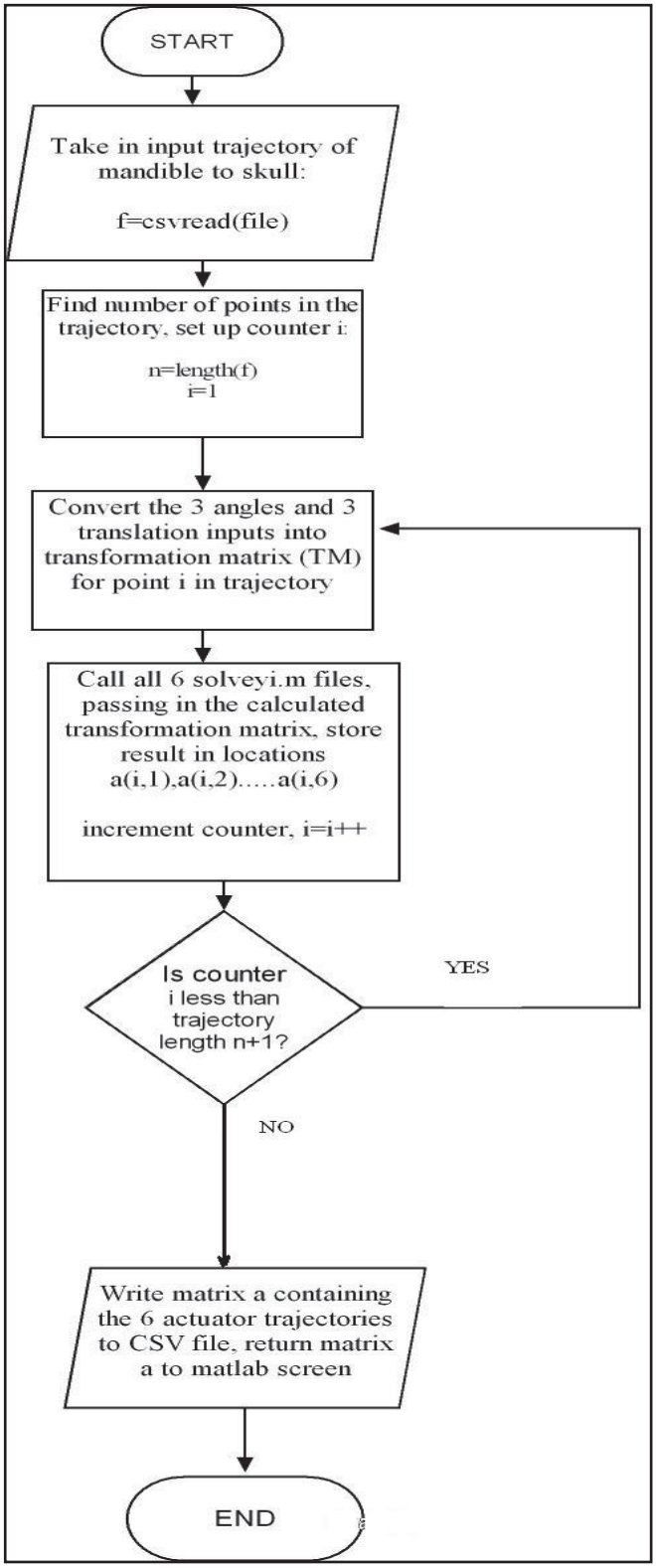

Figure 4.5 Flowchart of intersolve.m M-file

SolidWorks cosmos motion is also able to provide inverse kinematics solutions by running a simulation and recording traces on each of the actuators, and was used to successfully validate the inverse kinematic solutions found in Matlab.

4.6. Jacobian and Singularity Analysis

From a RSS linkage, the velocity of point S_i on the coupler in frame $\{C_i\}$ can be found by

$$^{C_i}V_{S_i} = -(^{C_i}GS_i \times ^{C_i}z_i)\dot{\theta}_i \tag{12}$$

where $^{C_i}V_{S_i}$ is the velocity of S_i in $\{C_i\}$; $^{C_i}GS_i$ is the vector in $\{C_i\}$; $^{C_i}GS_i \times$ is a 3x3 skew-symmetrical matrix of the respective vector; $^{C_i}z_i$ is the axis of crank i in $\{C_i\}$; and $\dot{\theta}_i$ is a scalar quantity of crank angular velocity.

Projecting this velocity along the coupler yields a scalar V_{ms_i},

$$V_{ms_i} = -^{C_i}MS_i^T \bullet ^{C_i}V_{S_i} = -^{C_i}MS_i^T \bullet (^{C_i}GS_i \times ^{C_i}z_i)\dot{\theta}_i \tag{13}$$

in which $^{C_i}MS_i$ is a vector from point M_i to S_i in $\{C_i\}$.

Given linear velocity $^{M}V_m$ and angular velocity $^{M}\Omega_m$ of the mandible, expressed in $\{M\}$, the velocity of point M_i on the coupler can be found (Figure 4.3),

$$^{M}V_{M_i} = ^{M}V_m - ^{M}O_mM_i \times ^{M}\Omega_m \tag{14}$$

where $^{M}V_{M_i}$ is the velocity of M_i in $\{M\}$; $^{M}O_mM_i$ is the vector from O_m to M_i; and $^{M}O_mM_i \times$ is a 3x3 skew-symmetrical matrix of the respective vector.

Projecting this velocity along the coupler yields also a scalar V_{ms_i},

$$\begin{aligned} V_{ms_i} &= ^{M}MS_i^T \bullet ^{M}V_{M_i} = ^{M}MS_i^T \bullet (^{M}V_m - ^{M}O_mM_i \times ^{M}\Omega_m) \\ &= ^{M}MS_i^T \bullet ^{M}V_m - ^{M}MS_i^T \bullet ^{M}O_mM_i \times ^{M}\Omega_m \end{aligned} \tag{15}$$

Since both points S_i and M_i are on coupler *i* and the coupler is a rigid body, the two scalars in Eq. (13) and (15) are identical, i.e.,

$$-^{C_i}MS_i^T \bullet (^{C_i}GS_i \times ^{C_i}z_i)\dot{\theta}_i = ^{M}MS_i^T \bullet ^{M}V_m - ^{M}MS_i^T \bullet ^{M}O_mM_i \times ^{M}\Omega_m \tag{16}$$

Since the robot involves 6 RSS linkages, repeating Eq. (16) for *i*=1,2,…, 6, and assembling them yields,

$$\begin{bmatrix} -{}^{C_1}MS_1{}^T \bullet ({}^{C_1}GS_1 \times {}^{C_1}z_1) & 0 & \cdots & 0 \\ 0 & -{}^{C_2}MS_2{}^T \bullet ({}^{C_2}GS_2 \times {}^{C_2}z_2) & \cdots & 0 \\ \vdots & \vdots & \cdots & \vdots \\ 0 & 0 & \cdots & -{}^{C_6}MS_6{}^T \bullet ({}^{C6}GS_6 \times {}^{C_6}z_6) \end{bmatrix} \bullet \begin{bmatrix} \dot{\theta}_1 \\ \dot{\theta}_2 \\ \vdots \\ \dot{\theta}_6 \end{bmatrix}$$

$$= \begin{bmatrix} {}^{M}MS_1{}^T & -{}^{M}MS_1{}^T \bullet {}^{M}O_mM_1 \times \\ {}^{M}MS_2{}^T & -{}^{M}MS_2{}^T \bullet {}^{M}O_mM_2 \times \\ \vdots & \vdots \\ {}^{M}MS_6{}^T & -{}^{M}MS_6{}^T \bullet {}^{M}O_mM_6 \times \end{bmatrix} \begin{bmatrix} {}^{M}V_m \\ {}^{M}\Omega_m \end{bmatrix} \tag{17}$$

Denoting $\dot{\Theta} = (\dot{\theta}_1\ \dot{\theta}_2 \ldots \dot{\theta}_6)$ and $\dot{X} = ({}^{M}V_m\ \ {}^{M}\Omega_m)^T$ the above equation becomes

$$J_\theta \dot{\Theta} = J_x \dot{X} \tag{18}$$

in which J_θ and J_x are called inverse and forward kinematic Jacobian matrices, respectively. They can be calculated easily once the inverse solution has been made available.

Eq. (18) shows the relationship between the crank angular velocity ($\dot{\Theta}$) and the mandibular velocity ($\dot{X}$). When either of the two Jacobian matrices is singular, the robot is in a singular configuration where one or more degrees of freedom are uncontrollable instantaneously.

Letting $\|J_\theta\| = 0$ easily yields the singular configurations at which a coupler MS_i is normal to the y-axis of frame {Ci}, i.e. coupler MS_i and crank GS_i are folded in a line. In the motion planning, the robot should be commanded to avoid this singular configuration.

Each row of J_x is made up of a vector of coupler MS_i and a vector that is normal to both O_mM_i and MS_i. Hence, as long as the couplers are not parallel to each other, each row of vector will be independent and consequently the forward Jacobian J_x will never become singular. The robot was so designed without having this singularity at all as motion becomes physically constrained before any crank can become parallel to its linkage.

4.7. Review of Motion Control

Having established methods of defining required trajectories of individual actuators in the MRJ, we now turn our attention to the implementation of such motion using motion control techniques. This section reviews motion control and relates it to MRJ control problem.

Motion control in context of the MRJ involves position control during the non-occluding phases of the mastication cycle. Force control is then enabled as food-teeth and teeth-teeth contact is made. This section will only look at motion control how it relates to pure position control of the lower jaw. Chapter 7 will cover force control as it relates to the MRJ.

4.7.1. *Linear and Non-Linear PID Control*

Figure 4.6 below shows the PID control loop (Martin, 2001). PID control takes feedback from an encoder or tachometer, and forms a corrective control signal based on the current magnitude of the error (proportional gain), the accumulated sum of past errors (integral gain) and on how fast the error is changing (differential gain). Linear PID control assumes the system being controlled can be modelled by linear differential equations, while non-linear PID control is required when the system cannot be estimated as linear.

Because the MRJ's inertia varies with time depending on its pose during a trajectory, and the fact that there is a high degree of coupling between the six actuation units, the system is considered non-linear. The non-linearity of the system means the control loop below would only work perfectly at any one time instant that the PID constants had been tuned for. There are several approaches to allow PID control of such a non-linear system; many require accurate knowledge of the dynamics of the robot.

Craig in introduction to robotics describes several methods of dealing with non-linear systems. Local linearization is an approach that can be taken when nonlinearities are no severe. Local linearization uses linear approximates of the system in the neighbourhood of the operating point. For the MRJ this approach has some merit as most chewing movements are contained in a relatively small workspace.

Another approach for control of non-linear systems is to include a linearization block in the feedback loop. The linearization block cancels out the nonlinearity of the system leaving the closed loop overall linear and able to be controlled using linear PID control. This method requires an accurate system model to be formed in order to predict and cancel out nonlinearities as the manipulator moves throughout the workspace.

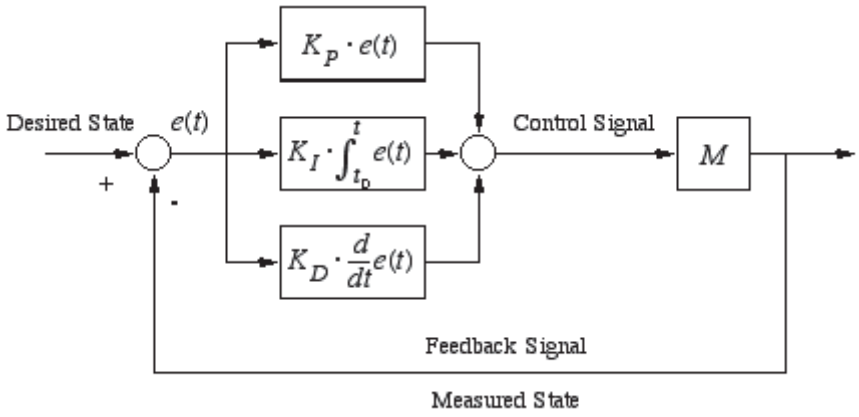

Figure 4.6 PID control loop (Martin, 2001)

Fuzzy adaptive PID control is another type of algorithm used to deal with non-linear systems. PID constants can be tuned for various positions and or loads and be updated (adapt) during motion as the robots operating conditions change. For the MRJ, adaptive control would allow different sets of PID control between opening and closing phases, where target loads and speeds required of the robot vary.

In approximating any non-linearity, the approach of over-damping the system is considered conservative and prudent. By setting PID constants for maximum possible loads, the system is likely to remain in control during all commanded motion, the sacrifice being less than optimal performance during some portions of the motion (Craig, 1989).

4.7.2. *Modelling MRJ Actuators*

Craig (1989) defines a model of a geared DC motor with load, comparable to each of the six actuators of the MRJ. Craig states that with a current amplifier driver such as the AMP19540 used in the Galil control system of the MRJ, we can assume actuators are pure torque sources and can be controlled directly through the scaling of the motors torque constant.

Effective inertia of the geared DC motor with load is defined in equation below.

$$\text{Effective inertia} = I + n^2.\ I_m$$

Where I is the load inertia, in this case a portion of the inertial of the mandible and linkages, I_m is the inertial of the motor rotor, and n is the gear ratio.

Inertia of the motor rotor of the Maxon motors used in the MRJ is $33\ \text{gcm}^2$ (appendix A), and the gear ratio is 66, giving the second term in equation above equal to $143748\ \text{gcm}^2$.

The total mass of the lower jaw of the MRJ is 155g, its inertia dependent on which axis of rotation are chosen and is shared between all six actuators. Assuming even distribution of mass over the four actuators responsible for vertical movements, and assuming $I = MR^2$ for point mass acting at right angles to each crank, we have inertia of $87\mathrm{gcm}^2$. It can be seen that the motor inertia acting before the gear reduction represents a significant portion of the total effective inertia seen at each crank. Changes in load inertia due to dynamics of the moving lower jaw during free motion are not likely to change the total effective inertia seen at each of the driving DC motors by any significant amount. For the purpose of the next section, I have assumed each DC motor can be modelled as linear and any changes in load inertia can be handled as disturbances and do not need to be catered for in the control scheme.

4.8. Implementing Individual PID Control in Galil

This section illustrates the application of the Galil motion control system described in chapter 3 to the MRJ motion control problem.

Because trajectories are of complex shape, and are recorded by sampling discrete points over time, using a point-to-point control scheme is most suited. Galil provides a contour mode, where a constant time difference is specified, and an incremental position change over that time window is implemented on each axis. This allows complex paths to be followed, and by specifying small enough time differences, smooth motion can be re-created. A range of time differences were specified during motion commands in contour mode from 2ms to 32ms.

WSDK software allowed PID constants to be tuned for each of the actuators. WSDK servo design kit allows several different tuning algorithms to be run to select the best PID values. Because our motion involves traversing many discrete points over time, the 'point-to-point' tuning method proved most suitable. This method allows an error limit/tolerance to be specified and finds the PID constants that result in the fastest settling time. The robot was then run using a trajectory already simulated in SolidWorks, first without food, then with food acting as a disturbance.

The next section shows results from these experimental runs on the MRJ.

4.8.1. *Position Control No Load*

The motion in Fig 4.7 below was performed with no food in the jaw and upper jaw removed so there is no additional load on the lower jaw. Results show position errors within 1 degree, and control signal reaching 2.2V out of a maximum of 10V. Amplifier gain of 0.7A/V gives maximum current of 1.54A.

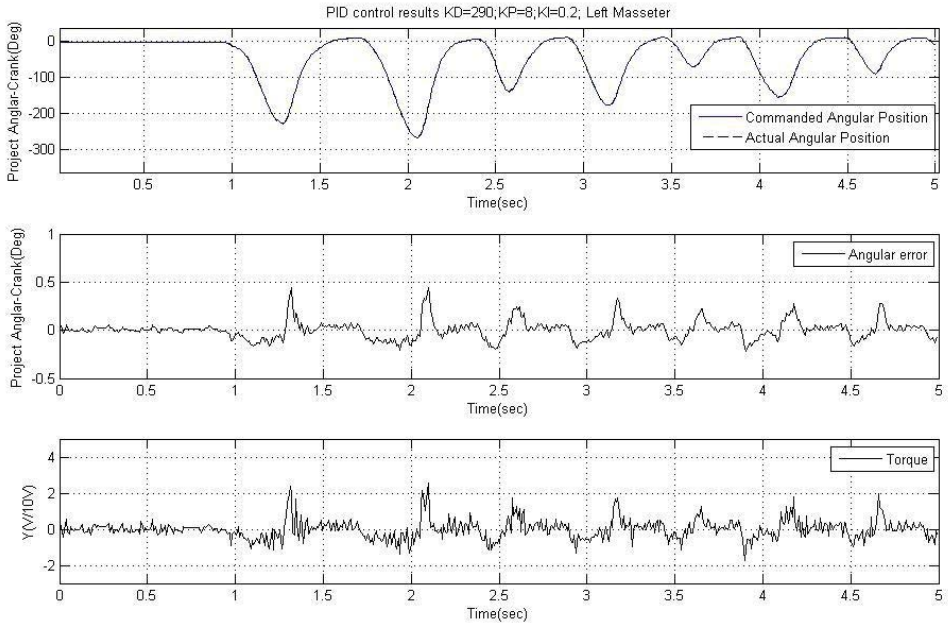

Figure 4.7 Position, Position Error, Control signal, Crank velocity, and Crank Acceleration Results Running 'Motion 2003' for First Seven Chewing Cycles on Left Masseter actuator.

Experimental runs with all actuators remaining within 1 degree of position error proved a satisfactory initial low level position control of the MRJ.

4.8.2. *Position Control Load Disturbance*

While position control of the MRJ was intended for free motion during non-occluding phase of the MRJ, it was thought worthwhile to test the robustness of the individual PID control of each actuator to various levels of external disturbance. It was expected that as external load increased, position errors would arise as the tuned PID constants became less efficient at reducing errors to zero.

Figure 4.8 below shows results of experiments using the MRJ to chew foam, Bluetac and a hard cover book. Errors increased but not by a significant amount and the MRJ remained under control during the experiment with no control signal exceeding the 10V maximum. Further experiments using the individual PID control scheme will be detailed in chapters 6 and 7.

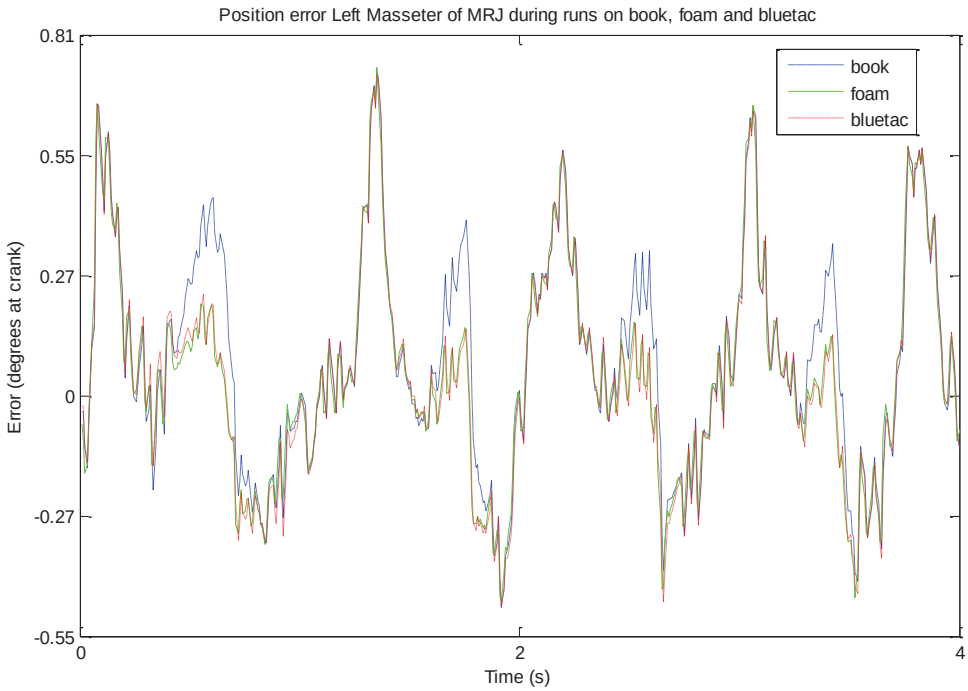

Figure 4.8 Results of experiments using the MRJ to chew foam, Bluetac and a hard cover book.

5. TRAJECTORY IMPLEMENTATION ON MRJ

This chapter begins with a description of the recording of the mastication movements of a human subject using an Articulograph AG500 (Carstens. & Carstens., 2006). Accuracy checks on the raw data are also described in this first section. The second section describes how a fixed frame is attached to the human subject and how this frame is recreated on the MRJ. Finally robotic reproduction of the measured molar movements is described and properties of the implemented chewing trajectory presented, and paper findings concluded.

5.1. Recording and Processing Mastication Movements

The movement to be recorded was of a 24 year old male with no known pathology that would cause unusual jaw movement during chewing. The food sample used was a 5 gram mixture of oats, nuts and honey. Fig. 5.1 shows the AG500 with Global co-ordinate system illustrated. The origin of the Global co-ordinate system is central to the AG500 cube. Points recorded by the AG500 are initially in this Global co-ordinate system and shall be represented in the general sense as, ${}^{Global}P$.

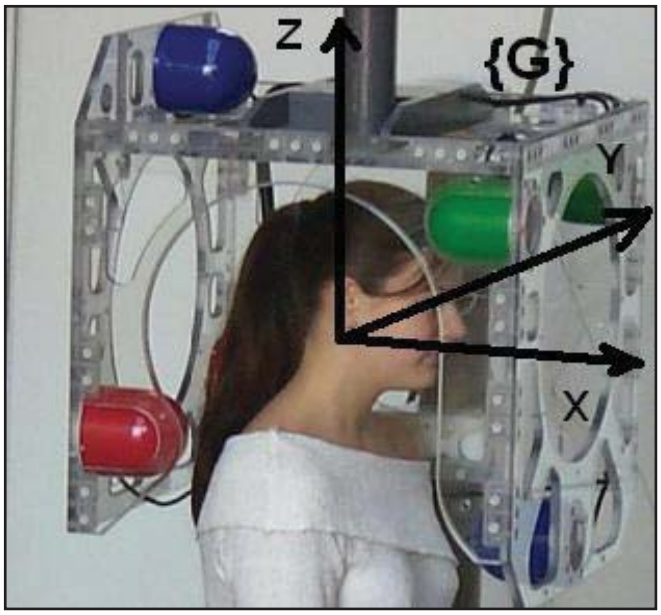

Figure 5.1 AG500 with Global co-ordinate system (Carstens. & Carstens., 2006).

For six degree of freedom movements to be recorded an Articulograph AG500 was set up at Massey University in Auckland New Zealand. The AG500 was designed with the principle function of digital recording, presentation and evaluation of the movements of tongue, lips, lower jaw and soft palate during the production of speech. The lower jaw tracking capability makes it ideal for tracking jaw movements during mastication also.

In order to find the three rotations and three translations of the lower jaw, we first assume the lower jaw is a rigid body. Simulation results indicate muscle forces acting on the mandible cause mandible deformations of very small scale, and as such can safely be neglected for our purposes in this paper (van Essen et al., 2005).

The AG500 requires a number of sensors to be placed on the subject, two or more on the head to allow for any head movement during the measurements to be removed, and three or more on the subject's lower jaw by attachment to the subject's teeth. To prevent unwanted artifacts the lower jaw sensors were placed away from the molars which were expected to do all of the chewing. Head sensors were placed behind the ears where there is little soft tissue between the sensor and skull bone which we aim to locate.

In order to assess the accuracy of the data collected from the AG500, distances between sensors fixed to the subjects head and lower jaw were calculated during the recording. For reliable data we expect there to be very little relative movement between sensors attached to either the head or mandible.

Table 5-1 between shows the standard deviations and ranges of distances between sensors placed on the head, and also those placed on the mandible during the recording of the chewing trajectory. The expected random error as stated in the manual (Carstens. & Carstens., 2006) for the AG500 is +/- 0.5mm, so a range of around 1mm is expected and unavoidable. It can be seen from table 1 that ranges exceed this for all four measured distances during the chewing motion. Standard deviations however show that most of the distances recorded vary by a margin of 0.17mm to 0.28mm from mean and so the assumption of sensors being fixed relative to the rigid body they are placed on is acceptable. The total jaw movement range during the chewing was around 14mm making errors of magnitude 0.28mm (2%) and up to 0.79mm (5.6%) acceptable for our purposes.

Table 5-1: Range and standard deviation of sensor distances.

Sensor Pair	Range of distances (mm)	Standard Deviation of distances (mm)
Right canine and incisor	1.40	0.21
Left canine and incisor	1.21	0.16
Left canine and right canine	1.58	0.28
Left ear and right ear	1.33	0.17

Head movement is calculated and subtracted by a program supplied with the AG500. From the positions of the three sensors located on the moving mandible it is now

possible to establish a co-ordinate system and calculate the three translational movements and three rotations of the mandible during the chewing motion. To establish an initial co-ordinate system the Z-axis displacement of the incisor sensor is searched for its maximum value and this taken as jaw fully closed. This 'jaw closed' position is used to set up the 'Sensor frame', a fixed frame set up purely by the position of the three lower jaw sensors at jaw closed position, once head movement has been removed. Fig. 5.2 below shows the Sensor frame established on a SolidWorks model of a lower jaw.

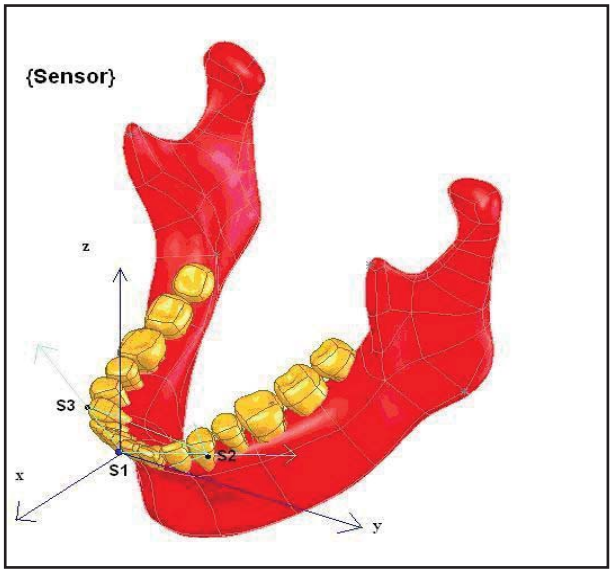

Figure 5.2: Sensor frame established at jaw closed position from location of three lower jaw sensors, S1, S2, and S3

Vectors pointing from the incisor sensor to the sensors located on the left and right canines are used in a cross product to form a perpendicular vector (Z-axis) pointing 'vertical' to the plane the 3 sensors lie on. The Y-axis is formed by the vector pointing from right canine sensor (subject's point of view) to left canine sensor, with the X-axis being the perpendicular cross product of Y and Z. The established sensor frame can be described in the Global co-ordinate system illustrated in Fig. 5.1 as the transformation:

$$ {}^{Global}_{Sensor}T = \begin{bmatrix} 1.026 & 0.0644 & -0.0899 & 111.2 \\ -0.0792 & 1.000 & -0.1594 & -17.67 \\ 0.0796 & 0.1652 & 1.000 & -67.49 \\ 0 & 0 & 0 & 1.000 \end{bmatrix} \quad (19) $$

And the inverse transformation can be found:

$$ {}^{Sensor}_{Global}T = \left({}^{Global}_{Sensor}T\right)^{-1} \quad (20) $$

Points can now be described in the sensor frame by equation 3 below:

$$^{Sensor}P = {}^{Sensor}_{Global}T . {}^{Global}P \tag{21}$$

In order to calculate the three translational and three rotational terms of the moving lower jaw during mastication, the three sensors are used to set up a moving Mandible frame in the same way the fixed Sensor frame was formed. The Mandible frame is co-incident to the Sensor frame at time = 0. Transformations of the Mandible to the Sensor frame that fully describe the six degrees of motion of the jaw are shown in equation 22 below:

$$^{Sensor}_{Mandible}T = \left({}^{Global}_{Sensor}T\right)^{-1} \cdot {}^{Global}_{Mandible}T. \tag{22}$$

The Sensor frame allows us to view the movements of the mandible relative to the initial position of the mandible. For this frame a vertical movement in the Z direction involves movement perpendicular to the plane the three sensors lie on. Because only three teeth are involved in the attachment of this frame there is likely to be large differences between different subjects and in particular between subjects and the MRJ. In the next section we describe another frame which takes into consideration all teeth locations of the subject to form an averaged 'Skull' frame that is likely to align with the 'Skull' frame formed through the same process on the MRJ.

5.2. Mapping Teeth to Create Skull Frame

The SolidWorks and mathematical models of the MRJ define movements relative to a 'Skull' frame. This frame is attached to the MRJ such that the molars lie on the X-Y plane, and 'vertical movement' in the Z-direction can be defined as any movement in the direction that is normal to the plane the molars lie on. The Y-axis is parallel to the line pointing from the right molar on the SolidWorks model to the left molar, with X-axis being normal to the established Z-Y plane. Fig. 5.3 below shows the Skull frame attached to the SolidWorks model of the lower jaw.

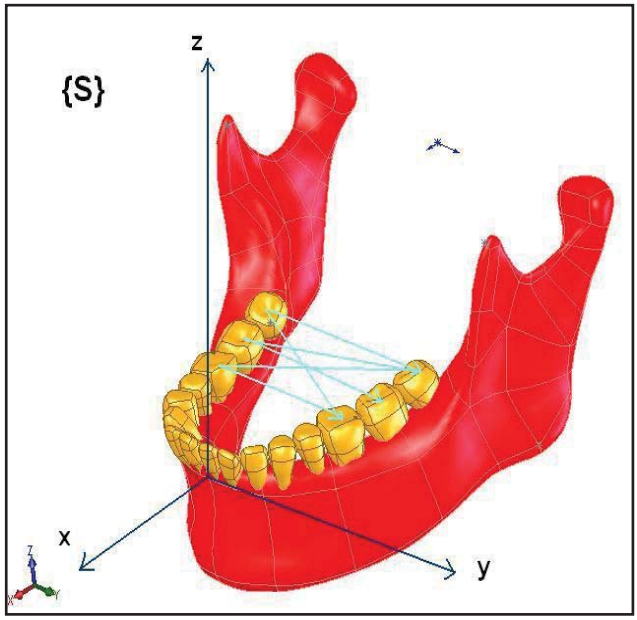

Figure 5.3 Skull frame attached to the SolidWorks model of the MRJ

In order to reproduce recorded mastication movements on the MRJ, we first must attach a Skull frame to the human subject; this is done by mapping the subject's teeth in the Sensor frame.

With the three sensors defining the Sensor frame still in place, a fourth sensor is traced around the midpoints of subjects lower teeth, positions are recorded in the Global co-ordinate system. Positions of all lower teeth are then defined with respect to the Sensor frame using equation 21. Fig. 5.4 shows how tooth positions in the Sensor frame are used to establish five Z-axes by taking the cross product of two intersecting vectors between the rear five teeth. The five Z-axes are averaged to form the Z-axis of the Skull frame attached to subject.

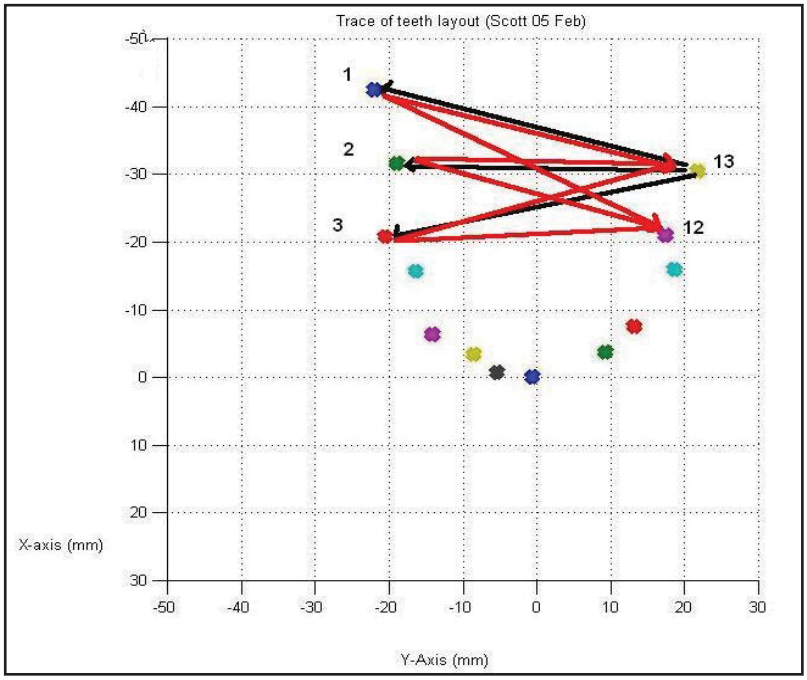

Figure 5.4: X-Y plot showing locations of subject lower teeth described in the Sensor frame, and the vectors used to establish the Skull frame Z-axis. The subject's rear left molar is omitted due to measurement error.

Fig. 5.5 shows the establishment of the Skull frames Y-axis from the measured teeth positions in the Sensor frame. Five Y-axes are calculated using ten teeth locations, and an average taken to form the final Y-axis of the Skull frame.

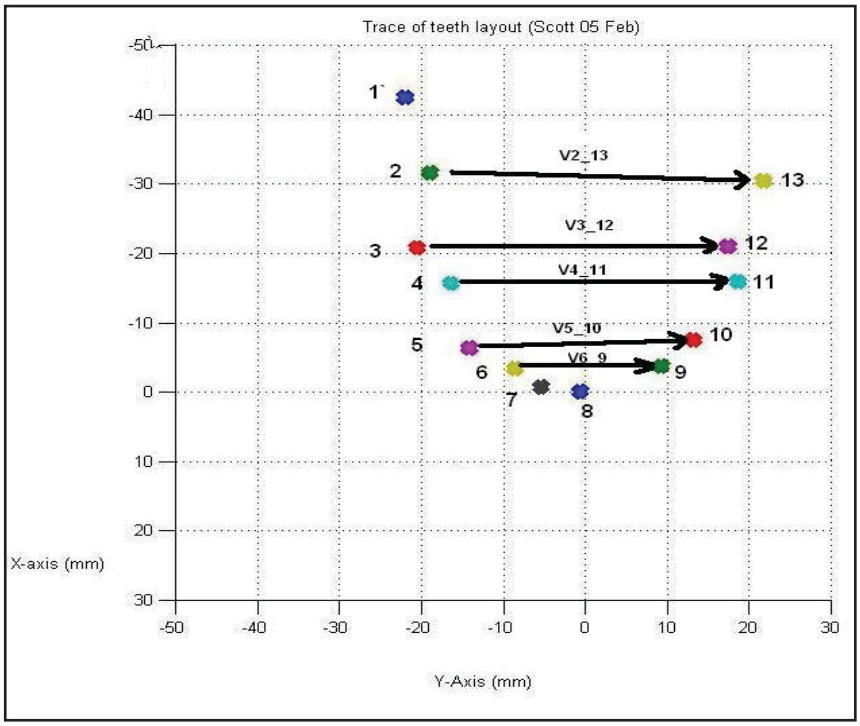

Figure 5.5: X-Y plot of subject's lower teeth and the vectors defining the Skull frames Y-axis

Finally the X-axis of the Skull frame is formed by taking the cross product of the Z and Y axes. The final result can be described in the transformation mapping the Skull frame onto the Sensor frame in equation 23 below.

$$ {}^{Sensor}_{Skull}T = \begin{bmatrix} 1.000 & -0.0044 & 0.0396 & 0 \\ 0.0044 & 1.000 & 0.0045 & 0 \\ -0.0396 & 0.0012 & 1.000 & 0 \\ 0 & 0 & 0 & 1 \end{bmatrix} \tag{23} $$

In this case the Skull and Sensor frames have similar orientations, with roll-pitch-yaw of -0.07, 2.27, 0.25 degrees separating them. It was chosen to keep the origin of the Skull frame the same as that of the Sensor frame. Transformations of the Mandible frame can now be expressed with respect to the Skull frame by equation 24.

$$ {}^{Skull}_{Mandible}T = {}^{Skull}_{Sensor}T \cdot {}^{Sensor}_{Mandible}T \tag{24} $$

By using many teeth as landmarks we have the best chance of aligning the Skull frame as set up on the human subject with the Skull frame set up on the MRJ, making reproduction of the recorded mastication movements more accurate.

5.3. Robotic Reproduction

Because the teeth on the robotic jaw differ from those of the subject it is only possible to reproduce movement at any one tooth. Because most of the chewing in the recorded mastication movement was done on the left molars, we will aim to recreate the motion of this point.

From the measurements of the subject's teeth, location of the subjects left molar is known and fixed in the Mandible frame. We can define a new 'Molar' frame and define it with respect to the Mandible frame as:

$$ {}^{Mandible}_{Molar}T = \begin{bmatrix} 1 & 0 & 0 & {}^{Mandible}LMPx \\ 0 & 1 & 0 & {}^{Mandible}LMPy \\ 0 & 0 & 1 & {}^{Mandible}LMPz \\ 0 & 0 & 0 & 1 \end{bmatrix} \tag{25} $$

The new transformation describing motion at the subject's left molar point can then be found in the Skull frame:

$$ {}^{Skull}_{Molar}T = {}^{Skull}_{Mandible}T \cdot {}^{Mandible}_{Molar}T \tag{26} $$

We can also describe the molar's motion with respect to the molars position and orientation at jaw closed by defining a fixed 'Molar Ref' frame with respect to the fixed Skull frame where,

$$ {}^{Sensor}_{Molar\,Ref}T = {}^{Mandible}_{Molar}T \tag{27} $$

$$ {}^{Skull}_{Molar\,Ref}T = {}^{Skull}_{Sensor}T \cdot {}^{Sensor}_{Molar\,Ref}T \tag{28} $$

And

$$ {}^{Molar\,Ref}_{Molar}T = ({}^{Skull}_{Molar\,Ref}T)^{-1} \cdot {}^{Skull}_{Molar}T \tag{29} $$

Before the recorded trajectory can be implemented on the MRJ, we first must smooth the random error present in the recorded data. This was achieved by using the Matlab function 'butter' to calculate parameters for a low pass Butterworth filter of order 2 and specified cut off frequency of 10Hz. These parameters were chosen through trial and error, with outcome objective to have a smooth but true representation of the data without introducing any phase shift. The parameters were used in Matlab function 'filtfilt' to smooth all raw data collected from the AG500. Results of smoothing can be seen in fig. 5.6, where the Z-displacement of the incisor point sensor in the Global frame is shown both before and after smoothing. The first five seconds consists of the subject clenching their teeth on the food sample, so little movement is detected.

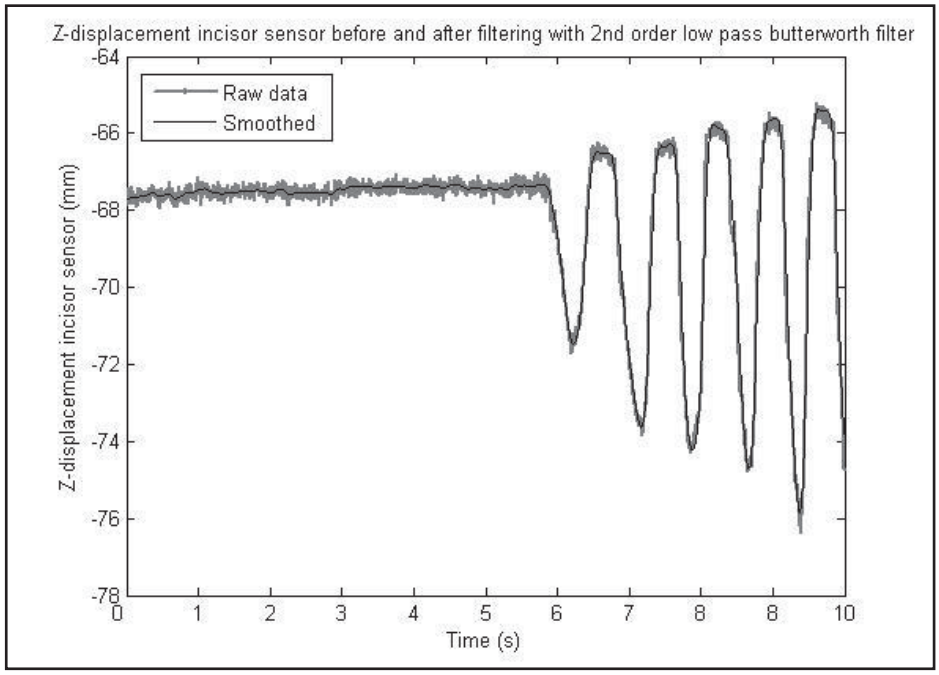

Figure5.6: Data collected from AG500 before and after smoothing.

Once the trajectory is smoothed we can now perform the inverse kinematic calculations to solve for the six DC motor actuations at every recorded robotic pose, as illustrated in fig. 8 with more details of the calculation available in (Xu et al., 2008). The robotic pose will be past in the form of the transformation matrix mapping Molar frame to Molar Ref frame as found in equation 10. A series of m-files were created in matlab to run through the large sets of recorded data and produce the 6 actuator trajectories, and then further produce the Galil programs as text files ready to be downloaded directly to the Galil DMC 1860 motion control card.

5.4. Conclusion:

The mapping of a subject's teeth locations has allowed us to align a biological jaw with a robotic jaw of differing dimension by using consistent methods based on common landmarks to create a Skull frame on both jaws. Furthermore by locating the left molar in the Skull frame, the motion of this point is known and can be accurately reproduced on the robotic mechanism. Both these measures act to ensure the molar action of interest is reproduced by the robotic jaw is the same as that of the human subject.

6. FORCE ESTIMATION AND CHEWING WITH THE MRJ

As detailed in the previous chapter, the geometries of a human subject and the robotic jaw are different. As such the trajectory of the jaw with 6DOF can be faithfully reproduced at only one location on the robot. From the point of view of the magnitude and direction of the forces applied to the food it makes more sense to focus on the first molar on the active side rather than the more commonly reported incisor point. This consideration casts some doubt on some of the analysis of lateral and vertical amplitudes reported in the mastication physiology literature where magnitudes are compared between subjects. Similar jaw geometric differences will exist between the different subjects used in those studies. Comparison of molar trajectories would be a more fundamentally sound basis for analysis.

For these reasons, the trajectories recorded on the human subject were translated from the incisor point to the active molar using the techniques described in Chapter 5. The coordinate system from the recorded trajectory and the robot were then aligned, providing a specified molar trajectory on the robot with the full 6 degrees of freedom (DOF) (x, y, z positions and roll, pitch, yaw angles). In this way the accurate reproduction of the molar and the functionality of the working surfaces of the teeth are achieved. Actuator positions could then be calculated using the inverse kinematics of the robot (Chapter 4.3). By reproducing these human trajectories with the mastication robot, it is then possible to measure information on the resistance forces and deformation of food samples in real time and in three dimensions.

The true trajectory of the molars (and hence deformation of the food) will be potentially altered by passive compliance in the robotic design (i.e. backlash) or by the active compliance instigated by the control strategy used. As will be explained in more detail in Chapter 7, torque limits were set on each actuator, meaning that if the resistance to mandible movement is too high, the position of this actuator will be held (while the others continue to move) until it becomes able to move again within the torque limits. In this way the molar movement and food deformation could vary from the original set trajectory. It should be noted that this partial transfer from motion control to force control allows the fine detail of the molar trajectory during the occlusal portion of the motion to be defined by the gliding movement caused as the active surfaces of the opposing molars passing over each other.

To provide information on the magnitude and direction of the forces applied to the food during chewing, some method of estimating the forces must be employed. This chapter outlines how force measurement was achieved before outlining experiments where the mastication robot was applied to the chewing of real foods. To give some validation of the robot function and the method to estimate the forces, a simplified one dimensional crushing movement with a flat surface (rather than teeth) was used. This trajectory allowed direct comparison of the resulting forces with uni-axial compression tests carried out on a standard texture analyser used by food scientists. Following this, comparison of the forces measured by a 6-bar linkage chewing device equipped with force sensors was carried out by simulating its two dimensional trajectory in the 6DOF parallel robot. Finally experiments using a real three dimensional trajectory were carried out. Although for this scenario there was no data to compare the chewing robot results with, the simulations demonstrated how the magnitude and directions of the forces on the teeth changed when a real jaw trajectory was used.

6.1. Force Measurement

Rather than using load cells or other sensors to directly monitor force on the food in this work, the measured torques recorded for each of the robots six actuators were used. The Galil DMC-1860 motion control card together with Galil supplied software was used to record the encoder positions and motor torque data. The Galil DMC-1860 can record the control signal sent to each actuator at any time instant. When operating in current source mode, this control signal is directly proportional to the current sent to the actuator, with the factor of proportionality being the amplifier gain set by jumper AG1 on the AMP-19540. With the torque constant of the DC motors also known, the actuator torque can be found dynamically during motion.

The approach used was based on a report by Simpson, Cook and Li (2002) where a SCARA robot with high gear reduction of 80:1 similar to the 6RSS MRJ, was used to measure a small force of 3.5N at the end-effector from DC motor currents. The method involves taking consideration for inertia, friction, and position dependent force components. By running the trajectory first without food, all three of these components can be measured and removed from the food runs provided accurate position control throughout the movement is maintained.

One factor that could compromise accurate position control is the occurrence of saturated control signals as the total torque required to both accelerate the jaw and overcome forces due to food exceeds torque limits. For this reason it is an advantage to keep acceleration in joint space to a minimum. However it can be seen in the 6-dof experiments run at full speed that some acceleration can be tolerated, food forces are

not extreme and only small positional errors are created allowing accurate force calculations to be obtained.

From the motor torque, forces can be calculated and projected through the 6-RSS linkages. The six force vectors can then be summed giving three dimensional force components on the active molar expressed in the final Skull frame. By using transformations the calculated force can be expressed in the Molar frame giving an insight into forces on the robots molar during chewing.

The main problem with this approach is that this calculated force is not the force due to the food alone, but rather the combined forces involved in producing the motion and involved in compressing the food. Simpson et al (2002) developed a detailed model of the dynamics of the system, including inertia, viscous friction, coulomb friction, and position dependent torque variations so that these effects could be subtracted to leave motor torques related to the compression of a spring at the end-effector only. The same data can be obtained empirically by simply running the motion first without any external forces acting on manipulator, with the following assumptions made:

1. All actuators remained in control, where force due to food did not exceed torque limits set on any of the six actuators.

2. Frictional and position dependent force components are unchanged with changing load.

The first requirement needs to be checked after every run as the forces required to achieve the set trajectory are not known till after an experiment is completed. Data logging of position errors together with control signals for all six actuators during the motion ensures that the control signals do not enter the limiting state where position errors will accumulate and commanded motion differs from actual motion. Matlab code was written to search the data for any excessive positional errors or limited control signals and produce a pass or no-pass result. Error limits were selected from a sensitivity analysis of the resultant force calculations on the accuracy of the jaw position data.

These assumptions were justified for all three chewing trajectories presented here. With both jaw and individual crank velocity kept close to constant to reduce the likely-hood of saturated control signals due to high acceleration demands, the only significant forces to be overcome other than the force due to food are those of the motor rotors inertia and friction.

The final force due to food was then estimated by removing the forces required to perform free motion running of the trajectory from the forces calculated from the

motion performed with the food. Based on these assumptions the force due to food can be calculated from the actuator torques.

The raw data collected by the DMC-1860 consists of 12 fields, six being the control signals for the actuators, and six being the positional errors for the six actuators, all recorded as a function of time. Testing of assumption 3 above was first carried out to confirm no actuators were run in a torque limited state. The forces on the food were then calculated through the linkages shown in Fig. 6.1.

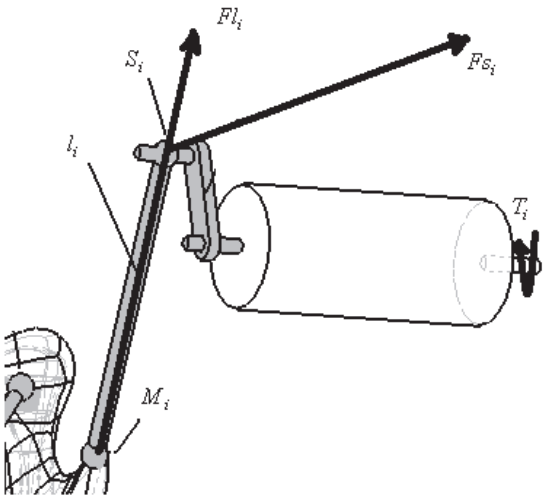

Figure 6.1 Torques and forces of a representative actuator 'i'

First the control signal is converted into a current value based on amplifier gain of 0.7 A/V.

$$Ci = 0.7Vi \tag{30}$$

where Ci is the current through actuator i, and Vi is the control signal in volts for actuator i. The actuator torque T_i is then calculated using the DC torque constants of the actuators.

$$T_i = 25.9C_i \times 66 \tag{31}$$

where the torque constants for the motors were 25.9mNm/A, and the gearing factor magnified the torque by the ratio 66:1. From this, the actuator torque through the axis the actuators lie on is known, and could be converted to a force at points S_i where the actuator cranks are joined through spherical joints to links L_i.

$$Fs_i = \frac{T_i}{G_i C_i} \tag{32}$$

in which Fs_i is the force at point S_i, and G_iC_i is the length of crank C_i.

This force at points S_i is directed at 90 degrees to the crank link C_i, and the force though links L_i connecting the crank link to the mandible can be found by projecting this force onto the link L_i at a given time instant. It is noted that because of the spherical joints on either end of links L_i, no torques can be transmitted through the link and any force transmitted must be in the direction of the link at that time instant.

$$Fl_i = \frac{Fs_i \bullet {}^{M}M_i S_i}{\left\| {}^{M}M_i S_i \right\|} \tag{33}$$

where Fl_i is the force transmitted through link i, ${}^{M}M_i S_i$ is the vector from point S_i to point M_i measured in the mandible reference frame. The six forces could then be summed to give the resultant force acting on the mandible.

$$Fm = \sum_{i=1}^{6} Fl_i \tag{34}$$

where Fm is the force at the mandible.

Initial experiments were carried out to verify the force calculation method and its associated assumptions, by comparing results with uni-axial compression tests made on a TAXT2 texture analyser (Bourne, 2002). The uni-axial test is a simple linear crushing motion with a flat probe and platform. The force-distance profile is recorded in one dimension using a load cell. The machine allows the cross head speed to be set, with two force thresholds used to set trigger recording at the start and end points of the motion. Compression was run at 1mm/second, and a force threshold of 0.1N was selected to trigger recording. Although the motion and teeth shape are not representative of the motion occurring during chewing, this method has been widely used to describe food texture (Bourne, 2002).

Three samples were tested. A model food consisting of cast silicon rubber was used as this had very well defined properties. The material is completely elastic so the resisting force would increase on compression and it would relax to its original shape after it is released. Two real foods were used including a muesli bar, (a collection of whole and flaked cereals bound together with a sticky sugar or honey based syrup) and uncooked dry noodles. The muesli bar was expected to deform on teeth-food contact after which individual particles can become trapped between the occlusal surfaces of the teeth and fracture or cutting of these components may occur. Dry noodles are an example of a hard brittle food that will fracture under stress.

The vertical 1DOF movement of the Texture Analyser was reproduced on the chewing robot so that the force applied on the texture analyser was aligned with the Skull

frames z-axis. Consequently there was no motion in the x- and y-axes of the Skull frame, or rotation about any of the three Skull axes. The velocity was set to be constant at 1mm/s in the positive direction of the Skull frames z-axis. There was no acceleration specified during the movement. The displacement and velocity-time profiles of the 1DOF trajectory are shown in Figs. 6.2 and 6.3 below.

Before the force measurement could be replicated on the mastication robot, some modifications were required. The TATX2 uses two flat aluminium surfaces to compress the food sample between. To test comparable geometries, the robots lower set of teeth were removed leaving the flat machined aluminium mounting plate which is comparable to the base used on the texture analyser. The upper set of teeth was replaced with a machined aluminium block (much larger in area than the food sample), with flat surfaces comparable to the upper probe used on the texture analyser.

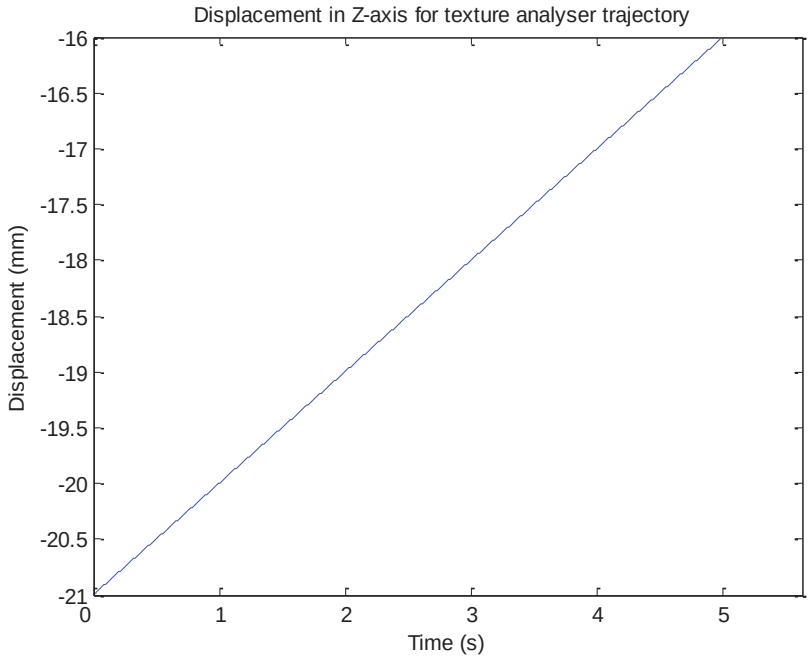

Figure 6.2 Z-axis displacement of the lower jaw in the Skull reference frame for the 1DOF trajectory

The texture analyser motion was then programmed to run on the masticatory robot and the forces were recorded as the food was compressed. It should be noted that actuations are required for all six motors to achieve this linear trajectory. Comparisons of the vertical forces are shown for the silicon rubber model food system in Fig. 6.4.

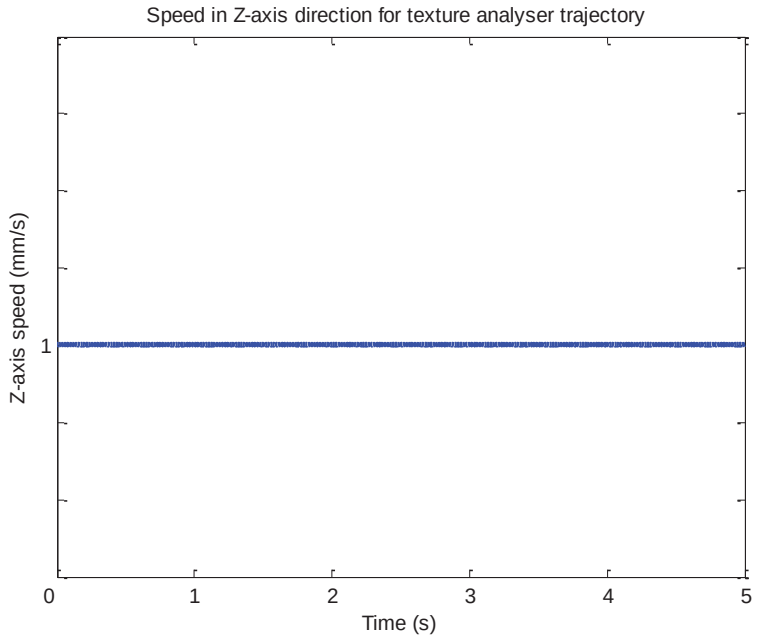

Figure 6.3 Velocity of the lower jaw plate in the Skull reference frame.

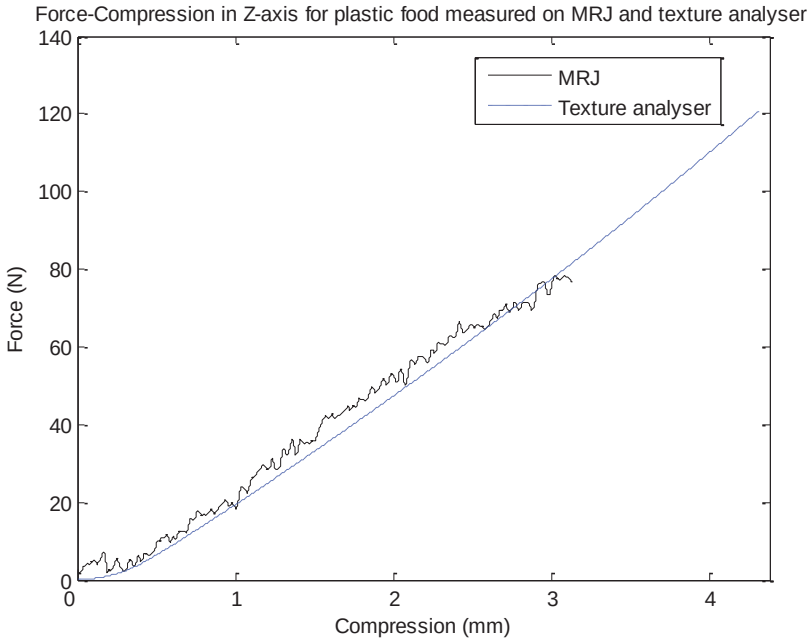

Figure 6.4 Typical force profile on the 20mm plastic food sample as measured by the chewing robot (MRJ) and the texture analyzer for a 1DOF motion.

It can be clearly seen in Fig. 6.4 and Table 6-1 that there is very good agreement in the shape and magnitude of the force-deformation curves for the silicon rubber material, suggesting that the force in the chewing robot is being calculated correctly.

Table 6-1 Comparison between the chewing robot and the texture analyzer force measurements in the silicon rubber model food system

Plastic food force measured at 3mm compression (N)	
Chewing robot	Texture Analyser
Mean =77.875	Mean=78.26
S.d = 1.4549 (n=4)	S.d = 0.873 (n=3)

'S.d' = standard deviation on 'n' replicate measurements

The force-distance curve measured for muesli bars (Fig. 6.5) shows more complex mechanical behaviour than for silicon rubber. Although the curve is approximately linear, curvature is observed due to the multiple components present in muesli bars which possess different mechanical properties. There is again very good agreement between the uni-axial compression test and the chewing robot. The mean results after 4mm of compression are summarised in Table 6-2.

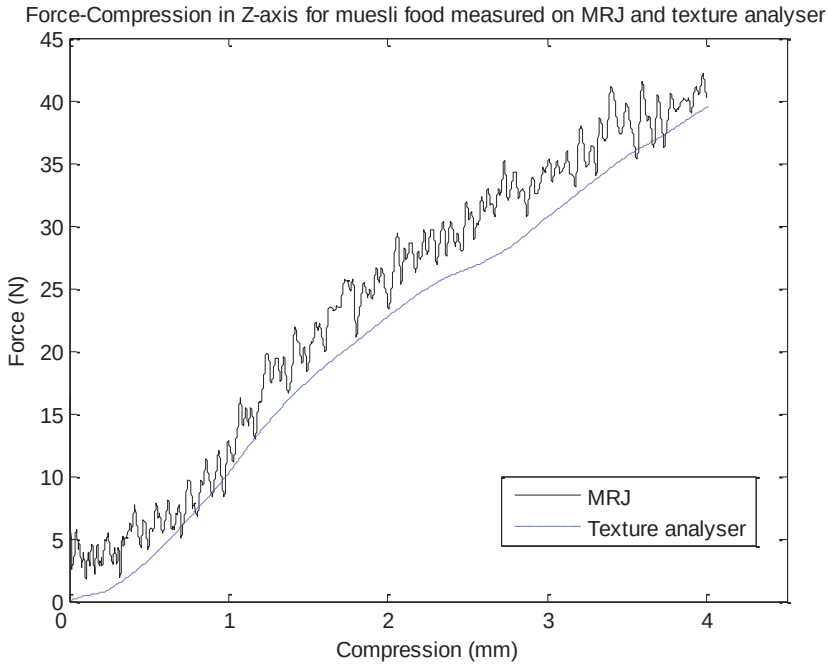

Figure 6.5 Typical force profile as measured by the chewing robot and texture analyzer for 1DOF motion on a muesli bar food sample

Table 6-2 Comparison between the chewing robot and the texture analyzer force measurements in the muesli bar food system

Muesli bar food force measured at 4mm compression (N)	
Chewing robot	Texture Analyser
Mean =34.0	Mean=38.5
S.d = 4.98	S.d = 5.31
(n=4)	(n=5)

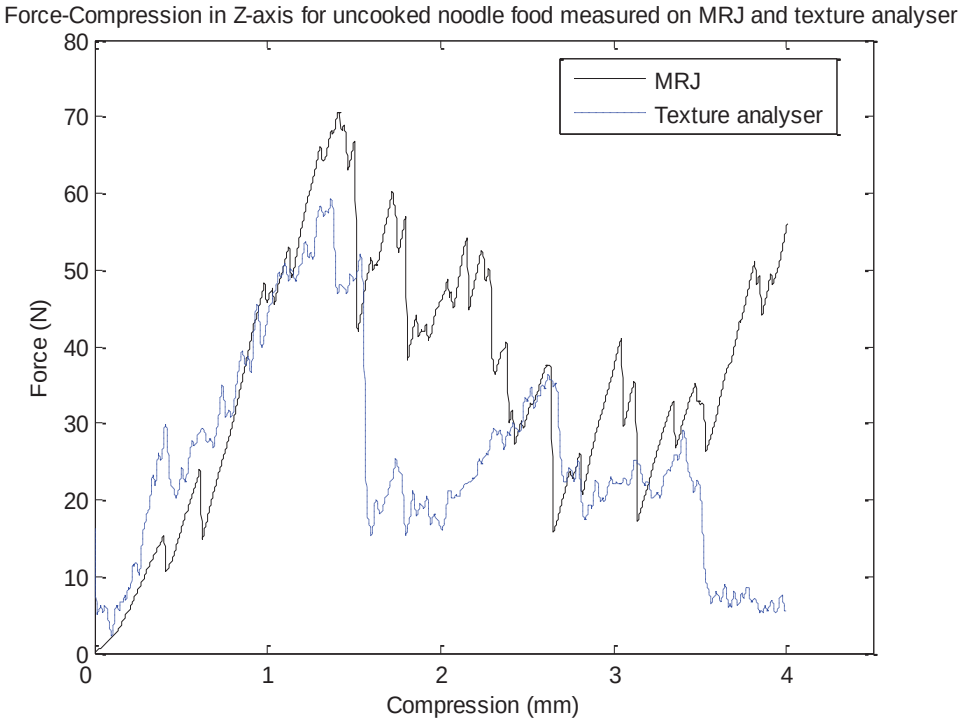

Figure 6.6 Typical force profile as measured by the chewing robot and texture analyzer for 1DOF motion on an uncooked noodle food sample

Table 6-3 Comparison between the chewing robot and the texture analyzer force measurements in the uncooked noodle food system

Uncooked noodle food force measured at max breaking point (N)	
Chewing robot	Texture Analyser
Mean =65.9	Mean=53.8
S.d = 8.00	S.d = 14.7
(n=3)	(n=4)

Uncooked noodles are a hard brittle material which fractures on compression rather than deforming. This can be seen in Fig. 6.6 below where for both the texture analyser

and the chewing robot, multiple fracture events are observed over the first 1.5mm. When a fracture event occurs, the resistance of the force is momentarily relaxed, before building again. A peak force is observed of 60-70N after which a large fracture failure is observed. The force then builds again because by this stage much of the open airspace between the noodles has been filled with broken particles and these fragments begin to be compressed.

Both methods demonstrate this fracture behaviour exhibiting similar peak forces, initial fracturability (force at the first failure event), and strain at failure (product deformation at the point where peak force is observed). The magnitude of the reproducibility within each test method was similar to the differences observed between the chewing robot and the texture analyser. This is shown in Table 6-3.

Overall the results show the chewing robot can function well as a 1DOF texture analyser machine and the force calculation method is valid. These forces applied on the food were contributed to by all of the actuators involved in the robotic movement.

6.2. Experiments with Two-DOF Chewing Trajectory

To validate the chewing robot against more complex trajectories, it was compared against force profiles collected using a 6-bar linkage chewing robot equipped with force sensors. The 2D linkage robot achieves a proscribed two dimensional molar trajectory with anatomically correct dentition. The linkage chewing machine incorporates a 3D force sensor integrated under the lower jaw which allows the resultant forces on the food to be recorded as foods undergo mastication. The motion was run at approximately 2mm/s in the z-axis direction on both the linkage robot and the 6DOF parallel chewing robot, to ensure any possible influence due to robot dynamics was minimised.

The trajectory of the 2D machine reproduced in the 6DOF chewing robot. The original data recorded using the 2D robot encoder consisted of 370 points for the full cycle. Fig. 6.7 below shows the actual trajectory actuated in the 2D chewing robot. Note that occlusion of the molar teeth occur at z-axis displacements greater than 0. Negative values represent the opening and closing phases of the motion.

Because force measurements are of interest during the occlusion phase, the closing position and angle were matched with the 6DOF chewing robot. Exact reproduction of the non-occlusal phase was not required and so the non-occlusion phase was truncated to allow the trajectory to fit within the 6DOF chewing robots smaller workspace. As this part of the trajectory is not where the food is compressed, it would not affect the forces recorded. The roll pitch and yaw angles of the mandible were all held constant at 0 degrees. Fig. 6.8 shows the full trajectory applied to the 6DOF

chewing robot. Only the occlusal phase of the trajectory in Fig. 6.8 involved food compression.

Figure 6.9 shows the implemented trajectory during which forces were measured. Inspection of the velocity and acceleration of the trajectory was important as it is possible that any large acceleration during the movement could lead to errors in the force calculation. Figs. 6.10 and 6.11 show the velocity and acceleration profiles of the mandible movement.

It can be seen that there are a number of sharp inflection points in both the velocity and acceleration plots due to the discrete nature of the data used. Motion was implemented with linear interpolation between points. An attempt was made to smooth the motion by using an Akima spline in SolidWorks and taking more points for the trajectory but an improvement was not seen. Despite the spikes, the magnitude of acceleration is small and unlikely to cause problems when calculating forces.

A typical force profile from running the 2D trajectory on both the 6DOF chewing robot and the 2D chewing machine is shown in Fig. 6.12 for the 20mm silicon rubber model food system.

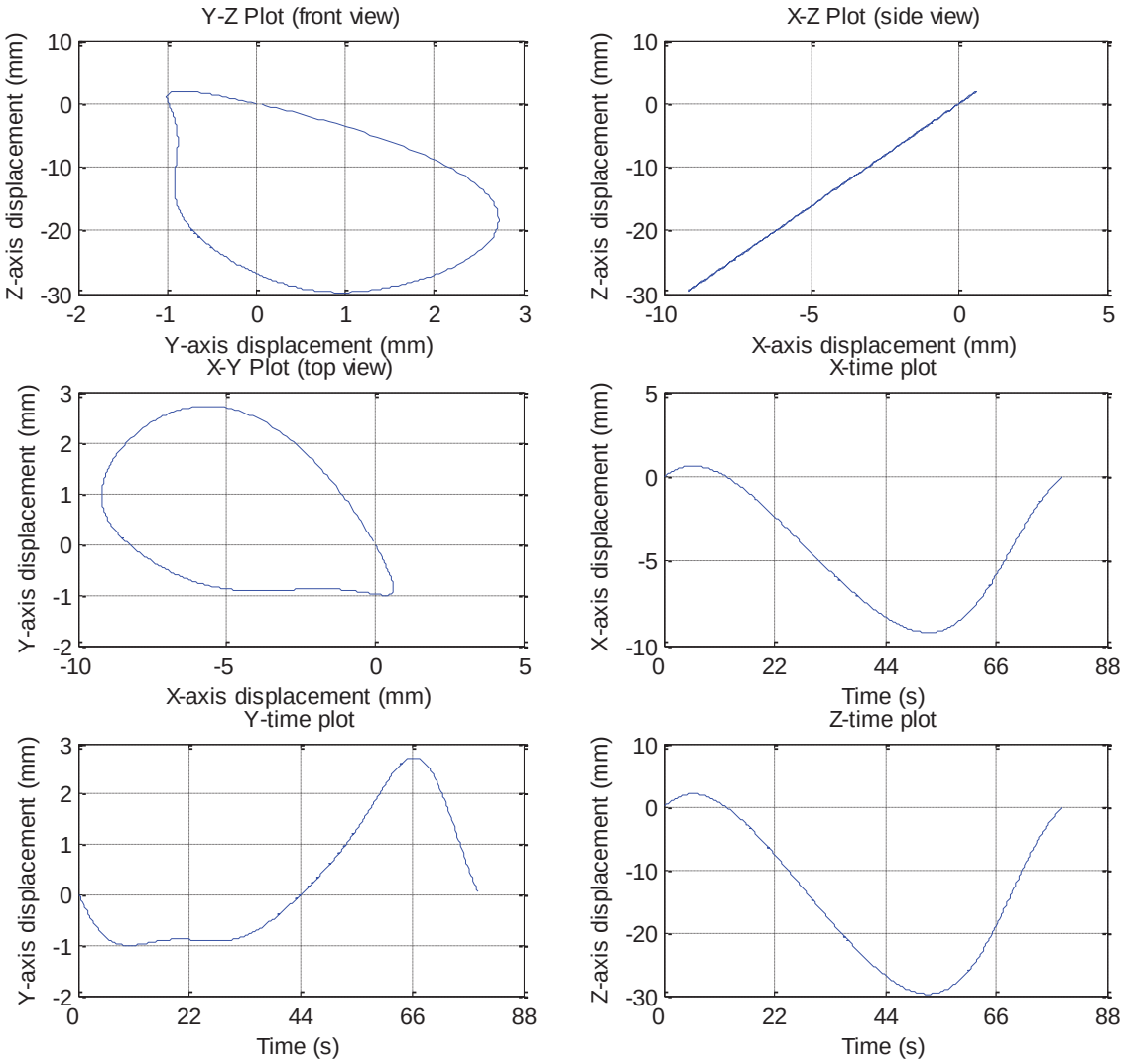

Figure 6.7 Trajectory implemented on 2D linkage chewing robot during experimental trials

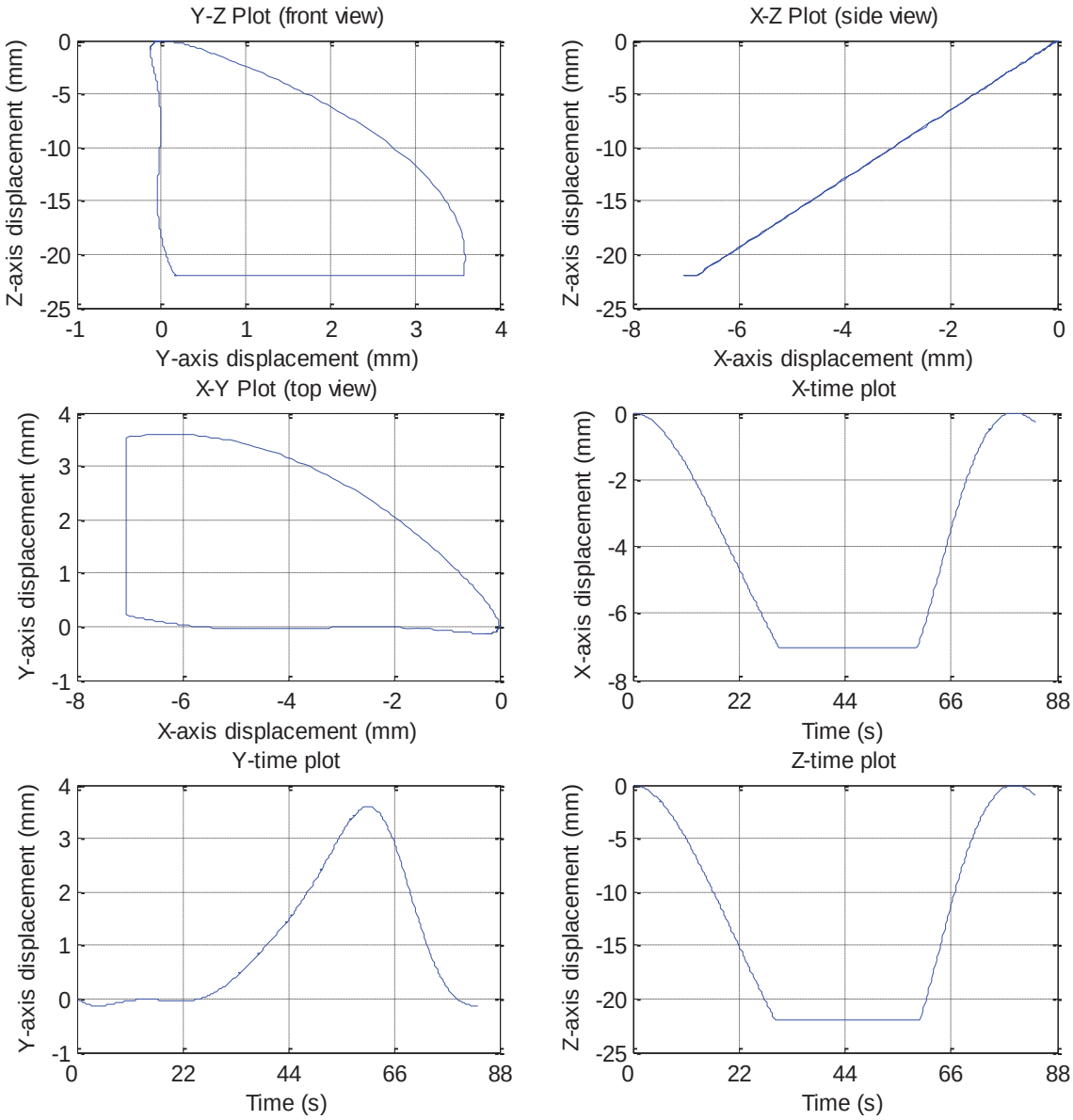

Figure 6.8 The 6DOF chewing robot trajectory implemented to approximate the 2D chewing robot motion

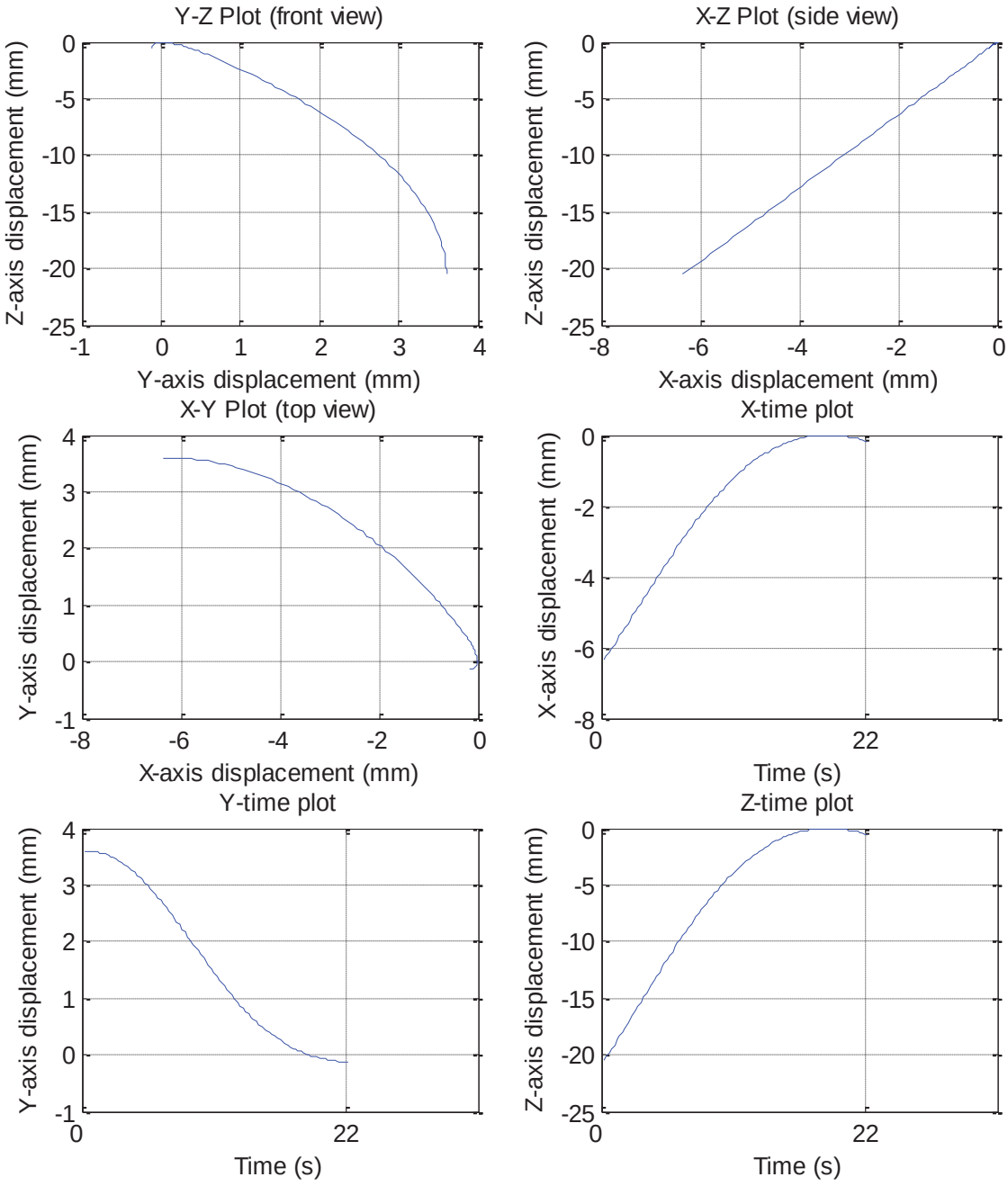

Figure 6.9 Occluding phase of the 2D trajectory as implemented on the 6DOF chewing robot.

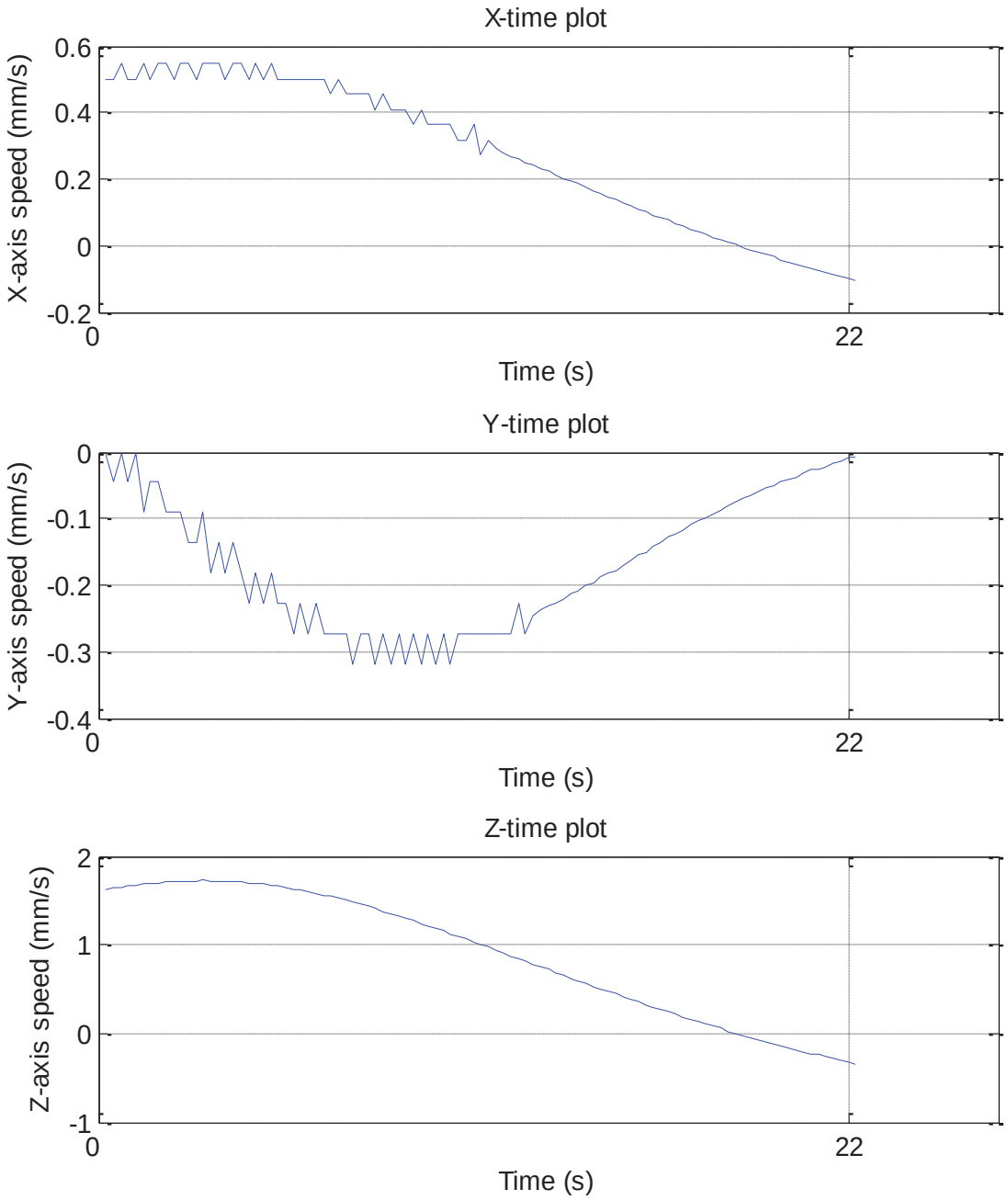

Figure 6.10 Mandible (molar) velocity implemented in the chewing robot during reproduction of the 2D linkage robot trajectory

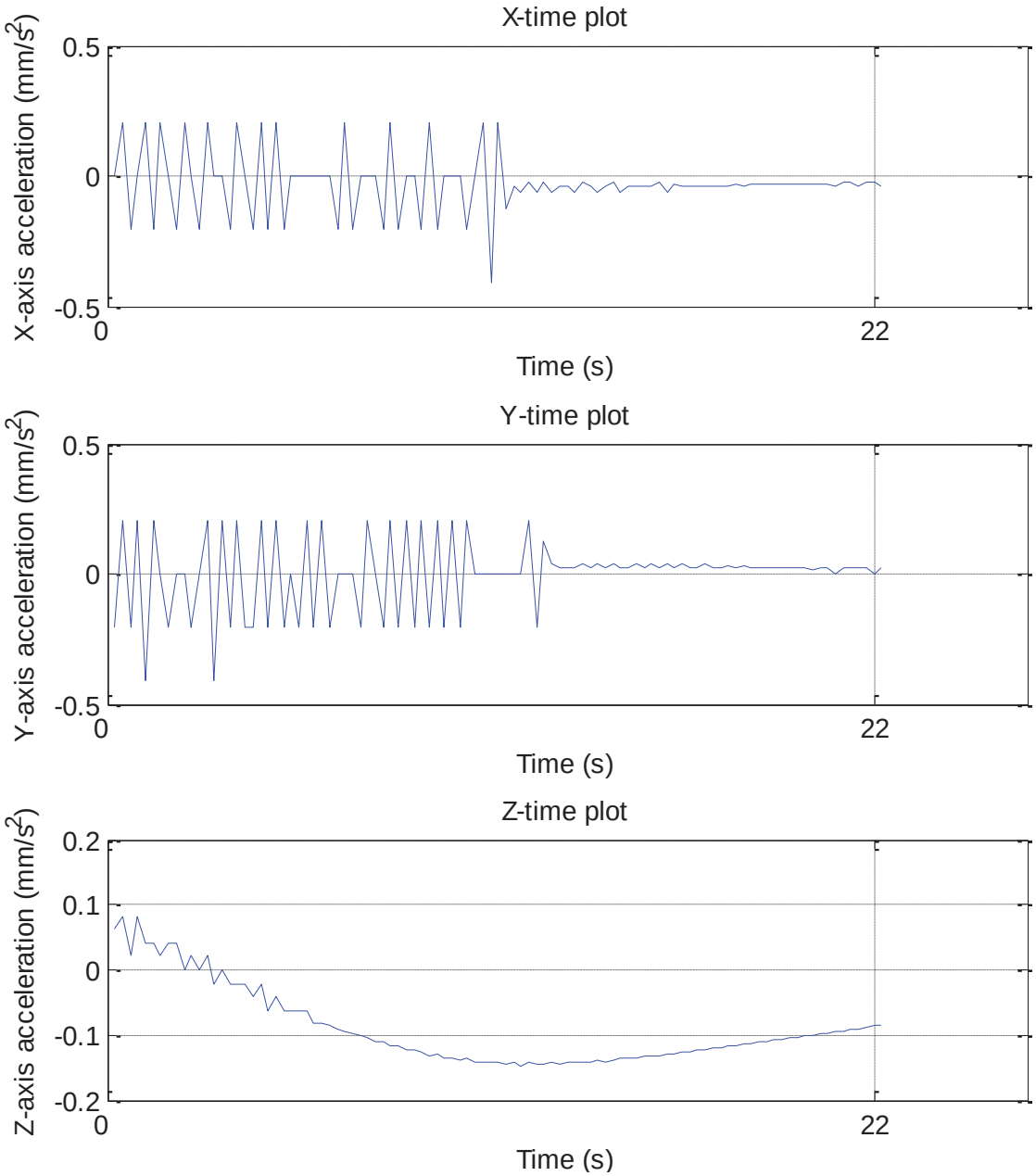

Figure 6.11 Mandible (molar) acceleration implemented in chewing robot during reproduction of 2D linkage robot trajectory

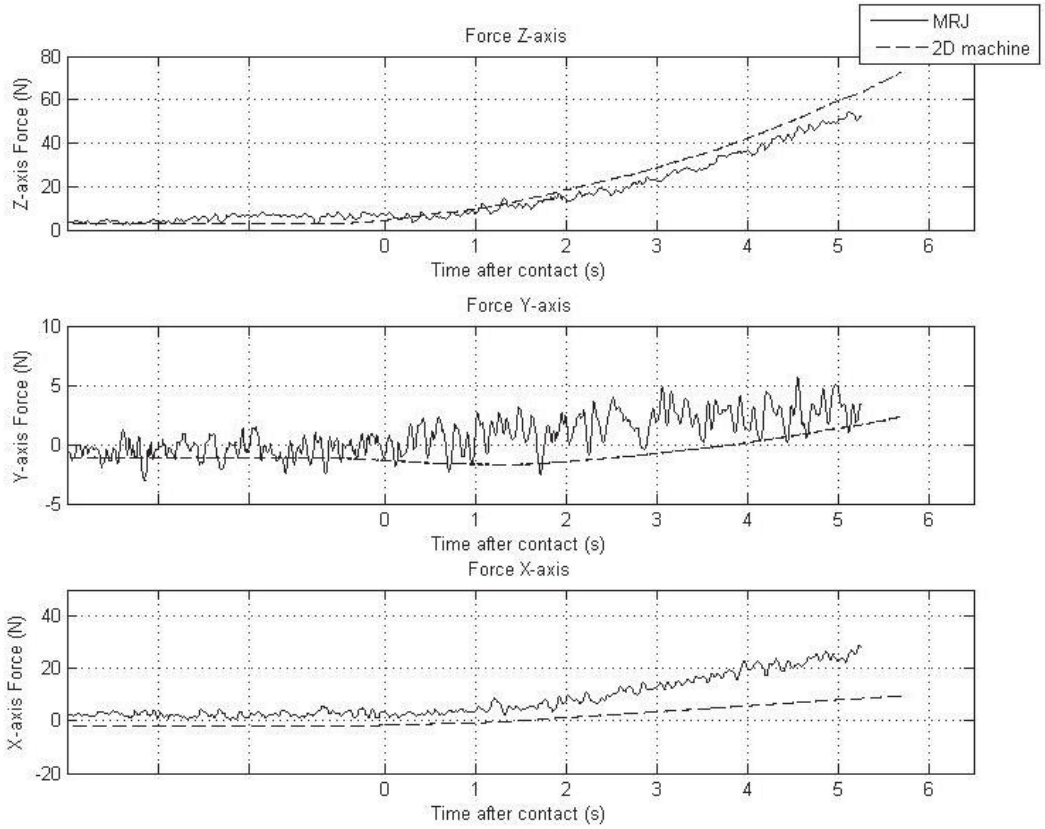

Figure 6.12 Forces measured during chewing of a 20mm silicon rubber model food using 6DOF chewing robot and the 2D chewing machine.

All runs showed similar results, with the 6DOF chewing robot providing slightly less z-axis force, and slightly more x-axis force. Table 6-4 below shows the mean forces measured after 5 seconds for several experiments.

Table 6-4 Comparison of mean forces in each direction from replicate chewing experiments on silicon rubber food models

Silicon rubber model food force measured at 5 seconds.					
x-axis force (N)		y-axis force (N)		z-axis force (N)	
Chewing robot	2D machine	Chewing robot	2D machine	Chewing robot	2D machine
Mean=25.95	Mean=7.56	Mean=4.29	Mean=1.69	Mean=52.48	Mean=58.03
S.d=1.59	S.d=0.78	S.d=0.30	S.d=0.44	S.d=1.53	S.d=1.38
(n=5)	(n=3)	(n=5)	(n=3)	(n=5)	(n=3)

It can be seen that there are significant differences in the forces measured in the x-axis direction, with the 6DOF chewing robot measuring more force. It is unlikely that such large forces would be applied to the food in the x- direction (anterior-posterior) due to the very small mandible movement that occurs in this direction during the food-teeth contact portion of the experiment. It is thought that under loaded conditions (i.e. when the teeth come into contact with the food) the loss of passive compliance

combined with the geometric arrangement of the robot causes the propagation of reaction forces in some of the jaw joints. Similar behaviour was observed in the one dimensional experimental trials (data not shown) where significant x-direction forces were observed although the only x-dimensional movement was that caused by mechanical compliance. Further work is required to resolve this issue before the device could be used to characterise the forces applied to food samples. Direct measurement of the forces on the molar teeth in 3D would add some clarification of what is occurring during the loaded operation of the robot. Despite these differences, there is very good agreement in the trend and magnitude of the forces applied on the food.

Fig. 6.13 shows similar experimental results during chewing of biscuits. As expected for brittle food systems such as biscuits, the results show multiple fracture events occurring during deformation. As observed for the silicon rubber food model above, significant forces were applied in the x-direction. The similarity in shape between the z- and x- direction forces reinforces the explanation discussed above. The magnitude of force in the x-direction is highly correlated to the force applied in the z-direction and it may be that as more vertical load is applied, the internal resistance of the robot linkages increase in the x-direction.

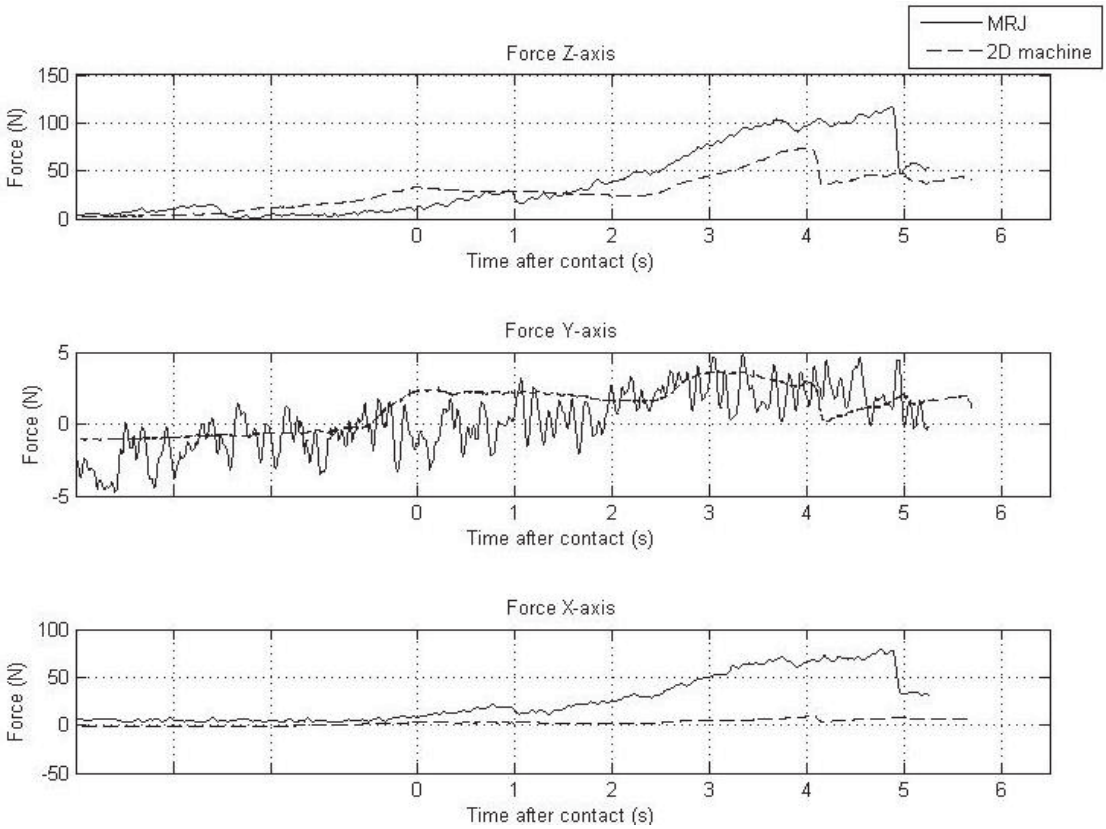

Figure 6.13 Forces measured during chewing of a biscuit using the 6DOF chewing robot and the 2D chewing machine.

Table 6-5 compares the average differences in force in each direction for several replicate experiments. It can be seen that for both machines there is a relatively large spread of forces for the different trials, especially in the z-axis. This is typical of a brittle food where multiple fracture events occur during compressive strain. Similar experiments were carried out for muesli bar food samples (Fig. 6.14). This experiment showed excellent agreement in the z-dimension between the 6DOF chewing robot and the 2D chewing machine.

Table 6-5 Comparison of mean forces in each direction from replicate chewing experiments on biscuit food samples

Silicon rubber model food force measured at 5 seconds.

x-axis force (N)		y-axis force (N)		z-axis force (N)	
Chewing robot	2D machine	Chewing robot	2D machine	Chewing robot	2D machine
Mean=25.95	Mean=7.56	Mean=4.29	Mean=1.69	Mean=52.48	Mean=58.03
S.d=1.59	S.d=0.78	S.d=0.30	S.d=0.44	S.d=1.53	S.d=1.38
(n=5)	(n=3)	(n=5)	(n=3)	(n=5)	(n=3)

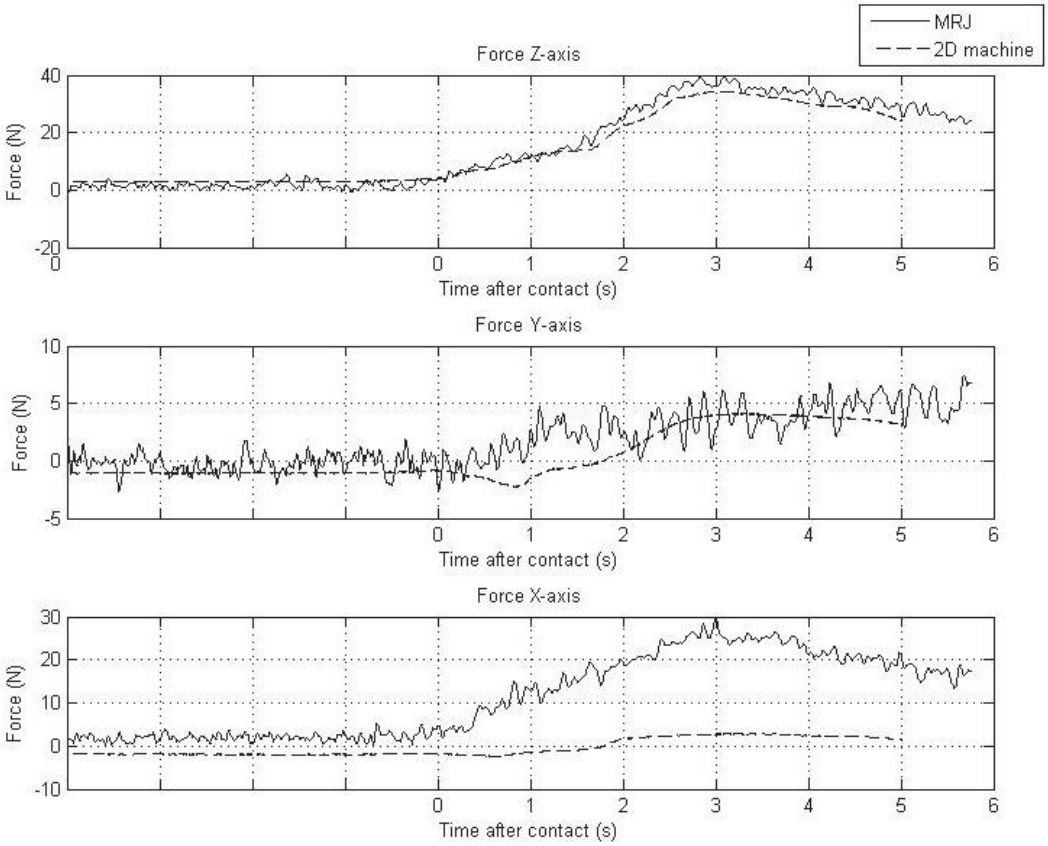

Figure 6.14 Forces measured during chewing of a muesli bar using the 6DOF chewing robot and the 2D chewing machine.

The resistance force due to the shearing lateral movement of the trajectory is evident in the recorded force measurements in the y-axis. There is good agreement in the

magnitude of this component of the forces applied to the foods. The problem with measured forces in the x-direction, as discussed above was again present during the experiments with muesli bars. Table 6-6 below shows that there was good repeatability in the measured forces in the y- and z-axes and good agreement between the two chewing machines.

Table 6-6 Comparison of mean forces in each direction from replicate chewing experiments on muesli bar food samples

Muesli Bar force measured at 4 seconds					
x-axis force (N)		y-axis force (N)		z-axis force (N)	
Chewing robot	2D machine	Chewing robot	2D machine	Chewing robot	2D machine
Mean=24.04	Mean=4.31	Mean=3.48	Mean=2.30	Mean=37.31	Mean=29.81
S.d=12.36	S.d=2.11	S.d=1.39	S.d=1.46	S.d=15.10	S.d=8.07
(n=4)	(n=4)	(n=4)	(n=4)	(n=4)	(n=4)

6.3. Experiments with Six-DOF Chewing Trajectory

A jaw trajectory recorded from a human subject using the AG500 Articulograph (see Chapter 5) was run on the 6DOF chewing robot with various food samples. The resulting forces were then analysed, both at the chewing surface and for the six actuators. This was carried out as the robot was designed from biological principles and the six actuators mimic the work of the biological muscles of the human subject. The full trajectory implemented on the robot is shown in Fig. 6.15. The plot showing z-axis displacement versus time shows the dynamics of the chewing process. As the number of chewing cycles increase, the z-axis displacement at the top of the chewing motion reduces. This is likely to reflect the breakdown of the food properties so that the molars come closer together due to the reduced resistance imparted by the foods. Close to full occlusion occurs after approximately 10 chewing cycles.

The displacement plot for the y-axis shows that lateral movement during the opening phase of each chewing cycle was most often to the right. After six cycles, a short series of cycles were directed to the left. This could have been done to maintain the position or manipulate the orientation of the food on the occlusal table between cycles. Alternatively it could signal transfer of the bolus to the other side of the dental arch for a few chewing cycles.

The x-axis displacement also changed throughout the chewing process. During the initial few chewing strokes, the amplitude of the anterior-posterior movements was relatively large. The amount of forward jaw movement decreased as the food breaks down and the trajectory of the teeth during the teeth-food contact period moves closer to 0 mm z-axis displacement. During this later stage where much smaller

forward movements occur, it can be seen that the x-axis displacement approaches 0 mm, showing that the molar teeth are correctly aligned for occlusion.

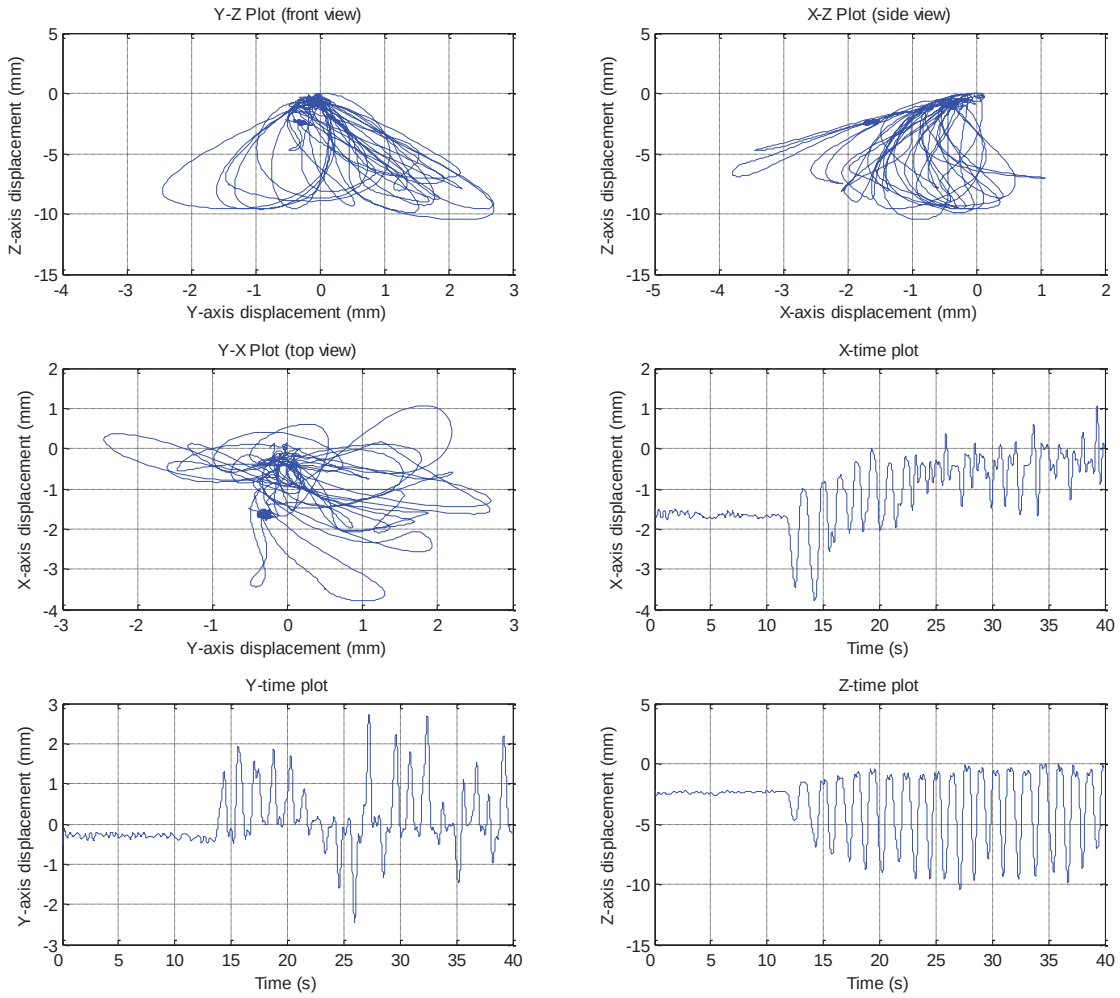

Figure 6.15 3D human trajectory converted for implementation on the chewing robot. Note that in the first 14 seconds the jaw position was held constant to provide a reference point for the orientation of the jaw

As this is a real chewing trajectory it has 6 degrees of freedom. The roll, pitch and yaw movements are shown in Fig 6.16. The tilting of the jaw forwards as the jaw is opened can be seen in the pitch-time plot. This is the largest rotational movement and the maximum angle (at maximum z-axis displacement) is relatively uniform between cycles. The roll and yaw angles follow a consistent pattern but do exhibit a transfer from positive to negative directions periodically during the mastication duration. These observations correspond to the cycles where measurements of negative x- and y-axis displacements were recorded, indicating that it is most likely that the active chewing side was switched for these few cycles.

For the experiments run on food samples, only a single chewing cycle was implemented. The occlusion movement starting at approximately 20 seconds into the trajectory was selected as it was one of the wider opening movements so larger food

samples could be tested. Fig. 6.17 shows the single closing chewing trajectory run on the foods. Looking from the top view (x-y plane) it can be seen that the molars approach the upper teeth from the right and rear of intercuspal occlusion and move slightly beyond the intercuspal position in the y-dimension. Movement in the z-axis does not reach occlusion, suggesting that during the particular bite, for which the measurements were recorded, the food did not fully deform and teeth to teeth contact could not occur. This explains why the maximum x-axis position was about 1mm behind the intercuspal location. If the jaw continued on to reach 0mm in the z-axis, the 1mm or so of forward movement (x-axis) of the jaw to reach full occlusion would occur.

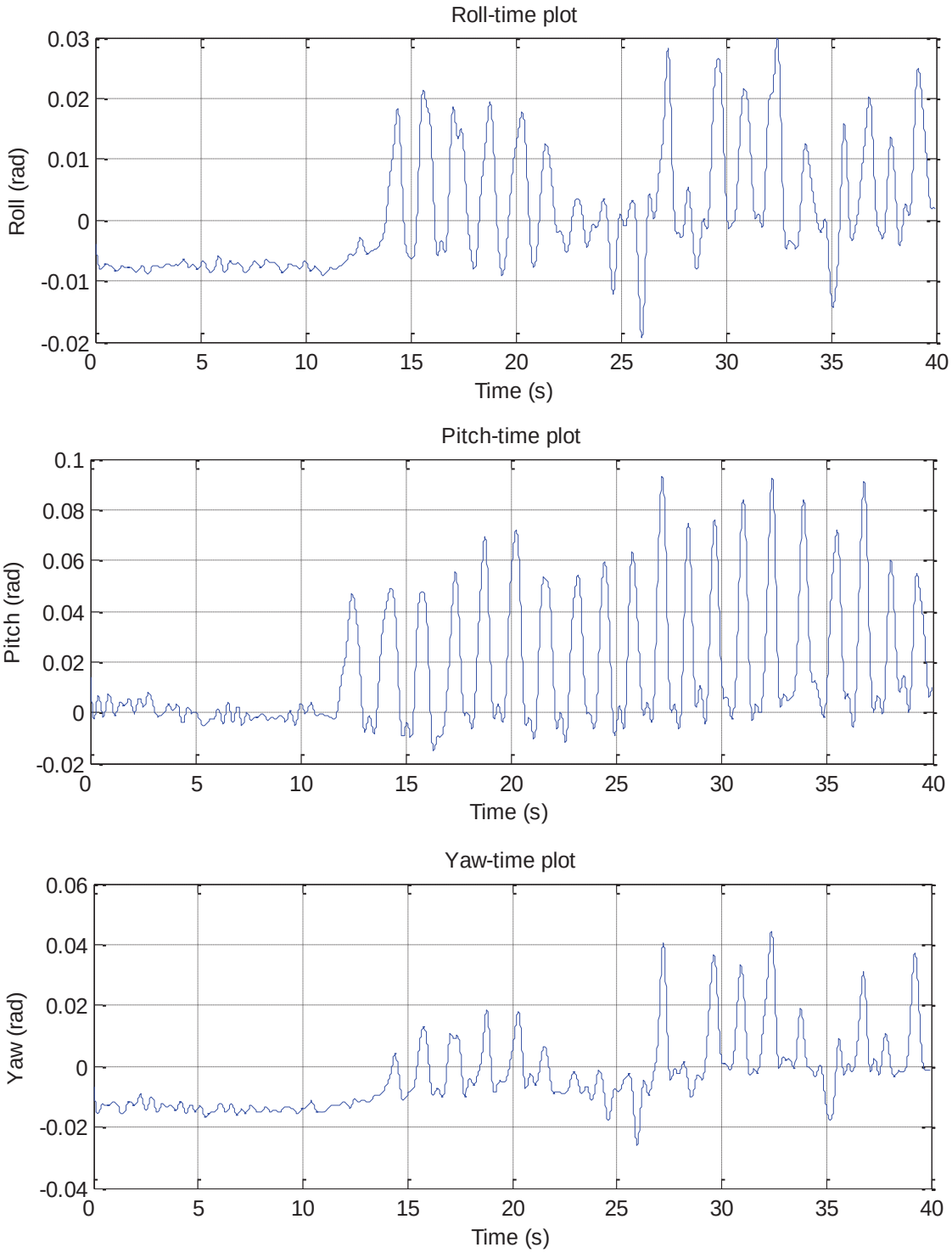

Figure 6.16 Jaw angle profile for the 3D human jaw trajectory implemented on the chewing robot

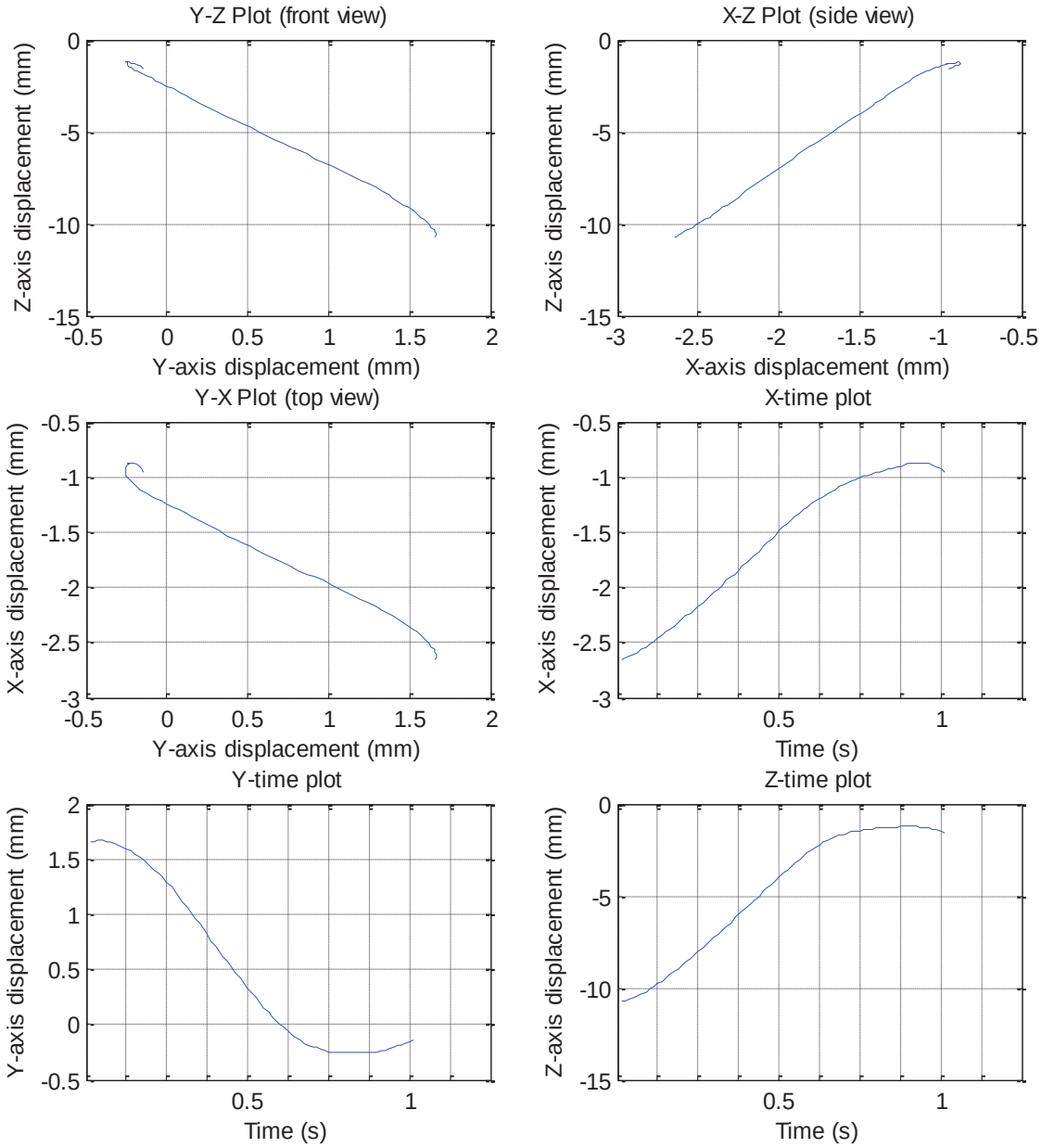

Figure 6.17 A single chewing cycle implemented on the chewing robot to simulate 3D human chewing movements.

The changes in mandible rotation used to simulate the recorded human masticatory cycle during the occlusal phase are summarised in Fig. 6.18. The pitch (rotation about the y-axis) is the motion of the jaw closing, and approached an approximately flat angle at the point where the teeth contact each other. As expected, this angle is the largest of the three rotational dimensions of the jaw. The roll (rotation about the x-axis), represents the angle that the teeth twist in the lateral direction. The teeth become aligned as they approach each other. The yaw (rotation about the z-axis) can be interpreted as the chin pointing left or right and similarly rotates to be back in line with the upper jaw by the time of tooth contact. It can be seen that in the trajectory there is some rotational movement occurring on the teeth before full occlusion occurs,

and this will apply more complex stress patterns on the food than that which occurred during the one and two dimensional trajectories implemented in the earlier experiments.

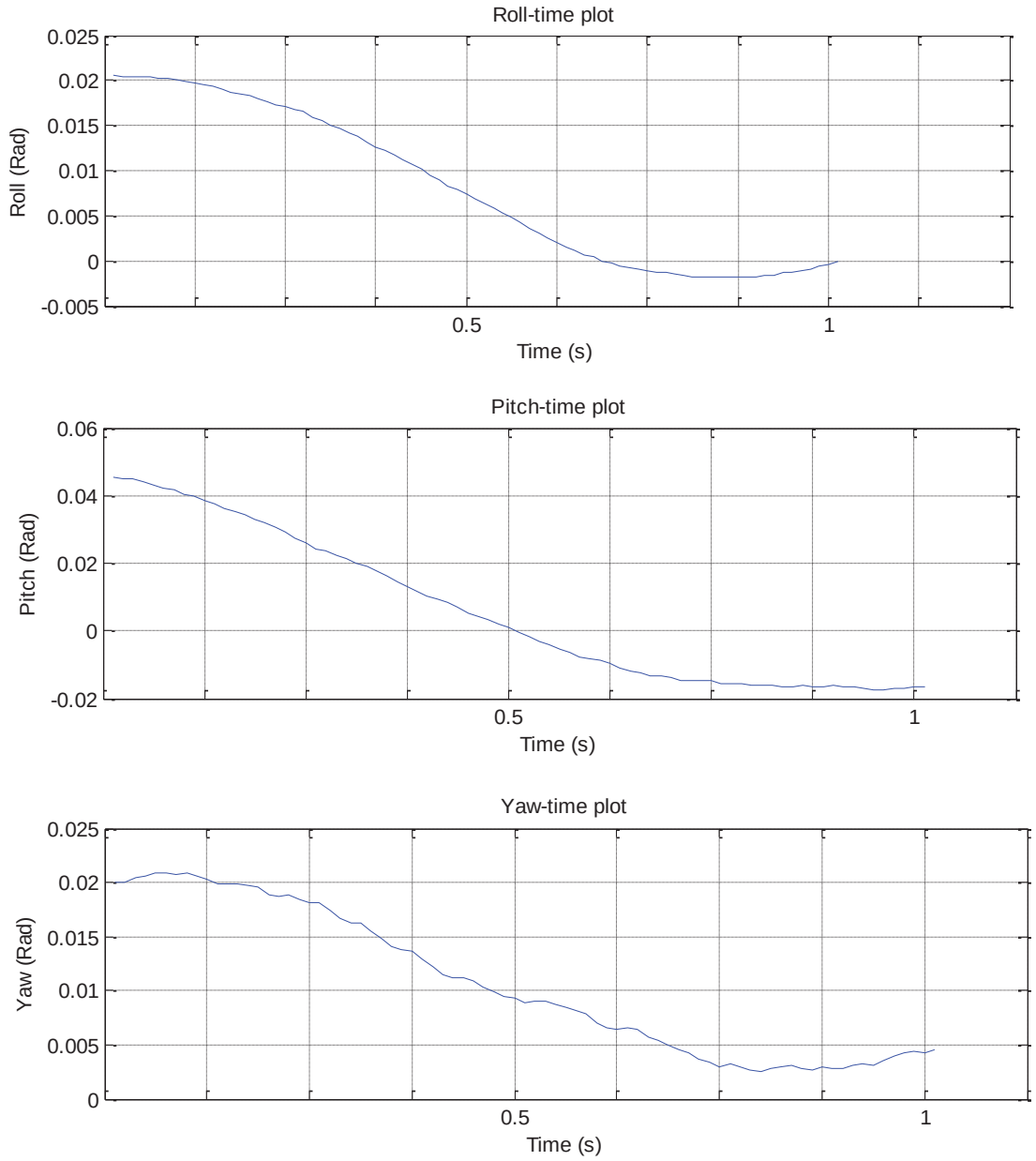

Figure 6.18 Jaw rotation angle – time profiles during the implemented simulated human chewing cycle

Fig. 6.19 shows the velocity profile implemented during this phase of the trajectory. It can be seen that in each direction, the jaw velocity increased to a maximum before reducing to zero at the point where opening was initiated.

Force results were recorded for three food samples using this section of the trajectory at full human speed. Biscuit, marshmallow and corn thins were used to demonstrate application of the chewing robot to real human mastication simulation. These foods

were used as their dimensions were small enough to be able to place the foods between the upper and lower molars at the start of the implemented trajectory. Biscuits were used to represent a moderately hard, brittle food and to allow comparison with the results observed for this product using the 2D trajectory outlined above. The use of marshmallows tested operation of the robot with a soft partially elastic food that exhibited no fracture behaviour. Corn thins are an extruded maize-flour based product with a light porous structure. The material is 'crunchy' and undergoes fracture on compression but is tougher than the biscuit product.

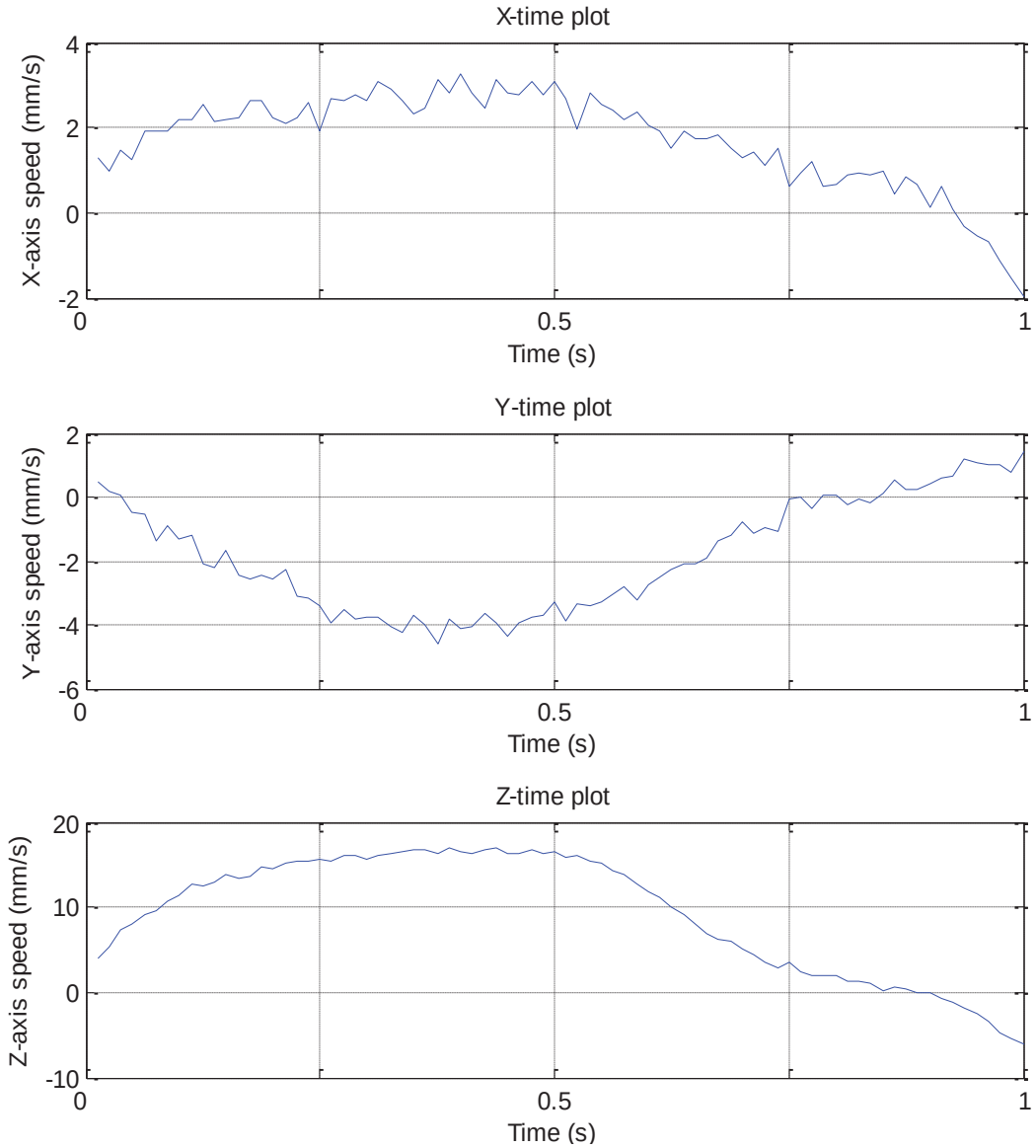

Figure 6.19 Jaw velocity profile implemented in the single cycle human chewing simulation

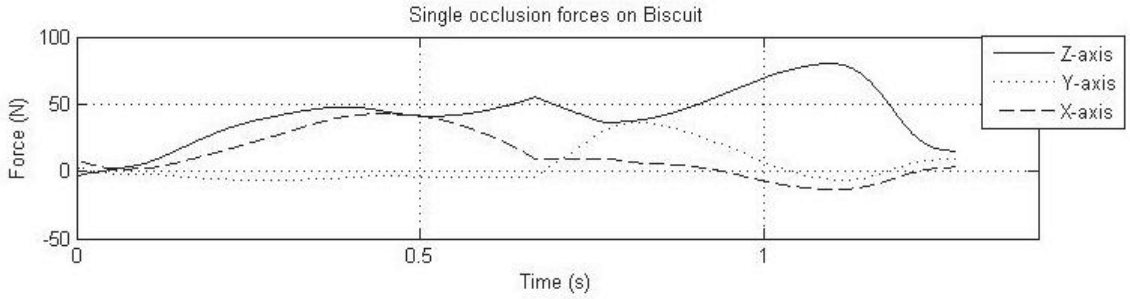

Figure 6.20 Measured force profiles on the molars during simulated 3D human trajectory applied to biscuit.

Fig. 6.20 shows the recorded force profiles applied during chewing of biscuits. The curve is relatively smooth in comparison with the jagged force profile observed for biscuits using the previous 2D experiments (Fig. 6.13). This was due to the much shorter sample time used for the human trajectory experiments. At faster jaw speed, fracture events occur in very quick succession and as a result, the force relaxation recorded after fracture at low speed will not be as evident. From the results in the z-direction, two larger scale force relaxations were evident during the compression phase of the cycle, indicating failure and that associated large scale structural changes did occur in the sample.

At the start of the cycle the x-axis data was again strongly correlated with the increase in force in the z-direction. The x-axis movement of the jaw is occurring at this time, so force in this direction might be expected. As discussed above however, this could indicate the propagation of some internal forces in the linkages of the robot. It is interesting however that after about 0.5 seconds, this force drops away to almost zero. At the same point there is an increase in y-axis force. A detailed analysis of the forces within the robot is required to resolve whether or not these measured forces are actually being applied onto the food or due to internal load dependent friction in the mechanism. This must be carried out before a full analysis of the data in terms of food resistances can be made. The direct measurement of the forces applied onto the teeth may be more appropriate than calculating them from the motor torques.

Figure 6.21 shows the measured force profiles recorded during a similar experiment using marshmallow as the food system. Due to soft texture of the food, the measured magnitudes of the forces in each direction are low. This could reflect the trajectory used in this experiment where complete occlusion and hence complete deformation of the product was not made. This result highlights an important issue in operation of the robot. If human trajectories are simulated exactly, the forces measured are those that must be applied to achieve this specified degree of deformation on the food. An alternative strategy would be to set the robot to achieve full occlusal trajectory but implement some form of force control that allows incomplete deformation of the food if the resistance of the food is too high. Operation of this second approach using

different torque thresholds on the robot could be carried out until the actual human trajectory is matched. This would provide information on the force limits used during human mastication for subjects and how these might vary for different food types or the trajectory used.

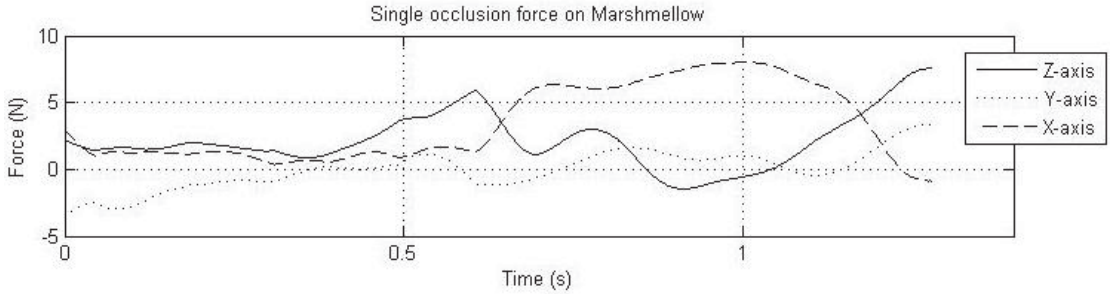

Figure 6.21 Measured force profiles on the molars during a simulated 3D human trajectory applied to marshmallow

Fig. 6.22 shows the force profile measured using the chewing robot for the corn thin food product. A similar pattern in which x-axis force is present during the early stages of the motion which is later translated into y-axis direction forces. There is a steady increase in vertical forces until at just after 1 second the forces are reduced as the jaw begins the opening phase of the trajectory. The inflection points on the curve suggest fracture events occurring as observed for the biscuit product. The next stage of development in the robot must resolve whether internal friction forces within the robotic linkages are contributing to the measured x- and y-axis forces when the jaw is under load. Implementation of a miniature 3D force sensor such as used in the 6-bar linkage robot could provide direct measurements of the local forces applied on the food.

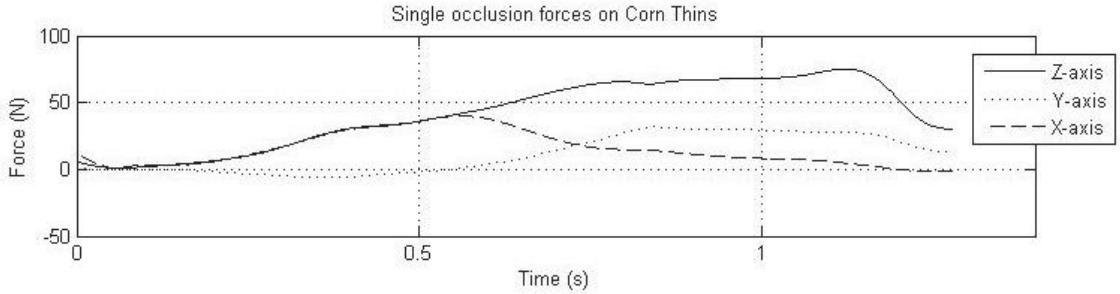

Figure 6.22 Measured force profiles on the molars during simulated 3D human trajectory applied to corn thins

6.4. Conclusion

The application of the 6RSS MRJ to food chewing experiments was described. The force vector applied on the active molar was calculated from the measured torques applied on the six actuators using an analysis of forces through the linkage mechanism. A series of experiments were carried out using model and real food systems. Experiments where the robot jaw was made to follow a one dimensional trajectory showed very good agreement with measured force-deformation curves measured by uni-axial compression testing. As a further stage of validation of the robot, the molar trajectory of a 6-bar linkage chewing robot was reproduced. Good agreement was observed between the z- and y- direction force-profiles measured using both machines, but significant x-axis forces were recorded on the parallel mechanism robot. It is thought that these could be due to internal friction in the linkages under conditions where the jaw is loaded. Experiments were also carried out simulating 3D recorded human trajectories showing expected profiles in the z-direction but unexplained force profiles in the x- and y-dimensions. Further work interpreting these forces or alternatively the direct measurement of forces using a sensor is required before accurate force measurement can be assumed with the MRJ.

The work here shows promise for application of the robot to characterise food texture, however a number of future developments are required before simulation of complete chewing sequences can be carried out. One of the key features that must be added to achieve this is retention and manipulation of the food bolus between chewing cycles.

7. FORCE CONTROL

In the previous chapter techniques to enable position control of the MRJ were shown and performance assessed in joint space. The application of position control for non-occluding phases of the chewing cycle has shown to be effective. This chapter deals with the motion control of the MRJ once food comes in contact with the jaw where position control without regard to forces acting on the jaw becomes less appropriate.

In the first section the force control problem as it relates to partially constrained tasks is discussed. Force control related to human mastication is examined next. Passive force control using the inherited passive compliance of the MRJ is accessed by estimating the stiffness of the MRJ in both joint and task space by using the jacobian matrix formed in chapter 3.

The next section describes in detail an active compliance/impedance method using the torque limiting function in Galil. Application of the torque limiting method is then described with experiments run on various artificial foods of different hardness and its suitability for motion control during food contact periods is assessed.

7.1. Force Control in Partially Constrained Tasks

The motion control problem of the MRJ involves movement in a partially constrained task space as the lower jaw teeth encounter food and the upper teeth. Food properties are unknown and to assume a complaint environment that would allow pure position control is risky. Human jaw movement around the maximum intercuspal point at jaw closed position is dependent on teeth geometry with very fine grinding movements of around 0.35mm reported which suggest force control is operating in the biological model to allow the tooth geometry to be followed. For these reasons a force control scheme for the MRJ is to be investigated.

Yoshikawa (2000) reviews the state of the art in force control for robot manipulators. Two basic approaches are identified as hybrid control and impedance control.

Hybrid Force Control:

Hybrid control proposed by Raibert and Craig (1981) selects the directions in which the position of the end-effector of a manipulator is to be controlled and the directions in which the forces exerted by the end-effector on the environment are to be controlled, and gives control so position and force trajectories can be followed simultaneously. Usually the hybrid control system uses two feedback loops for separated force and position control.

Craig (1989) suggests a hybrid scheme to solve the problems of partially constrained tasks and defines a framework for control in partially constrained tasks by defining natural position and force constraints that arise from the contact between an end-effector and the work environment. Artificial constraints are defined by Craig as the desired motion or forces we command. For good control in partially constrained task spaces every degree of freedom should be controlled to meet either a position or force constraint, whether that constraint be naturally occurring or artificially due to a planed position or force profile. For this purpose, Craig (1989) suggests a hybrid position/force control will solve three problems:

1. Position control of a manipulator along directions in which a natural force constraint exists.
2. Force control of a manipulator along directions in which a natural position constraint exists.
3. A scheme to implement the arbitrary mixing of these modes along orthogonal degrees of freedom of an arbitrary frame.

If we consider the case of the MRJ, we see there are two main phases in the chewing cycle under which some form of force control is needed. The first is the crushing phase where the jaw first comes into contact with a food sample upon closing. Provided excessive forces are not reached, the next phase is the grinding phase where teeth slide over each other in an effort to reach the maximum intercuspal position. During this grinding phase it is the tooth geometry that determines the jaw movement. This grinding phase has been shown to involve only very small movements of around 0.35mm but is also likely to contain large force changes depending on the particular food sample.

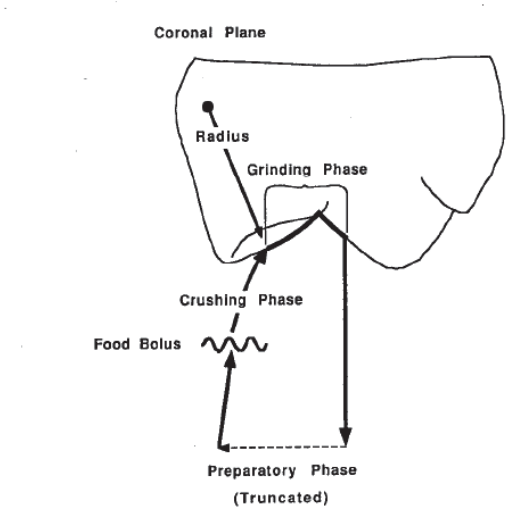

Figure 7.1 The two main phases that require force considerations (T. R. Murphy 1965).

For the MRJ it can be seen that the teeth and food provide natural position constraints which are related to the foods physical properties and to the geometric characteristics of the contacting teeth surface. The position constraints act in the normal direction to the teeth surface during teeth contact if we consider friction to be negligible. Position constraints due to food contact is less well defined as different foods will cause different degrees of forces both at a normal to the foods surface as well as horizontally and laterally as sharing forces occur during food break down.

Natural forces are constrained to zero in all 6 DOF during the non-contact 'preparation' phase. Here we say forces are constrained to zero as they relate to forces of contact, inertia is not considered in this framework for partially constrained tasks. Therefore according to Craig's framework, we require 6DOF position control during the non-contact phases in which natural force constraints exist. For phases with food and teeth contact we require force control to replace position control along directions where natural position constraints exist due to the food and teeth. Craig allows an arbitrary constraint frame to be set up so force can be controlled in one axis of this frame, while orthogonal axes are position constrained. This assumes unconstrained motion is possible in the axes orthogonal to the axes which has encountered the position constraint and requires force control. Vukobratovic (1997) claims such a partition of force and position control in the real world is not possible and questions the hybrid position-force control method on that basis.

For the position and force constraints to be accurately defined on the MRJ we require accurate information of both the geometry of the tooth surface and the physical properties of the food being crushed. As it is unrealistic to define the foods properties before every cycle to determine which degrees of freedom require force control, an alternative approach that allows force control to take over only when position constraints in a particular degree of freedom are encountered is recommended.

Impedance Control:

The impedance control approach originally proposed by Hogan (1985) aims to control position and force by adjusting the mechanical impedance of the end-effector to external forces generated by contact with the environment This is a generalisation of stiffness control and admittance (compliance) control as described by Yoshikawa (2000) Impedance control provides large mechanical impedance in directions in which accurate position control is to be maintained so that a contact force acting as a disturbance does not create position errors. Mechanical impedance can be reduced in directions where is it desirable to sacrifice accurate control of position in order to achieve some degree of control over contacting forces. Typical methods of achieving large impedance is by setting a large proportional gain to the feedback error, and for reduced impedance a smaller proportional gain is used.

Advantages of impedance control are the easy transition from non-contact to contact phases where unlike the hybrid method, no switching of control modes is necessary. Impedance control also allows a form of force control in a constrained environment even when there is no knowledge of the shape or elasticity of the object in contact.

For the MRJ, impedance control seems well suited as the properties of the contact object (food) are not initially known and it can be implemented without needing to fit a bulky force sensor. The unique arrangement of the actuators in the MRJ may allow jaw impedances to be controlled in Cartesian space by modifying the proportional gains on individual actuators. The Pterygoid actuators are arranged in such a way that impedance in the X and Y axes of the Skull frame may be reduced by reducing the feedback gains on these two actuators. In a similar way, impedance in the Z-axis of the Skull frame may be reduced by reducing feedback gains on the Temporalis and Masseter actuators.

7.2. Force control in Human Chewing

When considering the best method of force control during food and teeth contact phases, a close look at how the human system performs this function may provide useful insight. Future work on higher level control involves neural networks to allow the robot to react to sensed inputs the same way as a human does, so the closer the alignment of this lower level force control to the biological system the better, in particular using similar force sensing and control methods may prove advantageous.

McCarragher (1994) assesses human sensing ability during a constrained task demonstration with the aim of applying similar sensing techniques to robotics. In particular human's ability to sense and react to force is examined by removing all other senses and attempting a simple insertion task. Through examining the forces registered during the insertion task and the subject's reaction to these forces, the base

assumption that humans sense force during the task at a single point is challenged. McCarragher (1994) concludes that the control theoretic models of human sensing ability proved to be insufficient due to the human ability to sense force from more than a single source.

Physiological studies suggest that human force sensing uses neural receptors in the muscles, joints and skin (Ottenhoff, van der Bilt, van der Glas, & Bosman, 1992). This means for the human system, where ever there is a muscle there is an ability to sense force, allowing force information from multiple points during a movement. The muscle receptors do not have access to the conscious mind and so a human may sense force without knowing how he does so. This suggests force sensing and related decisions during human chewing is intuitive and relies on an innate ability derived from many years of evolution rather than a logically thought out process that may be easily replicated using a single point force sensor located at the end-effecter.

Bosman (2004a) studied human control mechanisms during mastication. Bosman concludes that is it mainly the sensory feedback provided by the spindles in the closing muscles of mastication that determine the facilitatory response of Masseter muscles due to a hard food. It was shown that force feedback from the soft tissue around the teeth that house the Periodontal Mechanoreceptors was not significant in determining chewing response to hard foods in both animal and human studies. In the human studies, EMG response to hard foods were unchanged after anesthetising the tissues housing the periodontal mechanoreceptors and it was concluded that it was the muscle spindles and not the periodontal mechanoreceptors that account for the muscle response to the forces induced by the hard foods.

With regard to force sensing and control in the MRJ, the use of the biologically placed actuators as a means to both sense and control force in a similar way a human muscle would has some merit and may be similar to how a human senses and controls forces during chewing. The placement of actuators in the same way as the closing muscles of mastication allows unique control methods to be successfully applied to the MRJ. These methods will be discussed in detail in the next section.

7.3. Force Control on Similar Robots

The WJ-series robots use both position and force control when performing chewing motions (H. Takanobu et al., 2000). Like the MRJ a biological basis is used for the design of the robot and its control systems. Takanobu describes the sensory organs involved in human mastication in a similar way to findings. He suggests there are two main sensors in the muscles of mastication, one is the muscle spindle and the other is the Golgi tendon receptor. Takanobu's work on the WJ series of mastication robots reflects these findings with actuators aligned with the major muscles of mastication

and tension sensors integrated into each actuator. The WJ series robots took advantage of these actuator placements by controlling the left and right Pterygoid with pure position control and including force control for the other actuators (H. Takanobu et al., 2002). Allowing pure position control for the Pterygoid is justified as the function of these muscles is to control the horizontal and lateral movements involved in sharing foods which are unlikely to be position constrained in the same way as vertical movements.

7.4. Force Control Method for MRJ

Objective:

Based on Craigs framework for motion control in partially constrained tasks the following is to be achieved on the MRJ:

1. Position control of the MRJ during phases where the jaw has no contact with food or teeth.

2. Force control of the MRJ along directions in which a natural position constraint arises due to a hard food or teeth contact.

3. A scheme to implement the arbitrary mixing of these modes along orthogonal degrees of freedom of an arbitrary frame.

Using knowledge of the geometry of the MRJ we can make some assumptions which may simplify the force control method:

1. Position constraints occur at a normal to the teeth surface under either tooth contact or food contact.

2. Upon contact with hard food or teeth the combined friction and share forces are not enough to provide a position constraint in X and a grinding motion in X and Z-axis of mandible frame is always possible during all chewing tasks.

3. For a position constraint to be identified in the vertical direction during motion, a force due to contact in this direction must exceed a threshold which may be changed depending on food.

A more specific objective from a pure robotics view point is to perform position control until reaching a force threshold in the Z-axis of the mandible frame, in which case force is controlled at a maximum level in this Z-axis direction while other degrees of freedom are free to follow their position controlled trajectories.

As a second objective, the biological functions of force control should be considered and used as a basis for meeting the first objective if possible.

Method:

The MRJ operates without any sensors to provide Cartesian feedback on either force or position. The position control scheme has assumed accurate modelling of the physical robot and ideal transmissions of movements in joint space to movements in Cartesian space so that an accurate joint space control scheme will lead to accurate control in Cartesian space. While this is not ideal from a pure robotics stand point, it is likely to be similar to how the human biological system operates, with muscles providing independent feedback on position and force.

A high degree of accuracy over force at a point on the mandible is not likely in the biological model and therefore should not be strived for when attempting to replicate the mastication process. It is more likely in the biological model that a series of forces in the muscles of mastication are controlled within limits after contact with food or teeth. Details of exactly how the biological system uses feedback from muscle spindles to achieve this, and whether there is a feed-forward anticipatory element is still subject of current research. It is speculated that the muscle spindles, in particular their role in the mono-synaptic reflex loop of individual muscles, is the cause of the sensory induced muscle response to unexpected forces during jaw closing [control mechanisms in human mastication]. Based on these findings, a method that controls force applied by each actuator to the mandible to regulate force in a vertically constrained direction is congruent with the overall aim of keeping functions as closely related to the biological model as possible.

Galil has a torque limiting function that allows a maximum torque to be specified for each axis. Intuitively this seems to fit our force control objective by allowing position control until a position constraint is hit demanding a high force where limiting torques in joint space will have the effect of controlling force to somewhere below the maximum force capable of being exerted by the robot. By careful selection of these torque limits throughout the movement it may be possible to control forces in the Z-axis of the mandible frame, while allowing position control of the other degrees of freedom to perform close to normal.

To perform force control in the Z-axis of the moving mandible frame once position constraints are hit, we need to specify a force in Cartesian space on the moving mandible frame, then use the Jacobian formed in chapter 3 to find corresponding joint torques. It then becomes a joint space problem of controlling joint torques to somewhere below the maximum Z-axis force at all times during food and teeth contact phases.

If we consider the static case and use the principle of virtual work, joints torques can be found from a specified Z-axis force as follows:

$$\tau = J^T(\theta)F \tag{35}$$

Where τ is the 6X1 joint torques required, $J^T(\theta)$ is the transpose of the Jacobian matrix for the six joint angles θ, and F is the desired force in Cartesian space. For our application the desired force in Cartesian space is defined as:

$F = \begin{bmatrix} 0 \\ 0 \\ F_Z \\ 0 \\ 0 \\ 0 \end{bmatrix}$, where F_Z is the specified maximum force in the Z-axis direction that we want to control.

With the trajectory pre-planned it is possible to create a set of joint torques for a specified Z-axis force that correspond the trajectory. This joint torques can be used as torque limits in joint space to limit force in Cartesian space.

While statically the above approach sounds reasonable, with motion commanded there is added torque demands on each actuator to overcome the friction and dynamics of highly geared motors, as well as the relatively small torques required to overcome dynamics of the free mandible which we will continue to consider as negligible. An algorithm that takes these added torques into consideration before the position constraint is hit, then treats the problem statically once position is constrained is required. One way of doing this is to run the trajectory without food, logging joint torques and then adding them to the calculated torques for the static case.

In addition to the problem of separating food related forces from the forces of free motion, applying torque limits that yield the desired Z-axis force without considering motion in other DOF's means no motion in these other degrees of freedom is possible as all torque is used maintaining the Z-axis force. Without force sensors it is not possible to implement a true hybrid position-force control scheme that ensures the correct joint torques to enable both force control in the Z-axis and position control in the other DOF's.

By examining the results of the equation that calculates torques from a specified force and assuming jaw closed pose, a simplification can be made that allows each actuator to be approximately mated with a Cartesian axis in a similar way to the WJ-3 robots independent treatment of the Pterygoid muscles as purely position controlled. This is taking advantage of the biological layout of the actuators, and may explain how the

independent muscle responses in the biological 'joint space' of the human lead to appropriate position and force movements of the mandible.

The approximation of the alignment of each actuator with a Cartesian axis will lead to some discrepancies in actual position for the DOF's that require pure position control, as well as discrepancies in the actual force that is controlled in the Z-axis direction. These discrepancies are likely to be small and are likely to lie within the desired accuracy determined by the biological model.

This can be thought of as a partial Cartesian-based impedence control scheme in that positions will still be controlled in joint space but force control is specified in Cartesian space. Implementation of this technique is shown in the next section where experiments were conducted that involved both position control and force compliance on real human chewing trajectories of 6-DOF.

7.5. Initial Chewing Experiments

7.5.1. *Masticatory Movements*

A series of experiments were carried out was to test whether or not the masticatory robot could follow a real-life human masticatory movement, if the robot could chew on foods of various texture properties, and if the robot could have a compliant ability in terms of giving way to an extremely hard food.

In the following experiments, the masticatory movement to be reproduced by the robot was specified by the trajectory of incisor point (IP) in three coordinates (Fig. 7.2) and the roll-pitch-yaw angles of the mandible (Fig. 7.3), in the skull system {*S*}. The masticatory movement was modified from a masticatory measurement made for a human subject chewing a hard food (Peyron, Lassauzay, & Woda, 2002). The mastication lasted 45.32 s and was sampled every 10 ms.

Given the above mandibular movement, the inverse kinematics were solved to determine the individual trajectory of each of the six crank actuations required for the robot to follow the mandible movement. Because the Galil controller used could only implement a trajectory of a time interval of 2^n ms (where n is an integer between 1 and 8) the actual mandibular movement that was sampled every 10 ms needed to be interpolated before its implementation in Galil. A cubic polynomial was found to be capable of converting a 10-ms interval trajectory to an executable 8-ms interval trajectory without significant distortion in the motion profile (in terms of angular displacement, velocity and acceleration).

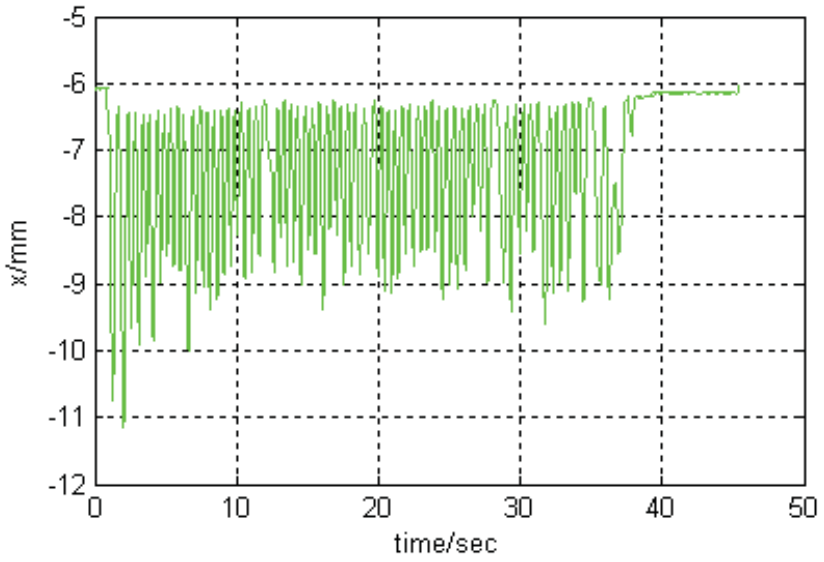

(a)

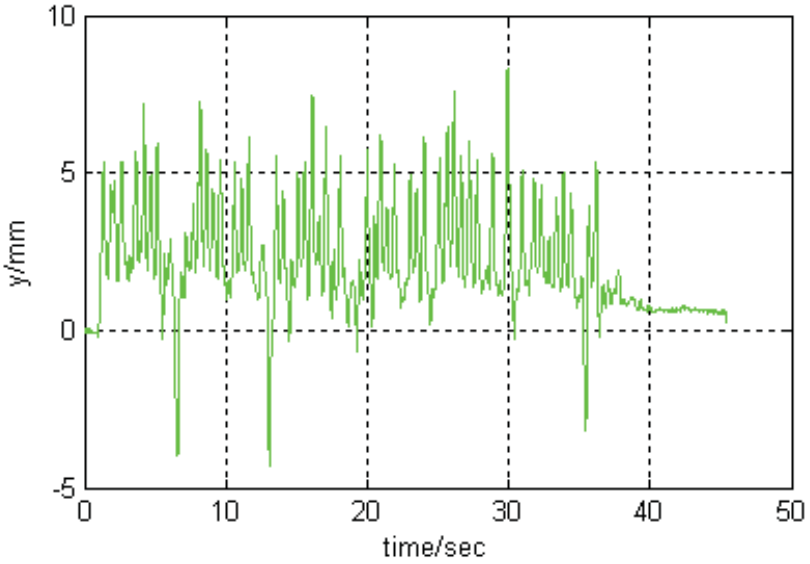

(b)

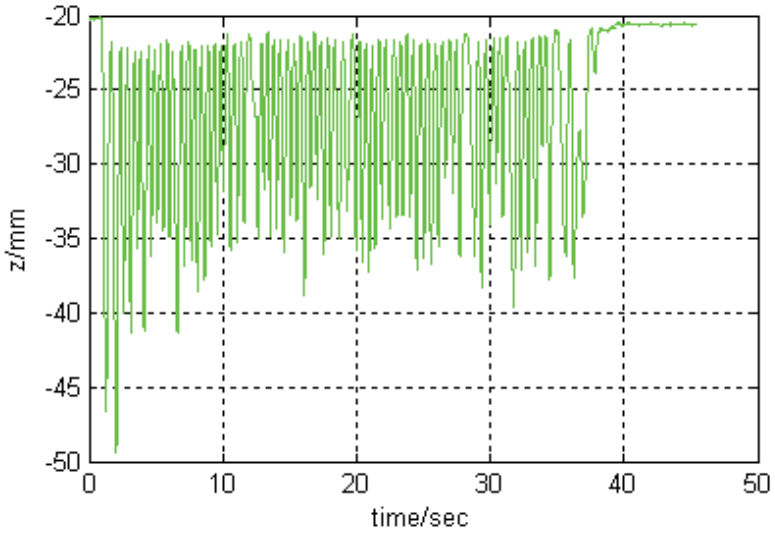

(c) Figure 7.2 Incisor's coordinates versus time, (a) *x*-axis, (b) *y*-axis and (c) *z*-axis.

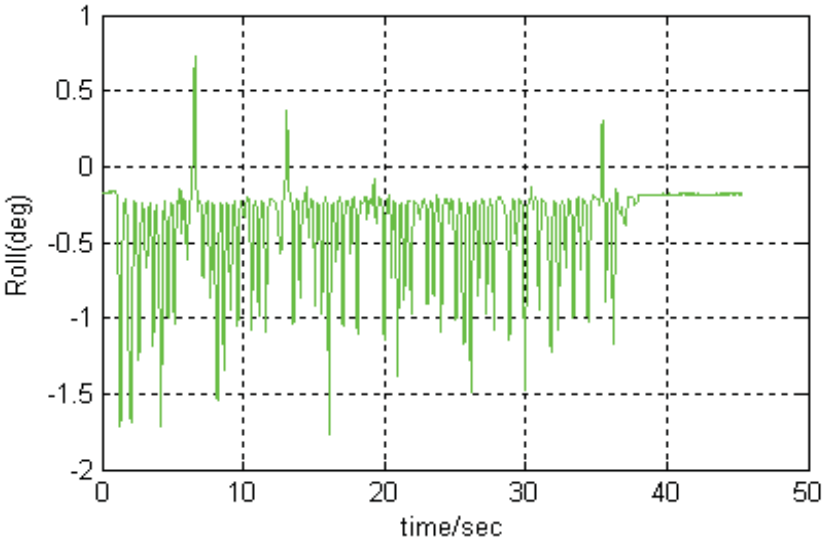

(a)

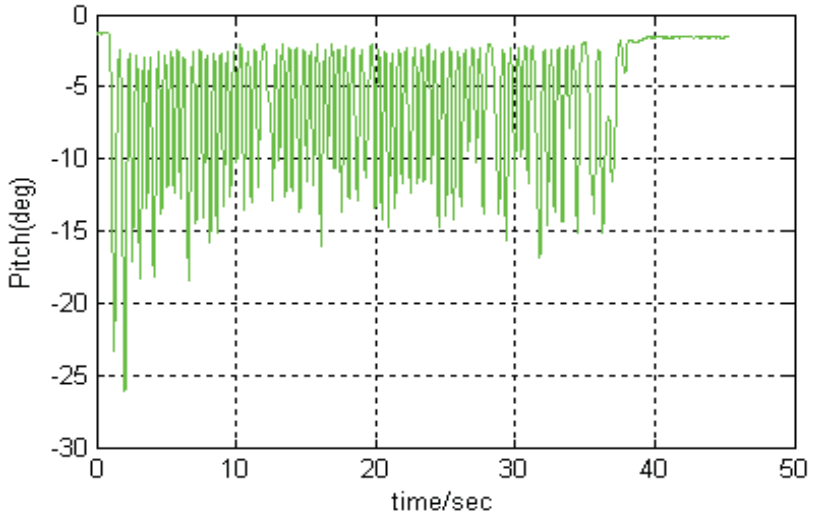

(b)

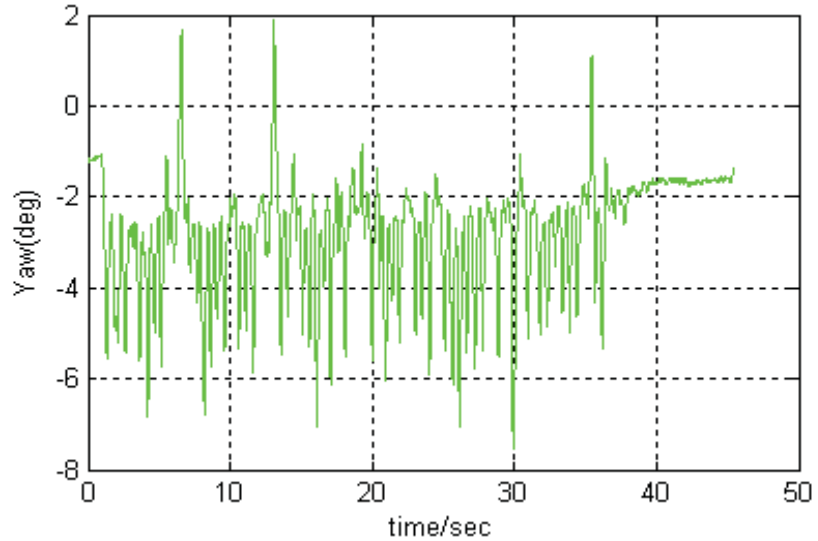

(c) Figure 7.3 Mandibular orientation versus time, (a) roll angle, (b) pitch angle, and (c) yaw angle.

It can be seen from Fig. 7.3(b) that the subject chewed predominantly on the left side and performed only three peaks of the lateral excursion movement to the right. It can also be seen in Fig. 7.3(c) that for the first couple of chewing cycles, for the following few chewing cycles, and for the rest of chewing process, the maximum mouth opening was approximately 30, 25 and 20 mm, respectively, given that the incisor tooth rested initially at position z=-20 mm.

7.5.2. *Robotic Chewing without Food*

During the first experiment no food was involved and the robot was commanded to freely follow the defined masticatory movement (Fig. 7.2 and 7.3) for 5 seconds. All the motors were under contour mode PID control with K_p=8, K_d=290 and K_i=0.2 with a time interval of 8 ms. Motor speed and acceleration were set to be auto adaptive and the motor torque was set at a maximum torque of 60% (i.e., ±6 V). The PID control was implemented using a Galil controller (Torrance, Pap, Xu, Bronlund, & Foster, 2006).

Only representative results are presented within this section. Fig. 7.4 shows the actuation of the right pterygoid actuator. The occlusion took place at a crank angle of around zero and full opening of the mouth occurred at the valleys of the crank angle profile. As can be seen in Fig. 7.5, there is negligible error during the occlusal phase of chewing. This is the most important phase of the chewing process as it is supposedly involves interactions between food and teeth. The maximum error (of less than 1^o) occurs during the transition from the opening to the closing phase of the mouth.

The motor torque (Fig. 7.4) varied at a frequency which was the same as that of the crank angle and reached a maximum at the point in time when the mouth transitioned from open to close. There was very little torque required during the opening and closing phases. These findings are self-explanatory given the fact that no food was involved during this particular chewing experiment. The other crank actuations behaved in correspondingly similar ways.

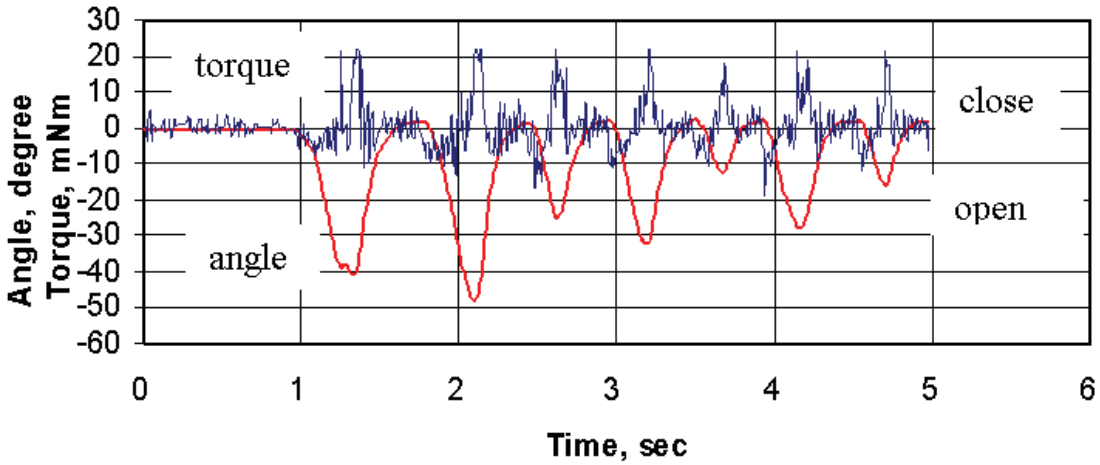

Figure 7.4 Actuation of right pterygoid actuator in free chewing.

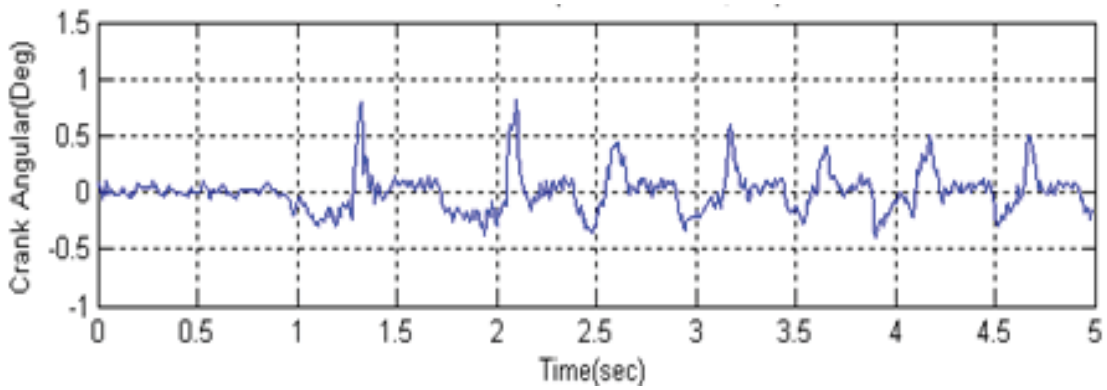

Figure 7.5 Error between the commanded and actual right pterygoid actuation in free chewing.

7.5.3. *Robotic Chewing of Simulated Foods*

In the following two experiments, foods were simulated by a 10-mm-thick aluminium plate for hard food and a 10-mm-thick foam plate for soft food. The masticatory robot was commanded to perform seven chewing cycles over the first 5 s (see the trajectories shown in Figs. 7.2 and 7.3); however, it was paused for 2.5 s in order that the simulated food could be inserted between the teeth when the mouth opened up during the first chewing cycle.

To avoid a large chewing force being exerted when the robot chewed on a hard plate (which would have resulted in the weakest part of the robot being damaged) the torque on the motor was limited. In the two experiments, the torque thresholds (Table 7-1) were set at the maximum torques for the free chewing, which generally occurred at maximum jaw open position during chewing. This approach was taken as it allowed a minimum level of torque limiting without effecting motion during the non-occluding, non-contact phases. The rest of the controller specifications were set the same as those used in the previous experiment.

Aluminium Plate as Food

For this experiment, an aluminium plate was inserted into the mouth and placed at the left side molars, which mirrored the left side chewing process specified in 7.5.1.

Table 7-1 Motor Torque Thresholds for Chewing Simulated Foods.

	Right Pterygoid	Left Pterygoid	Right Masseter	Left Masseter	Right Tempolaris	Left Tempolaris
Torque Limit	2.0V/10V	1.5V/10V	1.0V/10V	1.0V/10V	2.50V/10V	3.0V/10V

Fig. 7.6 shows the crank angle and torque of the right pterygoid actuator while the hard food was being chewed. Comparison between Figs. 7.4 and 7.6, reveals that there was no significant difference in either the crank angle or the torque between free chewing and chewing on hard food.

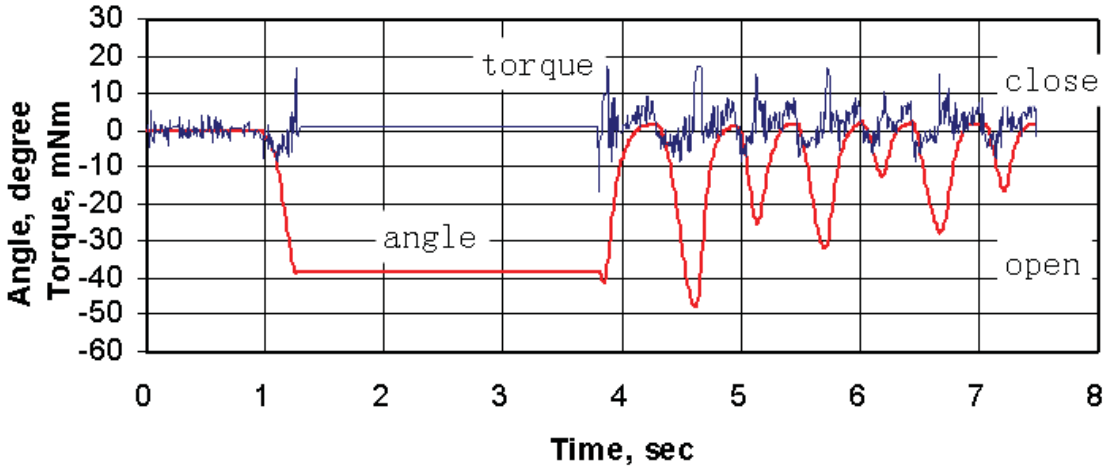

Figure 7.6 Actuation of right pterygoid actuator while chewing on hard food

Data from the robot kinematics, showed that the left and right pterygoid actuations were mainly responsible for the lateral movement of the jaw. When the robot chewed on the aluminium plate placed at the left, the jaw teeth slide on the plate surface and the left pterygoid actuator exhibited a slightly larger torque, although no torque limit was hit (shown truncated in Fig. 7.7(a)), than that which occurred during free chewing (Fig. 7.7(b)). The fact that left and right pteygoid actuations did not strike torque limits, and were able to follow prescribed trajectories during the movements on the aluminium plate illustrates no physical constraint in the Y-axis direction, consistent with assumptions made in the previous section

Robot kinematics show that the right temporalis and right masseter actuations were mainly responsible for the lifting/lowering of the right, non-chewing side of the jaw. When the hard plate was inserted at the left molars, their actuations did not differ significantly from those for free chewing. Fig. 7.8 shows the crank angle and the motor torque of the right masseter actuator for hard food.

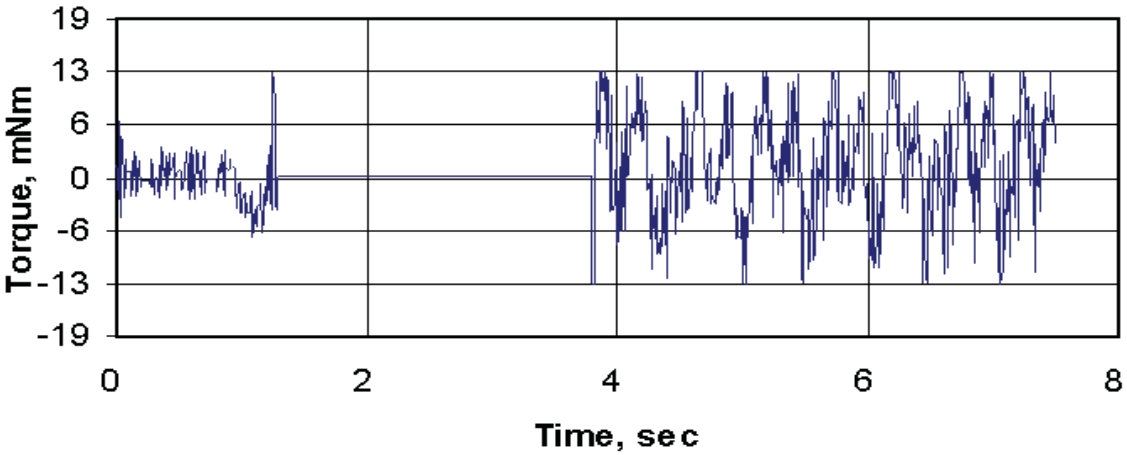

(a)

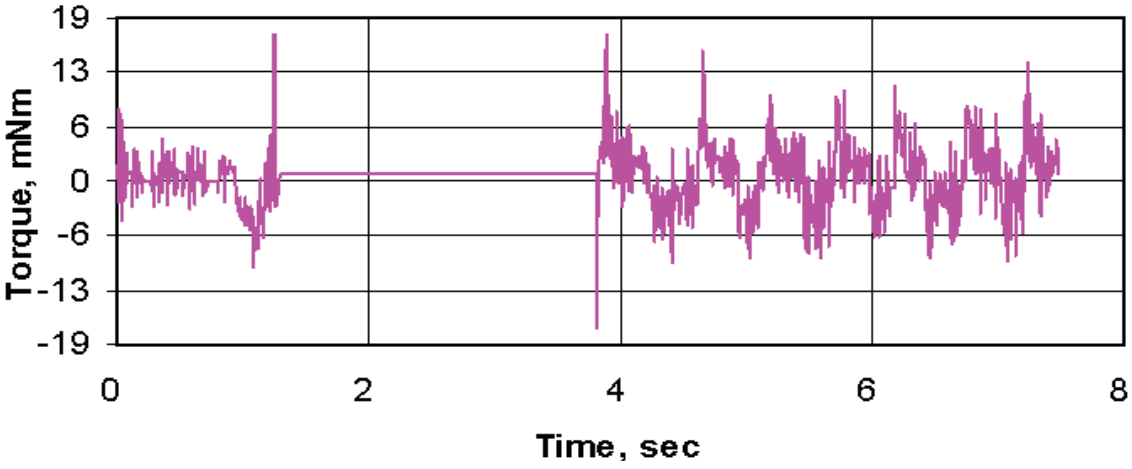

(b)

Figure 7.7 Torque of left pterygoid actuator for free chewing and hard food, (a) chewing on hard food and (b) free chewing.

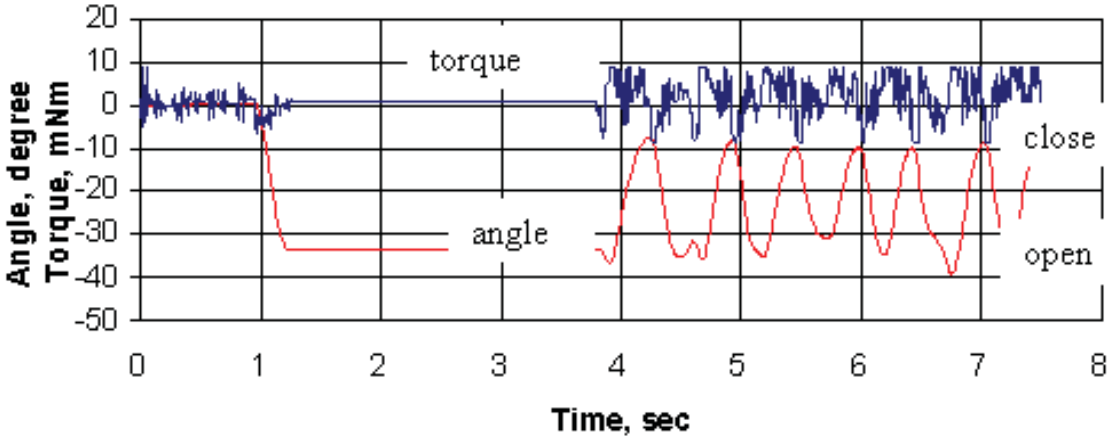

Figure 7.8 Actuation of right masseter actuator for hard food.

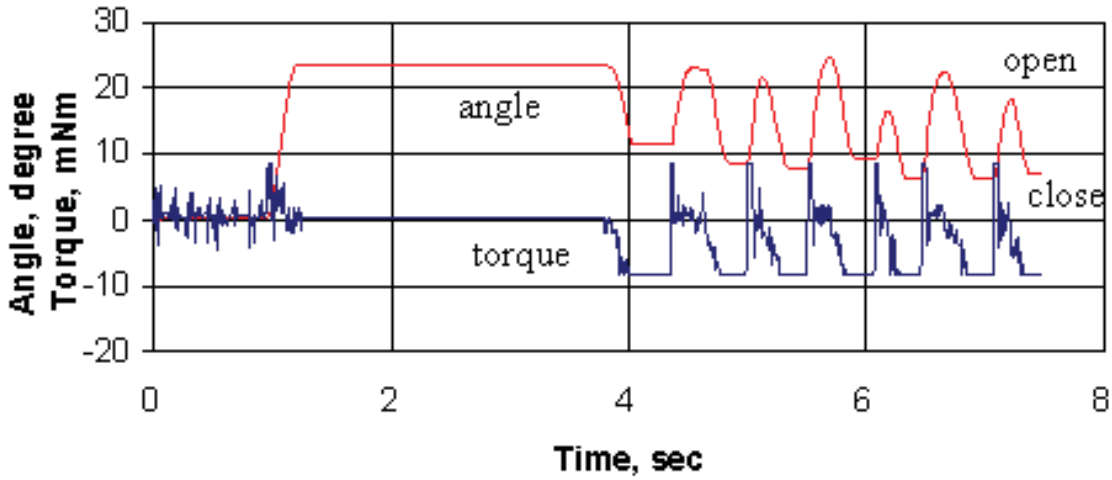

Figure 7.9 Actuation of left masseter actuator for hard food.

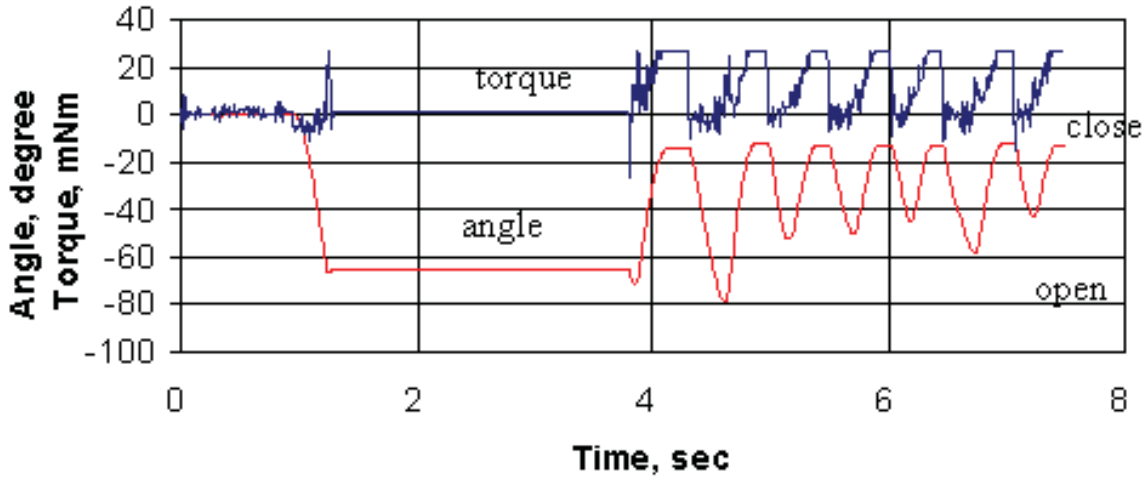

Figure 7.10 Actuation of left temporalis actuator for hard food.

Due to the hard plate having been inserted on the left molars, the left temporalis and left masseter actuations (responsible for the lifting of the left side of the jaw) differed greatly from those generated during free chewing. Because the plate is not compressible (with the forces possible using the actuators), the driving torques limited the motion, and the specified chewing trajectories of the two actuations could not be followed (as demonstrated in Figs. 7.9 and 7.10). It was found that the occlusal peaks of the chewing trajectory were truncated off. The actual trajectory involved an occlusal inaccuracy of between 5^{o} and 10^{o} at the crank shaft and the motor torque held at the threshold value during these periods.

This experiment showed that the robot motion was able to give way to the hard food by limiting the motor torque. This ability would thereby prevent the robot from being damaged when hard foods were being chewed, and illustrates a degree of force control in the vertical direction once the position constraint caused by the hard aluminium plate is hit. In this example, force is limited to an arbitrary level as torque limits were set at minimum levels so as to not interfere with position control during non-occluding phases.

Foam Plate as Food

In this experiment, a foam plate was inserted into the mouth in order that it would be chewed at both the left and right molars. The foam used was slightly rough in texture and could be broken into pieces when being chewed. Due to these properties, the lateral movement of the jaw was slightly frictional, as evidenced by the experimental results gathered from the left/right pterygoid actuations. However, none of the actuators behaved with any significant difference to the results observed whilst chewing without food.

7.6. Conclusion

This chapter looked at the force control problem as it relates to partially constrained tasks, which human mastication is. A unique force limiting method has been implemented using torque limiting on individual actuators. Actuator torque was examined during a mastication sequence involving free movement and movement with aluminium inserted to simulate a hard food. The torque limiting method allowed the left masseter and temporalis actuators, that provide the vertical movement on the aluminium plate, to stop being position controlled as the task became position constrained on the left side in the positive direction of the Z-axis.

By looking at actuator torques during the chewing of hard foods with the robot, unique insight can be gained into the human experience. Figure 7.9 and 7.10 illustrate high forces resulting in torque limits on the left masseter and temporalis, a human subject performing the same action would experience a reflex action in their masseter and temporalis muscles as their left molars contact the hard aluminium plate. By looking at actuator torques together with forces at the teeth on the Massey Robotic Jaw, more data is available to characterise food properties which leads to potentially better correlations with human sensory panels.

8. DISCUSSION AND FUTURE WORK

This chapter discusses the research carried out with respect to the research objectives outlined in chapter 1, and then proposes future work required on the robot.

8.1. Discussion

The closed form inverse kinematics for the novel mastication robot of 6-RSS mechanism was successfully solved for the first time, and the robots physical parameters were fully defined in appropriately designated co-ordinate frames. Matlab programs were written to perform Inverse kinematics for large trajectories, and results proved to have good agreement with the inverse kinematics performed by simulation in solidworks. Jacobian analysis of the novel robot was also successfully performed for the first time, and singularities found. The inverse kinematics allowed for the first time a set of six trajectories corresponding to the robots six actuators to be formed from a single target trajectory of the jaw.

Physical modifications of the robot to remove backlash inducing bevel gears and needless workspace restrictions were carried out to enable real human mastication movements to be performed on the robot.

Galil motion control hardware was selected and integrated into the novel robot. After considering robot dynamics together with the high gearing of each of the actuator driving units, a simplified PID control scheme was implemented where each actuator is controlled independently in a co-ordinated manner. Six degree of freedom motion was successfully commanded with acceptable accuracy in joint space.

The problem of dimensional differences between a human subject and the robotic jaw was solved by a novel land marking technique. The land marking technique enabled recorded human mastication movements at the molar of interest to be re-created in all six degrees of freedom on the novel robot for the first time.

The mastication robot was used in a number of experiments where real and model food samples were chewed. A method to control force under an upper limit by limiting actuator torques was successfully implemented, and may be used as a basis for a more complete biologically inspired force control algorithm. The torque limiting by individual actuators enabled position control during the force constrained non-occluding phases, and force limiting during the position constrained occlusion phases where teeth-food contact occurs.

Motor currents of the driving actuators were successfully used to calculate force at the jaw as the robot performed chewing sequences on the real and model food samples. Validation of the force calculation method was done by re-creating the action of a

TAXT2 texture analyser, both showed similar results. Further validation was done by recreating 2D motion of a linkage based chewing robot with 3D force sensor integrated, results were similar in the Z-axis direction, but significant differences occurred in forces in the Y-axis direction. The differences in forces could be due to internal friction of the Massey Robotic Jaw, which for calculation purposes was assumed to remain constant with changing load. Another area of possible error in force calculation is position error in task space due to backlashes in the two remaining bevel gears; this would lead to a different compression action on the food sample and hence different resulting forces. Despite the differences in forces in the Y-axis direction, food properties such as multiple breaks of brittle foods were able to be seen from the recorded force data during a single occlusion run, showing the robot has the ability to act as a food property analyser. Furthermore the robots biologically inspired actuator arrangement enables torques through different actuators to lead to new insight into what a human may experience when chewing a food.

8.2. Future Work

The Massey Robotic Jaw requires a food retention and manipulation system to enable it to chew several cycles. This work requires recreating the action of the human tongue and cheeks. Until this task is accomplished the MRJ will be limited to single occlusion cycles.

The two pterygoid actuators providing lateral movement to the robot have retained their bevel gears due to the difficulty of placing driving units directly inline with the cranks. It is unclear how significant the backlash that still exists on these two actuators affects the motion of the robotic jaw, and future work should be done to remove these bevels also. Chapter 6 illustrated unexpected forces in the lateral directions as the robot came into contact with food; it is possible that this backlash from the two pterygoid actuators has produced errors in task space position of the jaw, and hence the forces applied to the food sample.

A method to accurately track the Massey Robotic Jaw's position in task space is needed to confirm position accuracy in task space. Due to the robots DC motors, the articulargraph was unable to be used to track the robots motion. A vision based system such as that used by Rörle et al. could be used. If it is seen that motion in task space is not as expected, a second control loop may need to be implemented where task space position is feedback into the control system. This would require a new method to track the jaw in real time during motion, and formation of a forward kinematics algorithm that is fast enough to be used in the control loop.

Fitment of a 3D force sensor under the molars is suggested to help explain the unexpected forces calculated using actuator torques in the Y-axis. The force sensor would determine whether forces are due to inaccuracies of robot movement in task space or from frictional forces occurring in joints as the jaw is loaded.

A more complete force control strategy is required to enable human force profiles seen during mastication to be recreated on the robot. Chapter 7 forms a basis for which a more complete force control method could be formed. Torque limits can be dynamically updated during occlusion so force profiles can be created should position constraints be hit. Further experiments with a 3D force sensor can validate the assumptions used in chapter 7.

Further experiments using the robot to chew foods, preferably multiple cycles are required to assess how well the robot can perform as a food property analyser. Forces during the chewing experiments, plus torques from the robots six actuators can be used to characterise food properties, and comparisons made with human sensory panels. As the MRJ using human locations for the six actuators, comparisons of actuator torques with EMG data recorded from the human subject's muscles as they chew the same food would be useful.

9. CONCLUSION

A masticatory robotic model of crank actuation was presented, kinematic parameters having been derived according to the anatomy of its human jaw counterpart. The closed-form inverse kinematics was determined for joint actuations. The Jacobian matrices were derived, and their singularity was analyzed. The physical robot was presented and the mechanical and motion control system designs were discussed. Experimental measurements for chewing of simulated foods were conducted. The results of these experiments were analysed and compared in terms of both the crank actuations and driving torques required. The kinematic and dynamic models of a generic 6RSS robot are considered and simplified considering the special features of a practical chewing robot and the requirements of controller design. The robotic model was simulated for an inverse kinematics problem in SolidWorks/CosmosMotion. The issue of dynamic position and force control of a chewing robot with a 6RSS mechanism is addressed. An impedance control scheme is proposed to achieve the position and force control of the robot. A description on implementation of the controller is presented.

The application of the 6RSS parallel chewing robot to food chewing experiments was described. The force vector applied on the active molar was calculated from the measured torques applied on the six actuators using an analysis of forces through the linkage mechanism. A series of experiments were carried out using model and real food systems. Experiments where the robot jaw was made to follow a one dimensional trajectory showed very good agreement with measured force-deformation curves measured by uni-axial compression testing. As a further stage of validation of the robot, the molar trajectory of the 6-bar linkage chewing robot was reproduced. Good agreement was observed between the z- and y- direction force-profiles measured using both machines, but significant x-axis forces were recorded on the parallel mechanism robot. It is thought that these could be due to internal friction in the linkages under conditions where the jaw is loaded, further research is recommended in this area. Experiments were also carried out simulating 3D recorded human trajectories showing expected profiles in the z-direction but unexplained force profiles in the x- and y-dimensions.

Further chewing experiments conducted using real foods are required in order to test the functionalities and control algorithms of the robot constructed in this research. Such experiments could include force control experiments that extend on those described in chapter 7, where a vertical force is pre-defined to select appropriate torque limits using equation 35 and torques from free motion runs. The use of force sensors and additional encoders or other tracking method to find robot position in Cartesian space is suggested. Accurate force and Cartesian position data derived independently of the actuation system would allow further assessment of the

effectiveness of the control strategies and clarify force measurement issues discussed in chapter 6.

The addition of a functional tongue and cheek is a very challenging future step that is also necessary before the MRJ can be used for multiple chewing cycles.

10. REFERENCES

Agrawal, K. R., Lucas, P. W., & Bruce, I. C. (2000). The effects of food fragmentation index on mandibular closing angle in human mastication. *Archives of Oral Biology, 45*(7), 577-584.

Anderson, K., Throckmorton, G. S., Buschang, P. H., & Hayasaki, H. (2002). The effects of bolus hardness on masticatory kinematics. *Journal of Oral Rehabilitation, 29*(7), 689-696.

Bosman, F., Bilt, A., Abbink, J., & Glas, H. W. (2004a). NEUROMUSCULAR CONTROL MECHANISMS IN HUMAN MASTICATION. *Journal of texture studies, 35*(2), 201-221.

BOSMAN, F., BILT, A., ABBINK, J. A. N. H., & GLAS, H. W. (2004b). Neuromuscular control mechanisms in human mastication. *Journal of texture studies, 35*(2), 201-221.

Bourne, M. C. (2002). *Food Texture and Viscosity: Concept and Measurement*: Academic Press San Diego.

Carstens., B., & Carstens., B. (2006). *AG500 Manual* (3rd ed.). Bovenden: Carstens Medizinelektronik.

Craig, J. J. (1989). *Introduction to robotics* (Vol. 7): Addison-Wesley Reading, MA.

Daumas, B., Xu, W. L., & Bronlund, J. (2005). Jaw mechanism modeling and simulation. *Mechanism and Machine Theory, 40*(7), 821-833.

Hannam, A. G. (1997). Jaw muscle structure and function. *Science and Practice of Occlusion. Quintessence, Chicago, 41*.

Heath, M. R., & Prinz, J. F. (1999). Oral processing of foods and the sensory evaluation of texture. *Food Texture: Measurement and Perception. AJ Rosenthal, ed. Aspen: Gaithersburg, MD*, 18-29.

Hiiemae, K. M., & Palmer, J. B. (2003). Tongue movements in feeding and speech. *Critical Reviews in Oral Biology & Medicine, 14*(6), 413.

Hogan, N. (1985). *Impedance control: An approach to manipulation*.

Iwasaki, T., & Zheng, M. (2006). Sensory feedback mechanism underlying entrainment of central pattern generator to mechanical resonance. *Biological cybernetics, 94*(4), 245-261.

Klineberg, I. (2005). Interarch relationships of teeth. In I. Klineberg & R. Jagger (Eds.), *in Occlusion and Clinical Practice: An Evidence-Based Approach* (pp. 3-12). Edinburgh: Elsevier Limited.

Koolstra, J. (2002). Dynamics of the human masticatory system. *Critical Reviews in Oral Biology & Medicine, 13*(4), 366.

Lucas, P. W. (2004). *Dental Functional Morphology: How Teeth Work*: Cambridge University Press.

Martin, F. G. (2001). *Robotic explorations: a hands-on introduction to engineering*: Prentice Hall Upper Saddle River, USA.

McCarragher, B. J. (1994). *Force sensing from human demonstration using a hybrid dynamical model and qualitative reasoning*.

Meullenet, J. F., & Gandhapuneni, R. (2006). Development of the BITE Master II and its application to the study of cheese hardness. *Physiology & Behavior, 89*(1), 39-43.

Nakamura, Y., & Katakura, N. (1995). Generation of masticatory rhythm in the brainstem. *Neuroscience research, 23*(1), 1-19.

Okino, A., Inoue, T., Takanobu, H., Takanishi, A., Ohtsuki, K., Ohnishi, M., et al. (2003). *A clinical jaw movement training robot for lateral movement training*.

Ottenhoff, F. A., van der Bilt, A., van der Glas, H. W., & Bosman, F. (1992). Peripherally induced and anticipating elevator muscle activity during simulated chewing in humans. *Journal of Neurophysiology, 67*(1), 75-83.

Pap, J. S., Xu, W. L., & Bronlund, J. (2005). A robotic human masticatory system: kinematics simulations. *International Journal of Intelligent Systems Technologies and Applications, 1*(1/2), 3-17.

Peyron, M., Lassauzay, C., & Woda, A. (2002). Effects of increased hardness on jaw movement and muscle activity during chewing of visco-elastic model foods. *Experimental Brain Research, 142*(1), 41-51.

Raibert, M. H., & Craig, J. J. (1981). Hybrid position/force control of manipulators. *Journal of Dynamic Systems, Measurement, and Control, 102*(127), 126?133.

Risse, G. (2007). *Functional Anatomy vs. Straight - Wire Anatomy,Orientation for Diagnosis, Treatment, CMD*. Paper presented at the XIX International Congress of AIG, Associazione Italiana Gnatologia 1´st Congress of International Academy of Advanced Interdisciplinary Dentistry, IAAID.

Rörle, O., Anderson, I., & Pullan, A. (2005). *From jaw tracking towards dynamic computer models of human mastication*.

Simpson, J. W. L., Cook, C. D., & Li, Z. (2002). *Sensorless force estimation for robots with friction*.

Takanobu, H., Maruyama, T., Takanishi, A., Ohtsuki, K., & Ohnishi, M. (2000). Mouth opening and closing training with 6-DOF parallel robot. *Robotics and Automation, 2000. Proceedings. ICRA'00. IEEE International Conference on, 2*.

Takanobu, H., & Takanishi, A. (2003). *Dental robotics and human model*.

Takanobu, H., Takanishi, A., Ozawa, D., Ohtsuki, K., Ohnishi, M., & Okino, A. (2002). Integrated dental robot system for mouth opening and closing training. *Robotics and Automation, 2002. Proceedings. ICRA'02. IEEE International Conference on, 2*.

Takanobu, H., Yajima, T., Nakazawa, M., Takanishi, A., Ohtsuki, K., & Ohnishi, M. (1998). *Quantification of masticatory efficiency with a mastication robot*.

Torrance, J., Pap, J., Xu, W., Bronlund, J., & Foster, K. (2006). *Motion control of a chewing robot of 6 RSS parallel mechanism.* Paper presented at the in Proceedings of 3rd International Conference on Autonomous Robots and Agents (ACARA), Palmerston North, New Zealand.

van Essen, N. L., Anderson, I. A., Hunter, P. J., Carman, J. B., Clarke, R. D., & Pullan, A. J. (2005). Anatomically Based Modelling of the Human Skull and Jaw. *Cells Tissues Organs, 180*(1), 44.

Vukobratovi , M. (1997). How to control robots interacting with dynamic environment. *Journal of Intelligent and Robotic Systems, 19*(2), 119-152.

Wood, G., & Williams, J. (1981). Gnathodynamometers: measuring opening and closing forces. *Dental update, 8*(4), 239.

Wynne, W. P. D. (2005). *The art of articulation, 3*(1).

Xu, W. L., Torrance, J. D., Chen, B. Q., Potgieter, J., Bronlund, J. E., & Pap, J. S. (2008). Kinematics and Experiments of a Life-Sized Masticatory Robot for

Characterizing Food Texture. *Industrial Electronics, IEEE Transactions on, 55*(5), 2121-2132.

Yoshikawa, T. (2000). Force control of robot manipulators. *Robotics and Automation, 2000. Proceedings. ICRA'00. IEEE International Conference on, 1*.

APPENDIX A: MOTION CONTROL HARDWARE:

DMC1860 Control Card

PC/104, ISA, PCI Optima1–8 axes

(www.galilmc.com **/** Galil Motion Control, Inc.)

Specifications

System Processor

Motorola 32-bit microcomputer

Communications Interface

DMC-12x0:PC/104 with bi-directional, high speed FIFO
DMC-17xx: ISA with bi-directional FIFO plus auxiliary FIFO
DMC-18x0:PCI with bi-directional FIFO plus auxiliary FIFO, and DPRAM
Commands are sent in ASCII.A binary communication mode is also available as a standard feature

Modes of Motion:

Point-to-point positioning
Position Tracking
Jogging
2D Linear and Circular Interpolation with feedrate override
Linear Interpolation for up to 8 axes
Tangential Following
Helical
Electronic Gearing with multiple masters
Gantry Mode
Electronic Cam
Contouring
Teach and playback

Memory

Program memory size—1000 lines ´ 80 characters
254 variables
8000 array elements in up to 30 arrays

Filter

PID (proportional-integral-derivative) with velocity and acceleration feedforward
Notch filter and low-pass filter
Dual-loop control for backlash compensation
Velocity smoothing to minimize jerk
Integration limits
Torque limits
Offset adjustments
Option for piezo-ceramic motors

Kinematic Ranges

Position: 32 bit (±2.15 billion counts per move; automatic rollover; no limit in jog or vector modes)
Velocity: Up to 12 million counts/sec for servo motors
Acceleration: Up to 67 million counts/sec2

Uncommitted Digital I/O

DIGITAL INPUTS DIGITAL OUTPUTS CONFIGURABLE I/O

DMC-1210 thru -1240* 8 8 64 w/ DB-12064
DMC-1250 thru -1280* 16 16 64 w/ DB-12064
DMC-1710 thru -1740 8 8 64 w/ DB-14064
DMC-1750 thru -1780 24 16 64 w/ DB-14064
DMC-1810 thru -1840 8 8 64 w/ DB-14064
DMC-1850 thru -1880 24 16 64 w/ DB-14064

Uncommitted Analog Inputs

8 individual ±10 V analog inputs with 12-bit resolution
(16-bit available as an option)

High Speed Position Latch

Uncommitted inputs 1–4 latch X,Y, Z,W and 9–12 latch E, F, G, H axes
(latches within 0.1 microseconds without optoisolation and within
40 microseconds with optoisolation)

Dedicated Inputs (per axis)

Main encoder inputs—Channel A, A-,B,B-,I, I- (±12 V or TTL)
Dual encoder (for axes configured as servo)—Channel A, A-,B, B-
Forward and reverse limit inputs—optoisolated*
Home input—optoisolated*
Selectable high-speed position latch input—optoisolated*
Selectable abort input—optoisolated*

Dedicated Outputs (per axis)

Analog motor command output with 16-bit DAC resolution
Pulse and direction output for step motors
PWM output for servo amplifiers
Amplifier enable output
Error output (per card)
High-speed position compare output (per card)

Minimum Servo Loop Update Time

STANDARD -FAST†
1–2 axes: 250 µsec 125 µsec
3–4 axes: 375 µsec 250 µsec
5–6 axes: 500 µsec 375 µsec
7–8 axes: 625 µsec 500 µsec

Maximum Encoder Feedback Rate

12 MHz

Maximum Stepper Rate

3 MHz (Full, half or microstep)

** DMC-1200 has TTL limits,home, and general inputs.*
†Reduced feature set for -FAST.

DMC-12x0, DMC-17x0, DMC-18x0 Series
PC/104, ISA, PCI Optima1–8 axes

Hardware Accessories

ICM-1900 Interconnect Module

The ICM-1900 Interconnect Module breaks-out the 100-pin main cable and 25-pin auxiliary encoder cable into screw-type terminals for quick connection of system hardware. An ICM-1900 is required for each set of four axes.The ICM-1900 is contained in a metal enclosure with dimensions of 13.5" ´ 3.0" ´ 7.0" and 1/4" diameter keyholes for mounting.
The ICM is default configured for high amp enable (-HAEN). For low amp

enable, order ICM-1900-LAEN. Specify -OPTO for optoisolated outputs.

DB-14064 I/O Expansion

The DB-14064 is an optional board which provides 64 additional I/O for the DMC-17x0, and DMC-18x0 controllers (for the DMC-12x0 use the DB-12064).This board mounts directly onto the back of the controller and provides 64 I/O points configurable by the user as inputs or outputs. The I/O is accessible through two 50-pin IDC headers.

AMP-19540 Interconnect with Four 500 Watt Servo Drives

Galil's AMP-19540 is a 4-axis amplifier for driving brush or brushless motors up to 500 Watts.By interfacing directly to Galil's Optima controllers, it provides a cost-effective controller/drive solution for multi-axis applications. The AMP-19540 contains four transconductance, PWM amplifiers for driving brush or brushless motors.Each amplifier operates at 18 V to 80 V dc, up to 7 Amps continuous, 10 Amps peak.The AMP-19540 gain setting is easily configured with jumpers.The PWM switching frequency is 60 kHz. The AMP-19540 enclosure has dimensions of 6.8"´ 8.75"´ 1". It interfaces to the Optima controller with a single, 100-pin high density SCSI cable. Signals for each axis are brought out through D-type connectors located on the AMP-19540.For applications with less than three axes, the AMP-19520 twoaxis model is available. A shunt regulator option is also available.

AMP-19540

ICM-2900 Interconnect Module

The ICM-2900 breaks-out the 100-pin SCSI cable into removable screwtype terminals.One ICM-2900 is required for each set of four axes.The ICM-2900-FL has flanges which allow standard screw-type mounting. Specify -OPTO for optoisolated outputs.Specify -HAEN for high amp enable or -LAEN for low amp enable.

Power Requirements

+5V 750 mA
-12V 40 mA
+12V 40 mA

Environmental

Operating temperature: 0–70º C
Humidity: 20–95% RH, non-condensing

Mechanical

DMC-12x0
1–4 axes: 4.4" ´ 4.15" (2 stacked cards)
5–8 axes: 4.4" ´ 4.15" (3 stacked cards)
DMC-17x0
1–4 axes: 10.25" ´ 4.8"
5–8 axes: 13.25" ´ 4.8"
DMC-18x0
1–4 axes: 8.175" ´ 4.2"
5–8 axes: 12.28" ´ 4.2

Amplifier

AMP 19540 (www.Galilmc.com)

- Connects to Galil DMC-18xx PCI bus motion controller to provide a complete controller/drive solution with minimal wiring
- 18V to 80V dc; 7 Amps continuous, 10 Amps peak per axis
- Drives four servo motors up to 500 Watts each
- Configurable for driving brush or brushless motors
- High-bandwidth PWM drives with 60 kHz switching frequency
- Compact 6.8" x 8.75" x 1" metal enclosure
- Provides 15-pin Hi-density D-sub connectors for X,Y,Z and W axes
- Connects to DMC-18xx PCI controller with single 100-pin SCSI cable
- Shunt Regulator option is available

Power supply

To power the six 60W motors, a power supply of at least 360W was required. A 500W 24V DC output power supply was chosen to power both amplifiers.

Actuator DC motor

Maxon RE30 Brushed DC motor (www.Maxonmotor.com)

Motor Data							
	Values at nominal voltage						
1	Nominal voltage	V	12.0	18.0	24.0	36.0	48.0
2	No load speed	rpm	8170	8590	8810	8590	8490
3	No load current	mA	300	212	164	106	78.5
4	Nominal speed	rpm	7630	7900	8050	7810	7750
5	Nominal torque (max. continuous torque)	mNm	51.7	75.5	85.0	83.4	88.2
6	Nominal current (max. continuous current)	A	4.00	4.00	3.44	2.20	1.72
7	Stall torque	mNm	844	991	1020	936	1020
8	Starting current	A	60.5	49.8	39.3	23.5	19.0
9	Max. efficiency	%	86	87	87	87	88
	Characteristics						
10	Terminal resistance	Ω	0.198	0.362	0.611	1.53	2.52
11	Terminal inductance	mH	0.0345	0.0703	0.119	0.281	0.513
12	Torque constant	mNm / A	13.9	19.9	25.9	39.8	53.8
13	Speed constant	rpm / V	685	479	369	240	178
14	Speed / torque gradient	rpm / mNm	9.74	8.71	8.69	9.22	8.33
15	Mechanical time constant	ms	3.42	3.25	3.03	3.17	3.01
16	Rotor inertia	gcm²	33.5	35.7	33.3	32.9	34.5

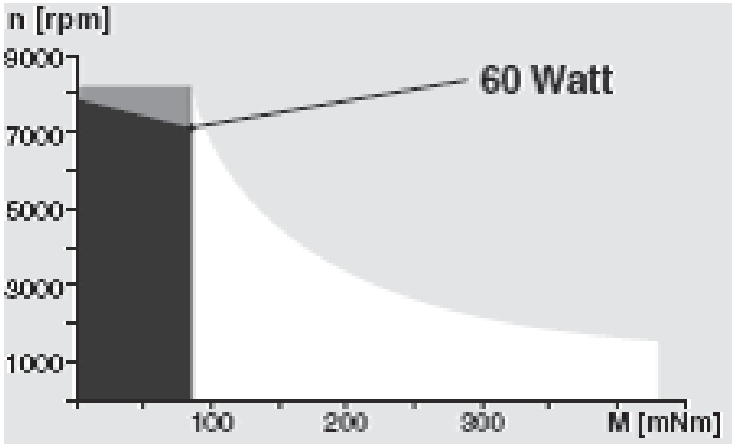

Motor performance diagram for brushed DC-motor RE 30 from Maxon Motor, Switzerland (Colors: black, recommended operating range; grey, continuous operation; white, short term operation).

APPENDIX B: MRJ CHEWING EXPERIMENT RESULTS

'Apple Bite' trajectory forces on Muesli and Apple.

Raw forces and torques from fast runs.

Note: Free motion forces are given in terms of effective force at the Jaw, this is not the same as the actual unbalanced force at jaw causing the jaw to accelerate. Most of the motor torque is used to accelerate the DC motors rotor.

.

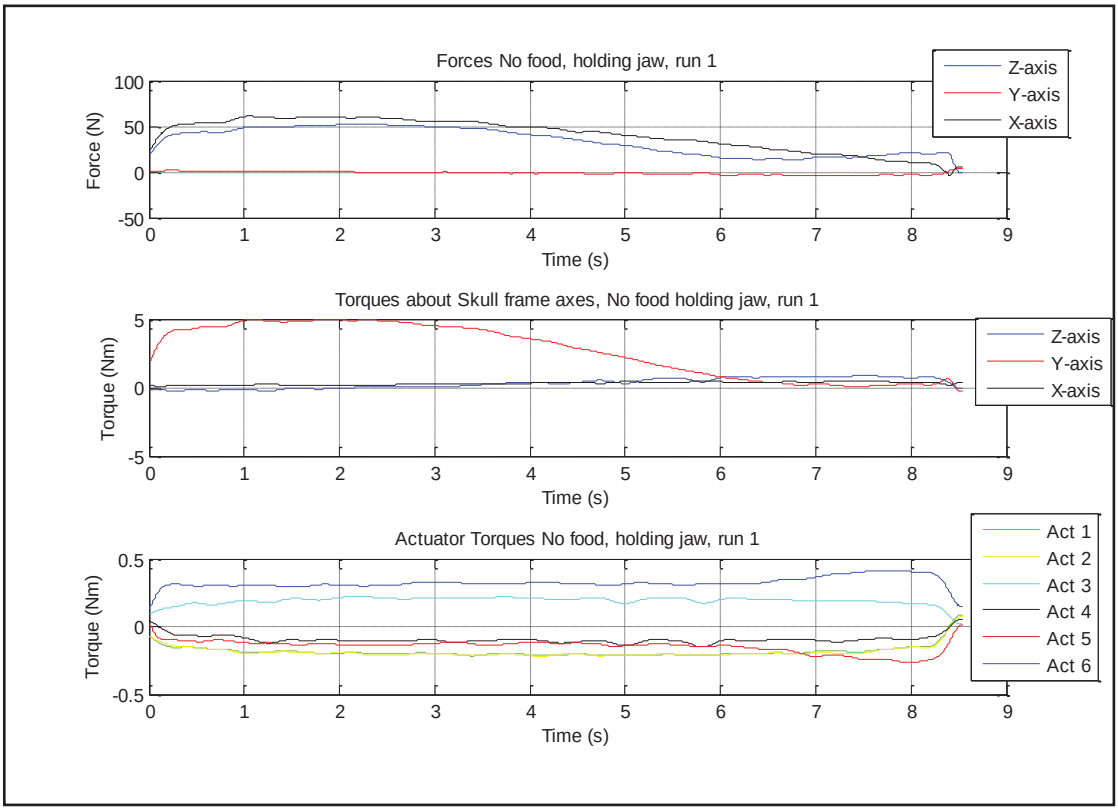

Appendix B Figure 1

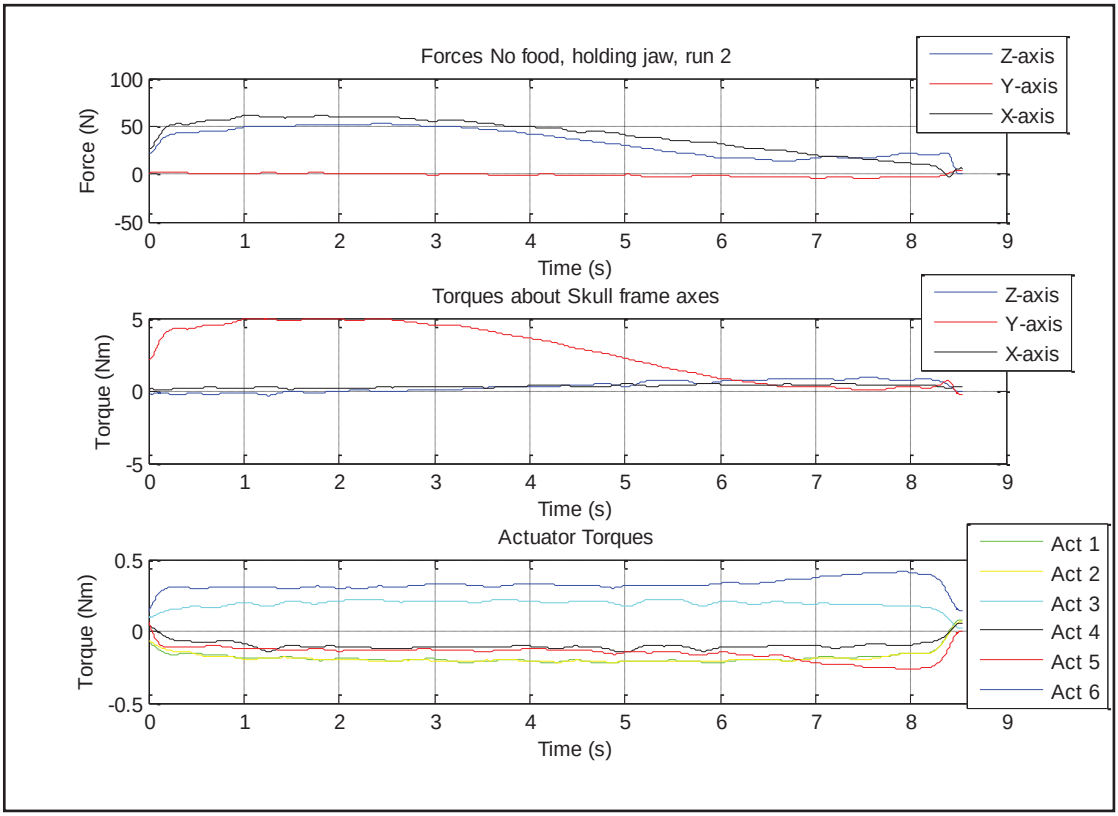

Appendix B Figure 2

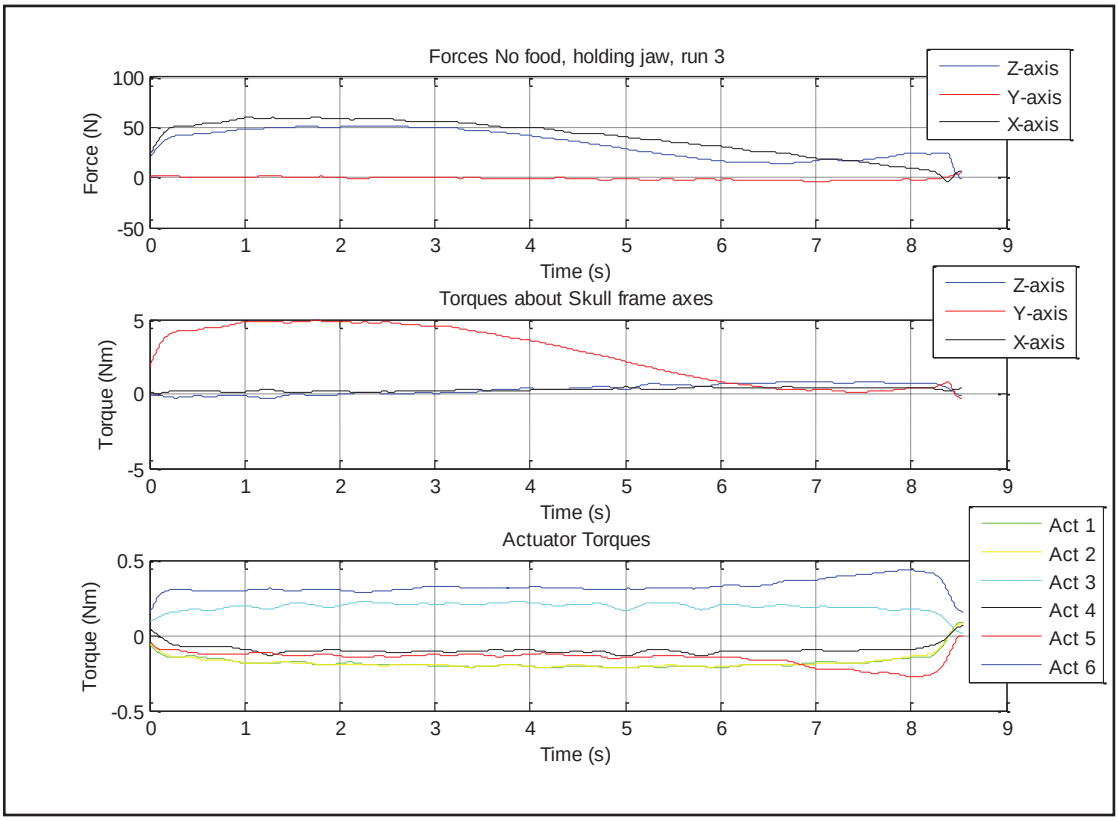

Appendix B Figure 3

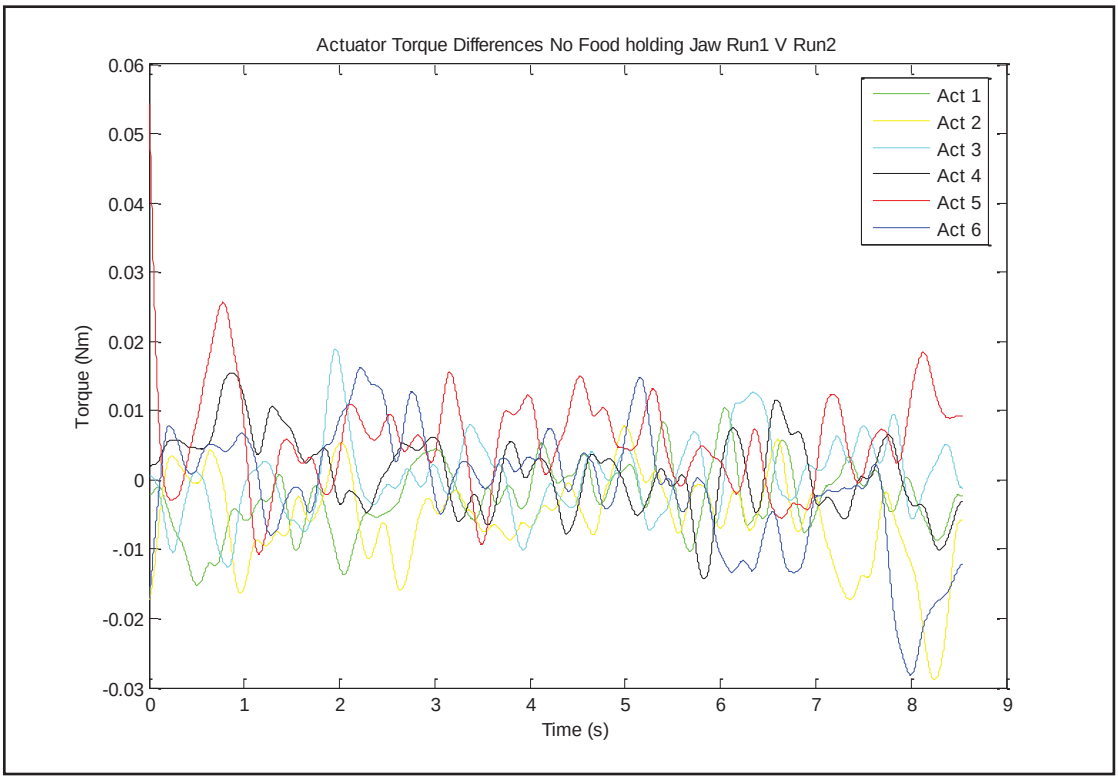

Appendix B Figure 4

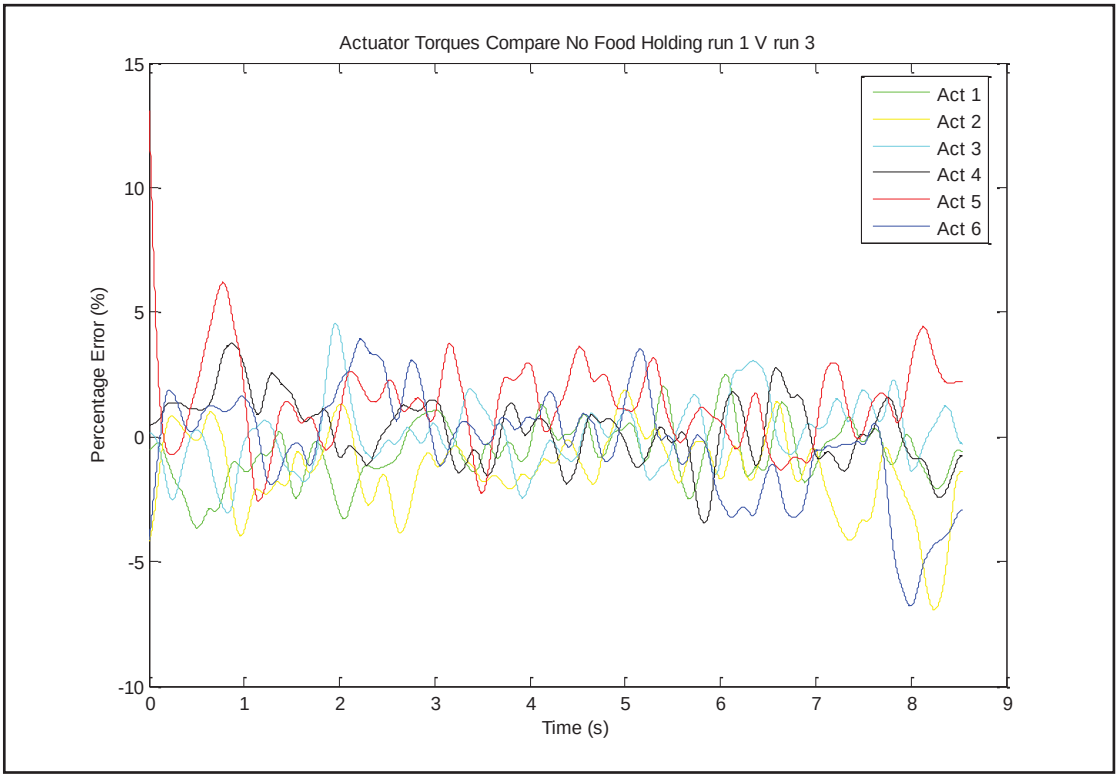

Appendix B Figure 5

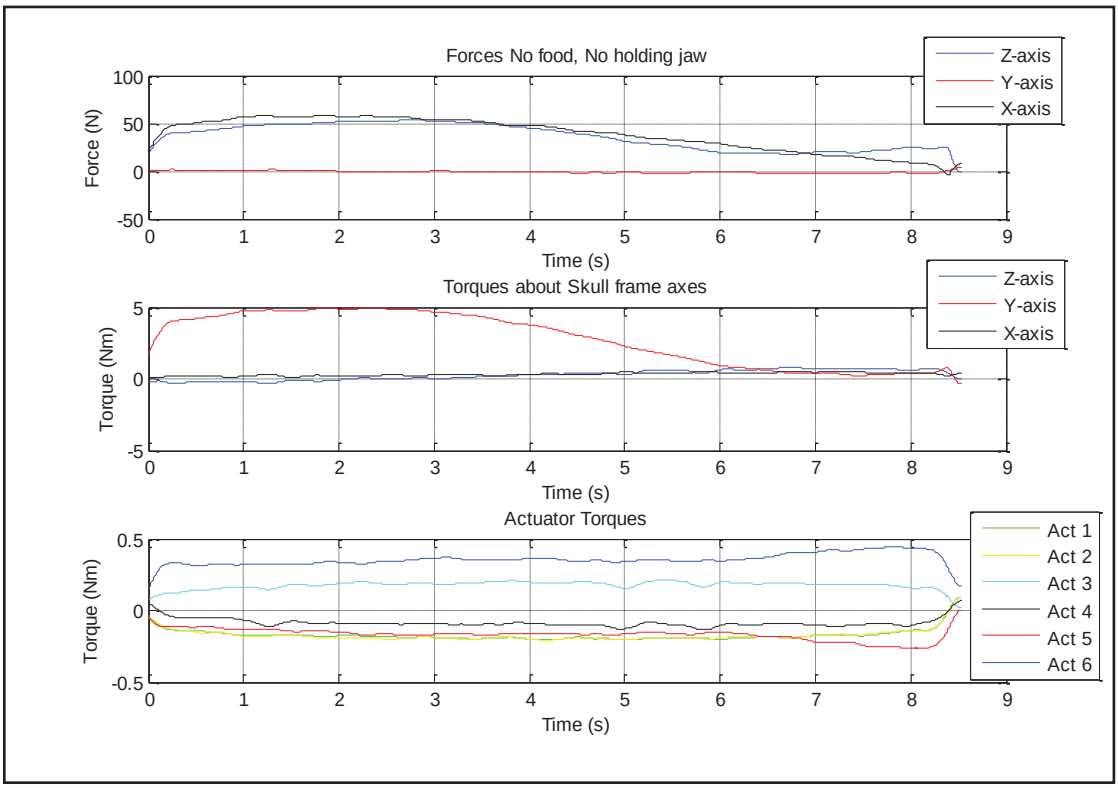

Appendix B Figure 6

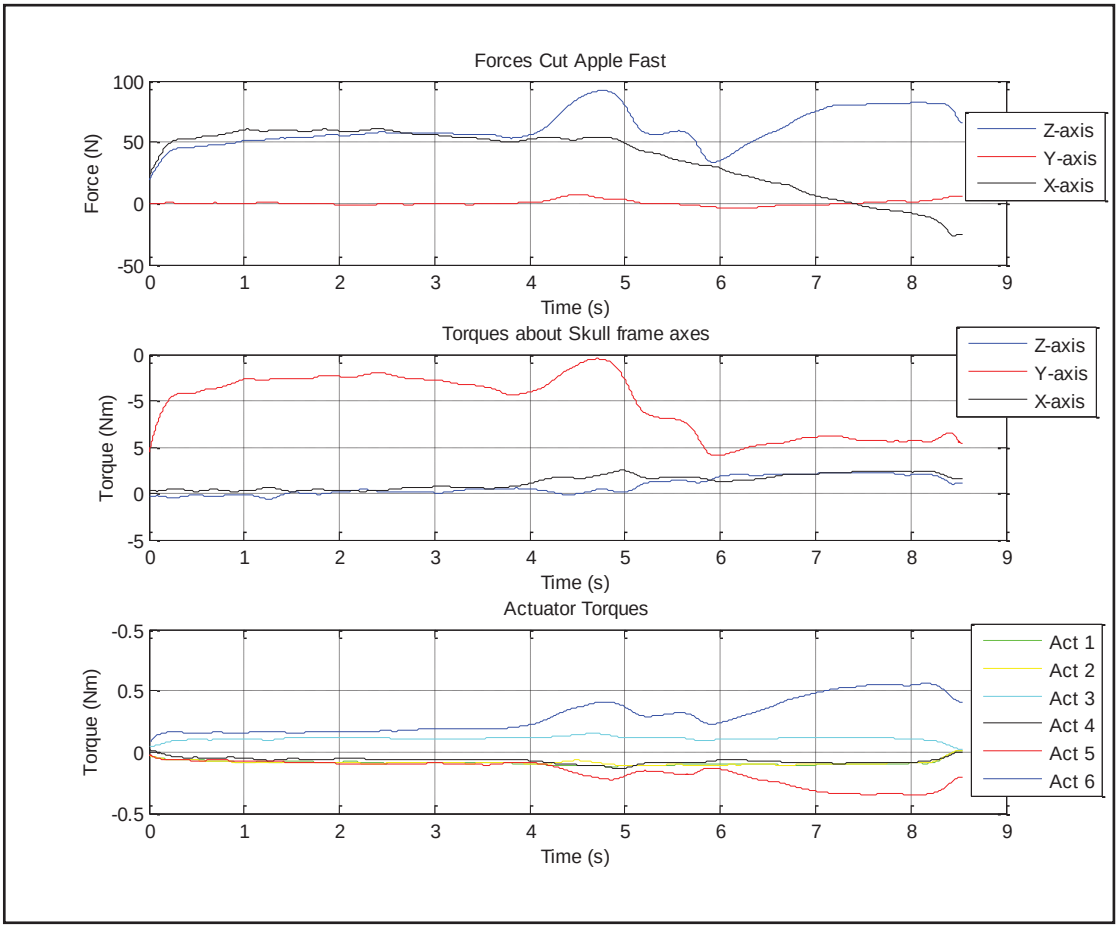

Appendix B Figure 7

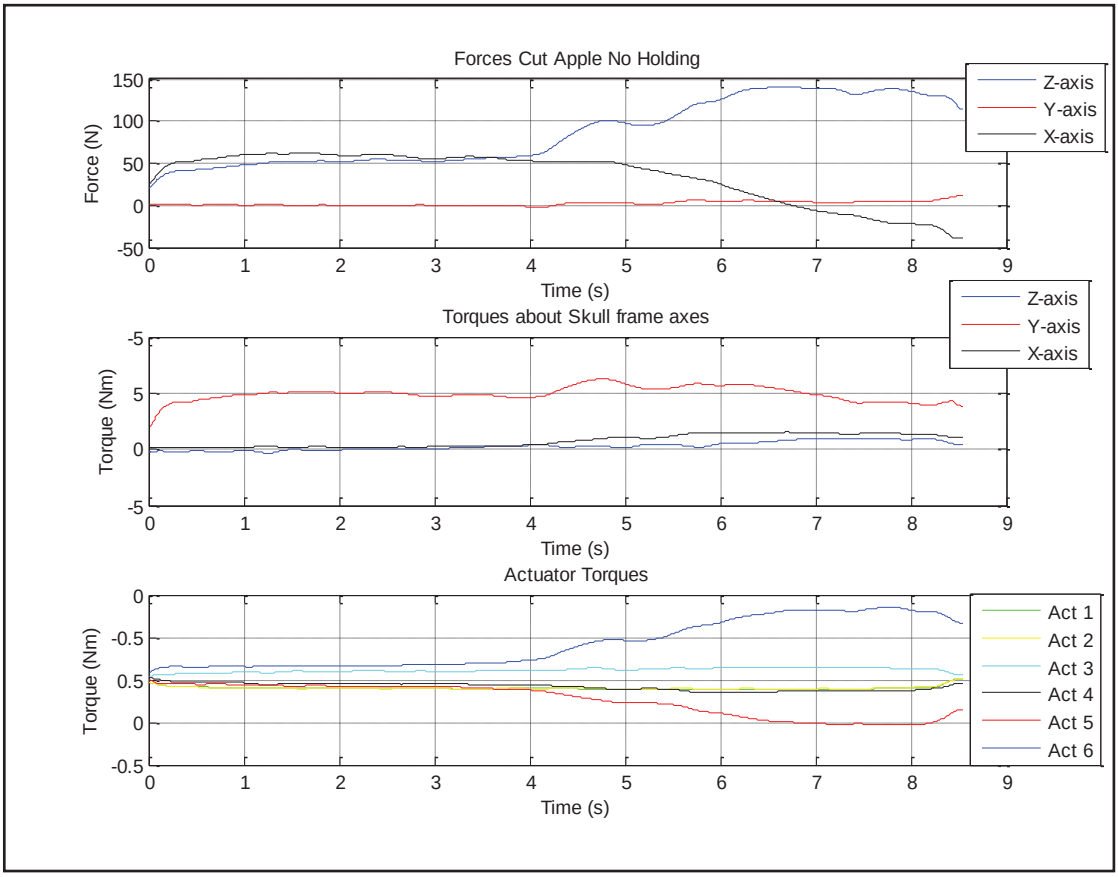

Appendix B Figure 8

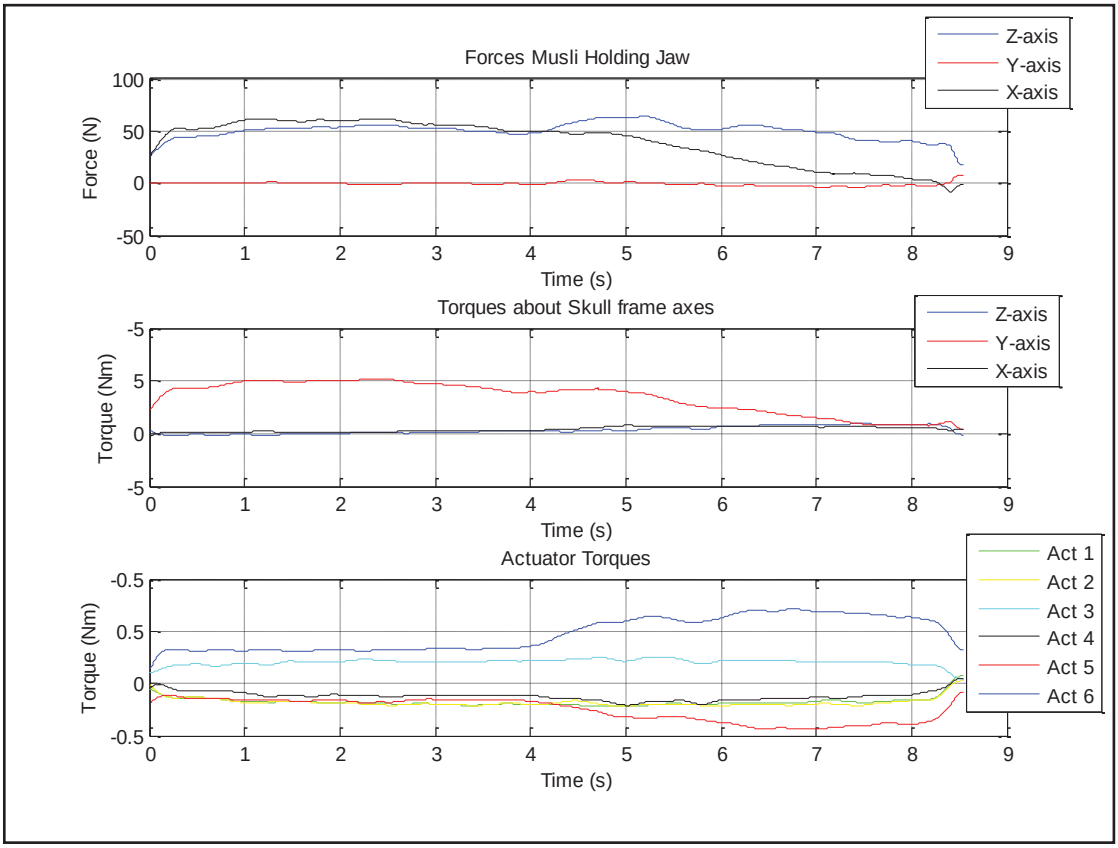

Appendix B Figure 9

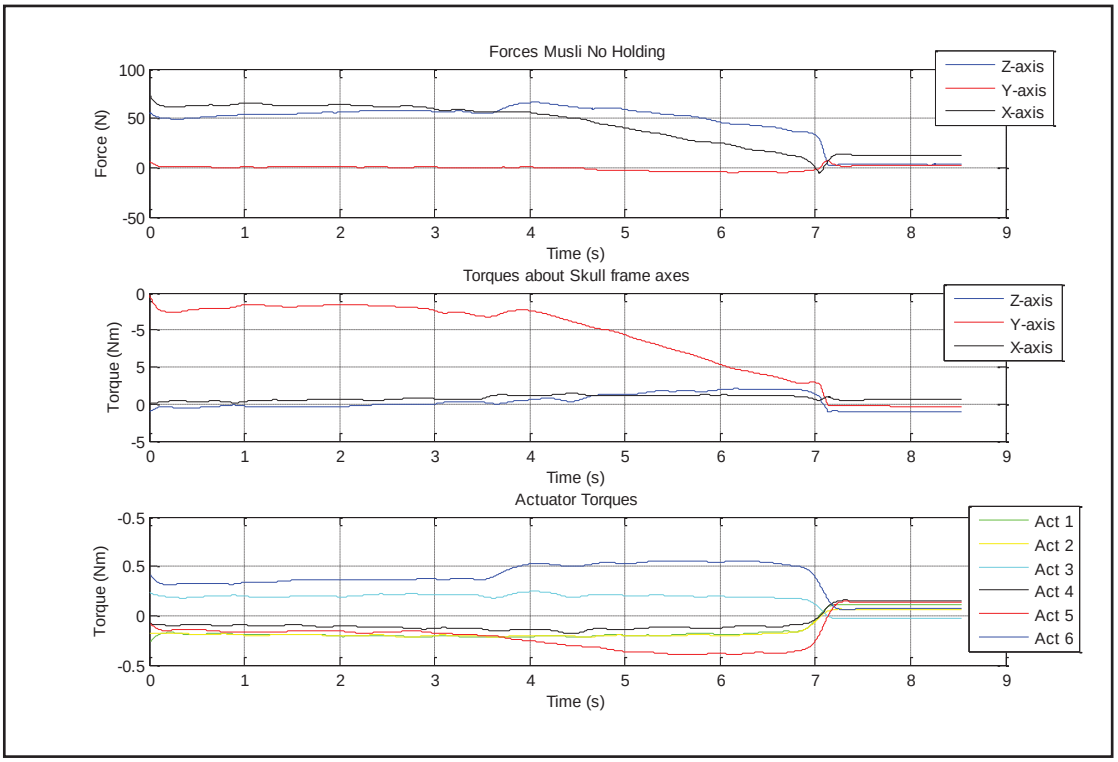

Appendix B Figure 1

Differential Forces:

Total ‘force’ measured less ‘force’ required to move the unload MRJ though the same motion; Can be thought of as ‘force attributed to food’.

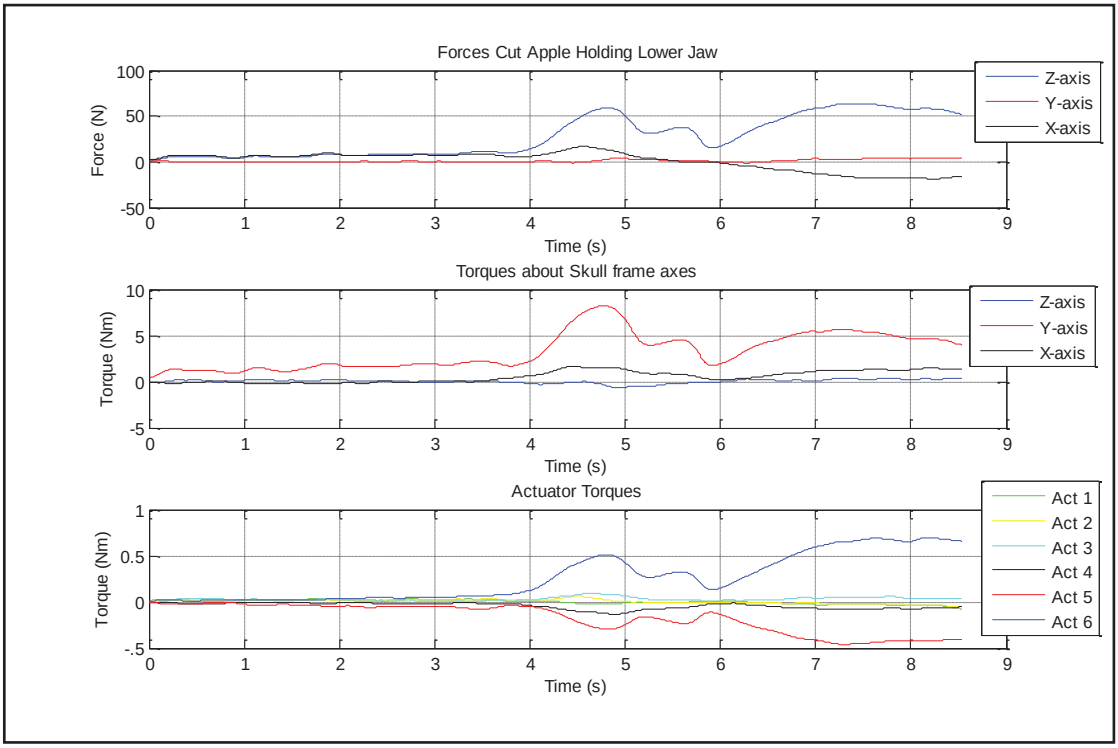

Appendix B Figure 11

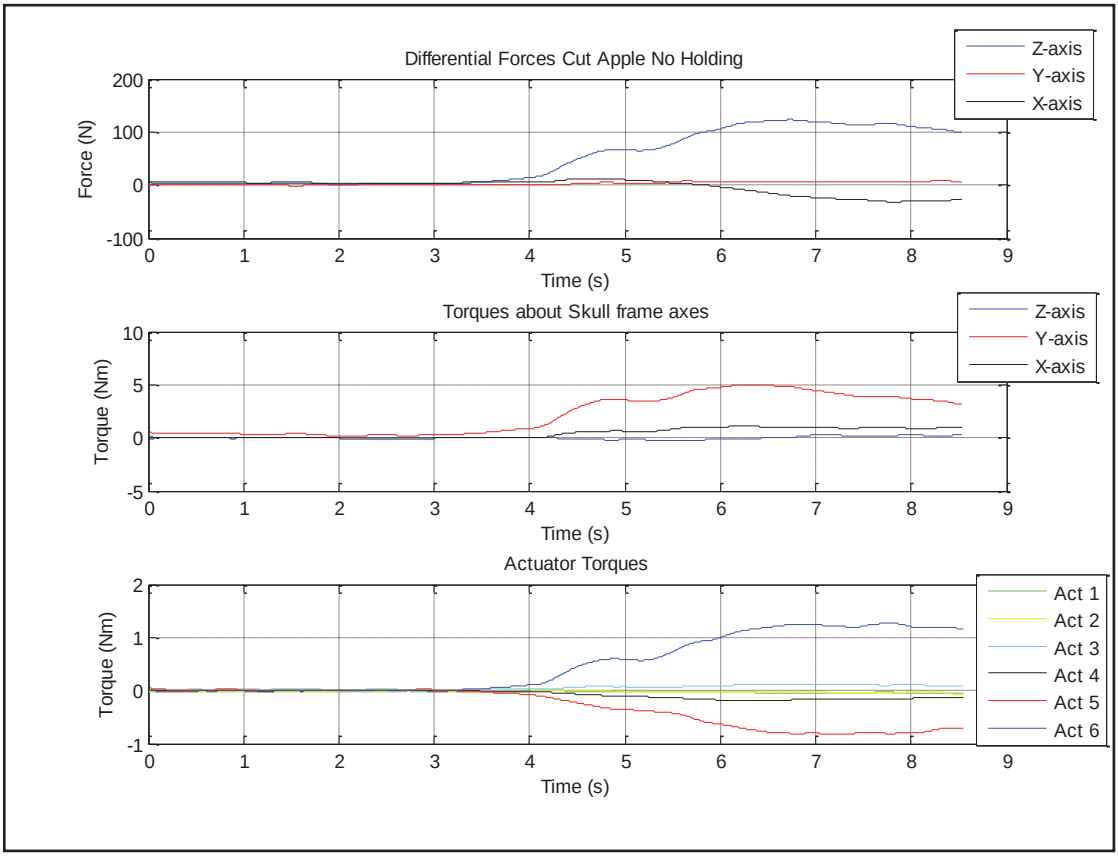

Appendix B Figure 12

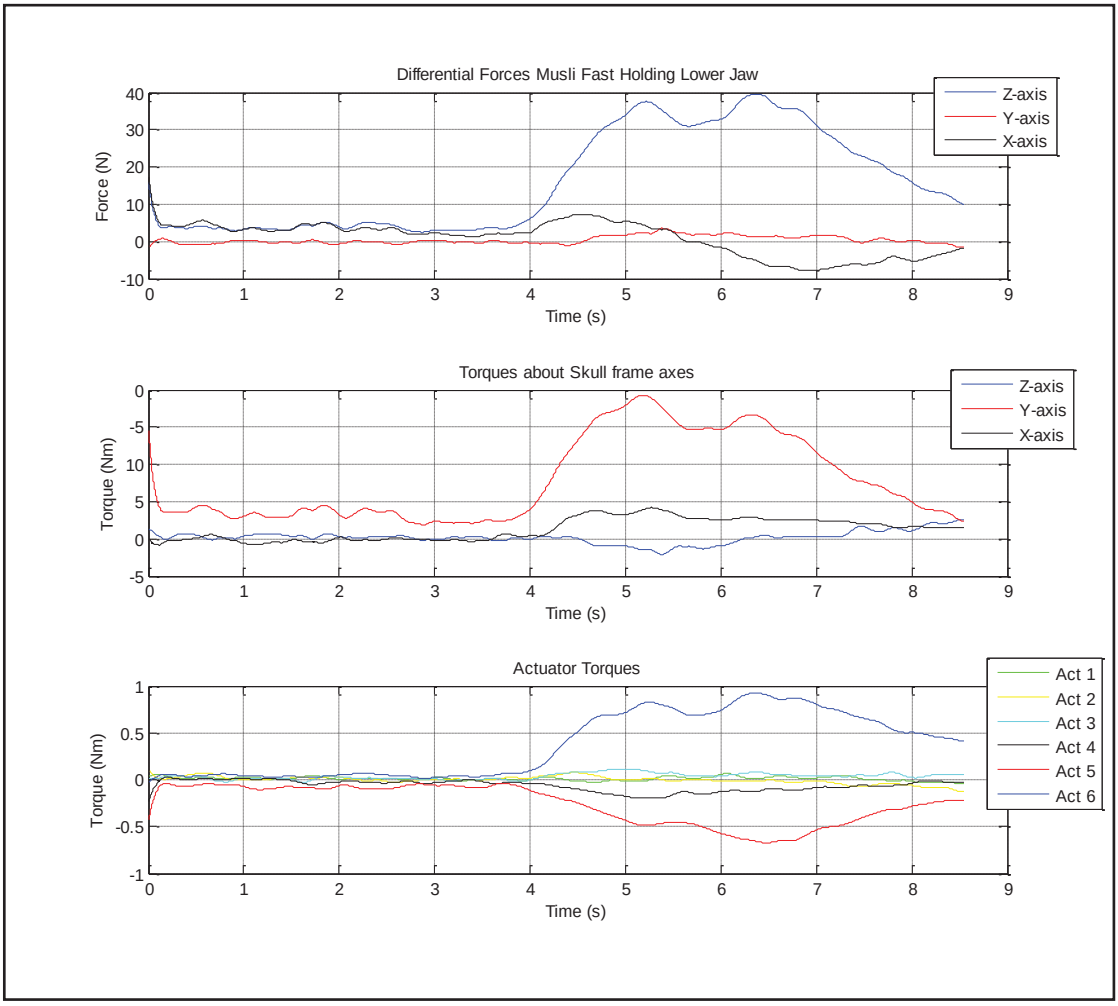

Appendix B Figure 13

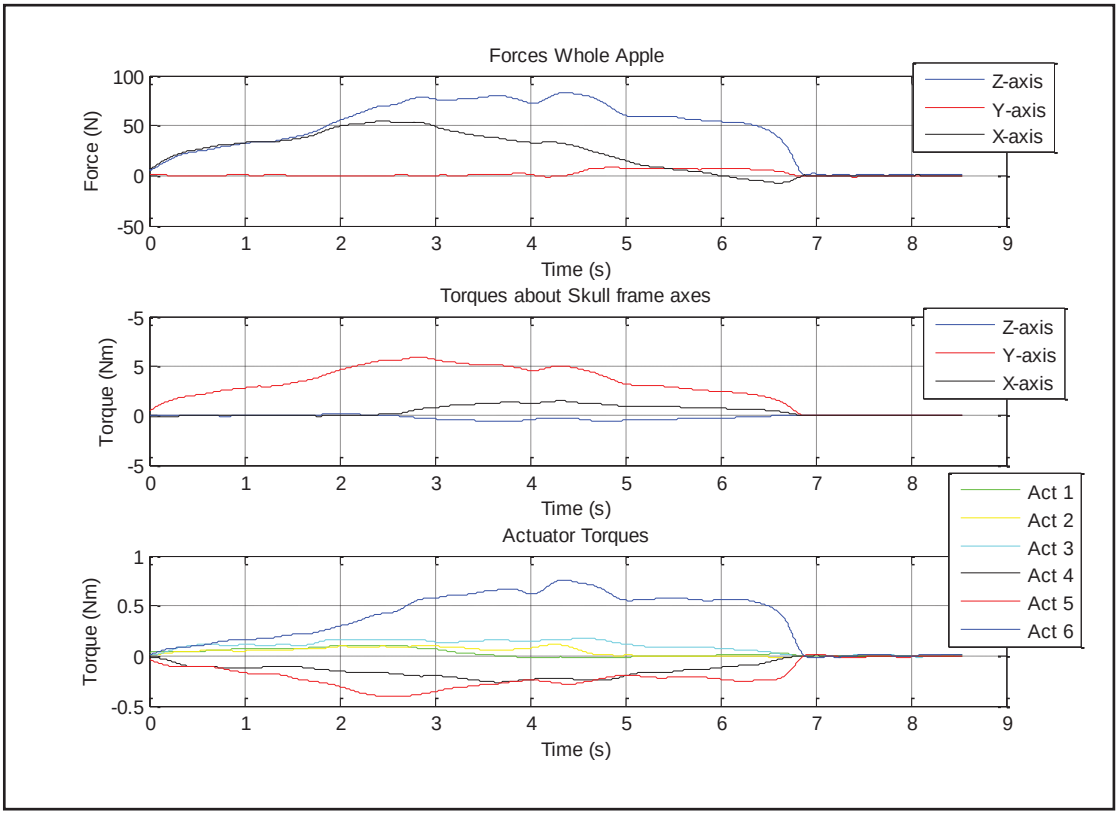

Appendix B Figure 14

APPENDIX C: INVERSE KINEMATICS WORKED EXAMPLE

1. INVERSE KINEMATICS

1.1 DISCRIPTION OF THE ROBOT MECHANISM:

The robotic jaw for which the inverse kinematics is to be applied to is shown in figure 1.1 below.

The robotic jaw is moved by 6 RSS type actuators, each actuator consisting of a driver unit (Di, i = 1,2,…6), crank (Ci, i = 1,2,…6), and coupler link (Li, i = 1,2,…6). The three joints are a revolute at the actuators ground point where the driving shaft connects to the crank (Gi, i = 1,2,…6), a spherical joint where the crank joins to the coupler linkage (Si, i = 1,2,…6), and a final spherical joint where the coupler linkage joins to the mandible (Mi, i = 1,2,…6).

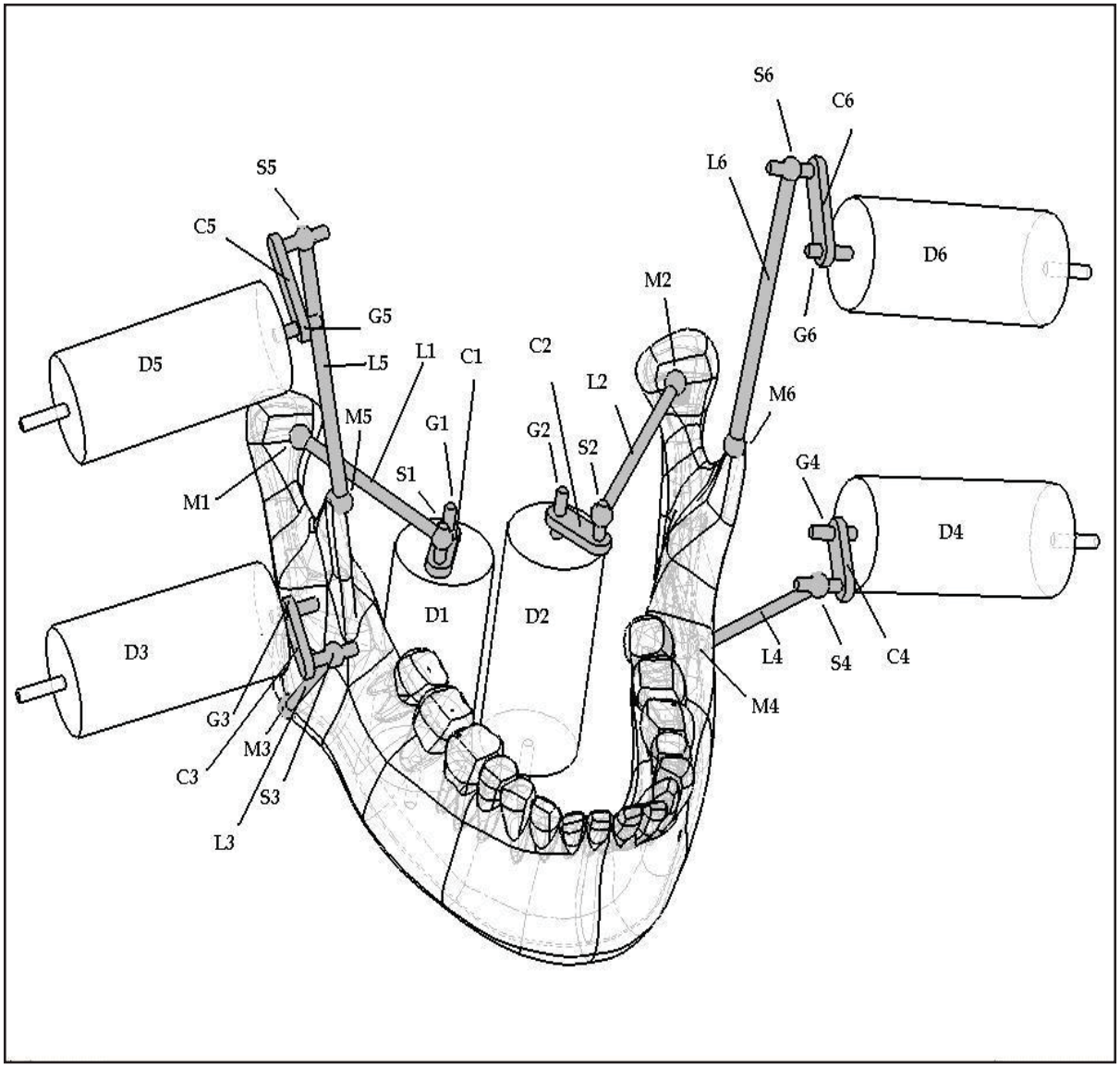

Appendix C figure 1.1: Robotic model.

1.2 DESIGNATED CO-ORDINATE SYSTEMS:

Appendix C figure 1.2 shows the location and orientation of the two major frames, the skull frame $OXYZ_S$ fixed to the skull and the mandible frame $OXYZ_M$ fixed to the mandible.

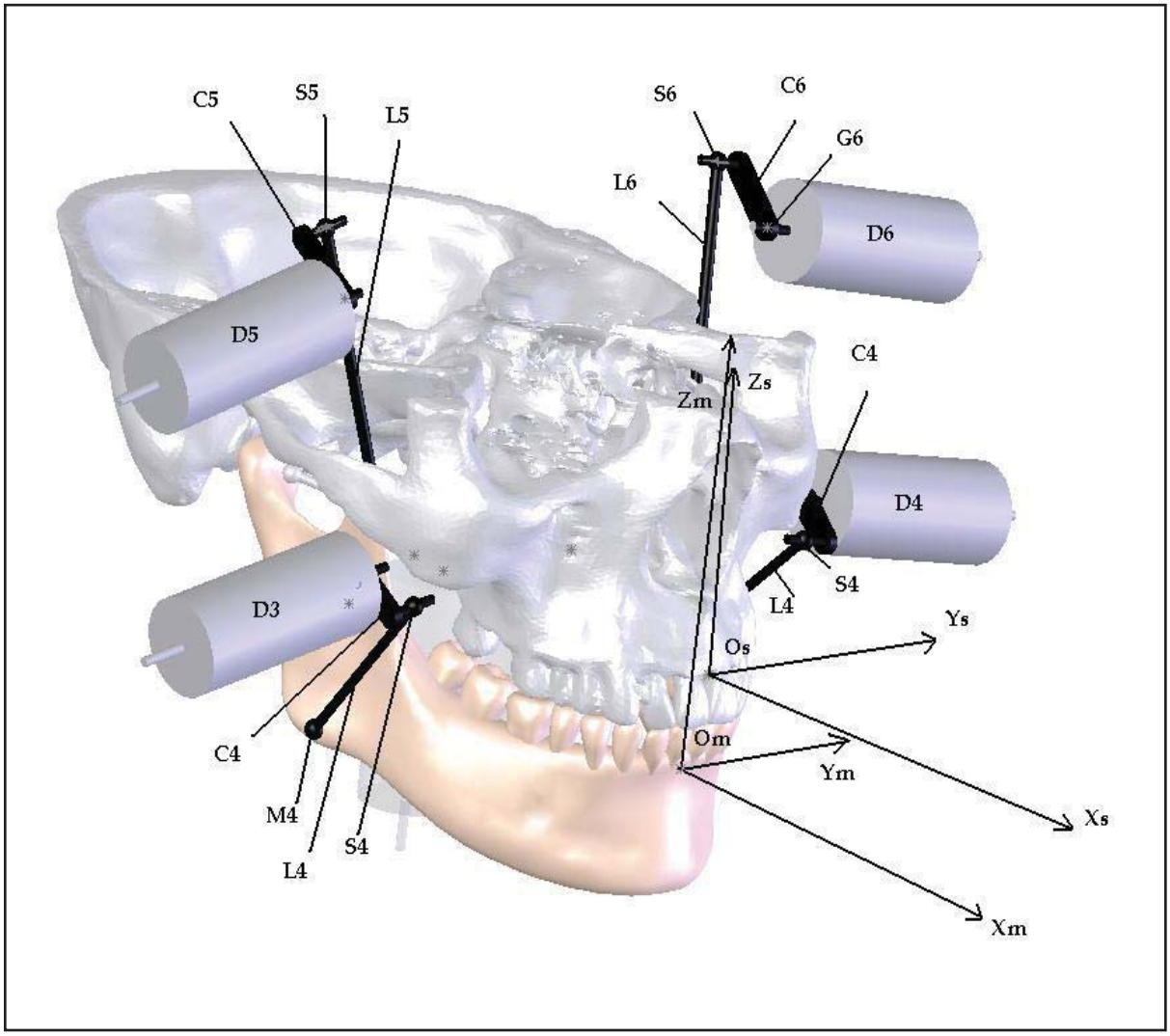

Appendix C figure 1.2: The 2 major co-ordinate systems, skull and mandible.

In addition to the two main frames seen in figure 1.2 above, I also have 6 frames {Ci}, $i = 1,2,...6$ for the 6 RSS actuators. The crank frames are fixed on the crank, with origin being at the point G_i, point S_i lying on the $X_{C.i}$ axis, and axis Z_i running through the centre of the driver unit.

Appendix C Figure 1.3 shows how the crank frames are located and orientated on the crank.

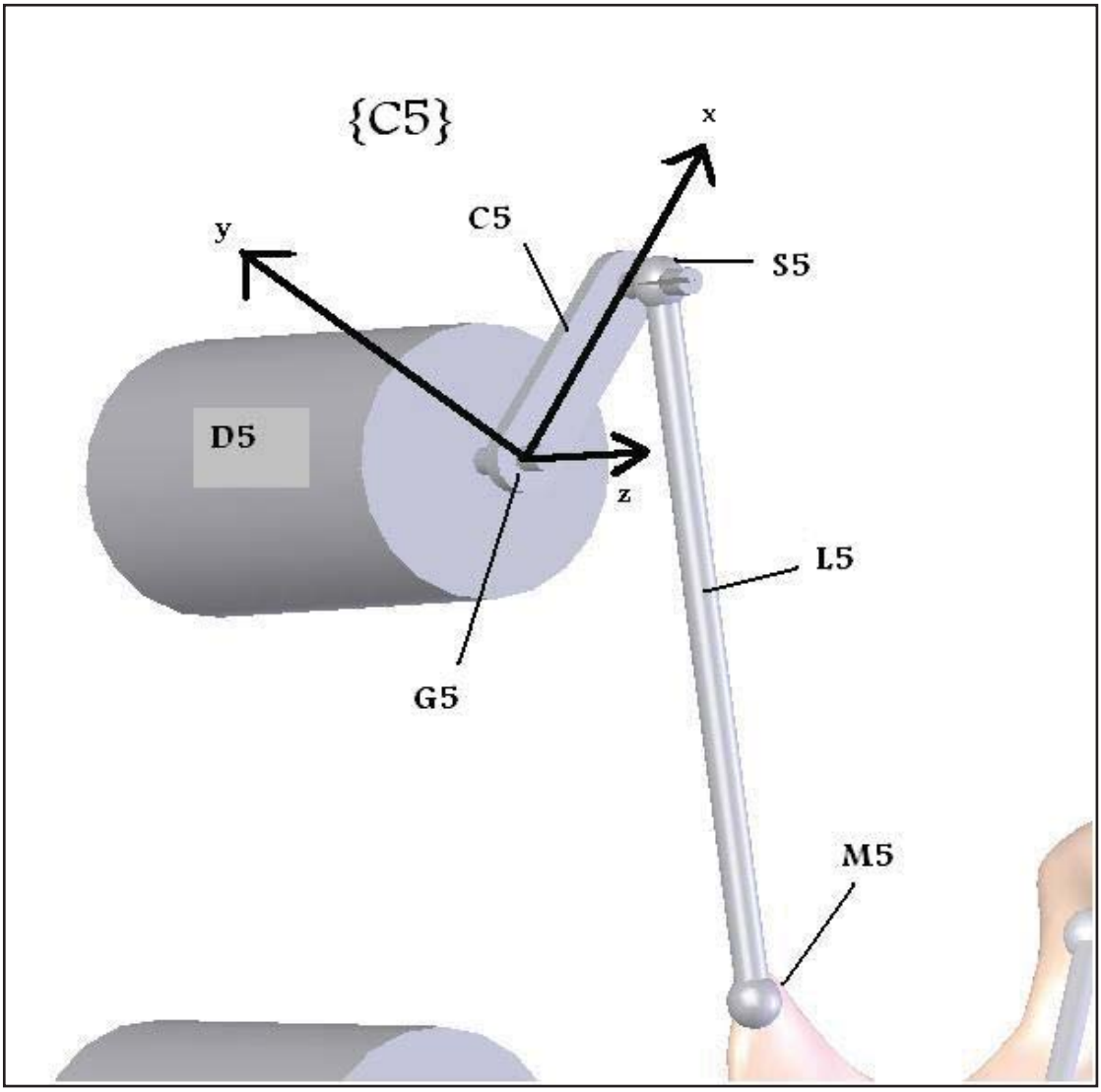

Appendix C Figure 1.3: Location and orientation of crank frame 1.

1.3 SOLVING TO FIND ACTUATION ANGLE OF CRANK FOR A GIVEN JAW TRANSFORMATION

From the specified motion we know at any instant the displacement and orientation of the mandible frame relative to the skull frame (${}^{S}_{M}T$) .

- $$ {}^{S}_{M}T = \begin{bmatrix} c\alpha c\beta & c\alpha c\beta s\gamma - s\alpha c\gamma & c\alpha s\beta c\gamma + s\alpha s\gamma & t(1) \\ s\alpha c\beta & s\alpha s\beta s\gamma + c\alpha c\gamma & s\alpha s\beta c\gamma - c\alpha s\gamma & t(2) \\ -s\beta & c\beta s\gamma & c\beta c\gamma & t(3) \\ 0 & 0 & 0 & 1 \end{bmatrix} \quad (1) $$

Where α, β, ψ and the translation vector t made up of x, y, and z components are given. Appendix C figure 1.4 below shows the three angles a, b, y and the three element vector t making up the transformation mapping the skull frame onto the mandible frame.

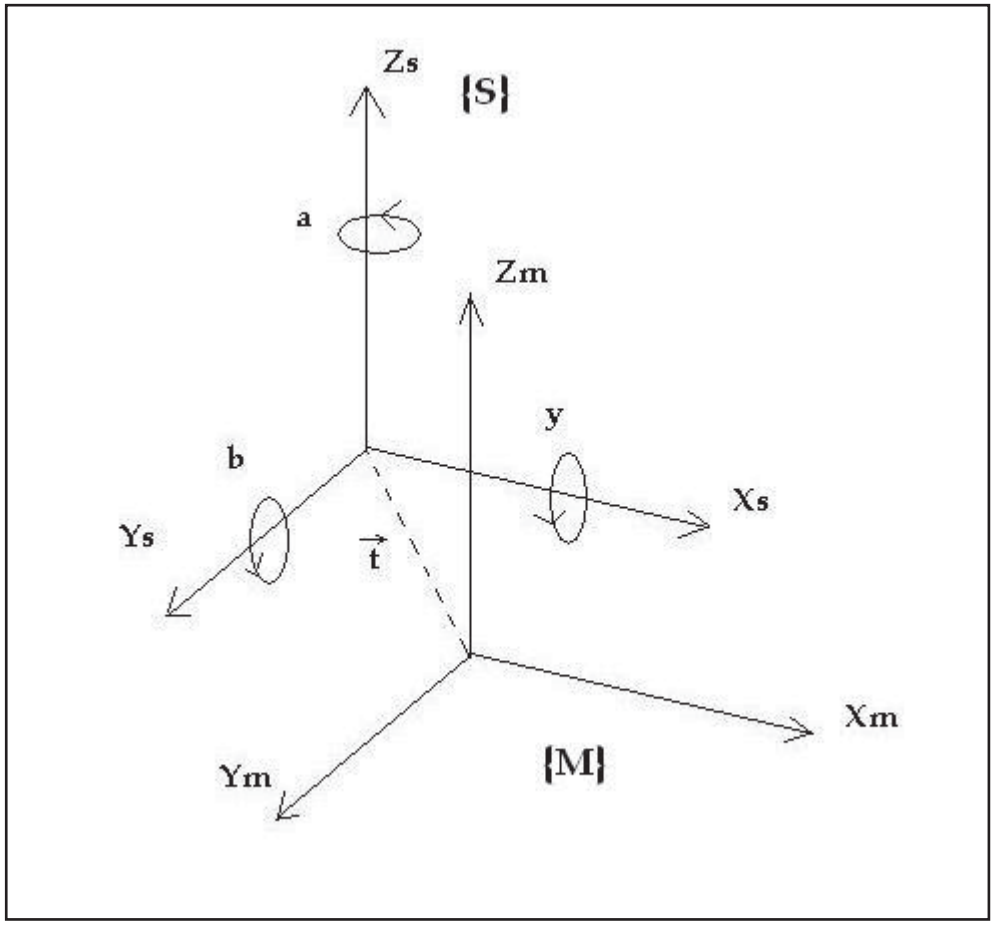

Appendix C Figure 1.4

For the initial/closed position as seen in figure 1.2, the translation vector

$$t = \begin{bmatrix} -6.1 \\ -0.1 \\ -20.2 \end{bmatrix}$$, units are in mm.

Using the XYZ fixed angles rotation scheme described in figure 1.4, the angles γ, β and α for rotation about skulls X, Y and Z axis's respectively are 0^0, 3^0 and 1.5^0.

This initial transformation is arbitrary but is important for internal calculations as input data is all relative to the mandible frame at jaw closed position.

Thus from equation (1) the initial transformation matrix mapping the mandible frame onto the skull frame is

$$ {}^{S}_{M}T = \begin{bmatrix} 0.9983 & -0.0262 & 0.0523 & -6.0900 \\ 0.0261 & 0.9996 & 0 & -0.07 \\ -0.0523 & 0.0015 & 0.9986 & -20.17 \\ 0 & 0 & 0 & 1 \end{bmatrix} $$

From the dimensions of the crank mechanism we also know ${}^{Ci}S_i$, the location of the spherical joint on the crank in the crank frame.

- ${}^{Ci}S_i$ known.

The transformation of the crank frame relative to the skull frame only changes by one angle of rotation about the crank frames Z-axis (given a Euler rotation scheme that leaves the Z-rotation to last, I use Z-Y-Z Euler scheme). The changing angle through the Z-axis of the crank frame is the actuation of the motor and is what we are trying to find. The crank frames origin is fixed relative to the skull frame and is known from the design also.

- ${}^{S}C_{org}$ known.

- ${}^{S}_{C}R_{Z'Y'Z'}(\alpha,\beta,\gamma)$ known apart from γ, the final rotation about final Z axis. Angles α and β are constant and are obtained from the geometry of the robot.

$$ {}^{S}_{C}R_{Z'Y'Z'}(\alpha,\beta,\psi) = \begin{bmatrix} c\alpha c\beta c\gamma - s\alpha s\gamma & -c\alpha c\beta s\gamma - s\alpha c\gamma & c\alpha s\beta \\ s\alpha c\beta c\gamma + c\alpha s\gamma & -s\alpha c\beta s\gamma + c\alpha c\gamma & s\alpha s\beta \\ -s\beta c\gamma & s\beta s\gamma & c\beta \end{bmatrix} $$

$$ {}^{S}_{C}R_{Z'Y'Z'}(\alpha,\beta,\psi) = \begin{bmatrix} Ac\gamma - Bs\gamma & -As\gamma - Bc\gamma & D \\ Cc\gamma + Fs\gamma & -Cs\gamma + Fc\gamma & E \\ -Gc\gamma & Gs\gamma & H \end{bmatrix} $$

where A,B,C,D,E,F,G and H are all constants dependent on the two fixed Euler angles, α and β.

An illustrated example of the Z-Y-Z Euler rotational scheme for rotation of skull frame onto crank frame 5 is shown below.

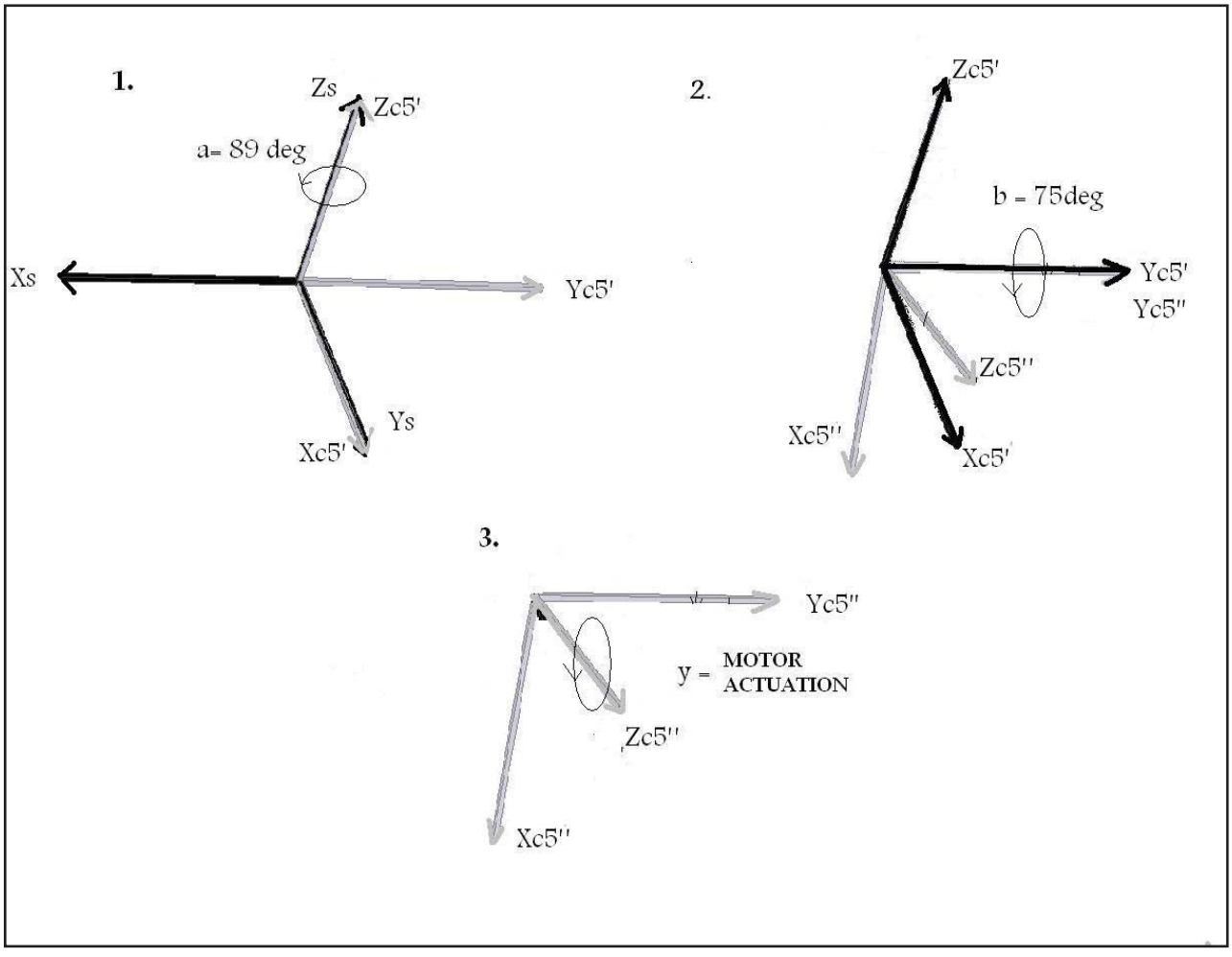

Appendix C Figure 1.5

- ${}^{S}_{C}T$ being made up of the above two is therefore also known apart from the γ angle.

$$ {}^{S}_{C}T = \begin{bmatrix} & {}^{S}_{C}R & & {}^{S}C_{ORIGIN} \\ & & & \\ 0 & 0 & 0 & 1 \end{bmatrix} $$

$$ {}^{S}_{C}T = \begin{bmatrix} Ac\gamma - Bs\gamma & -As\gamma - Bc\gamma & D & {}^{S}C_{ORG}(1) \\ Cc\gamma + Fs\gamma & -Cs\gamma + Fc\gamma & E & {}^{S}C_{ORG}(2) \\ -Gc\gamma & Gs\gamma & H & {}^{S}C_{ORG}(3) \\ 0 & 0 & 0 & 1 \end{bmatrix} $$

- ${}^{S}S = {}^{S}_{C}T.{}^{C}S$, the unknown γ is inherited.

$$ {}^{S}S = \begin{bmatrix} Ac\gamma - Bs\gamma & -As\gamma - Bc\gamma & D & {}^{S}C_{ORG}(1) \\ Cc\gamma + Fs\gamma & -Cs\gamma + Fc\gamma & E & {}^{S}C_{ORG}(2) \\ -Gc\gamma & Gs\gamma & H & {}^{S}C_{ORG}(3) \\ 0 & 0 & 0 & 1 \end{bmatrix} . \begin{bmatrix} {}^{C}Sx \\ {}^{C}Sy \\ {}^{C}Sz \\ 1 \end{bmatrix} $$

$$ = \begin{bmatrix} (\mathrm{A}*\mathrm{c}\gamma - \mathrm{B}*\mathrm{s}\gamma)*{}^{\mathrm{C}}\mathrm{Sx} + (-\mathrm{A}*\mathrm{s}\gamma - \mathrm{B}*\mathrm{c}\gamma)*{}^{\mathrm{C}}\mathrm{Sy} + \mathrm{D}*{}^{\mathrm{C}}\mathrm{Sz} + {}^{S}C_{ORG}(1) \\ (\mathrm{C}*\mathrm{c}\gamma + \mathrm{F}*\mathrm{s}\gamma)*{}^{\mathrm{C}}\mathrm{Sx} + (-\mathrm{C}*\mathrm{s}\gamma + \mathrm{F}*\mathrm{c}\gamma)*{}^{\mathrm{C}}\mathrm{Sy} + \mathrm{E}*{}^{\mathrm{C}}\mathrm{Sz} + {}^{S}C_{ORG}(2) \\ -\mathrm{G}*\mathrm{c}\gamma*{}^{\mathrm{C}}\mathrm{Sx} + \mathrm{G}*\mathrm{s}\gamma*{}^{\mathrm{C}}\mathrm{Sy} + \mathrm{H}*{}^{\mathrm{C}}\mathrm{Sz} + {}^{S}C_{ORG}(3) \\ 1 \end{bmatrix} $$

- ${}^{S}M = {}^{S}_{M}T.{}^{M}M$, 6 points where crank attaches to plate are known in skull frame by use of the given skull to mandible transformation.

$$ {}^{S}M = \begin{bmatrix} c\alpha c\beta & c\alpha c\beta s\gamma - s\alpha c\gamma & c\alpha s\beta c\gamma + s\alpha s\gamma & t(1) \\ s\alpha c\beta & s\alpha s\beta s\gamma + c\alpha c\psi & s\alpha s\beta c\gamma - c\alpha s\gamma & t(2) \\ -s\beta & c\beta s\psi & c\beta c\psi & t(3) \\ 0 & 0 & 0 & 1 \end{bmatrix} . \begin{bmatrix} {}^{M}Mx \\ {}^{M}My \\ {}^{M}Mz \\ 1 \end{bmatrix} $$

$$ = \begin{bmatrix} (c\alpha c\beta)^{M}Mx + & (c\alpha c\beta s\gamma - s\alpha c\gamma)^{M}My + & (c\alpha s\beta c\gamma + s\alpha s\gamma)^{M}My + & t(1) \\ (s\alpha c\beta)^{M}Mx + & (s\alpha s\beta s\gamma + c\alpha c\gamma)^{M}My + & (s\alpha s\beta c\gamma - c\alpha s\gamma)^{M}Mz + & t(2) \\ (-s\beta)^{M}Mx + & (c\beta s\gamma)^{M}My + & (c\beta c\gamma)^{M}Mz + & t(3) \\ & 1 & & \end{bmatrix} $$

We can now solve the following equation for the unknown angle γ:

$$ (M_i S_i)^2 = ({}^{S}S_{iX} - {}^{S}M_{iX})^2 + ({}^{S}S_{iY} - {}^{S}M_{iY})^2 + ({}^{S}S_{iZ} - {}^{S}M_{iZ})^2 \qquad (1) $$

where $(M_i S_i)$ is the length of the link between the two points $M_i S_i$.

After expanding equation (1) in Matlab we have:

$$ a = b\cos^2\gamma + b\sin^2\gamma + d\cos\gamma + e\sin\gamma + f \qquad (2) $$

Where a, b, d, e, and f are all constants.

$b\cos^2\Psi + b\sin^2\Psi$ can be factorised and the use of the trig identity $\cos^2 x + \cos^2 x = 1$ can be used to leave just the constant b. We now have equation (3) below.

$$g = d\cos\gamma + e\sin\gamma \qquad (3)$$

Where the new constant $g = a - b - f$. (4)

To solve, both the cos and sin terms are converted into tan terms using the identities below:

$$\sin x = \frac{2\tan x/2}{1+\tan^{2x} x/2}$$

$$\cos x = \frac{1-\tan^2 x/2}{1+\tan^2 x/2}$$

Equation (3) becomes after converting to tan's and simplification:

$$h\tan^2(\gamma/2) + i\tan(\gamma/2) + j = 0 \qquad (5)$$

Where h, i, and j are new constants;

$h = g + d$, subbing equation 4 for g we have

$$h = a - b - f + d \; . \qquad (6)$$

$$i = -2e \; . \qquad (7)$$

$j = g - d$, subbing equation 4 for g we have

$$j = a - b - f - d \; . \qquad (8)$$

Equation (5) can be solved using the quadratic formula to find the unknown angle γ as shown below:

$$\gamma = 2.\tan^{-1}\left[\frac{-i \pm \sqrt{i^2 - 4hj}}{2h}\right] \qquad (9)$$

1.4 CASE STUDY: SOLVING FOR ACTUATOR 5 AT JAW CLOSED POSITION

Parameters needed to define each of the six crank frames position and orientations are listed below in table 1.1. Appendix C figure 1.5 illustrates how the two angles α and β are used to define orientation of the crank frames.

Parameter description	**Symbol**	**Value**
First rotation skull frame to crank 1 frame.	α_1	0.00degrees
First rotation skull frame to crank 2 frame.	α_2	1.97 degrees
First rotation skull frame to crank 3 frame.	α_3	90.18 degrees
First rotation skull frame to crank 4 frame.	α_4	-87.99 degrees
First rotation skull frame to crank 5 frame.	α_5	89.14 degrees
First rotation skull frame to crank 6 frame.	α_6	-87.86 degrees
Second rotation skull frame to crank 1 frame	β_1	2.99 degrees
Second rotation skull frame to crank 2 frame	β_2	2.50 degrees
Second rotation skull frame to crank 3 frame	β_3	80.09 degrees
Second rotation skull frame to crank 4 frame	β_4	80.21 degrees
Second rotation skull frame	β_5	75.03 degrees

to crank 5 frame		
Second rotation skull frame to crank 6 frame	β_6	77.81 degrees
Crank 1 frame origin in skull frame	${}^{S}C1_{ORG}$	$\begin{bmatrix} -70.28mm \\ -14.04mm \\ 6.72mm \end{bmatrix}$
Crank 2 frame origin in skull frame	${}^{S}C2_{ORG}$	$\begin{bmatrix} -70.92mm \\ 10.42mm \\ 6.75mm \end{bmatrix}$
Crank 3 frame origin in skull frame	${}^{S}C3_{ORG}$	$\begin{bmatrix} -38.50mm \\ -60.91mm \\ 16.31mm \end{bmatrix}$
Crank 4 frame origin in skull frame	${}^{S}C4_{ORG}$	$\begin{bmatrix} -41.63mm \\ 58.89mm \\ 16.47mm \end{bmatrix}$
Crank 5 frame origin in skull frame	${}^{S}C5_{ORG}$	$\begin{bmatrix} -53.36mm \\ -58.69mm \\ 66.31mm \end{bmatrix}$
Crank 6 frame origin in skull frame	${}^{S}C6_{ORG}$	$\begin{bmatrix} -56.36mm \\ 55.74mm \\ 66.46mm \end{bmatrix}$

Appendix Table 1.1: Parameters describing crank frames location and orientation.

Angles were found by first measuring a point P in the crank frame, then measuring the same point in skull frame, and solving equation 10 below for the rotation matrix ${}^{S}_{C}R$. All measurements were done in Solidworks using the 'measure' tool.

$${}^{S}P = {}^{S}_{C}R.{}^{C}P + {}^{S}C_{org} \quad (10)$$

From ${}^{S}_{C}R$ the Z-Y-Z Euler angles can be found by use of the following:

$${}^{S}_{C}R = \begin{bmatrix} r_{11} & r_{12} & r_{13} \\ r_{21} & r_{22} & r_{23} \\ r_{31} & r_{32} & r_{33} \end{bmatrix}$$

$$\beta = A\tan 2(\sqrt{{r_{31}}^2 + {r_{32}}^2}, r_{33}) \tag{11}$$

$$\alpha = A\tan 2(\frac{r_{23}}{s\beta}, \frac{r_{13}}{s\beta}) \tag{12}$$

$$\gamma = A\tan 2(\frac{r_{32}}{s\beta}, \frac{-r_{31}}{s\beta}) \tag{13}$$

For crank 5:

Measuring a point on crank 5's Y-axis, ${}^{C}P = \begin{bmatrix} 0 \\ 18.34 \\ 0 \end{bmatrix}$. The same point in the skull frame is ${}^{S}P = \begin{bmatrix} -64.43 \\ -61.97 \\ 80.59 \end{bmatrix}$. And ${}^{S}C5_{org} = \begin{bmatrix} -53.36 \\ -58.69 \\ 66.31 \end{bmatrix}$

So subbing into equation 10 we have:

$$\begin{bmatrix} -64.43 \\ -61.97 \\ 80.59 \end{bmatrix} = \begin{bmatrix} r_{11} & r_{12} & r_{13} \\ r_{21} & r_{22} & r_{23} \\ r_{31} & r_{32} & r_{33} \end{bmatrix} . \begin{bmatrix} 0 \\ 18.34 \\ 0 \end{bmatrix} + \begin{bmatrix} -53.36 \\ -58.69 \\ 66.31 \end{bmatrix}$$

$$\begin{bmatrix} -64.43 \\ -61.97 \\ 80.59 \end{bmatrix} = \begin{bmatrix} 18.34r_{12} - 53.36 \\ 18.34r_{22} - 58.69 \\ 18.34r_{32} + 66.31 \end{bmatrix}$$

$$r_{12} = -0.6036$$

$$r_{22} = -0.1788$$

$$r_{32} = 0.7770$$

Measuring a point on crank 5's X-axis, ${}^{C}P = \begin{bmatrix} 15 \\ 0 \\ 0 \end{bmatrix}$. The same point in the skull frame is

${}^{S}P = \begin{bmatrix} -65.32 \\ -56.92 \\ 57.46 \end{bmatrix}$.

Subbing into equation 10 we have:

$$\begin{bmatrix} -65.32 \\ -56.92 \\ 57.46 \end{bmatrix} = \begin{bmatrix} r_{11} & r_{12} & r_{13} \\ r_{21} & r_{22} & r_{23} \\ r_{31} & r_{32} & r_{33} \end{bmatrix} . \begin{bmatrix} 15 \\ 0 \\ 0 \end{bmatrix} + \begin{bmatrix} -53.36 \\ -58.69 \\ 66.31 \end{bmatrix}$$

$$\begin{bmatrix} -65.32 \\ -56.92 \\ 57.46 \end{bmatrix} = \begin{bmatrix} 15r_{11} - 53.36 \\ 15r_{21} - 58.69 \\ 15r_{31} + 66.31 \end{bmatrix}$$

$$r_{11} = -0.7973$$
$$r_{21} = 0.1180$$
$$r_{31} = -0.5900$$

Measuring a point on crank 5's Z-axis, ${}^{C}P = \begin{bmatrix} 0 \\ 0 \\ 12.22 \end{bmatrix}$. The same point in the skull frame is ${}^{S}P = \begin{bmatrix} -53.54 \\ -46.75 \\ 68.95 \end{bmatrix}$.

Subbing into equation 10 we have:

$$\begin{bmatrix} -53.54 \\ -46.75 \\ 68.95 \end{bmatrix} = \begin{bmatrix} r_{11} & r_{12} & r_{13} \\ r_{21} & r_{22} & r_{23} \\ r_{31} & r_{32} & r_{33} \end{bmatrix} . \begin{bmatrix} 0 \\ 0 \\ 12.22 \end{bmatrix} + \begin{bmatrix} -53.36 \\ -58.69 \\ 66.31 \end{bmatrix}$$

$$\begin{bmatrix} -53.54 \\ -46.75 \\ 68.95 \end{bmatrix} = \begin{bmatrix} 12.22r_{13} - 53.36 \\ 12.22r_{23} - 58.69 \\ 12.22r_{33} + 66.31 \end{bmatrix}$$

$$r_{13} = -0.0147$$
$$r_{23} = 0.9771$$
$$r_{33} = 0.2160$$

Subbing $r_{31}, r_{32}, r_{33}, r_{13}$ and r_{23} into equations 11 and 12 the two fixed Euler angles α and β can be found.

$$\beta_5 = A\tan 2(\sqrt{(-0.59)^2 + (0.7702)^2}, 0.2137)$$

= 1.3095 rad

= 75.03 degrees

$$\alpha_5 = A\tan 2(\frac{0.9773}{\sin(1.3095)}, \frac{-0.0147}{\sin(1.3095)})$$

=1.584 rad

=89.14 degrees

The variable angle γ_5 can also be found for this jaw closed position using equation 13. I will use this angle derived from actual measurements to compare with the angle predicted by the formed inverse kinematics solution later in this section.

$$\gamma_5 = \text{Atan2}\,(\frac{0.7770}{\sin(1.3095)}, \frac{0.5900}{\sin(1.3095)})$$

=2.234 rad

=128.0 degrees

Having found the translation and the two fixed angles for the Z-Y-Z Euler rotations of skull frame to crank frames, transformation matrix's can be formed with the actuation angle γ being the only unknown variable. Transformation matrix's for the crank frames are listed below in table 1.2.

Parameter Description	**Symbol**	**Value**
Transformation matrix; skull frame to crank 1 frame	${}^{S}_{C1}T$	$\begin{bmatrix} 0.9986c\gamma_1 & -0.9986s\gamma_1 & 0.0521 & -70.2800 \\ s\gamma_1 & c\gamma_1 & 0 & -14.0400 \\ -0.0521c\gamma_1 & 0.0521s\gamma_1 & 0.9986 & 6.7200 \\ 0 & 0 & 0 & 1 \end{bmatrix}$
Transformation matrix; skull frame to crank 2 frame	${}^{S}_{C2}T$	$\begin{bmatrix} 0.9985c\gamma_2 - 0.0344s\gamma_2 & -0.9985s\gamma_2 - 0.0344c\gamma_2 & 0.0437 & -70.92 \\ 0.0344c\gamma_2 + 0.9994s\gamma_2 & -0.0344s\gamma_2 + 0.9994c\gamma_2 & 0.0015 & 10.420 \\ -0.0437c\gamma_2 & 0.0437s\gamma_2 & 0.9990 & 6.750 \\ 0 & 0 & 0 & 1 \end{bmatrix}$
Transformation matrix; skull frame to crank 3 frame	${}^{S}_{C3}T$	$\begin{bmatrix} -0.0029c\gamma_3 - 0.9999s\gamma_3 & 0.0029s\gamma_3 - 0.9999c\gamma_3 & -0.0164 & -38.50 \\ 0.1721c\gamma_3 - 0.0166s\gamma_3 & -0.1721s\gamma_3 - 0.0166c\gamma_3 & 0.9849 & -60.91 \\ -0.9851c\gamma_3 & 0.9851s\gamma_3 & 0.1721 & 16.31 \\ 0 & 0 & 0 & 1 \end{bmatrix}$
Transformation matrix; skull frame to crank 4 frame	${}^{S}_{C4}T$	$\begin{bmatrix} 0.0060c\gamma_4 + 0.9994s\gamma_4 & -0.0060s\gamma_4 + 0.9994c\gamma_4 & 0.0346 & -41.63 \\ -0.1699c\gamma_4 + 0.0351s\gamma_4 & 0.1699s\gamma_4 + 0.0351c\gamma_4 & -0.9848 & 58.89 \\ -0.9854c\gamma_4 & 0.9854s\gamma_4 & 0.1700 & 16.47 \\ 0 & 0 & 0 & 1 \end{bmatrix}$

Transformation matrix; skull frame to crank 5 frame	${}^{S}_{C5}T$	$\begin{bmatrix} -0.0032c\gamma_5 - 0.9999s\gamma_5 & 0.0032s\gamma_5 - 0.9999c\gamma_5 & -0.0148 & -53.36 \\ 0.2135c\gamma_5 - 0.0151s\gamma_5 & -0.2135s\gamma_5 - 0.0151c\gamma_5 & 0.9768 & -58.69 \\ -0.9769c\gamma_5 & 0.9769s\gamma_5 & 0.2135 & 66.34 \\ 0 & 0 & 0 & 1 \end{bmatrix}$
Transformation matrix; skull frame to crank 6 frame	${}^{S}_{C6}T$	$\begin{bmatrix} 0.0079c\gamma_6 + 0.9993s\gamma_6 & -0.0079s\gamma_6 + 0.9993c\gamma_6 & 0.0365 & -56.36 \\ -0.2109c\gamma_6 + 0.0374s\gamma_6 & 0.2109s\gamma_6 + 0.0374c\gamma_6 & -0.9768 & 55.74 \\ -0.9775c\gamma_6 & 0.9775s\gamma_6 & 0.2111 & 66.46 \\ 0 & 0 & 0 & 1 \end{bmatrix}$

Appendix Table 1.2

Other parameters needed for the inverse kinematics calculation are listed in table 1.3. Symbols can be seen in figure 1.6 below.

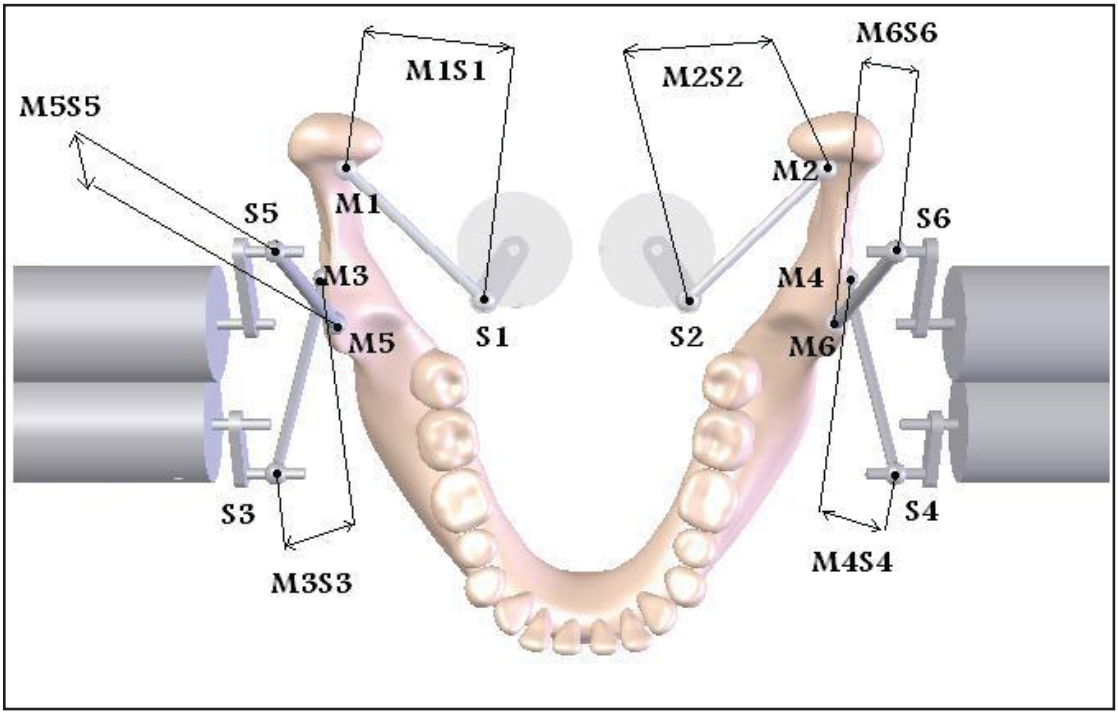

Appendix C Figure 1.6: The mandible showing key point locations and dimensions.

Parameter description	**Symbol**	**Value**
Spherical joint in crank 1 frame	${}^{C1}S_1$	$\begin{bmatrix} 10 \\ 0 \\ 6 \end{bmatrix}$
Spherical joint in crank 2 frame	${}^{C2}S_2$	$\begin{bmatrix} 10 \\ 0 \\ 6 \end{bmatrix}$
Spherical joint in crank 3 frame	${}^{C3}S_3$	$\begin{bmatrix} 10 \\ 0 \\ 6 \end{bmatrix}$

Spherical joint in crank 4 frame	${}^{C4}S_4$	$\begin{bmatrix} 10 \\ 0 \\ 6 \end{bmatrix}$
Spherical joint in crank 5 frame	${}^{C5}S_5$	$\begin{bmatrix} 15.003 \\ 0.02 \\ 6 \end{bmatrix}$
Spherical joint in crank 6 frame	${}^{C6}S_6$	$\begin{bmatrix} 15.003 \\ -0.02 \\ 6 \end{bmatrix}$
Joint between crank 1 and mandible with respect to mandible frame.	${}^{M}M_1$	$\begin{bmatrix} -79.75 \\ -41.10 \\ 38.77 \end{bmatrix}$
Joint between crank 2 and mandible with respect to mandible frame.	${}^{M}M_2$	$\begin{bmatrix} -79.75 \\ 41.10 \\ 38.77 \end{bmatrix}$
Joint between crank 3 and mandible with respect to mandible frame.	${}^{M}M_3$	$\begin{bmatrix} -60.85 \\ -44.70 \\ -5.83 \end{bmatrix}$
Joint between crank 4 and mandible with respect to mandible frame.	${}^{M}M_4$	$\begin{bmatrix} -60.85 \\ 44.70 \\ -5.83 \end{bmatrix}$
Joint between crank 5 and mandible with respect to mandible frame.	${}^{M}M_5$	$\begin{bmatrix} -53.25 \\ -43.00 \\ 43.87 \end{bmatrix}$
Joint between crank 6 and mandible with respect to mandible frame.	${}^{M}M_6$	$\begin{bmatrix} -53.25 \\ 43.00 \\ 43.87 \end{bmatrix}$
Length of link L1 between	M_1S_1	33.90mm

M1 and S1		
Length of link L2 between M2 and S2	M_2S_2	33.90mm
Length of link L3 between M3 and S3	M_3S_3	49.90mm
Length of link L4 between M4 and S4	M_4S_4	49.90mm
Length of link L5 between M5 and S5	M_5S_5	52.26mm
Length of link L6 between M6 and S6	M_6S_6	52.26mm

Appendix Table 1.3

Now that all the parameters are defined the actuation angles are able to be solved for a given mandible to skull transformation. I will continue by solving for γ_5, the actuation angle of crank 5, for the jaw closed position.

At jaw closed position, the mandible to skull frame transformation is

$$ {}^{S}_{M}T = \begin{bmatrix} 0.9983 & -0.0262 & 0.0523 & -6.0900 \\ 0.0261 & 0.9996 & 0 & -0.07 \\ -0.0523 & 0.0015 & 0.9986 & -20.17 \\ 0 & 0 & 0 & 1 \end{bmatrix} $$

${}^{S}M_5$, position of M_5 in the skull frame is calculated from the given transformation above:

$${}^{S}M_5 = {}^{S}_{M}T \,.\, {}^{M}M_5$$

$$= \begin{bmatrix} 0.9983 & -0.0262 & 0.0523 & -6.0900 \\ 0.0261 & 0.9996 & 0 & -0.07 \\ -0.0523 & 0.0015 & 0.9986 & -20.17 \\ 0 & 0 & 0 & 1 \end{bmatrix} . \begin{bmatrix} -53.25 \\ -43.00 \\ 43.87 \\ 1 \end{bmatrix}$$

$${}^{S}M_5 = \begin{bmatrix} -55.82 \\ -44.44 \\ 26.36 \\ 1 \end{bmatrix}$$

${}^{S}S_5$, position of S_5 in the skull frame is calculated from ${}^{S}_{C5}T$:

$${}^{S}S_5 = {}^{S}_{C5}T . {}^{C5}S_5$$

$$= \begin{bmatrix} -0.0032c\gamma_5 - 0.9999s\gamma_5 & 0.0032s\gamma_5 - 0.9999c\gamma_5 & -0.0148 & -53.36 \\ 0.2135c\gamma_5 - 0.0151s\gamma_5 & -0.2135s\gamma_5 - 0.0151c\gamma_5 & 0.9768 & -58.69 \\ -0.9769c\gamma_5 & 0.9769s\gamma_5 & 0.2135 & 66.34 \\ 0 & 0 & 0 & 1 \end{bmatrix} . \begin{bmatrix} 15.03 \\ 0.02 \\ 6 \\ 1 \end{bmatrix}$$

$$= \begin{bmatrix} -0.0684c\gamma_5 - 15.0012s\gamma_5 - 53.4485 \\ 3.2031c\gamma_5 - 0.2309s\gamma_5 - 52.8291 \\ -14.6569c\gamma_5 + 0.0195s\gamma_5 + 67.6212 \\ 1 \end{bmatrix}$$

Now using equation 1 we have:

$$(M_5S_5)^2 = ({}^{S}S_5(1) - {}^{S}M_5(1))^2 + ({}^{S}S_5(2) - {}^{S}M_5(2))^2 + ({}^{S}S_5(3) - {}^{S}M_5(3))^2$$

Subbing in our calculated values, and value for M_5S_5 from table 1.3.

$$(52.26)^2 = ((-0.0684c\gamma_5 - 15.0012s\gamma_5 - 53.4485) + 55.82)^2 +$$

$$((3.2031c\gamma_5 - 0.2309s\gamma_5 - 52.8291) + 44.44)^2 +$$

$$((-14.6569c\gamma_5 + 0.0195s\gamma_5 + 67.6212) - 26.36)^2$$

After expanding:

$$2731.10 = 225.09c^2\gamma_5 + 0.5033\times10^{-16}.c\gamma_5.s\gamma_5 - 1263.6c\gamma_5 + 225.09s^2\gamma_5 - 65.66s\gamma_5 + 1778.5$$

Comparing to equation 2 to equate coefficients:

$$a = b\cos^2\gamma + b\sin^2\gamma + c\times10^{-16}\cos\gamma.\sin\gamma + d\cos\gamma + e\sin\gamma + f$$

$a = 2731$
$b = 225.09$
$c = 2.59\times10^{-16}$
$d = -1263.6$
$e = -65.66$
$f = 1778.5$

Finding final coefficients by use of equation 6, 7 and 8.

$$h = a - b - f + d\ .$$

$$= 2731 - 225.09 - 1778.5 - 1263.6$$
$$= -536.19$$

$$i = -2e\ .$$

$$= -2(-65.66)$$
$$= 131.84$$

$$j = a - b - f - d$$

$$= 2731 - 225.09 - 1778.5 + 1263.6$$
$$= 1991.1$$

Subbing values into equation 9:

$$\gamma = 2.\tan^{-1}\left[\frac{-i \pm \sqrt{i^2 - 4hj}}{2h}\right]$$

$$= 2.\tan^{-1}\left[\frac{-131 \pm \sqrt{131^2 - 4 \times -536 \times 1991}}{2 \times -536}\right]$$

Answer1= $2(-1.06)$ = -2.12 rad = -121 degrees

Answer2= 2(-1.06+pi) = 4.16 rad = 238 degrees

Answer3 = 2(1.1176) = 2.23 rad = 128 degrees

Answer4= 2(1.1176-pi) = -4.05 rad = -232 degrees

Comparing all answers with the angle derived using equation 13 from actual measurements it's clear that answer3 above is the correct one. I will go into details on how the correct answer out of the four possible from equation 9 is found in the next section.

1.5 FORMING M-FILES FOR INVERSE KINEMATICS IN MATLAB

M-files were made for each actuator to return the actuation angle from a given mandible to skull transformation (${}^{S}_{M}T$). The 6 M-files are then used in another M-file which take in an excel file containing a trajectory of the jaw and returns the 6 corresponding trajectories of the actuators.

A description of how the two main m-files work is shown below:

1. **Solvey i .m (** $i = 1,2...6$ **)**

This m-file does a single calculation to find the actuation angle of the crank for a given point in the jaw trajectory (${}^{S}_{M}T$).

INPUT:

User defined (input every time m-file is called):

- ${}^{S}_{M}T$, transformation mandible frame to skull frame in the form of a 4 by 4 matrix.

From geometry of robot (input once only):

- ${}^{M}M$, mounting points on plate frame with respect to plate frame.
- ${}^{S}_{C}T$, transformation crank frame to base frame, with unknown terms cos γ and sin γ replaced by variables n and m.
- ${}^{C}S$, point S with respect to crank frame.
- MS, length of link between mounting point on plate and point S.

PROCESSING:

1. ${}^{S}M$, ${}^{S}S$ are calculated.
2. The constants/coefficients are found in Matlab by setting the unknown terms n and m to either -1, 0 or 1 before calculating the RHS of equation 1 so terms can be isolated.
3. In order to use equation 5 to solve for the unknown angle, the 3 constants needed for the quadratic equation must first be found. By looking at the procedure these constants are formed, I found that they are linear functions of the original constants/coefficients formed from expanding equation 1.
4. Finally four answers are found by solving equation 5. Of the four answers, the correct one was the same every time.

OUTPUT:

- A single crank angle in radians.

A flowchart illustrates the steps in Solvey i in figure 1.7:

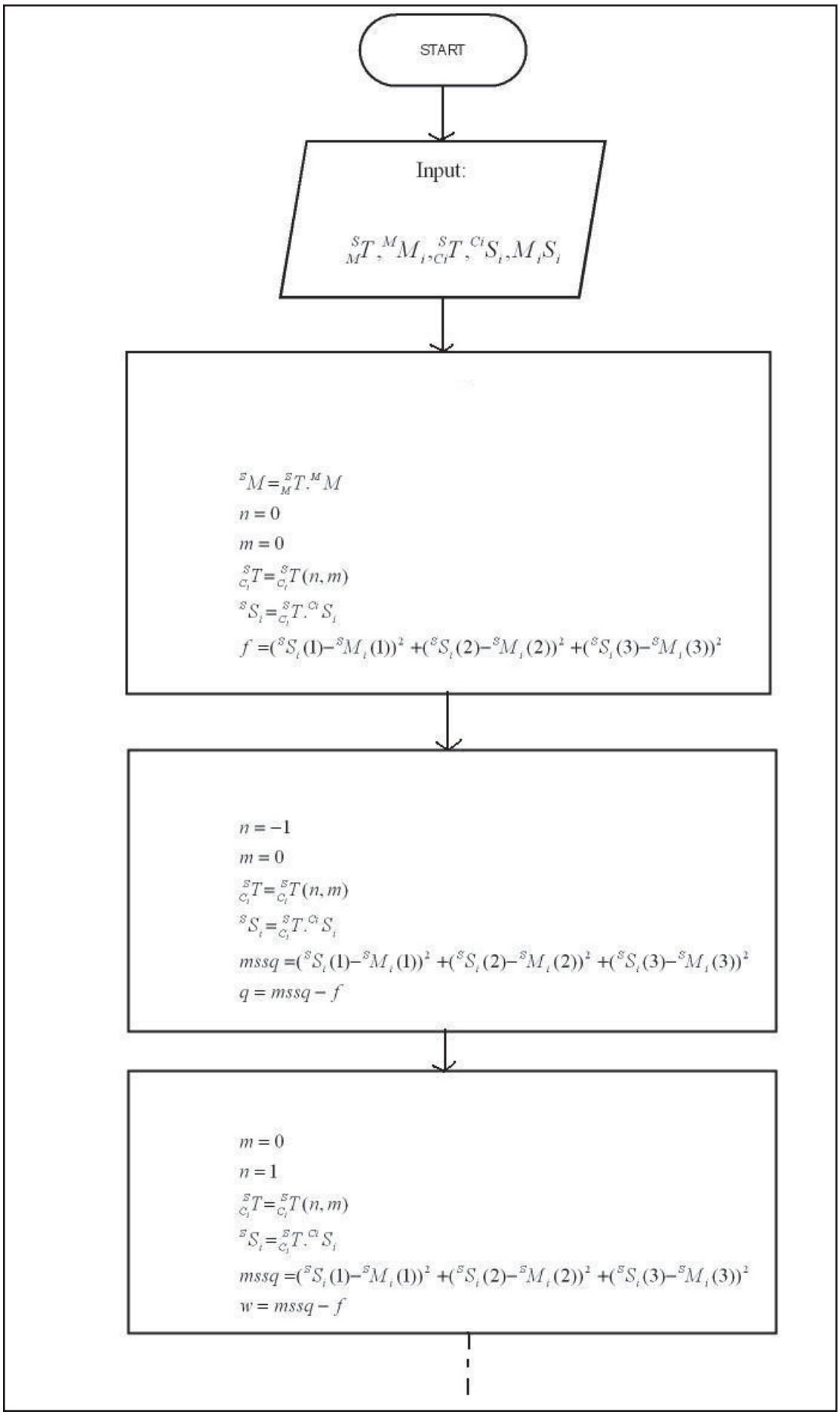
START
Input:
${}^{S}_{M}T, {}^{M}M_i, {}^{S}_{Ci}T, {}^{Ci}S_i, M_iS_i$
${}^{S}M = {}^{S}_{M}T.{}^{M}M$
$n = 0$
$m = 0$
${}^{S}_{Ci}T = {}^{S}_{Ci}T(n,m)$
${}^{S}S_i = {}^{S}_{Ci}T.{}^{Ci}S_i$
$f = ({}^{S}S_i(1) - {}^{S}M_i(1))^2 + ({}^{S}S_i(2) - {}^{S}M_i(2))^2 + ({}^{S}S_i(3) - {}^{S}M_i(3))^2$
$n = -1$
$m = 0$
${}^{S}_{Ci}T = {}^{S}_{Ci}T(n,m)$
${}^{S}S_i = {}^{S}_{Ci}T.{}^{Ci}S_i$
$mssq = ({}^{S}S_i(1) - {}^{S}M_i(1))^2 + ({}^{S}S_i(2) - {}^{S}M_i(2))^2 + ({}^{S}S_i(3) - {}^{S}M_i(3))^2$
$q = mssq - f$
$m = 0$
$n = 1$
${}^{S}_{Ci}T = {}^{S}_{Ci}T(n,m)$
${}^{S}S_i = {}^{S}_{Ci}T.{}^{Ci}S_i$
$mssq = ({}^{S}S_i(1) - {}^{S}M_i(1))^2 + ({}^{S}S_i(2) - {}^{S}M_i(2))^2 + ({}^{S}S_i(3) - {}^{S}M_i(3))^2$
$w = mssq - f$

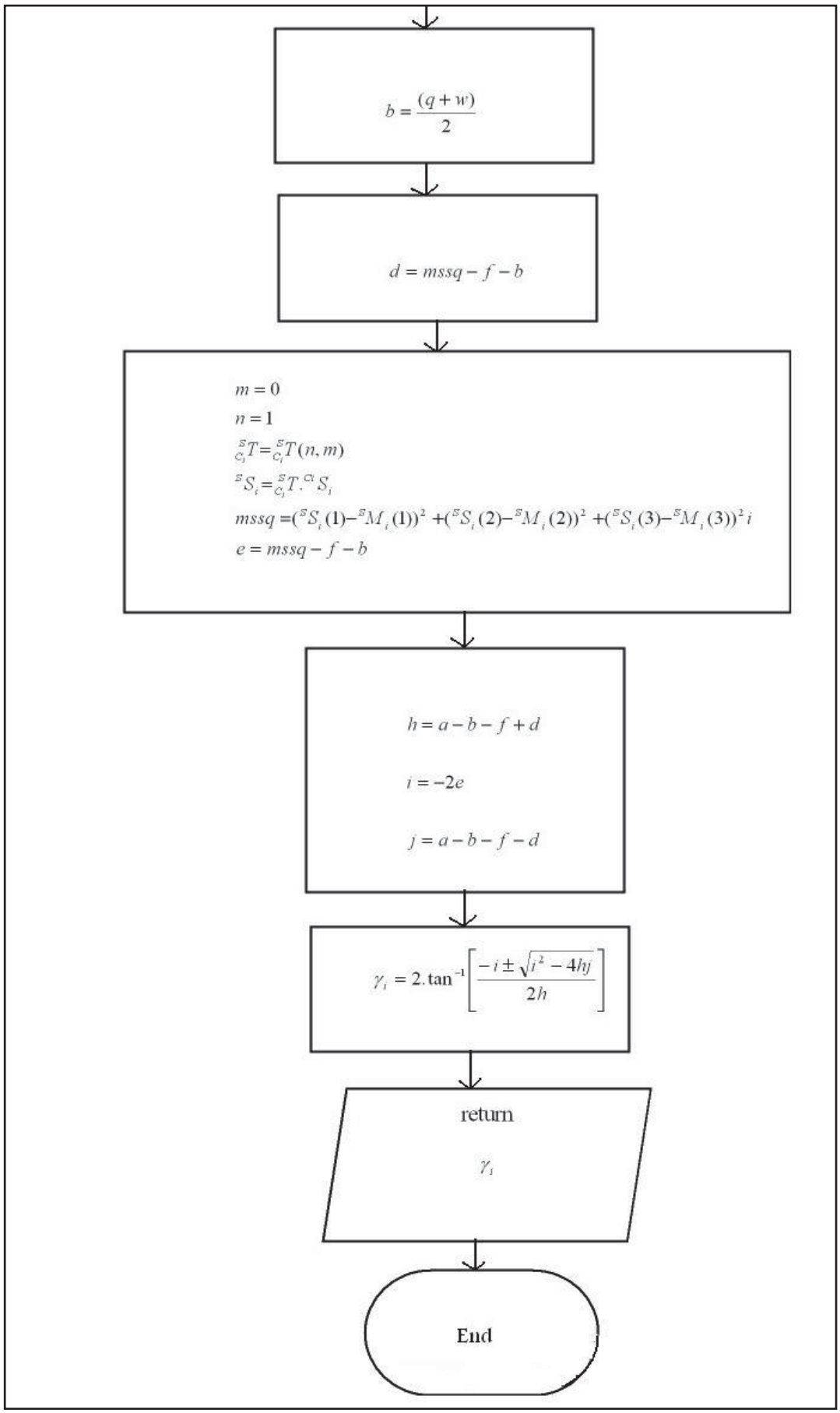

Appendix C figure 1.7: Flowchart of solveyi.m m-file.

2. **inversesolve.m**

This m-file takes a CSV file containing a jaw trajectory in terms of three position elements (x, y, z) and three angular elements (roll, pitch, yaw), and returns the 6 individual trajectories for the 6 crank mechanisms.

INPUT:

- User defined CSV file containing the jaw trajectory.

PROCESSING:

1. csvread.m is called to put trajectory data into a matrix in Matlab.

2. Starting at first point, convertTM.m is called to change the 6 input elements of the trajectory into a 4 by 4 transformation matrix so can be used by solvey.m.

3. solvey1.m through to solvey6.m are called to return the 6 crank angles.

4. Increment to next point in trajectory and loop back to step 2 until all points have been processed.

5. Solutions are saved in a matrix of 6 columns, one for each crank trajectory, and written to a CSV file.

OUTPUT:

- 6 individual trajectories for the 6 crank mechanisms in the form of a 6 column matrix (length determined by number of points in trajectory).

A flowchart illustrates the steps in intersolve.m M-file in figure 1.8 on the next page.

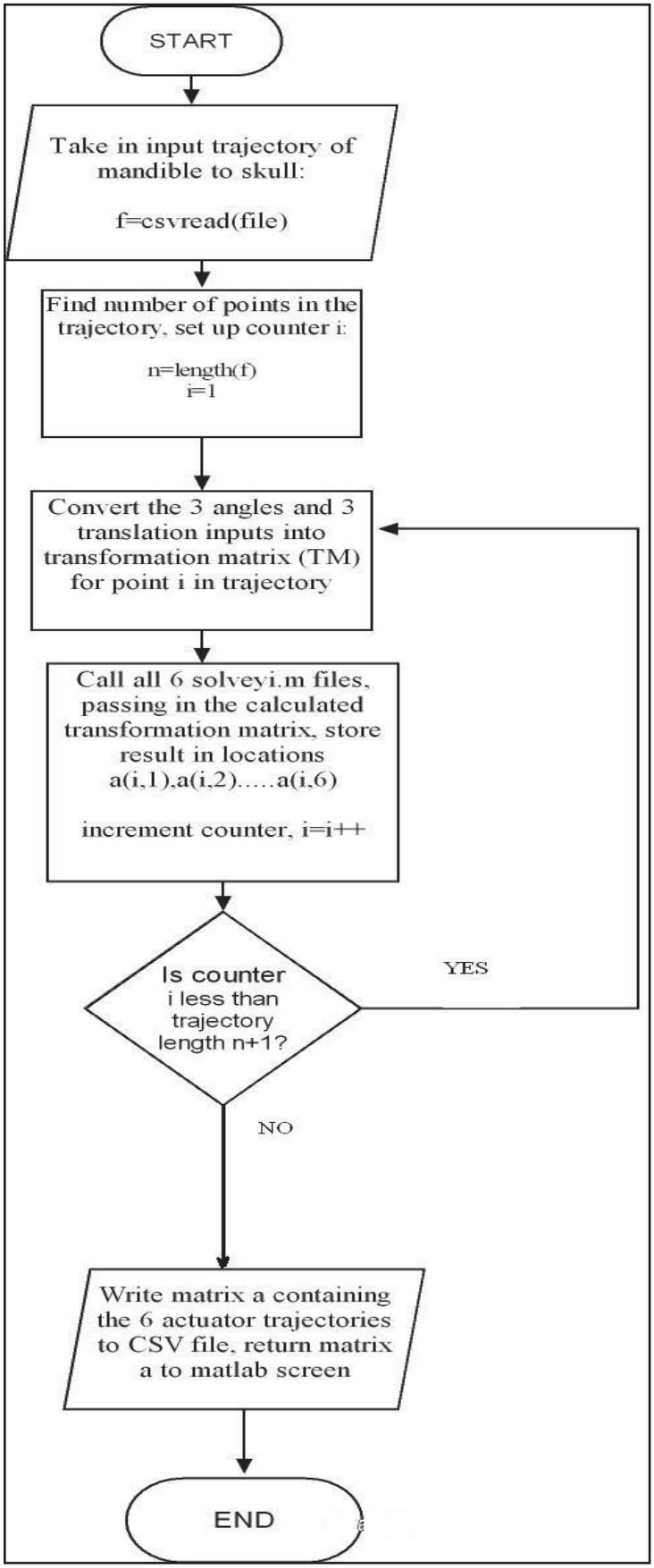

Appendix C figure 1.8: Flowchart of intersolve.m M-file.

1.5 RESULTS

To test the accuracy of my Matlab solution a simple trajectory consisting of 7 'chews' was implemented in COSMOS motion and then through Matlab. Time increments for the trajectory are 0.01 seconds. The trajectory was taken from Kylie Fosters two dimensional recordings, with added constraints on roll, pitch and yaw to allow simulation in Solidworks. The trace paths of this trajectory can be seen in figure 1.4 below.

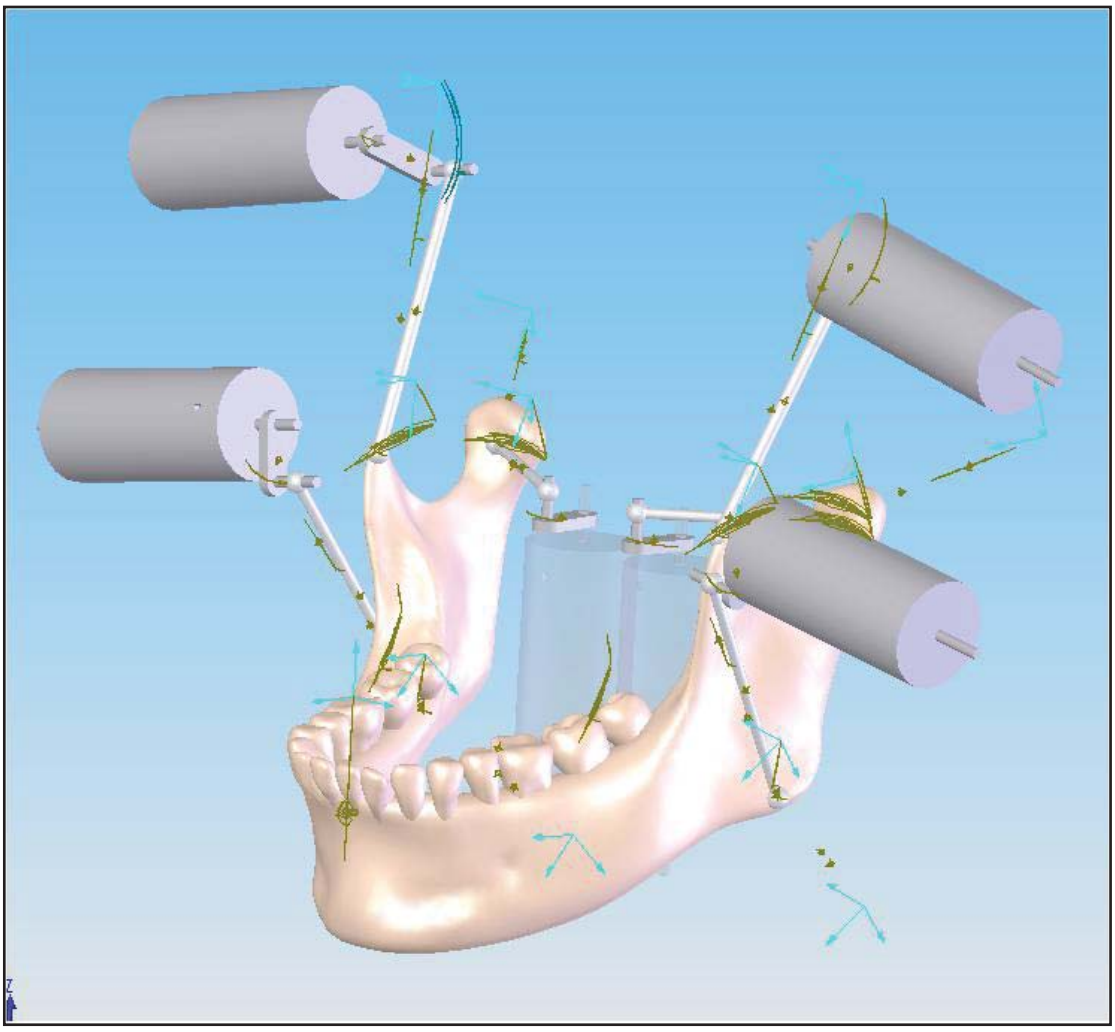

Appendix C Figure 1.4: Trace paths of a simple jaw trajectory.

The crank angles obtained from the COSMOS motion simulation were exported to a CSV file and compared with the crank angles from Matlab. Results for each actuator are given below.

- Actuator 1

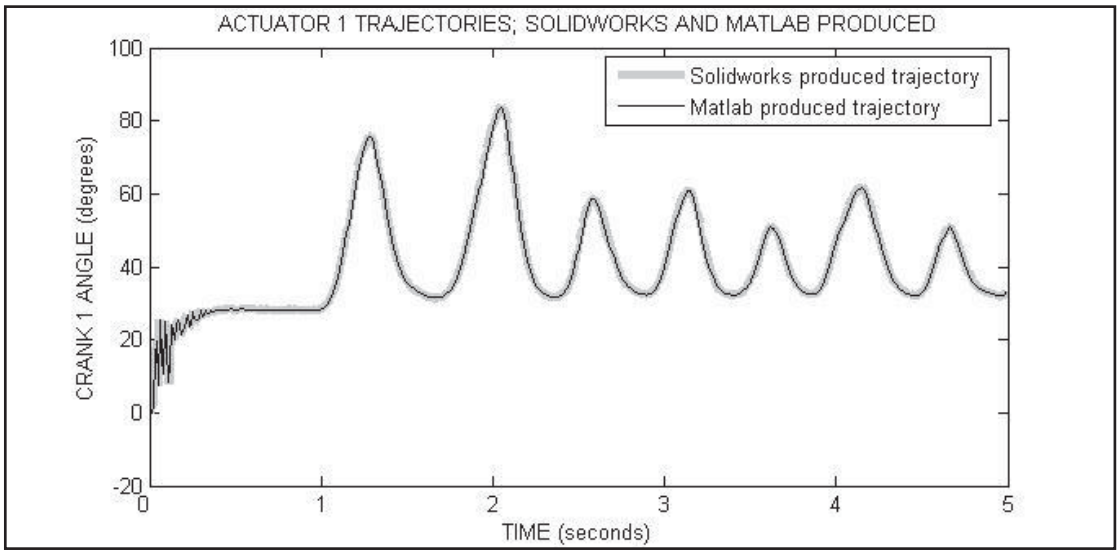

Appendix C figure 1.5: Crank 1 trajectory.

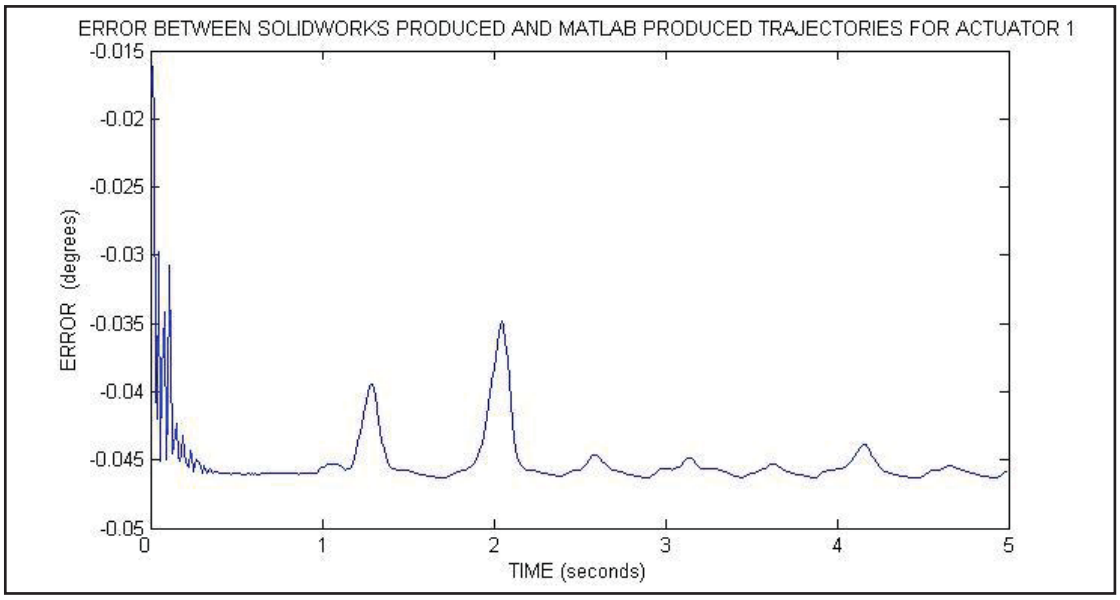

Appendix C figure 1.6: Error between Solidworks and Matlab produced trajectory for crank 1.

- Actuator 2

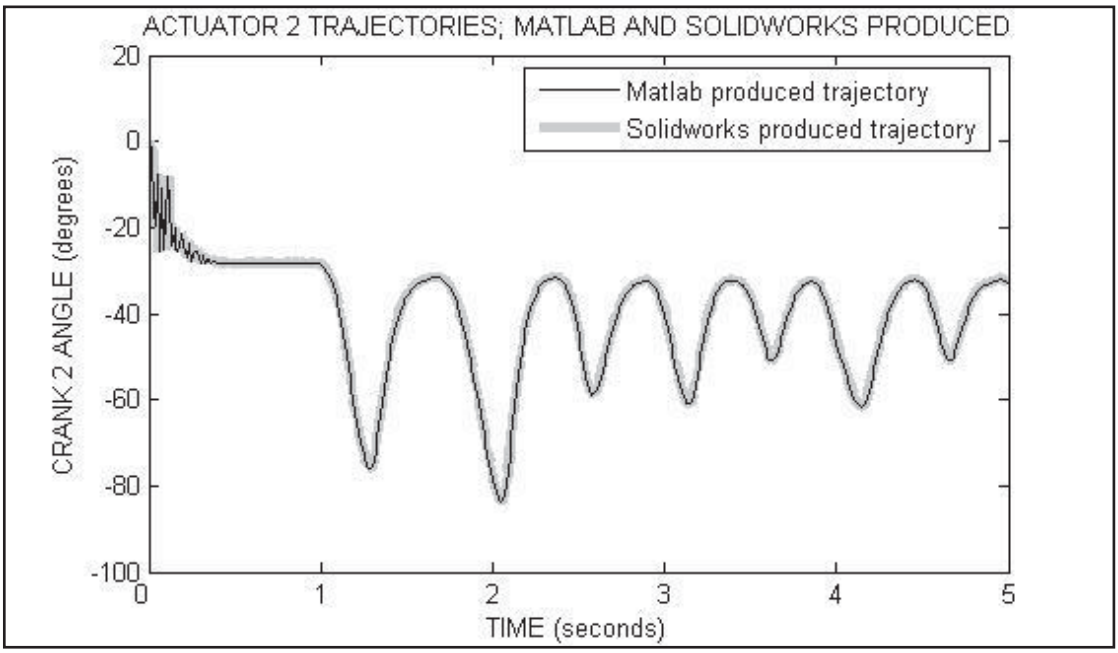

Appendix C figure 1.7: Crank 2 trajectory.

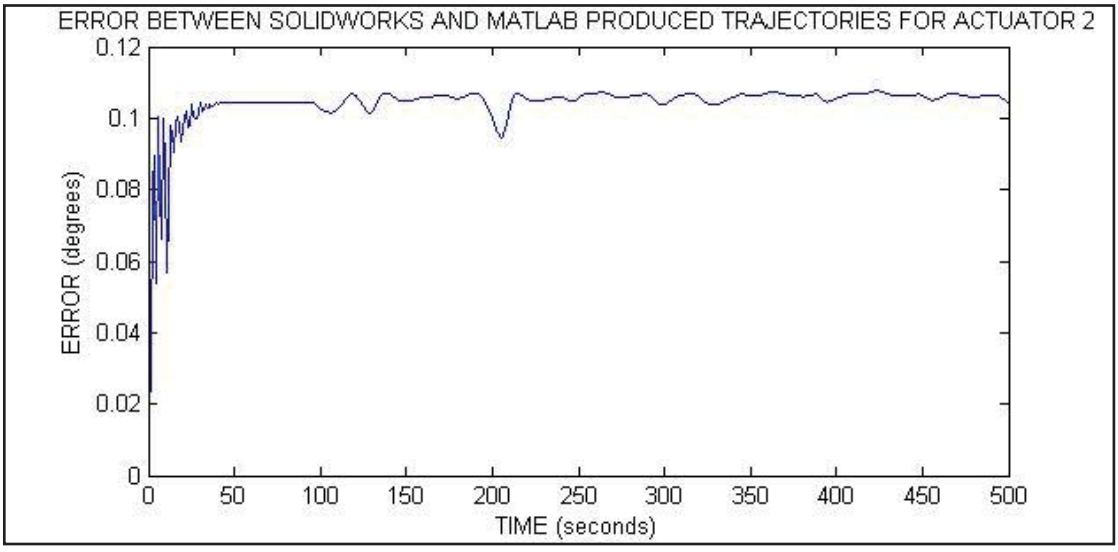

Appendix C figure 1.8: Error between Solidworks and Matlab produced trajectory for crank 2.

- Actuator 3

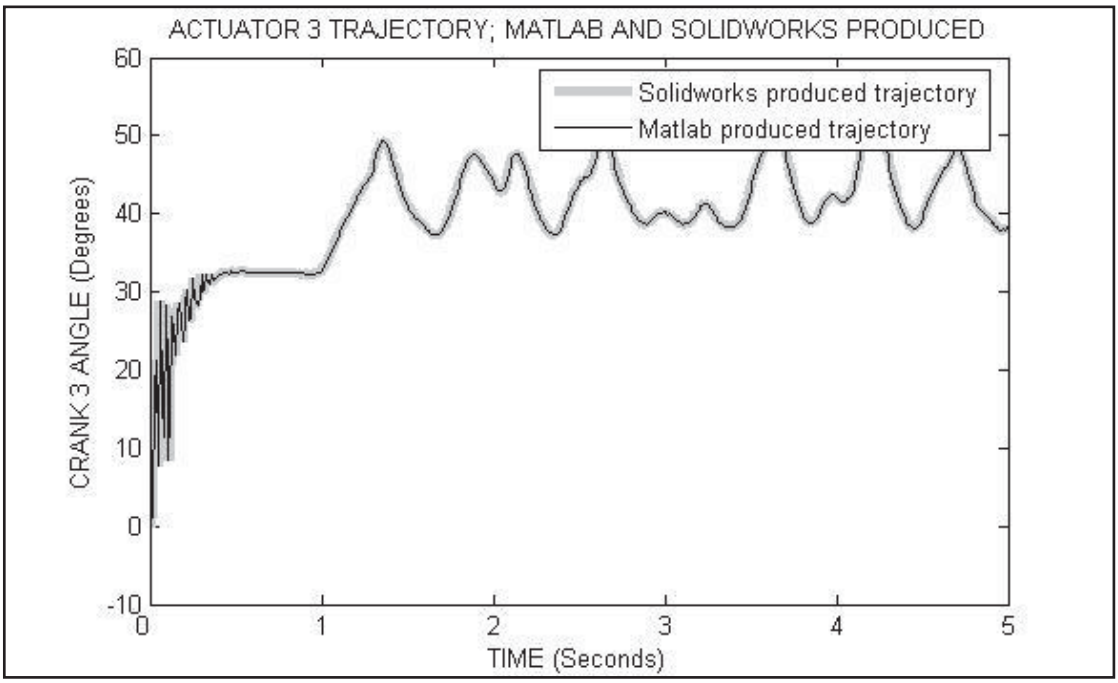

Appendix C figure 1.9: Crank 3 trajectory.

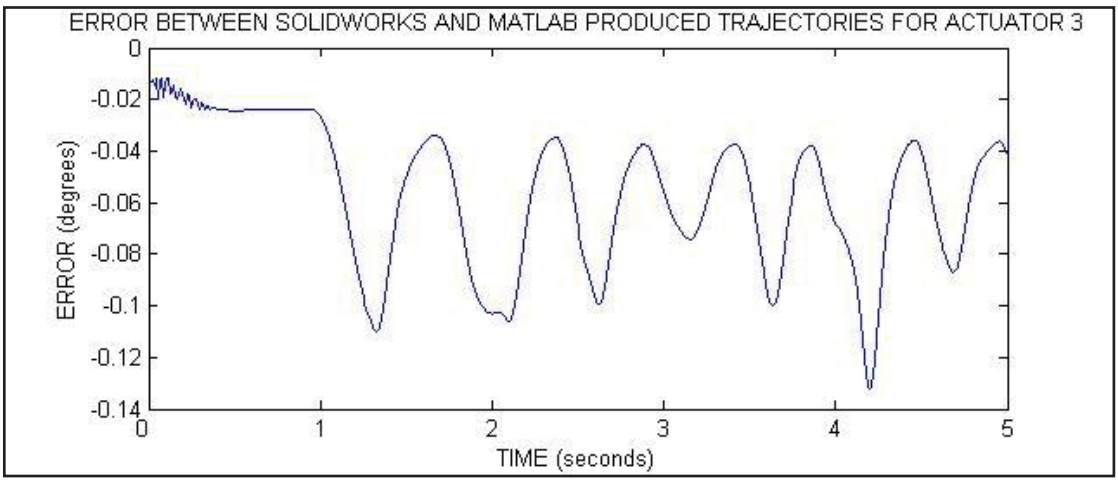

Appendix C figure 1.10: Error between Solidworks and Matlab produced trajectory for crank 3.

- Actuator 4

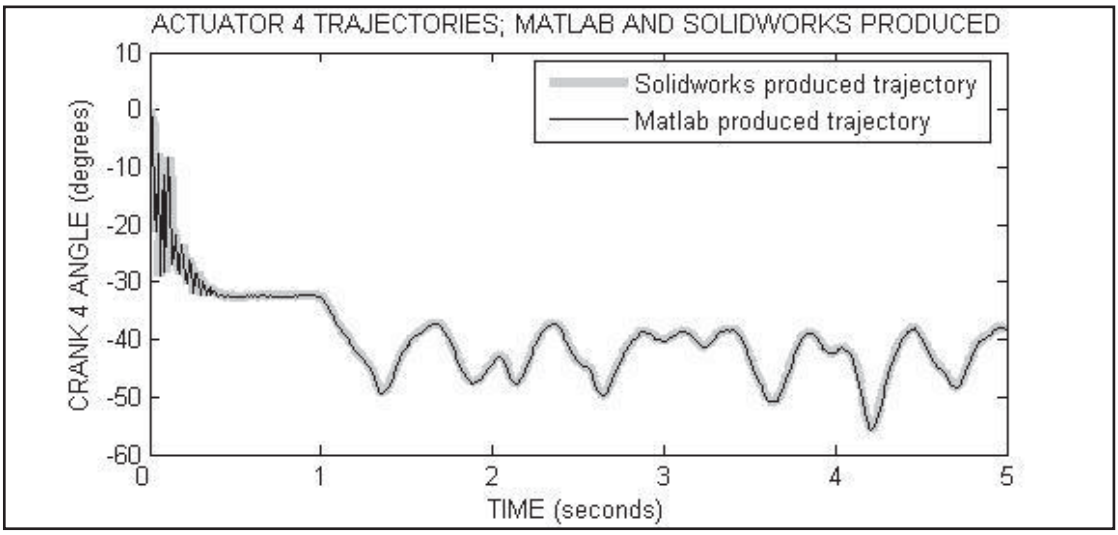

Appendix C figure 1.11: Crank 4 trajectory

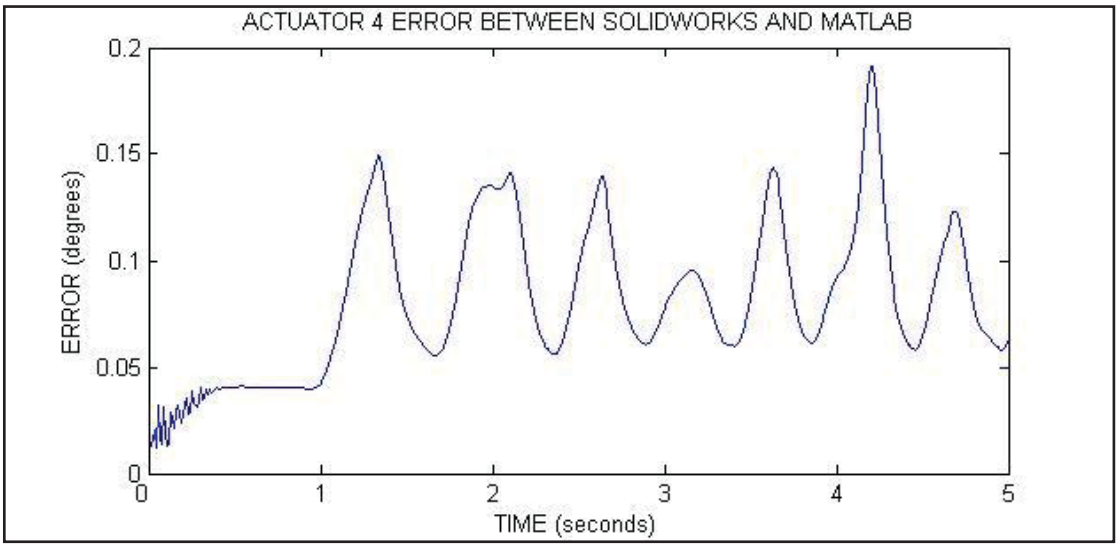

Appendix C figure 1.12: Error between Solidworks and Matlab produced trajectory for crank 4.

- Actuator 5

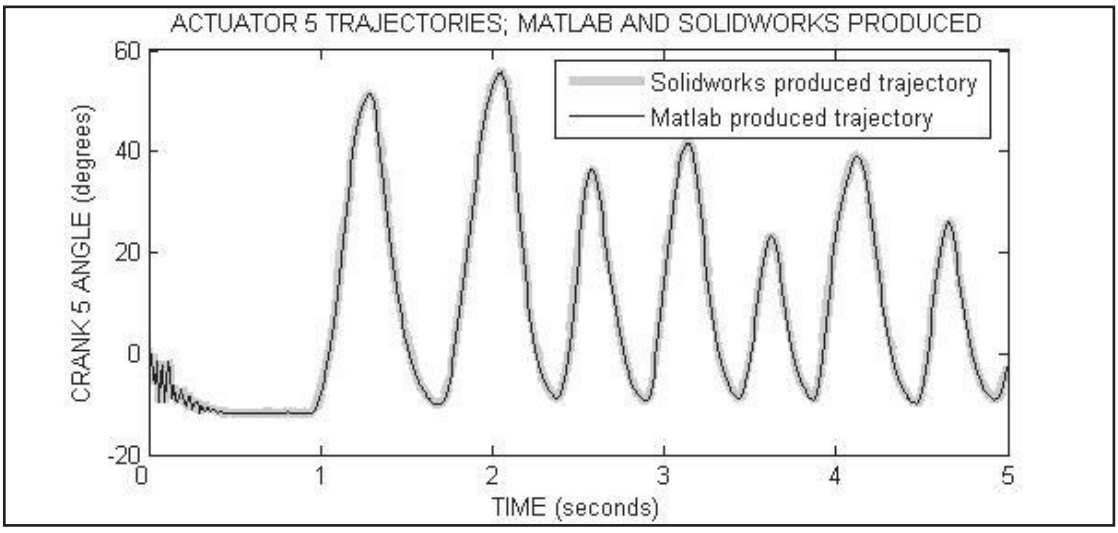

Appendix C figure 1.13: Crank 5 trajectory.

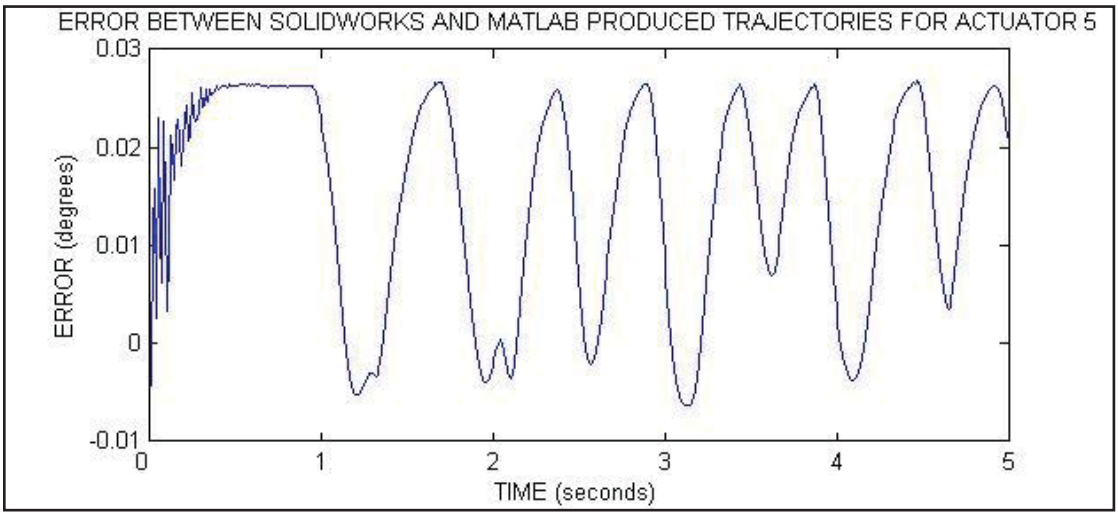

Appendix C figure 1.14: Error between Solidworks and Matlab produced trajectory for crank 5.

- Actuator 6

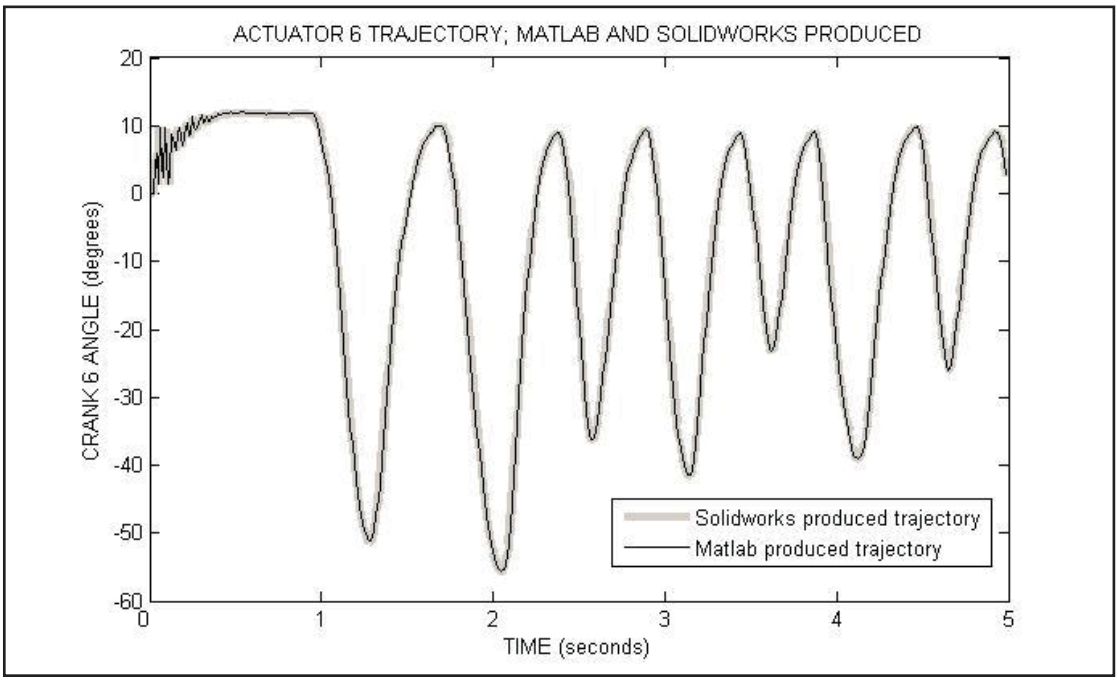

Appendix C figure 1.15: Crank 6 trajectory.

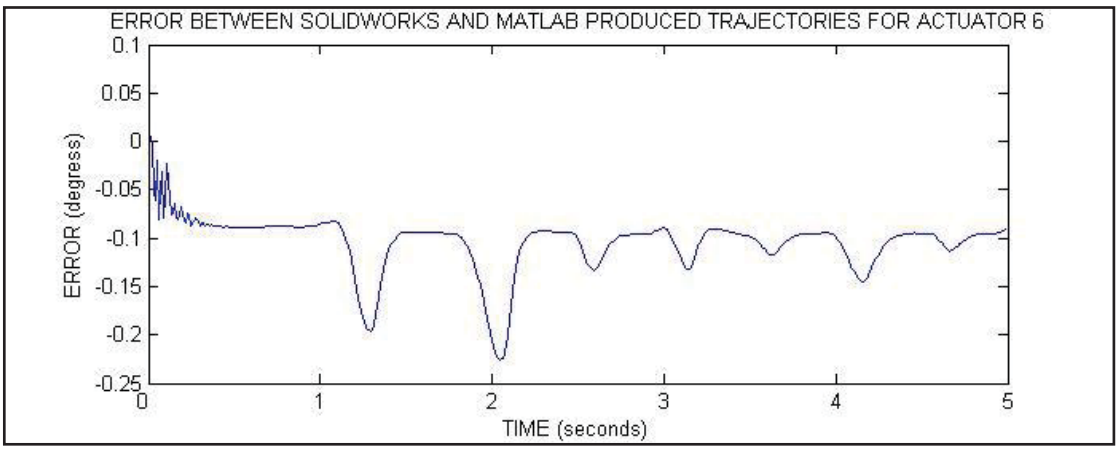

Appendix C figure 1.16: Error between Solidworks and Matlab produced trajectory for crank 6.

From the above graphs it can be seen that the Matlab and Solidworks produced trajectories are very similar, with the biggest difference between the two at any time being around 0.25 of a degree.

Errors are biggest at the half way point of the chew cycle where the jaw changes direction quickly.

Errors could be put down to the different interpolation method used. Matlab calculates discrete points which are graphed using linear interpolation between the points, where as Solidworks join the points with a cubic spline. Provided the time increments between points are kept small then these errors due to different interpolation methods will continue to be small.

APPENDIX D: ESTABLISHING SKULL FRAME ON SUBJECT WORKED EXAMPLE

Establishing the Skull reference frame on the human subject

After applying the 'normalization' procedure the articulorgraph recorded trajectory is now free of head movement, however it is still not in the form we require. All data is relative to the 'Global' articulorgraph reference frame (see figure 1). In order to re-create the trajectory we need it to be relative to a reference frame that is common to the robot model also. To do this a 'skull' reference frame needs to be established on the human subject in the same way it is established on the robotic model (see figure 2).

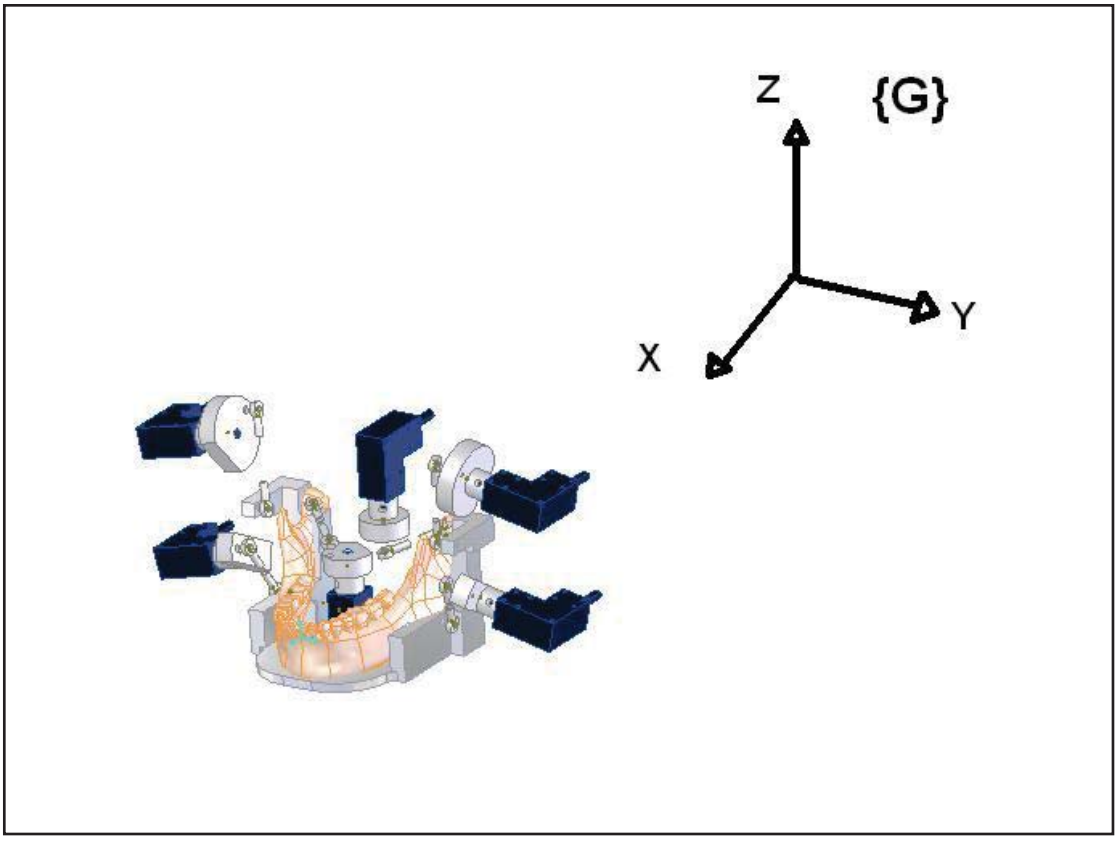

Appendix D Figure 1: Global articulograph reference frame in which the original recordings are made.

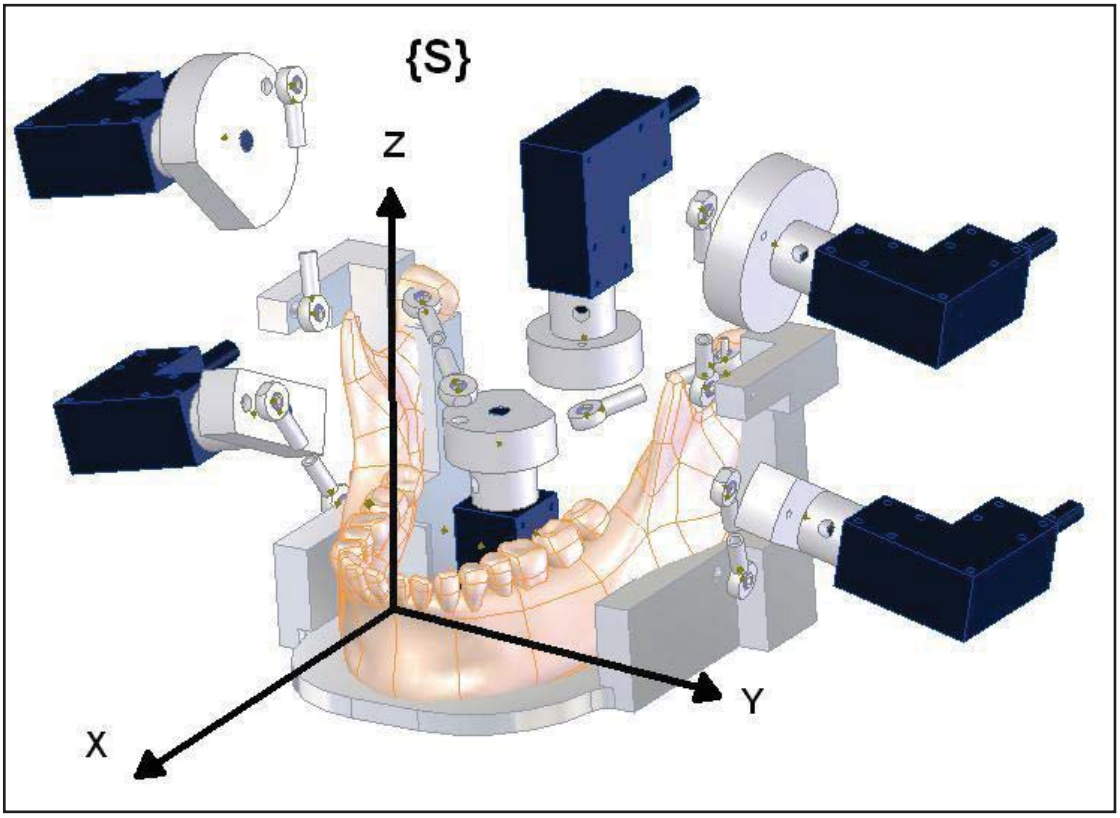

Appendix D Figure 2: Skull frame, set up on lower mandible at jaw closed position.

Objective:

Use the human subject's mandible at fully closed position to establish a 'skull' frame {S} on the human subject that all mandible movements during chewing can be made relative to. The established frame should be created in such a way that it can be accurately reproduced on the robotic model.

Method:

1. **Using the 3 fixed sensors on the teeth to establish {S}.**

The three sensors located at the incisor point, left canine and right canine can be used to define the 3 axes of the skull frame. Vectors pointing from the IP sensor to the sensors located on the left and right canines are used in a cross product to form a

perpendicular vector (Z-axis) pointing 'vertical' to the plane the 3 sensors lie on. The Y-axis is formed by the vector pointing from right canine sensor (subject's point of view) to left canine sensor, with the X-axis being the perpendicular cross product of Y and Z. Appendix C figure 3 below shows how the skull frame is established from the sensor locations.

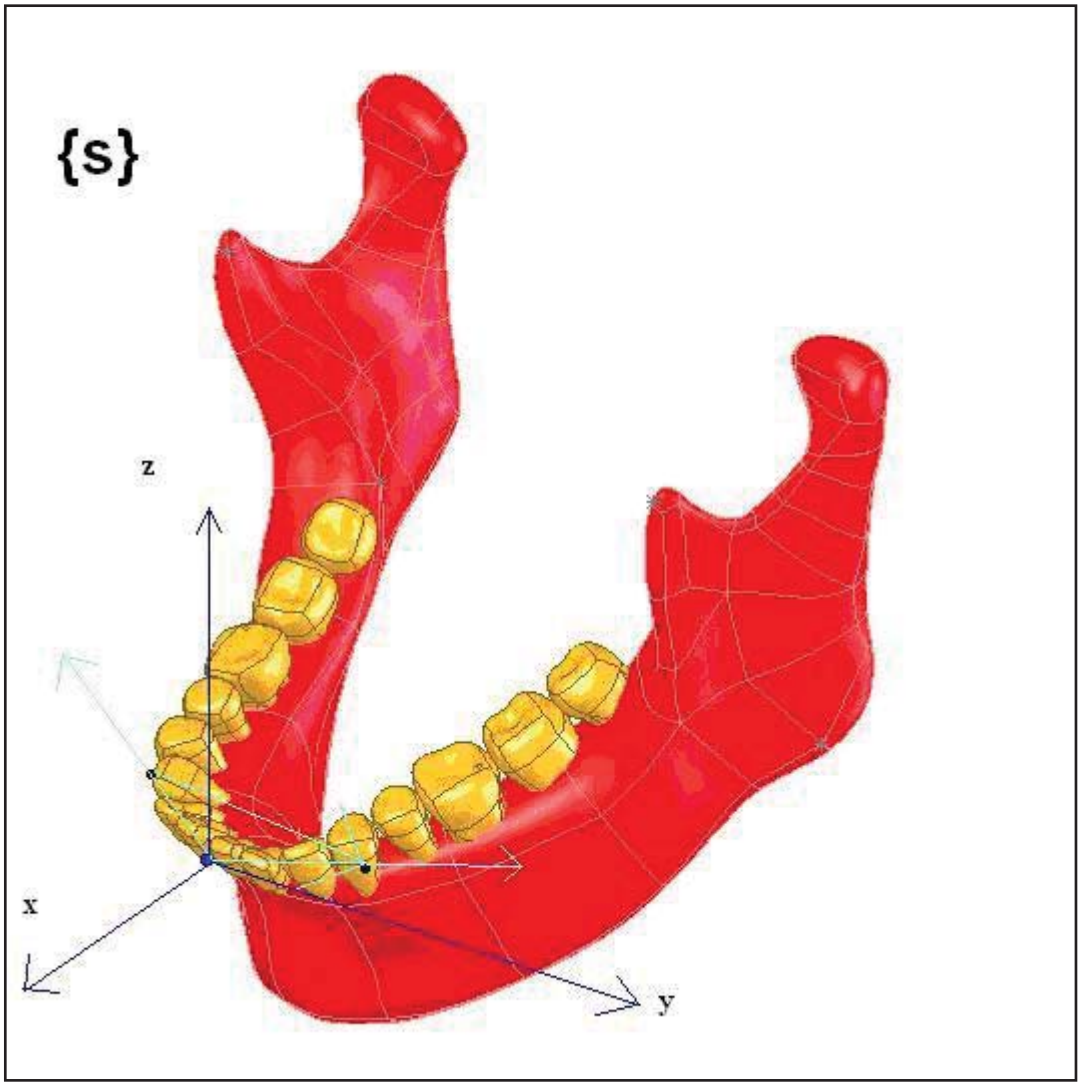

Appendix D Figure 3: Skull frame established from the 3 sensor locations.

The main problem with this method is the established frame will depend on the teeth layout of the subject, and because the robotic jaw uses a different set of teeth it is difficult to accurately re-create the frame on the robotic jaw. Also the exact location of the sensors on each tooth has an influence on the established frame.

Example:

The above method is used to establish the skull frame on the subject for a chewing experiment using Oats, called 'Oats 4'. The subject was ordered to clench their teeth for the first 10 seconds before chewing food so skull frame can be established. The procedure is carried out in matlab and is described below.

1. Raw data from sensors stored in arrays, all head movement removed.
2. Smoothing of all data using Butterworth low pass filter.
3. First 5 seconds of data is averaged so average location of sensors at jaw closed position is now known.
4. The averaged sensor locations at jaw closed position (in the global co-ordinate system) are used to establish the skull frame on the subject:

Incisor sensor, IP =

111.1710

-17.6738

-67.4883

Right canine sensor, RC =

99.7526

-35.2918

-71.3224

Left canine sensor, LC=

102.2087

2.8682

-65.0196

Vector pointing from Incisor to right canine, IP_RC =

RC – IP =

-11.42

-17.62

-3.832

Vector pointing from Incisor to left canine, IP_LC =

LC – IP =

-8.96

20.53

2.46

Vector pointing from right canine to left canine, RC_LC =

LC – RC =

2.52

38.15

6.31

Z-axis = (IP_LC cross IP_RC) / (| IP_LC cross IP_RC |)

= -0.0899

-0.1594

1.0000

Y-axis = RC_LC / | RC_LC |

= 0.0644

1.0000

0.1652

X-axis = y-axis cross z-axis

$$= \begin{matrix} 1.0263 \\ -0.0792 \\ 0.0796 \end{matrix}$$

And our established skull frame becomes:

$$\begin{matrix} 1.0263 & 0.0644 & -0.0899 & 111.1710 \\ -0.0792 & 1.0000 & -0.1594 & -17.6738 \\ 0.0796 & 0.1652 & 1.0000 & -67.4883 \\ 0 & 0 & 0 & 1.0000 \end{matrix}$$

Where the columns represent X, Y, and Z axis respectively. The final column is the translation to the origin of the established skull frame at the IP from the origin of the global articulorgraph frame.

Assuming this frame is coincident to the skull frame on the robotic model, the resultant trajectory is re-created on the robotic model, and is seen in figure 5 below:

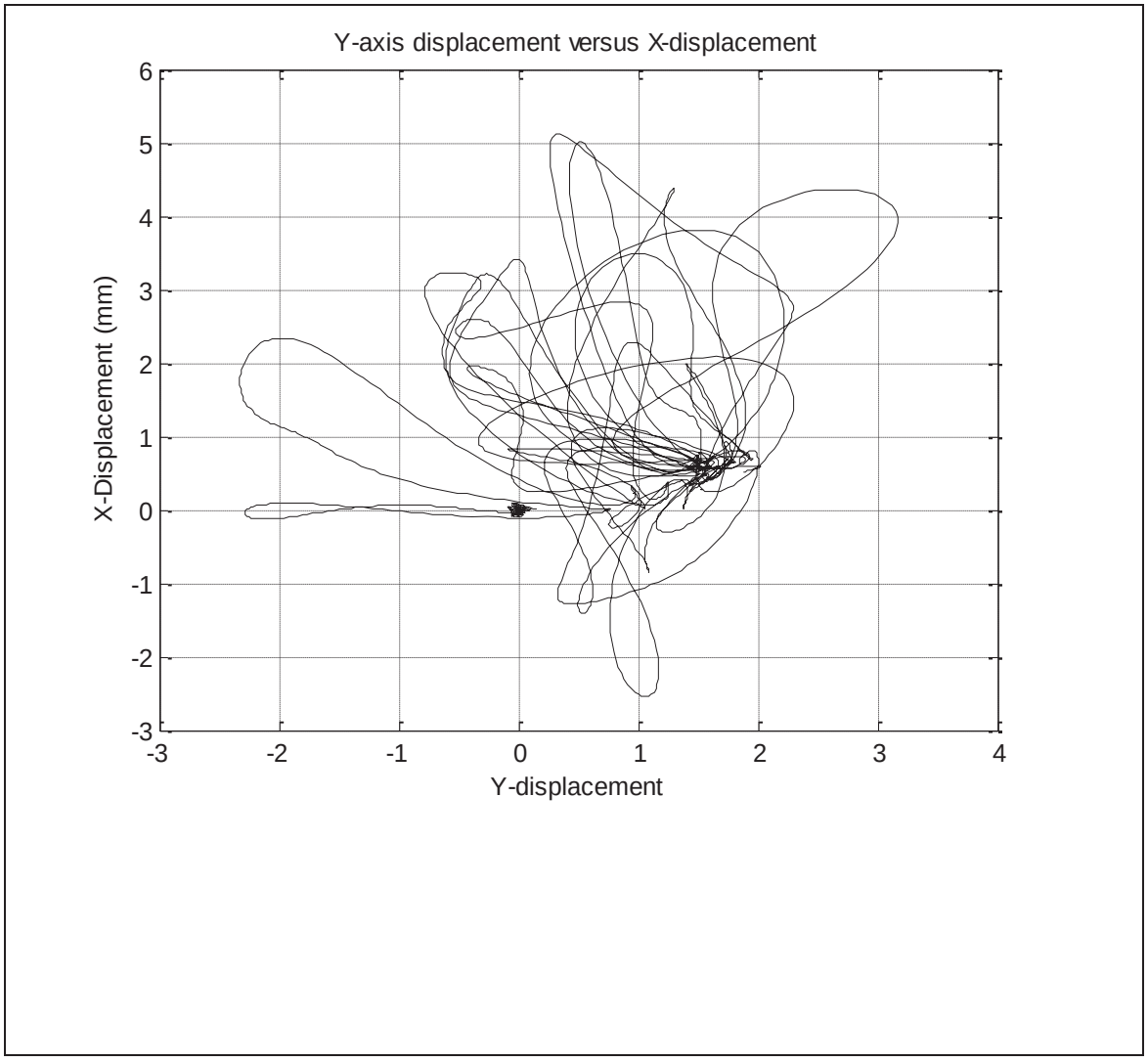
Y-axis displacement versus X-displacement
X-Displacement (mm)
Y-displacement
6
5
4
3
2
1
0
-1
-2
-3
-3
-2
-1
0
1
2
3
4

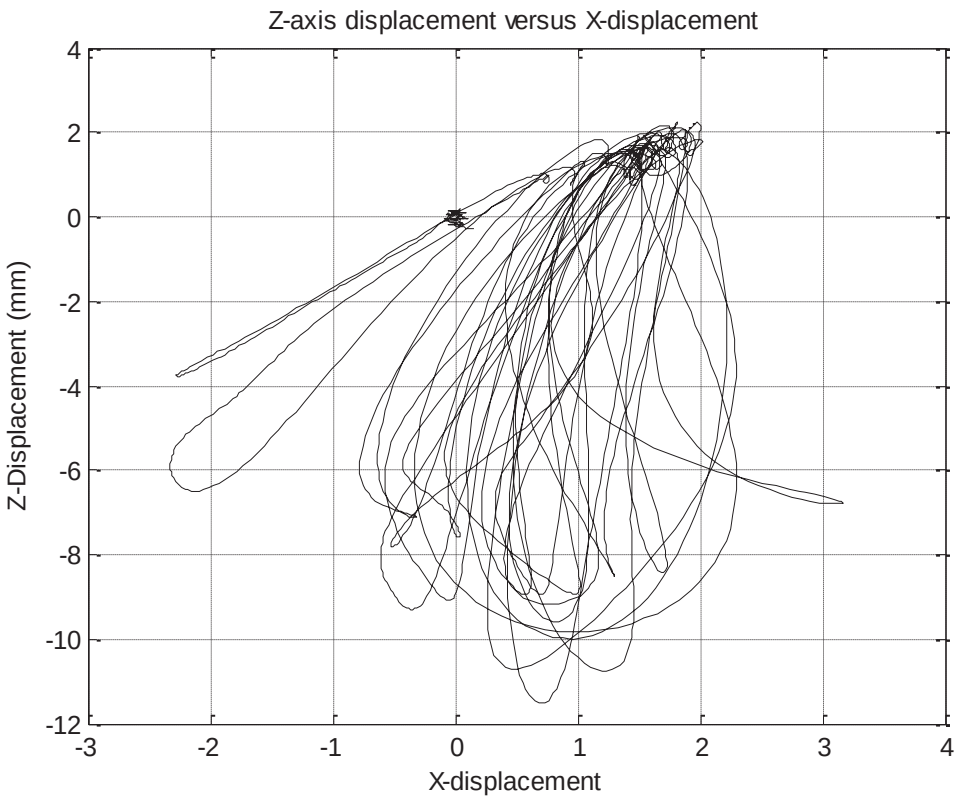
Z-axis displacement versus X-displacement
Z-Displacement (mm)
X-displacement
4
2
0
-2
-4
-6
-8
-10
-12
-3
-2
-1
0
1
2
3
4

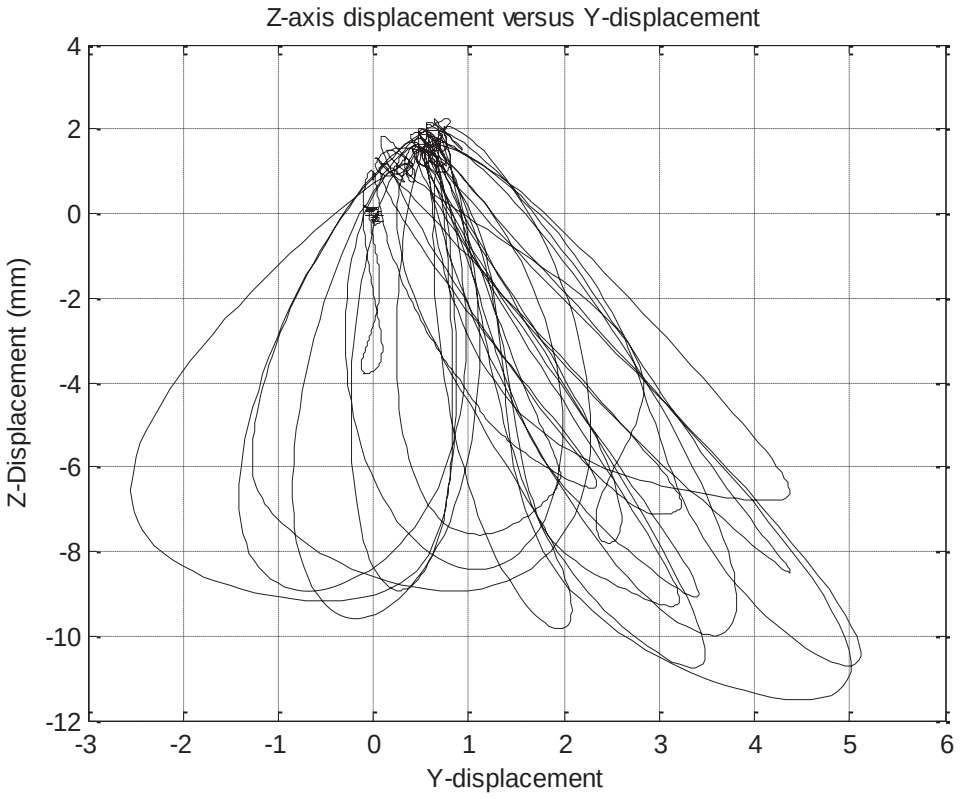
Z-axis displacement versus Y-displacement
Z-Displacement (mm)
Y-displacement
4
2
0
-2
-4
-6
-8
-10
-12
-3
-2
-1
0
1
2
3
4
5
6

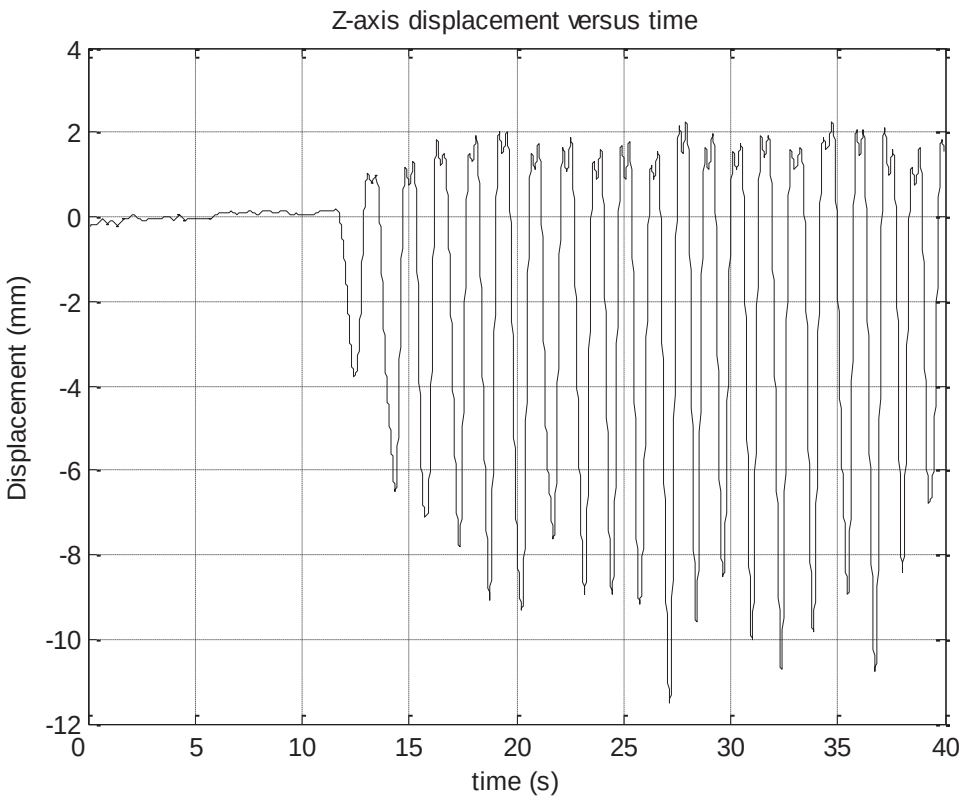
Z-axis displacement versus time
Displacement (mm)
time (s)
4
2
0
-2
-4
-6
-8
-10
-12
0
5
10
15
20
25
30
35
40

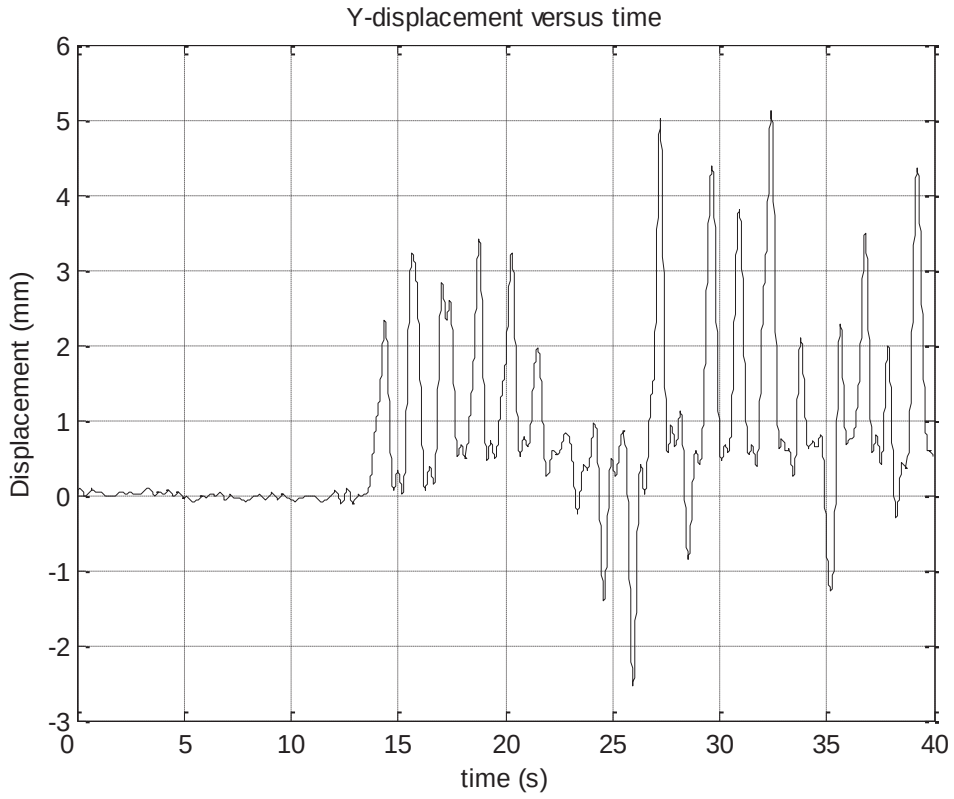
Y-displacement versus time
Displacement (mm)
time (s)
6
5
4
3
2
1
0
-1
-2
-3
0
5
10
15
20
25
30
35
40

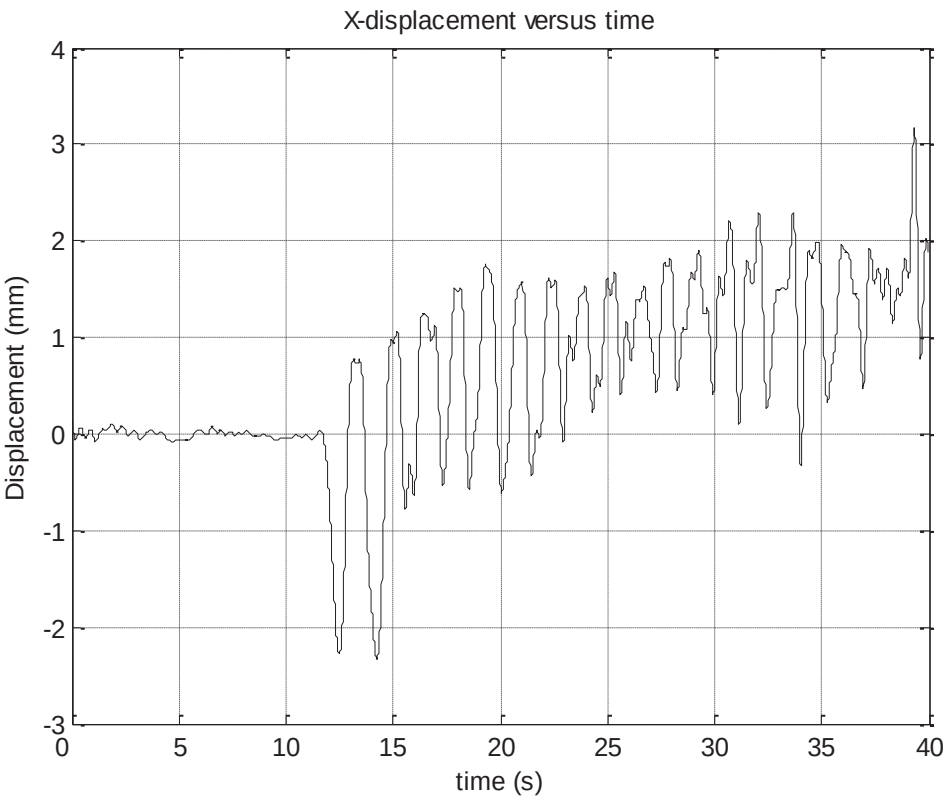
X-displacement versus time
Displacement (mm)
time (s)
4
3
2
1
0
-1
-2
-3
0
5
10
15
20
25
30
35
40

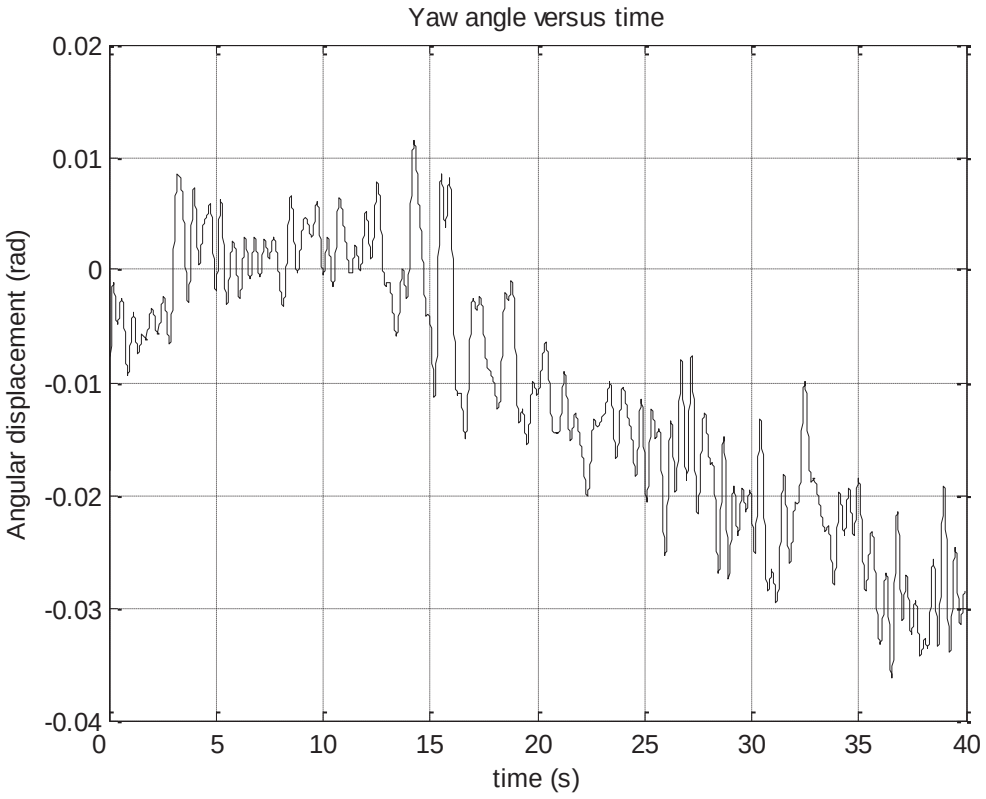
Yaw angle versus time
Angular displacement (rad)
time (s)
0.02
0.01
0
-0.01
-0.02
-0.03
-0.04
0
5
10
15
20
25
30
35
40

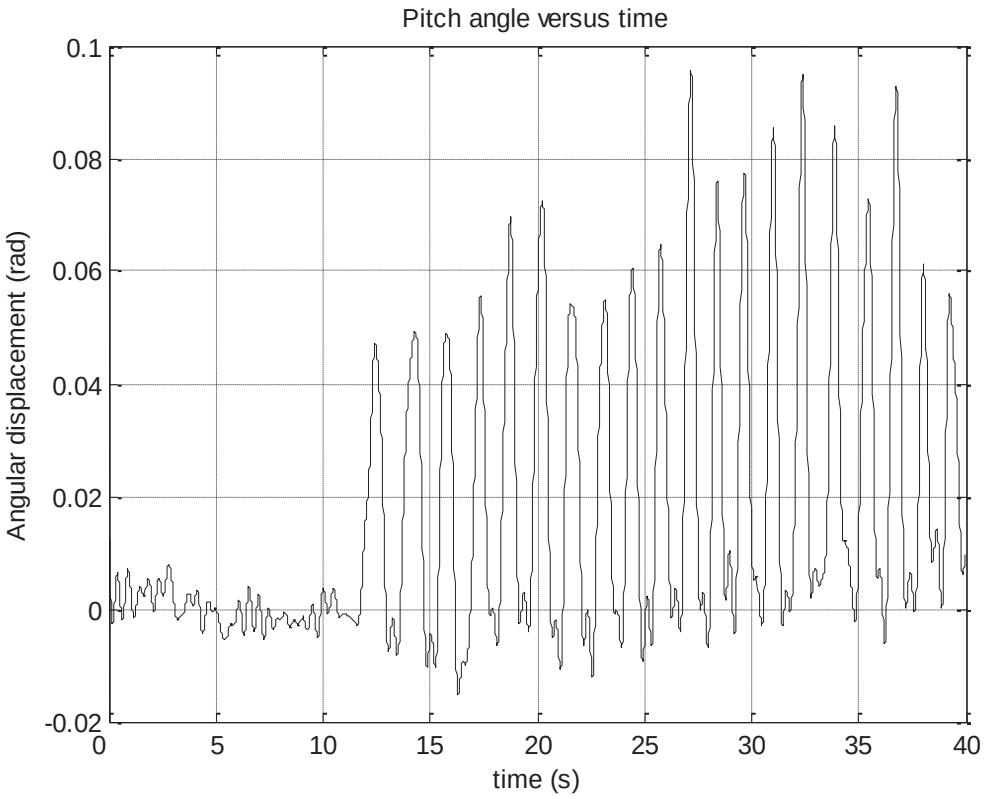

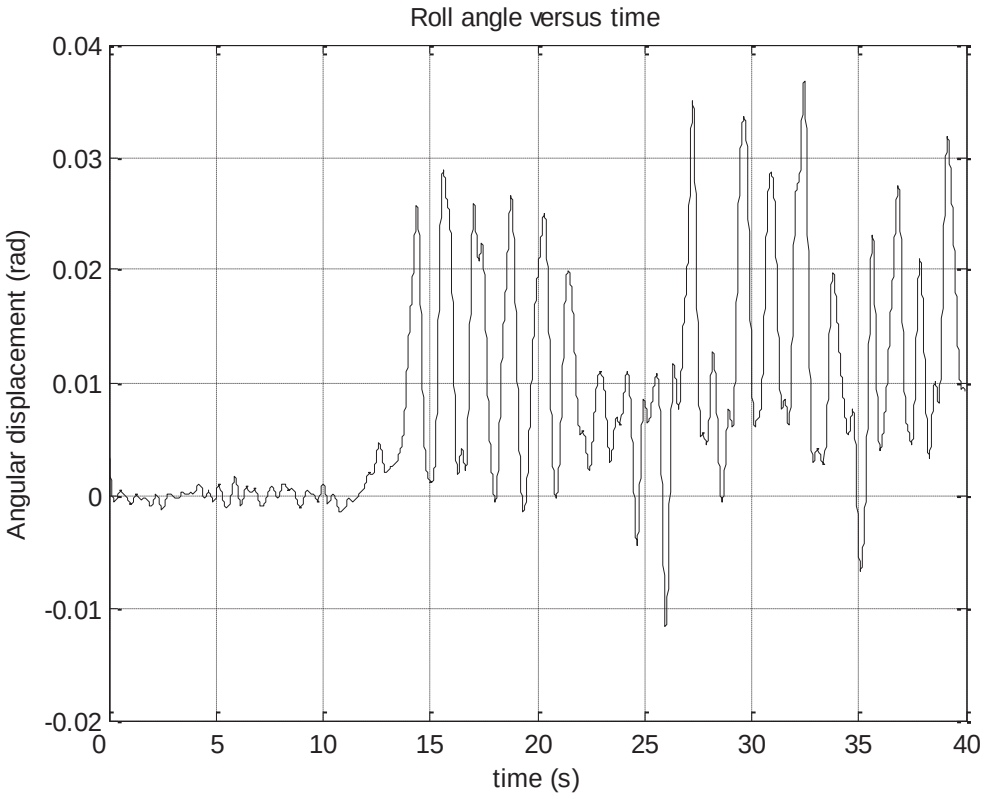

Appendix D Figure 5: Oats 4 trajectory using sensor locations to establish skull frame on subject.

2. Using the subject's molar locations to establish the skull frame {S}.

This method involves taking a trace of the subject's molars prior to running the chewing experiments so that all molar locations are known in a common reference frame. The molar locations are then used to set up the skull frame by averaging vectors pointing between any 3 molars to establish the axes (see figure 4). It is hoped that setting up the frame by averaging several vectors between teeth will allow the differences between robot and subject teeth layouts to be minimized.

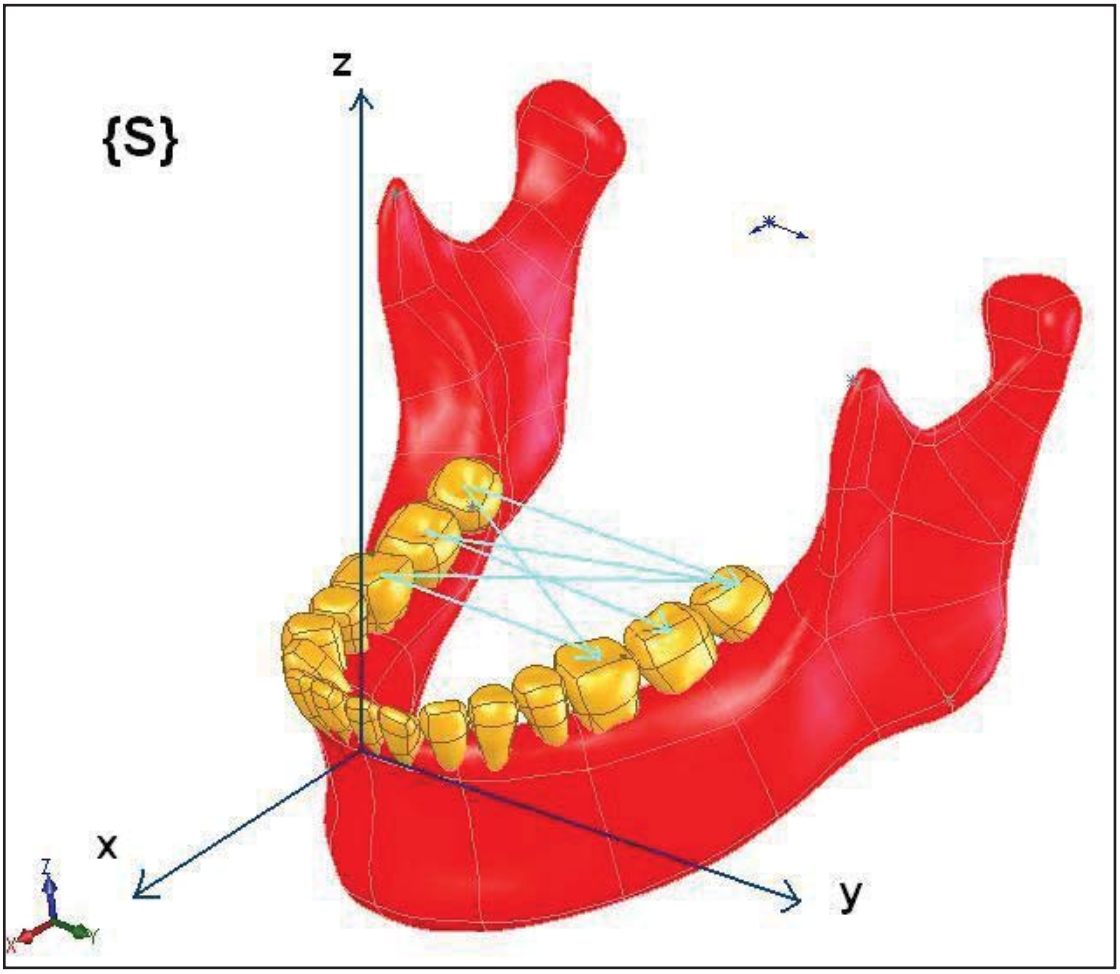

Appendix D Figure 6: Establishing the skull frame on the subject by averaging vectors between subject's molars.

Example:

The same experiment 'Oats 4' is used here, but this time the average of several frames, each using different teeth locations as illustrated in figure 6, are taken as the skull frame.

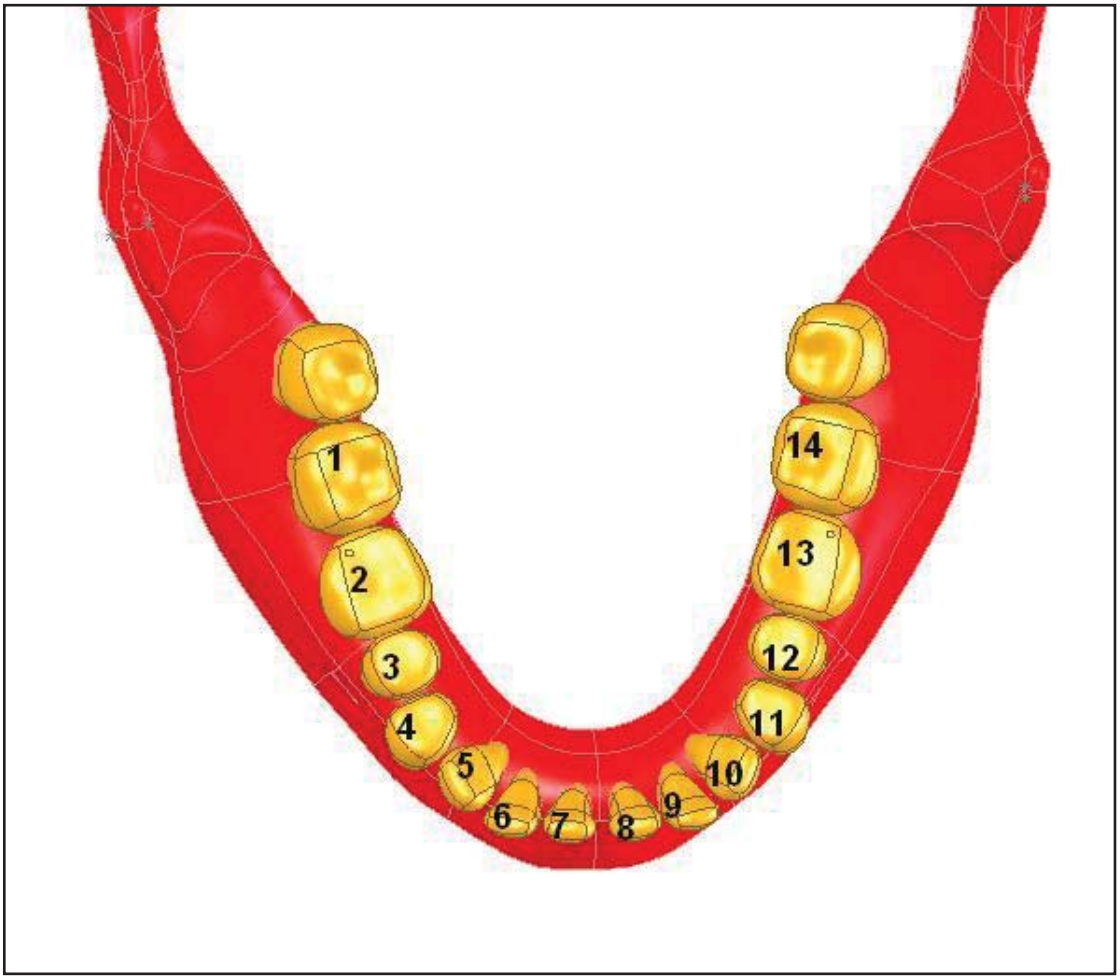

Appendix D Figure 7: Numbering of teeth.

A trace is taken of the subjects teeth by moving a sensor from tooth to tooth to find each tooth location relative to the fixed sensors on the incisor and canines. The trace is used together with the fixed sensors to establish several frames which are then average as described below:

1. For the trace data to be useful we need to calculate the frame established by the fixed sensors as in method 1 for each of the tooth recordings because jaw movement as the trace sensor is moved from tooth to tooth needs to be taken out of consideration.

$$^{Sensor}L1 = {}^{Sensor}_{G}T1 .{}^{G}L1$$
$$^{Sensor}L2 = {}^{Sensor}_{G}T2 .{}^{G}L2$$
$$^{Sensor}L3 = {}^{Sensor}_{G}T3 .{}^{G}L3$$
$$\vdots$$
$$^{Sensor}L14 = {}^{Sensor}_{G}T14 .{}^{G}L14$$

Where L1, L2 … L14 are teeth locations in Global, G, and Sensor reference frames.

${}^{Sensor}_{G}T1$, ${}^{Sensor}_{G}T2$ … ${}^{Sensor}_{G}T14$ are the transformations from the sensor frame fixed on the subjects jaw, and the global articulorgraph frame at each time instance as the trace sensor is moved around the 14 teeth.

The calculated locations of each tooth in the sensor frame are shown in table 1 below:

Tooth	Location in sensor frame [X] [Y] [Z] (mm)
L1	-42.2810 -22.0380 10.9626
L2	-31.4253

	-19.1779 11.2562
L3	-20.5722 -20.5336 10.6057
L4	-15.5195 -16.3813 8.2370
L5	-6.1652 -14.1856 11.8136
L6	-3.1614 -8.6114 10.6408
L7	-0.5138 -5.4075 9.4969
L8	0.1270

	-0.6320 8.7663
L9	-3.4837 9.2577 10.3546
L10	-7.3026 13.1425 11.0718
L11	-15.7363 18.5827 10.0475
L12	-20.7976 17.3734 10.1211
L13	-30.2218 21.7238 10.7722
L14	-41.3182

	30.4815 30.4594

Appendix D figure 8 shows the teeth locations visualised in a 3D plot. Point 14 is omitted from the plot and is not used in any calculation because it appears as an outlier, probably due to an error in the measurement process.

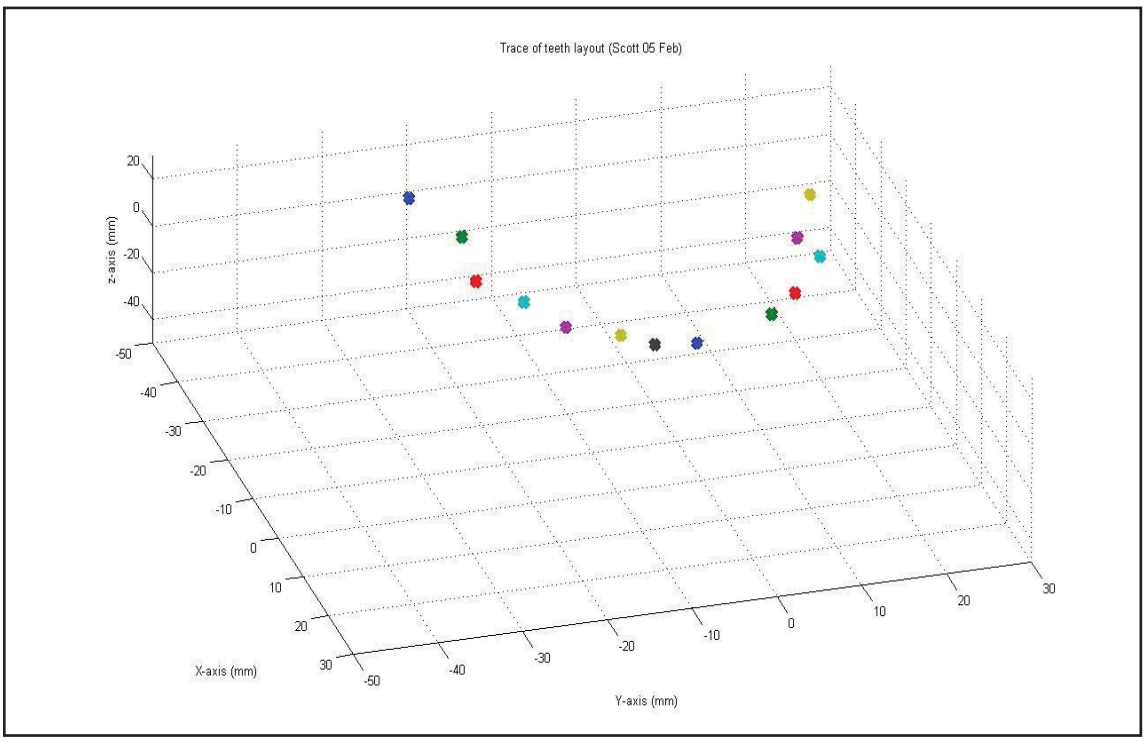

Appendix D Figure 8: Teeth locations in the 'sensor' reference frame.

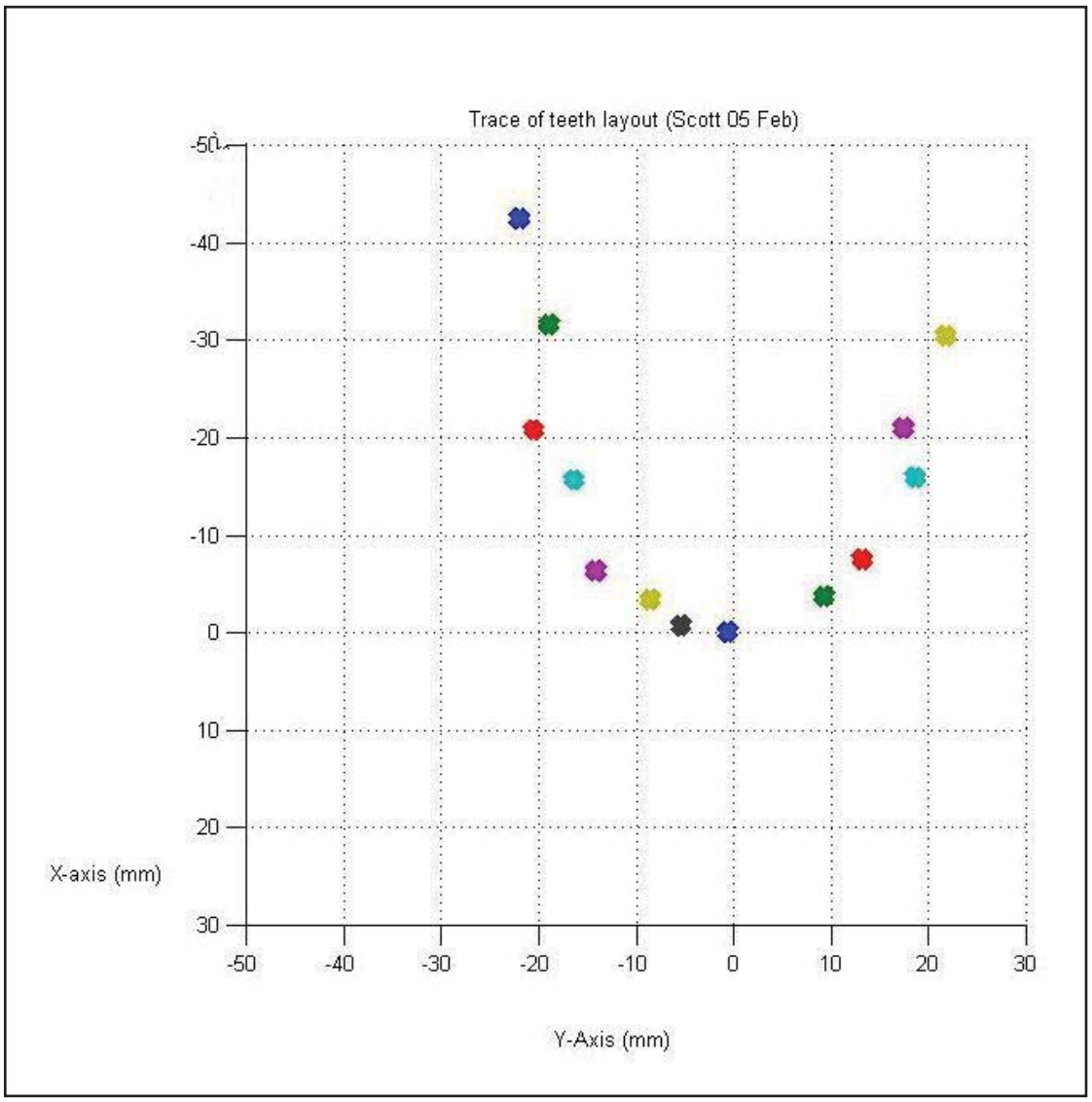

Appendix D Figure 9: Top view of 'trace' of teeth.

The plot of the top view of the teeth locations show fairly good alignment of the Y and X-axes of the ideal skull frame where the head faces directly 'forward', and the X and Y-axes of the frame established from the sensors.

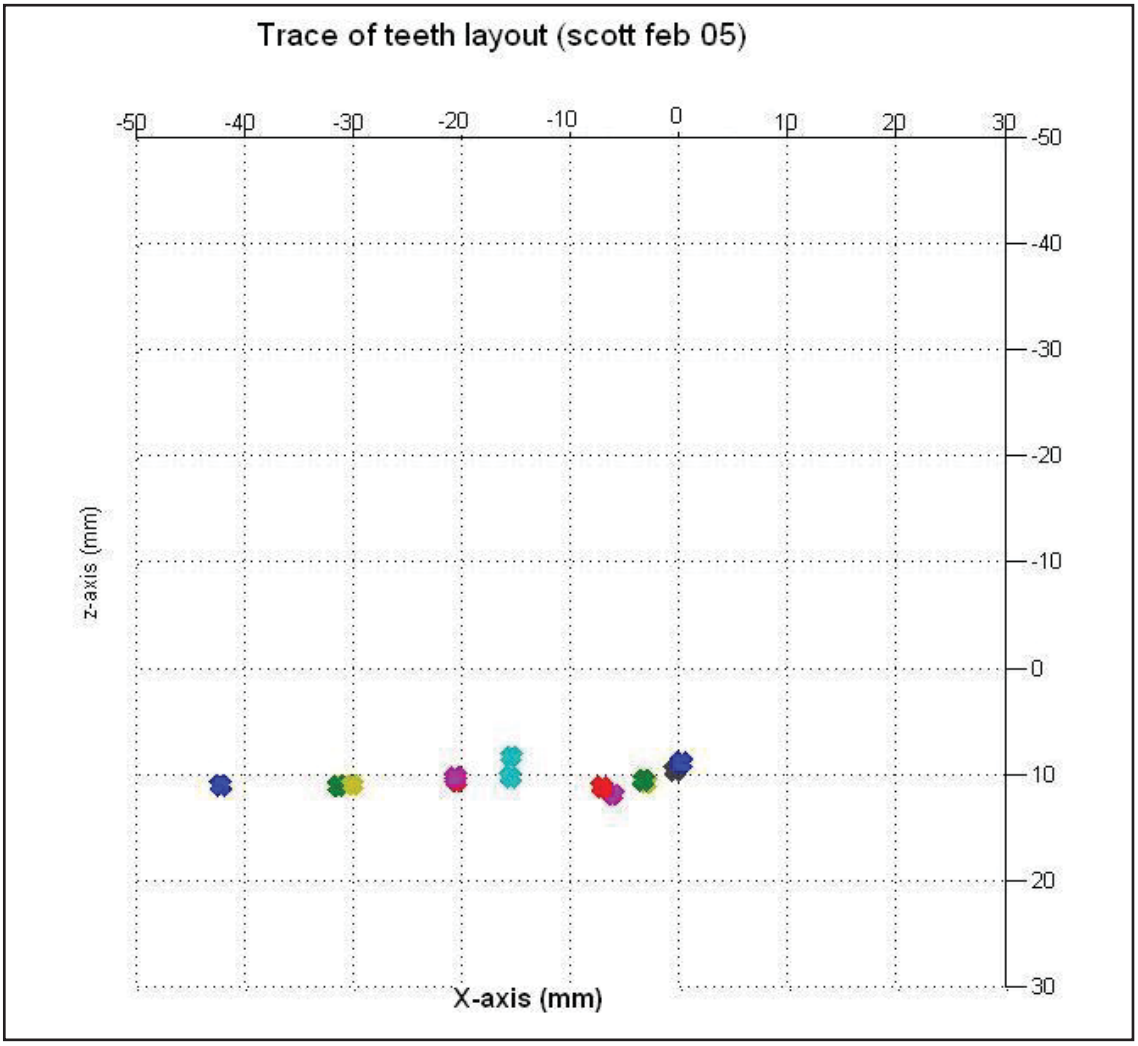

Appendix D Figure 10: Side view of teeth layout.

It can be seen that the frame established by the 3 fixed sensors gives a fairly good result if our aim was to define a plane parallel to the plane the teeth lie on. In this case it is unlikely that the averaging of vectors will cause a 'skull' frame that differs from the 'sensor' frame by any great degree.

2. The teeth locations are used to form vectors defining the Y-axis and horizontal plane. A number of Y-axis's and horizontal planes (Z-axis) are formed and the average taken. The X-axis is a cross product of the averaged Z and Y axes.

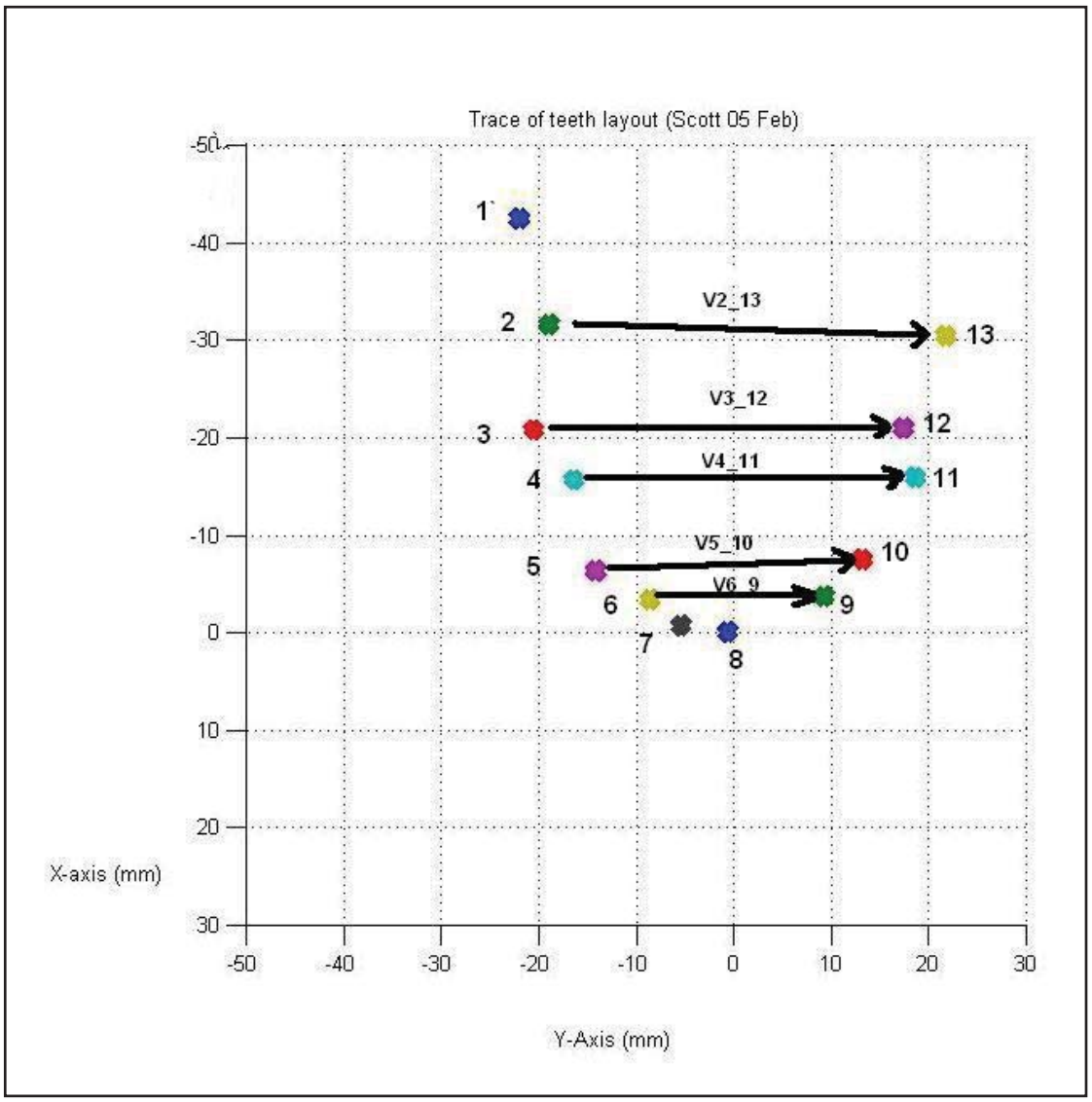

Appendix D Figure 11: Multiple vectors for establishing the Y-axis of the skull frame.

The skull frame's Y-axis is found:

Average vector = (V2_12 + V3_12 + V4_11 + V5_10 + V6 _9) / 5

1.2035

40.9018

-0.4840

+

-0.2253

37.9070

-0.4846

+

-0.2168

34.9640

1.8104

+

-1.1374

27.3281

-0.7418

+

-0.3223

17.8691

-0.2862

_____ ____

5

=

-0.1397

31.7940

-0.0373

Y-axis = Average vector / | Average vector|

= -0.0044

1.0000

-0.0012

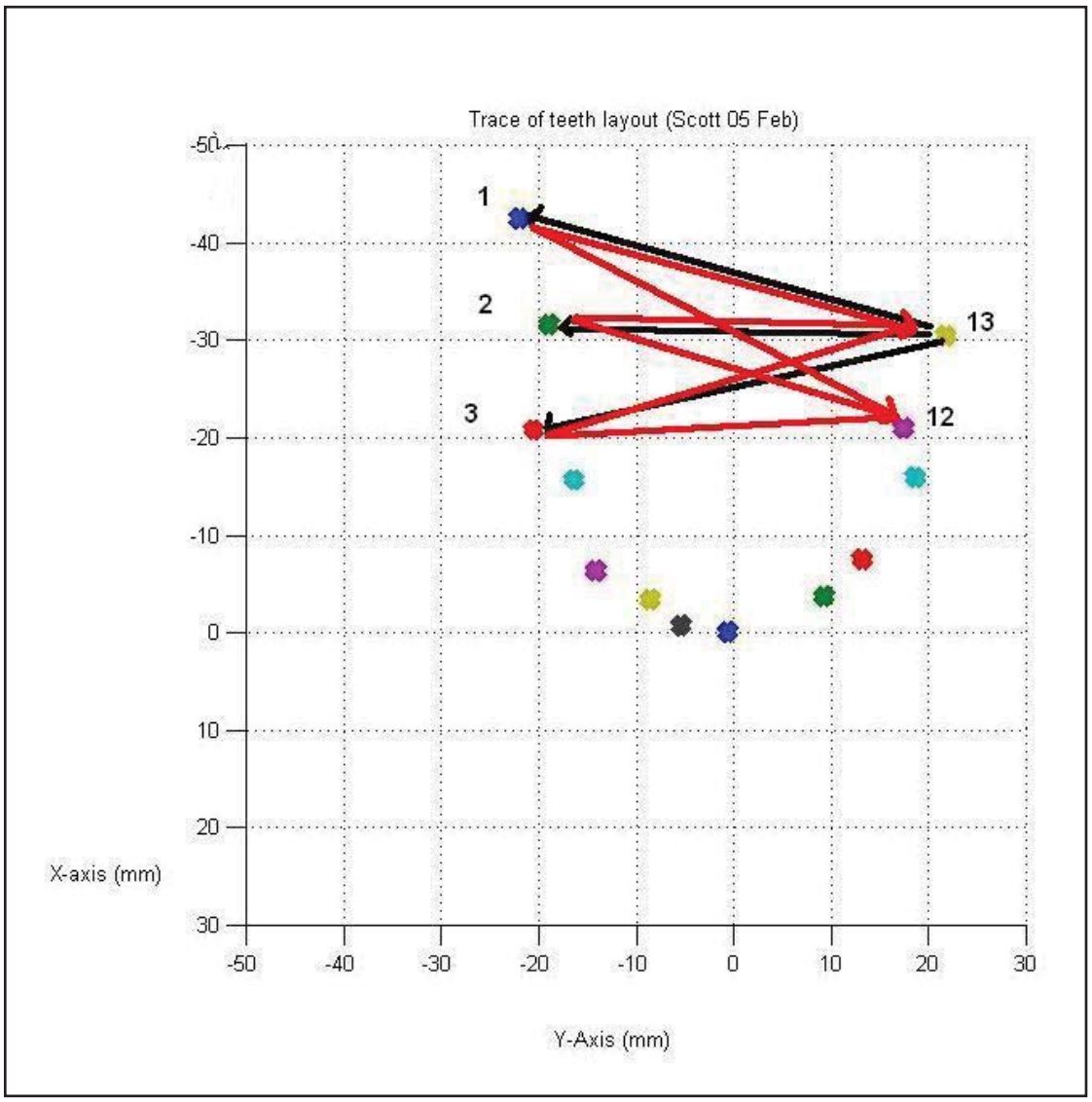

Appendix D Figure 12: Multiple intersecting vectors for establishing the Z-axis of the Skull frame.

Appendix C figure 12 shows how vectors are used to establish five Z-axes by taking the cross product of two intersection vectors between the rear 5 teeth. The 5 axes are averaged to form the skull frames Z-axis which will be normal to a plane that is a 'best fit' for the rear 5 teeth. The calculation is:

z-axis1 = (V1_12 cross V1_13) / | (V1_12 cross V1_13) |

= 0.0631

-0.0130

1.0000

z-axis2 = (V2_12 cross V2_13) / | (V2_12 cross V2_13) |

= 0.0735

0.0097

1.0000

z-axis3 = (V3_12 cross V3_13) / | (V3_12 cross V3_13) |

= 0.0752

0.0132

1.0000

z-axis4 = (V13_1 cross V13_2) / | (V13_1 cross V13_2) |

= -0.0304

0.0127

1.0000

z-axis5 = (V13_1 cross V13_3) / | (V13_1 cross V13_3) |

= 0.0165

-0.0002

1.0000

Skull Frame Z-axis = (z-axis1+z-axis2+z-axis3+z-axis4+z-axis5) / 5

= 0.0396

0.0045

1.0000

The Skull frame X-axis is now calculated from the Y and Z:

Skull frame X-axis = Y-axis cross Z-axis

= 1.0000

0.0044

-0.0396

So the final Skull frame can now be written as a transformation from the 'sensor' frame as:

$$ {}^{Sensor}_{Skull}T = \begin{bmatrix} 1 & -0.0044 & 0.0396 & 0 \\ 0.0044 & 1 & 0.0045 & 0 \\ -0.0396 & 0.0012 & 1 & 0 \\ 0 & 0 & 0 & 1 \end{bmatrix} $$

Here I have used the same point of origin for both sensor and skull frames. The roll-pitch-yaw angles respectively are -0.068, 2.27, 0.246 degrees, showing that the final established Skull frame is fairly closely aligned to the Sensor frame.

3. First 5 seconds of trajectory averaged and sensor frame ${}^{Sensor}_{G}T$ calculated as in method 1.

4. Final Skull frame calculated:

$${}^{Skull}_{G}T = {}^{Sensor}_{Skull}T^{-1} \cdot {}^{Sensor}_{G}T$$

$$= \begin{matrix} 1.0212 & 0.0621 & -0.1300 & 113.5876 \\ -0.0841 & 0.9990 & -0.1633 & -17.8787 \\ 0.1199 & 0.1689 & 0.9947 & -63.0117 \\ 0 & 0 & 0 & 1.0000 \end{matrix}$$

Compared to frame established solely by the 3 fixed sensors:

$$\begin{matrix} 1.0263 & 0.0644 & -0.0899 & 111.1710 \\ -0.0792 & 1.0000 & -0.1594 & -17.6738 \\ 0.0796 & 0.1652 & 1.0000 & -67.4883 \\ 0 & 0 & 0 & 1.0000 \end{matrix}$$

The trajectories created using this method for establishing the skull frame are shown below:

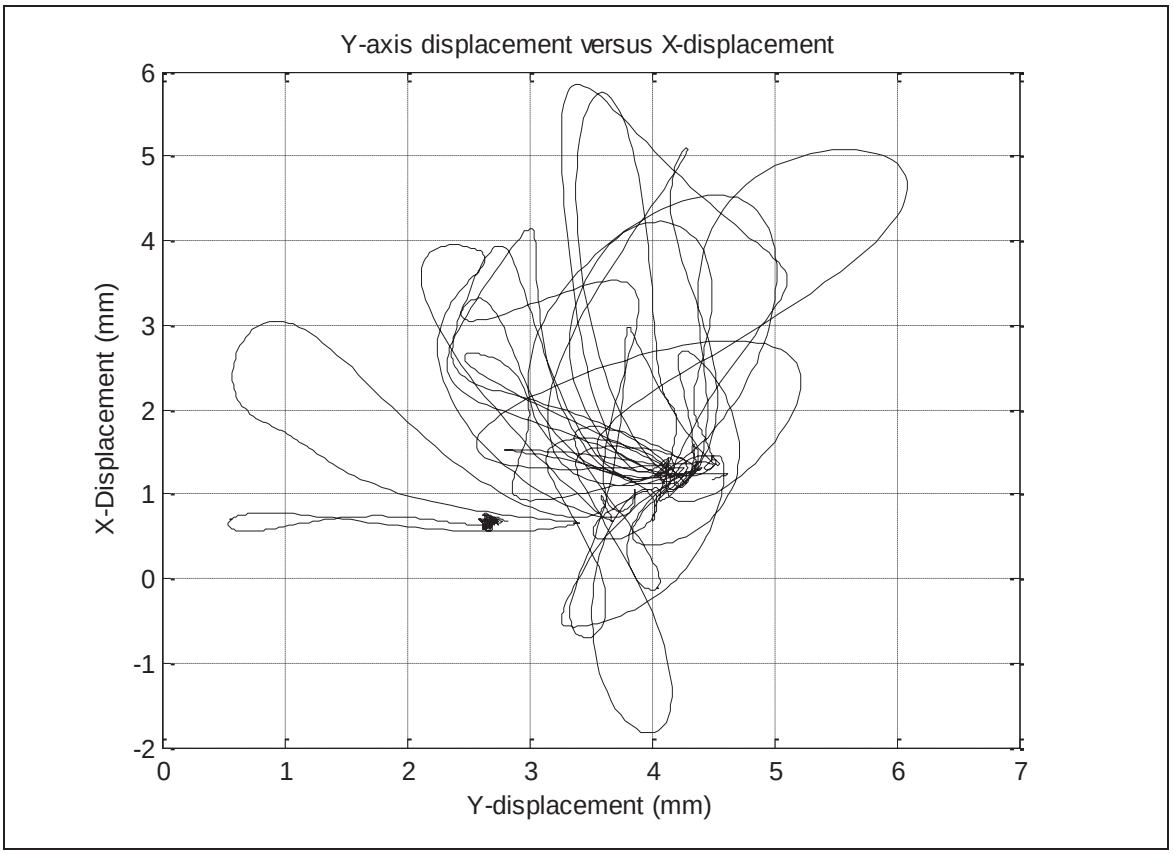

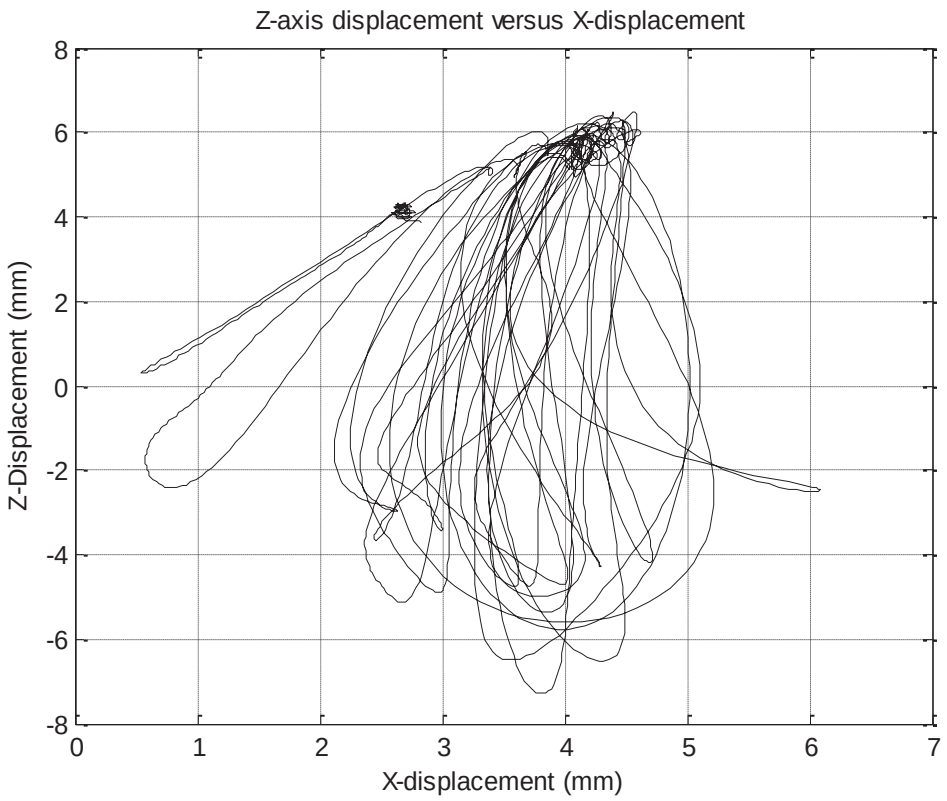
Z-axis displacement versus X-displacement
Z-Displacement (mm)
X-displacement (mm)
8
6
4
2
0
-2
-4
-6
-8
0
1
2
3
4
5
6
7

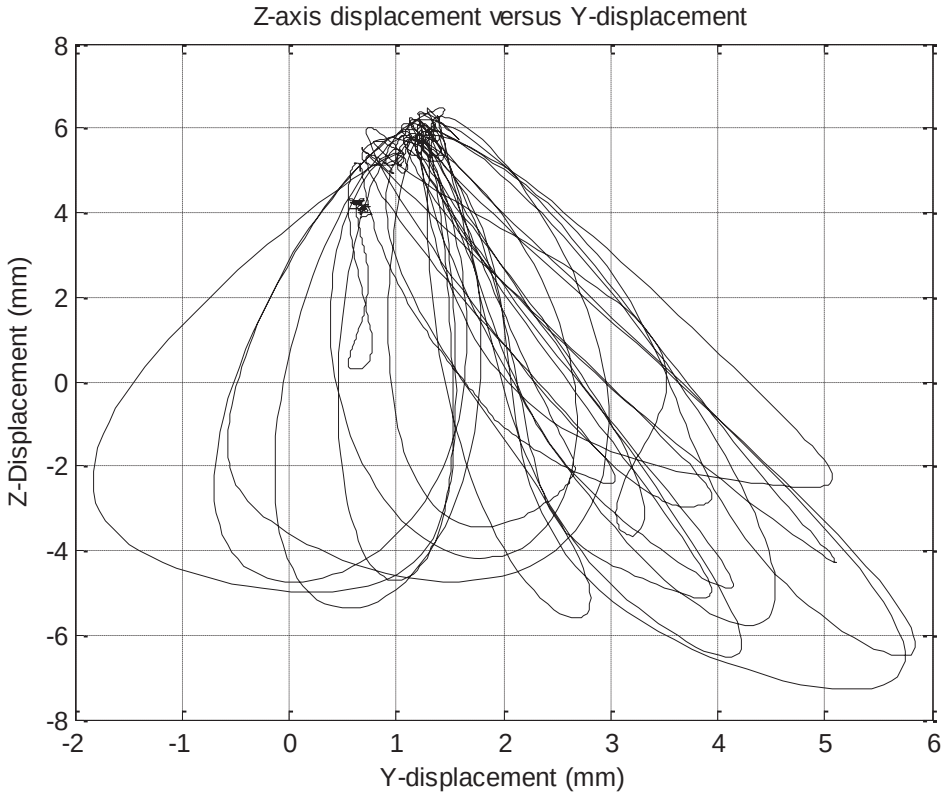
Z-axis displacement versus Y-displacement
Z-Displacement (mm)
Y-displacement (mm)
8
6
4
2
0
-2
-4
-6
-8
-2
-1
0
1
2
3
4
5
6

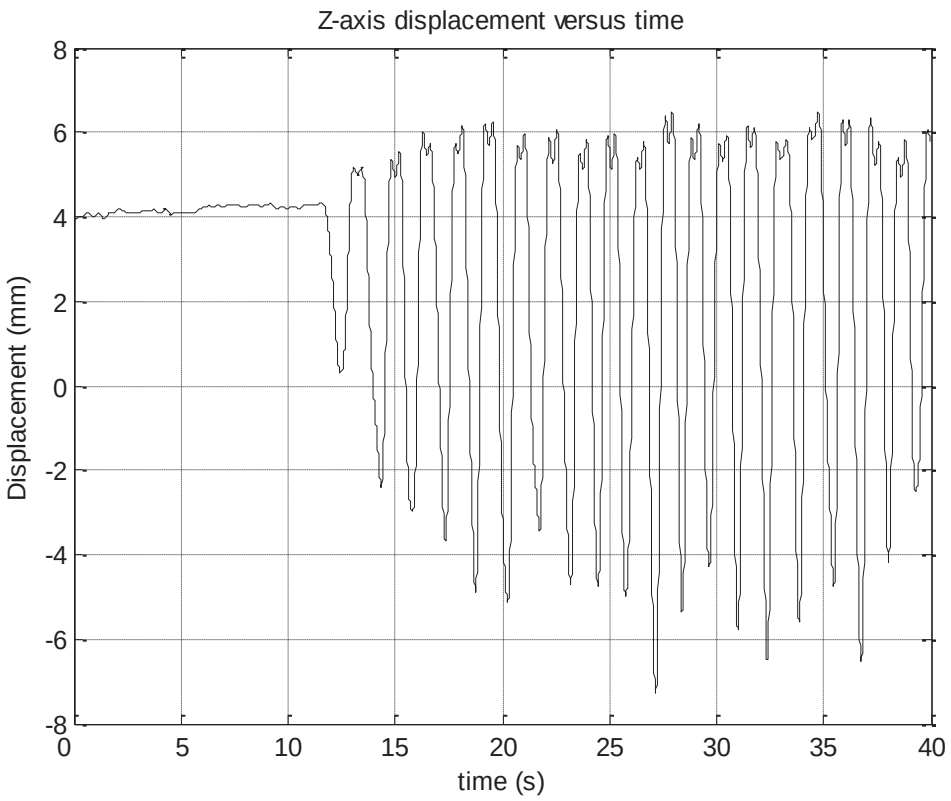
Z-axis displacement versus time
Displacement (mm)
time (s)
8
6
4
2
0
-2
-4
-6
-8
0
5
10
15
20
25
30
35
40

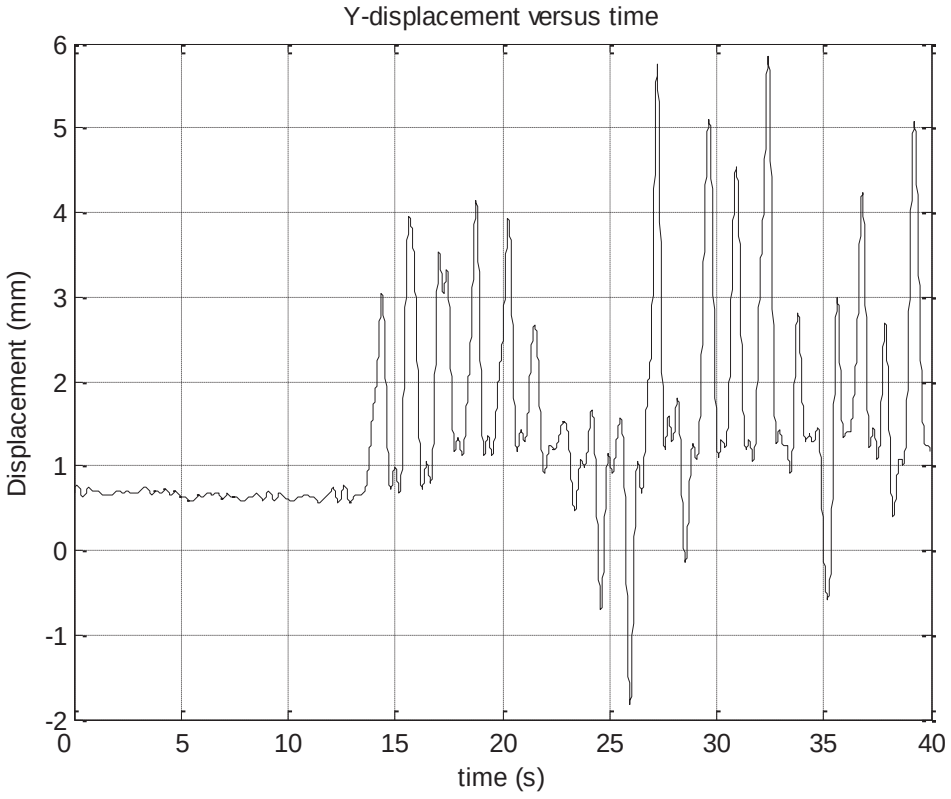
Y-displacement versus time
Displacement (mm)
time (s)
6
5
4
3
2
1
0
-1
-2
0
5
10
15
20
25
30
35
40

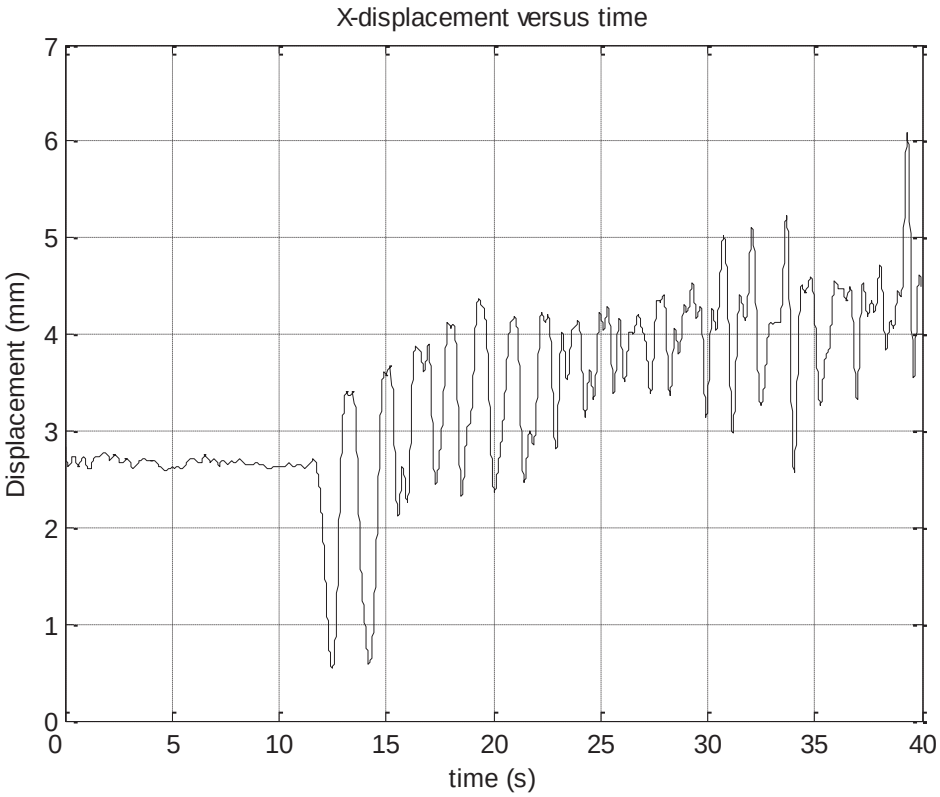
X-displacement versus time
Displacement (mm)
time (s)
0
1
2
3
4
5
6
7
0
5
10
15
20
25
30
35
40

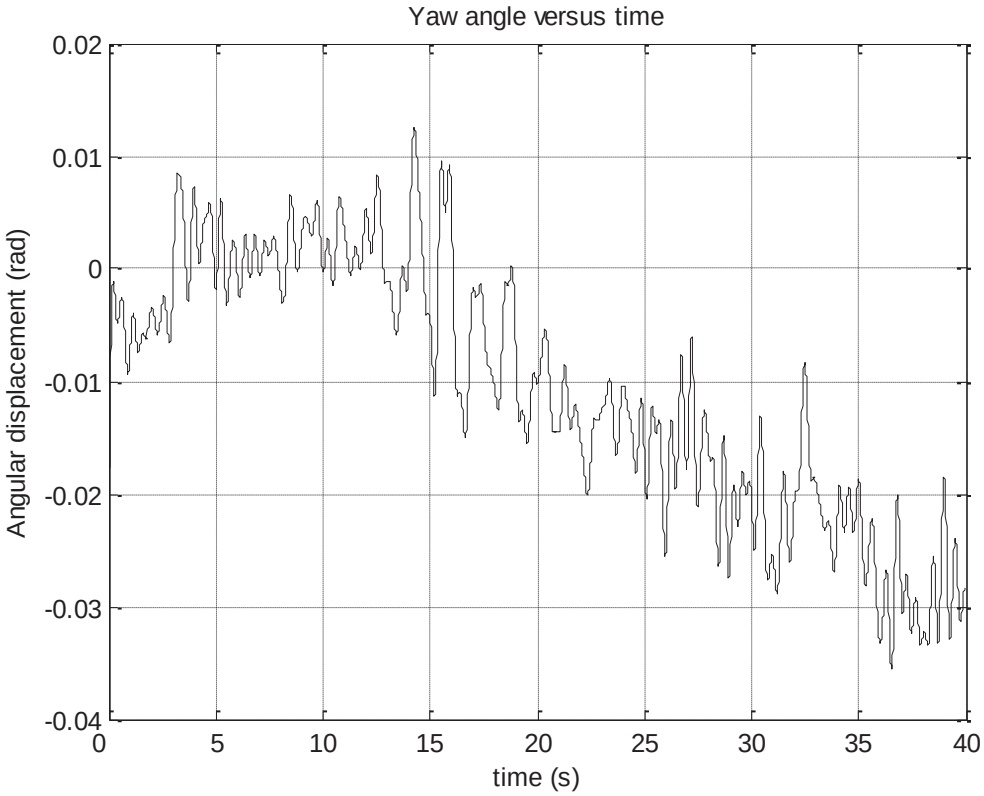
Yaw angle versus time
Angular displacement (rad)
time (s)
0.02
0.01
0
-0.01
-0.02
-0.03
-0.04
0
5
10
15
20
25
30
35
40

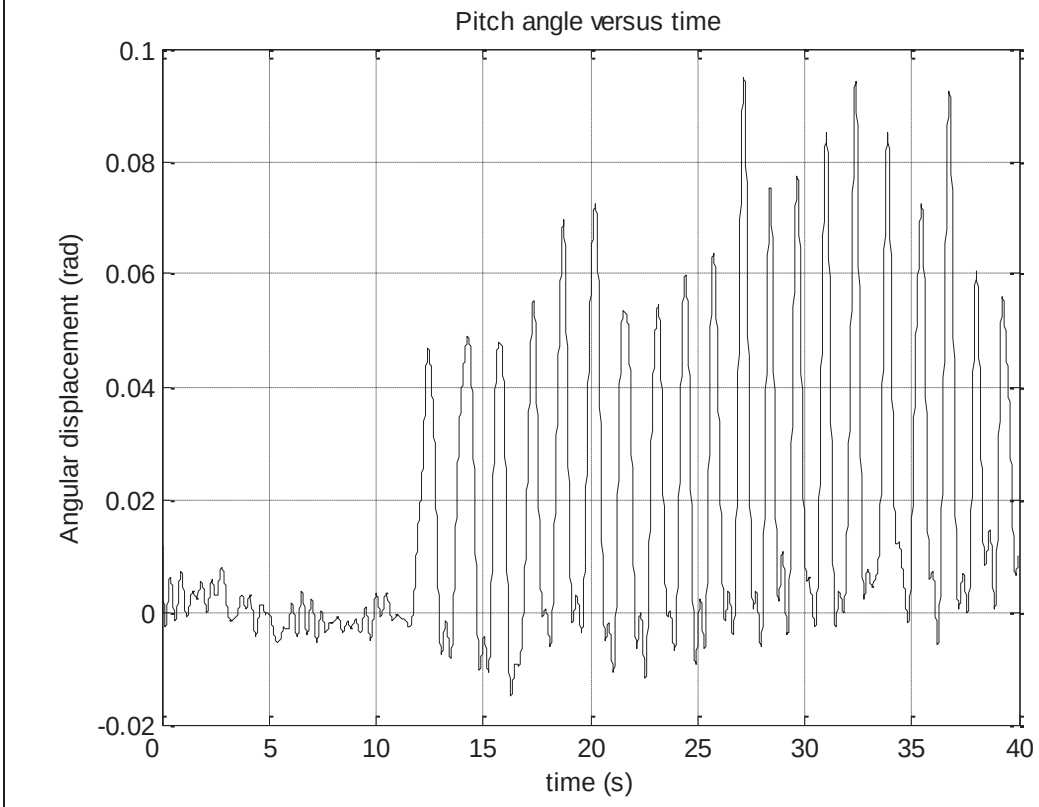
Pitch angle versus time
Angular displacement (rad)
time (s)
0.1
0.08
0.06
0.04
0.02
0
-0.02
0
5
10
15
20
25
30
35
40

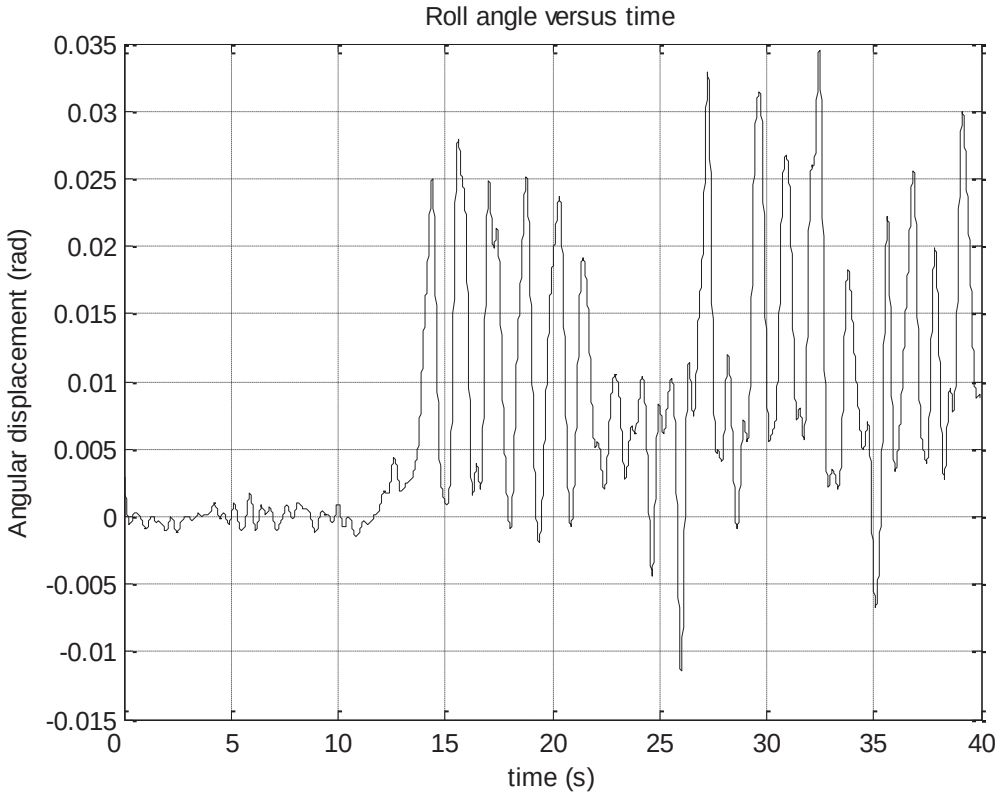
Roll angle versus time
Angular displacement (rad)
time (s)
0.035
0.03
0.025
0.02
0.015
0.01
0.005
0
-0.005
-0.01
-0.015
0
5
10
15
20
25
30
35
40

Appendix D Figure 13: Trajectories relative to skull frame set up from teeth locations.

It can be seen that there is now an offset of around 4mm in the positive z direction.

3. **Using a mould of subject teeth for use on the robotic jaw.**

This is the only way to ensure the reference frame established on the subject aligns with that used when reproducing the trajectory on the robotic jaw.

For this method a mould needs to be taken of the subject's teeth, the mould is then imported into Solidworks and incorporated into the physical robot to be used for reproducing this subject's chewing patterns. Exact locations of the 3 sensors on the subjects teeth much be known so that these points can be re-created on the Solidworks model of the subjects teeth. The accuracy of the produced skull frame in the Solidworks model is limited only by how accurately the locations of the sensors can be placed on the Solidworks model of the teeth.

To help improve accuracy the registration of points on all teeth can be achieved using the trace technique on the subject's teeth and these points placed on the solidworks model of the teeth also. On both the subject and Solidworks model, the averaging of vectors between the registered points will ensure a skull frame that is common to both subject and robotic model.

APPENDIX E: AG500 RECORDING ANALYSIS

1. Accuracy of raw data (both before and after head movement correction)

- Quoted accuracy in manual is 0.5mm.
- Several factors are mentioned which can influence accuracy.
- Actual accuracy of raw data is unknown.

Objective:

Find accuracy of recorded jaw motions in the AG500, and the effect if any of head movement correction on this accuracy. If error is proportional to degree of movement estimate a percentage error to be used with the recorded data.

Method:

Use a random selection of trials from each of Oliver, Mike, and Peter and measure distances between the sensors on teeth and between sensors on head. Ideally the distances between sensors located on the teeth should remain fixed during the chewing trial, as should the sensors located on the head. Any differences in distances can be attributed to measurement error, either systematic or random.

Results:

- OLIVERS TRIALS:

Oliver used 3 head sensors and 3 teeth sensors for these recordings. The trials analysed were of chews on a piece of rubber. They were conducted with the lights off.

Trial16

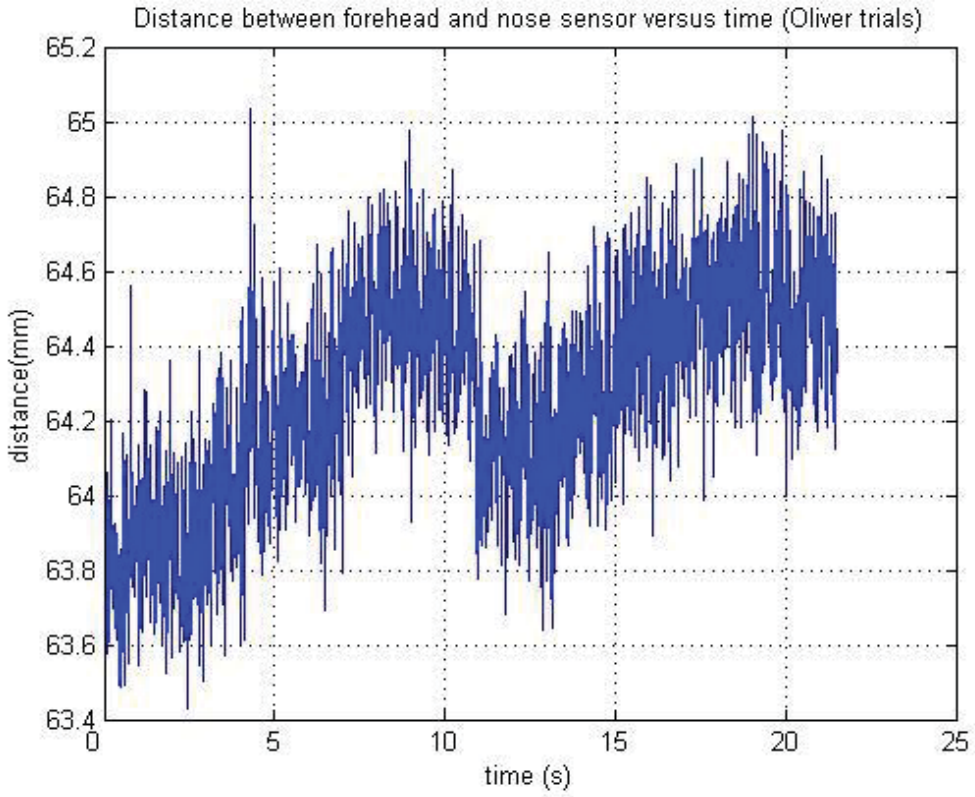

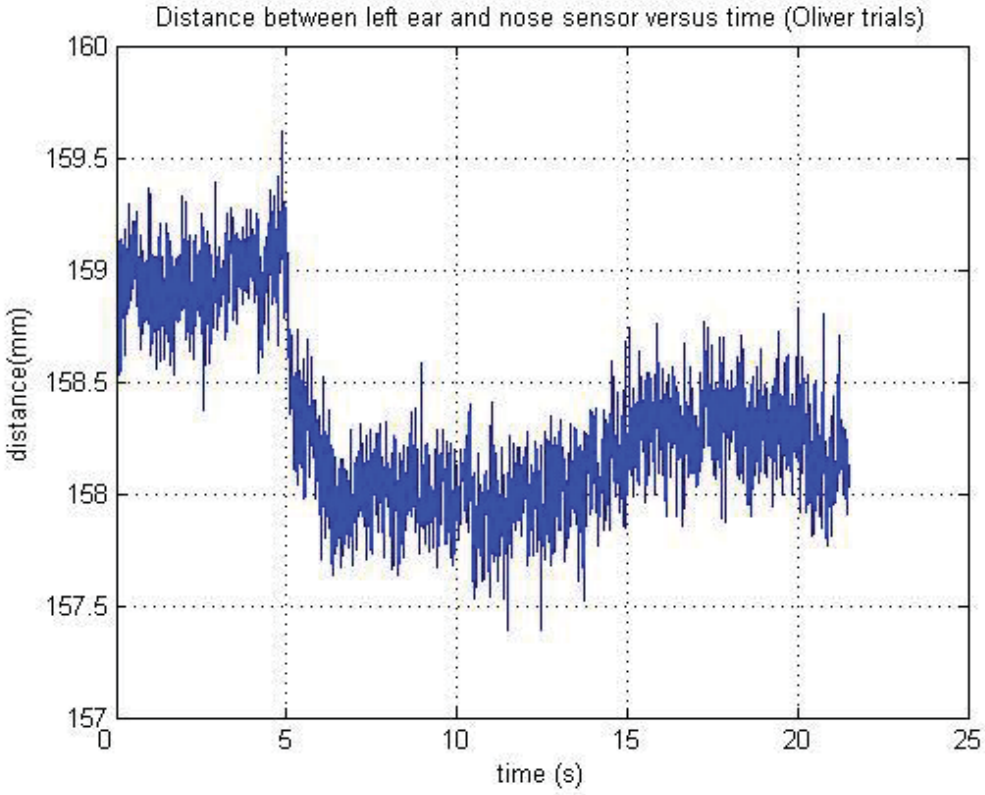
Distance between left ear and nose sensor versus time (Oliver trials)
distance(mm)
time (s)
160
159.5
159
158.5
158
157.5
157
0
5
10
15
20
25

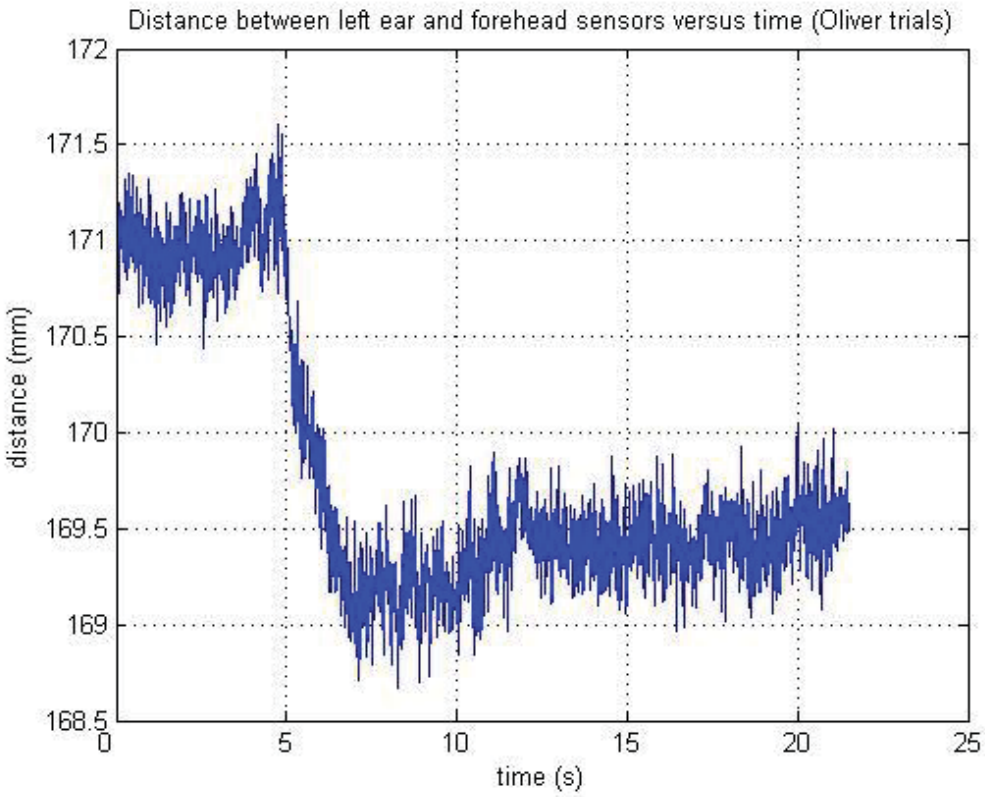
Distance between left ear and forehead sensors versus time (Oliver trials)
distance (mm)
time (s)
172
171.5
171
170.5
170
169.5
169
168.5
0
5
10
15
20
25

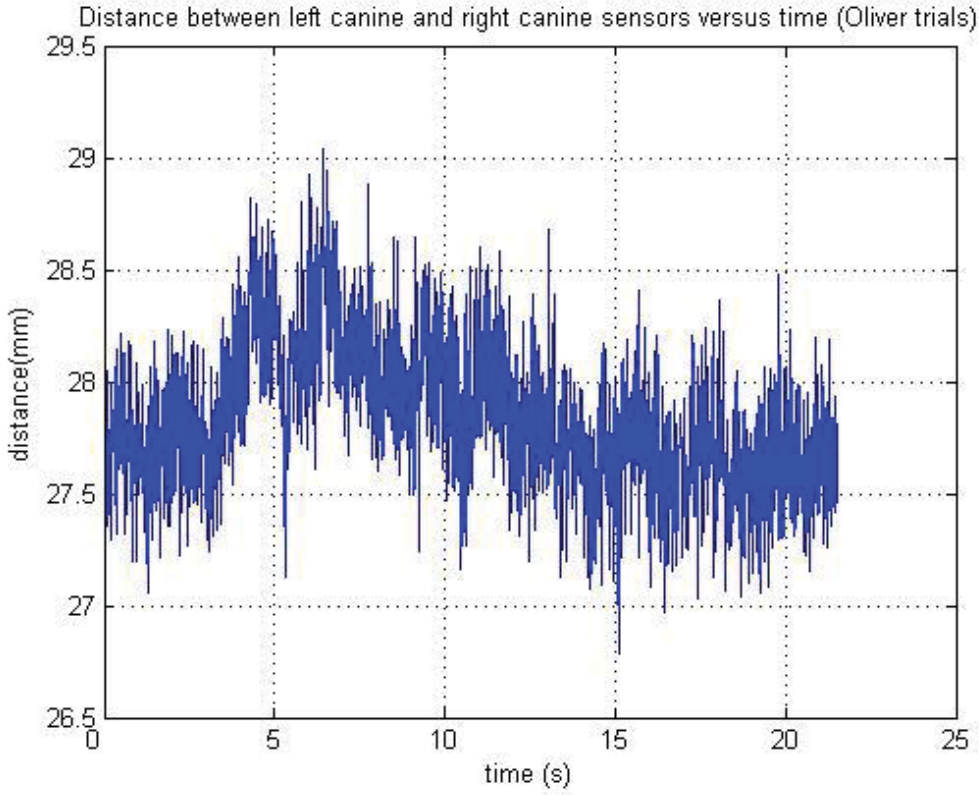
Distance between left canine and right canine sensors versus time (Oliver trials)
distance(mm)
time (s)
29.5
29
28.5
28
27.5
27
26.5
0
5
10
15
20
25

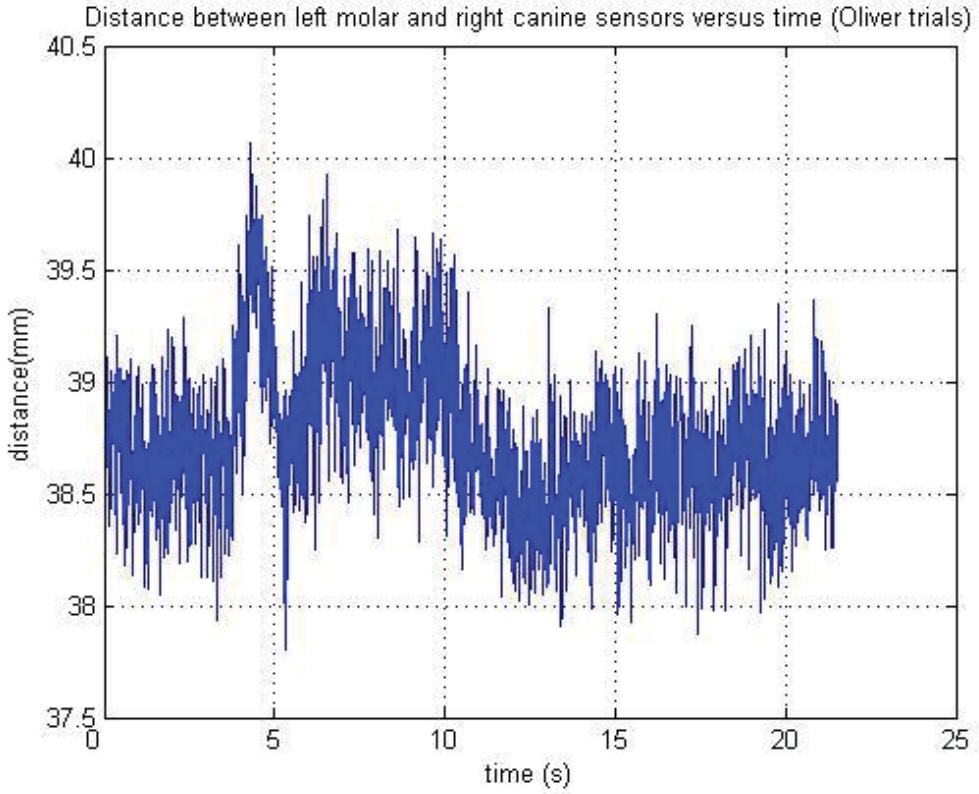
Distance between left molar and right canine sensors versus time (Oliver trials)
distance(mm)
time (s)
40.5
40
39.5
39
38.5
38
37.5
0
5
10
15
20
25

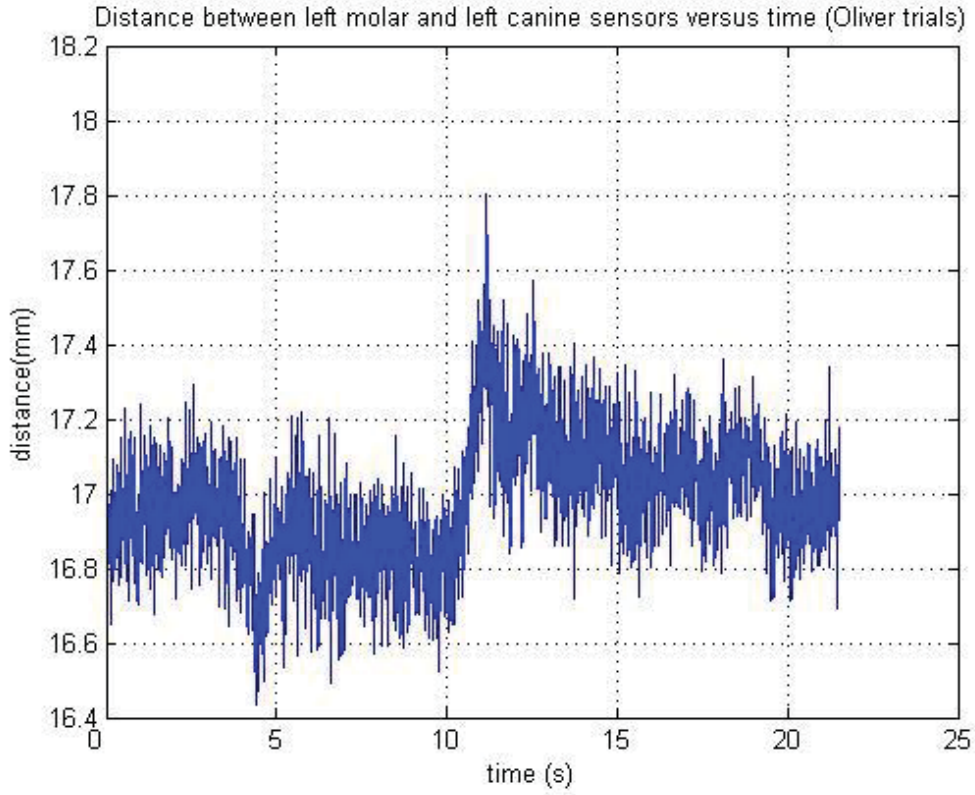

Appendix E Figure 1.

Respective ranges of the above graphs are:

2.2506mm

2.2614mm

1.3718mm

1.6052mm

2.2301mm

2.9394mm

Fairly consistent differences of around 2-3mm seen in this trial.

The same trials before head movement corrected yielded the following ranges:

1.6986mm

1.9191mm

1.0240mm

1.6270mm

1.9555mm

2.3975mm

Figures are of similar magnitude.

Trial17

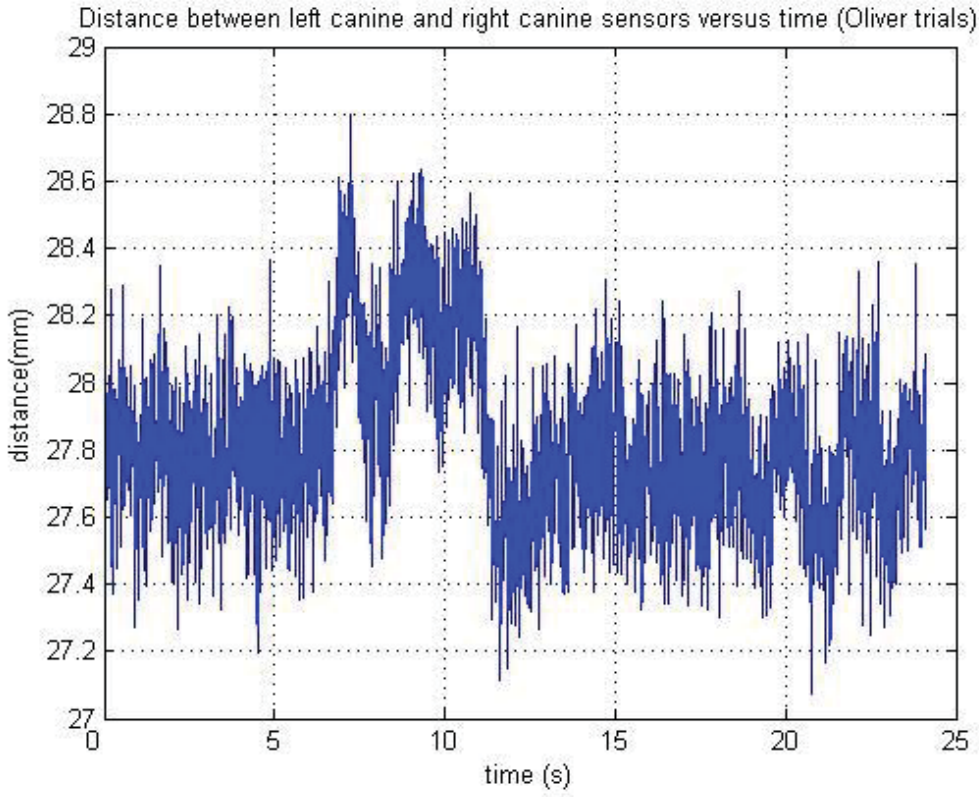
Distance between left canine and right canine sensors versus time (Oliver trials)
distance(mm)
time (s)
29
28.8
28.6
28.4
28.2
28
27.8
27.6
27.4
27.2
27
0
5
10
15
20
25

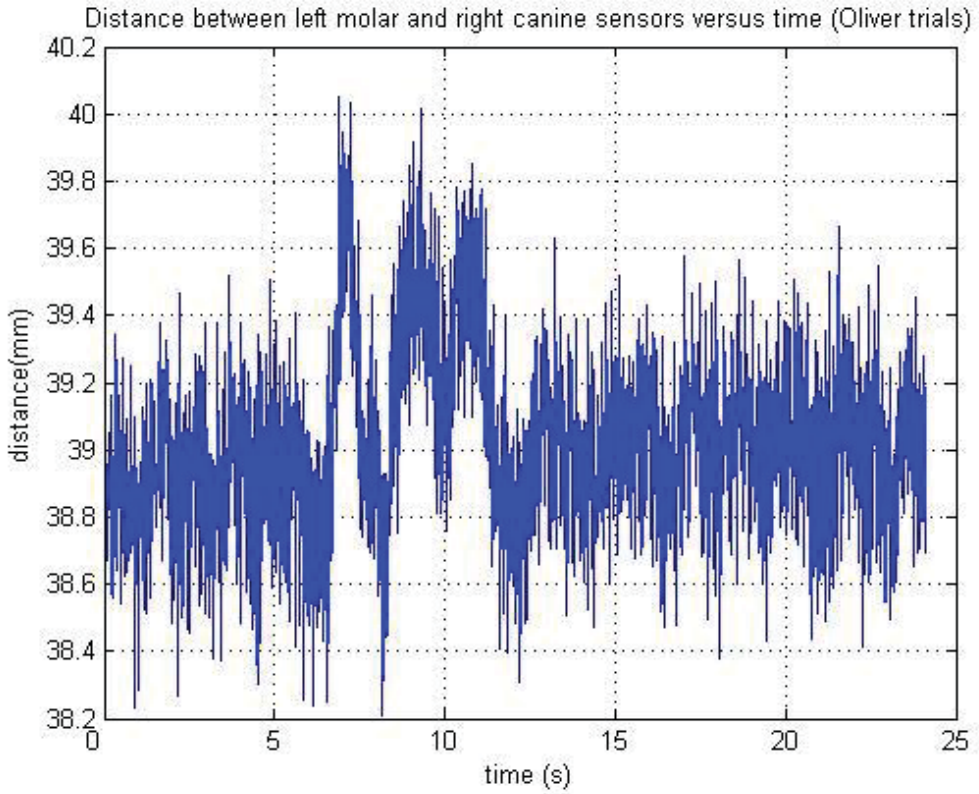
Distance between left molar and right canine sensors versus time (Oliver trials)
distance(mm)
time (s)
40.2
40
39.8
39.6
39.4
39.2
39
38.8
38.6
38.4
38.2
0
5
10
15
20
25

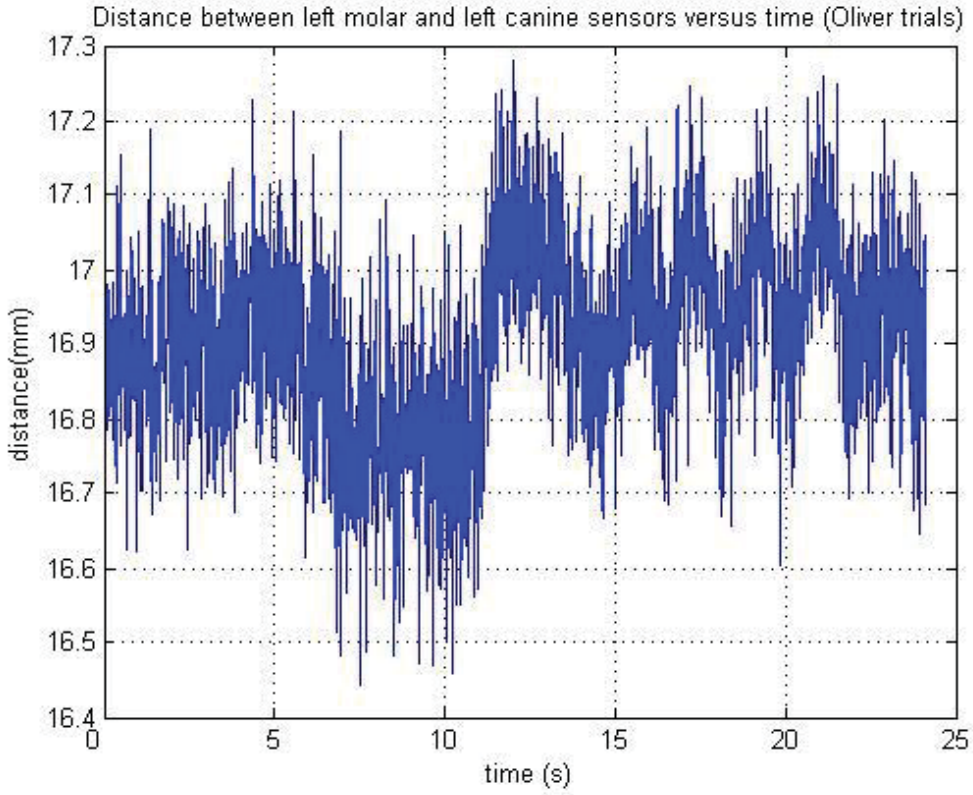
Distance between left molar and left canine sensors versus time (Oliver trials)
distance(mm)
time (s)
17.3
17.2
17.1
17
16.9
16.8
16.7
16.6
16.5
16.4
0
5
10
15
20
25

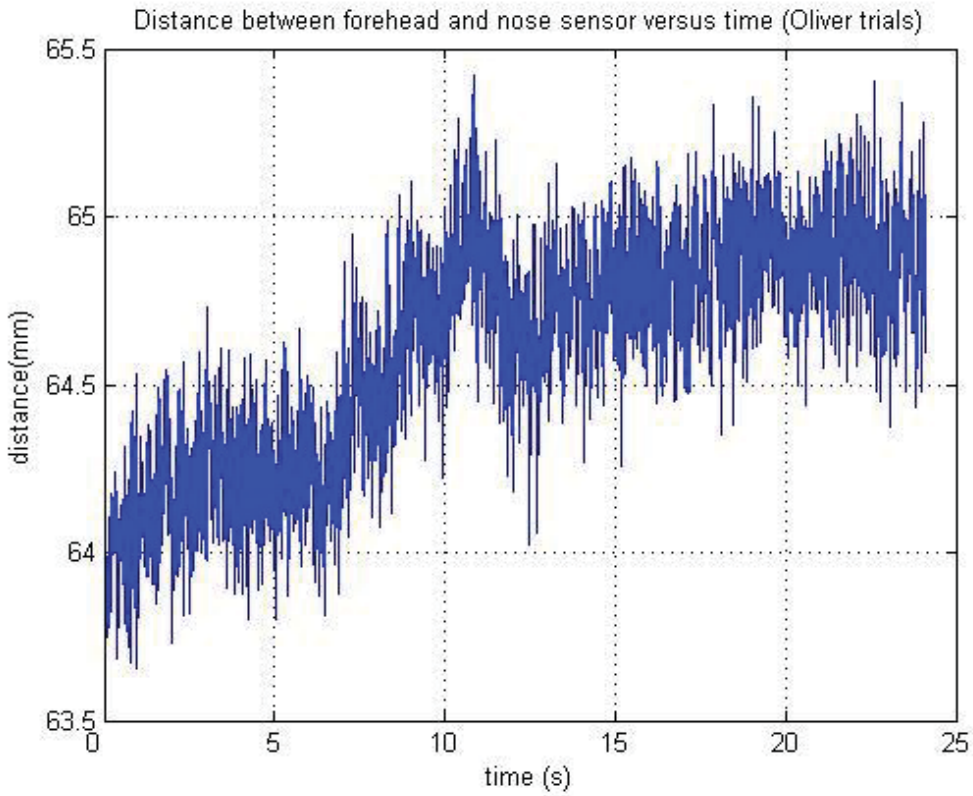
Distance between forehead and nose sensor versus time (Oliver trials)
distance(mm)
time (s)
65.5
65
64.5
64
63.5
0
5
10
15
20
25

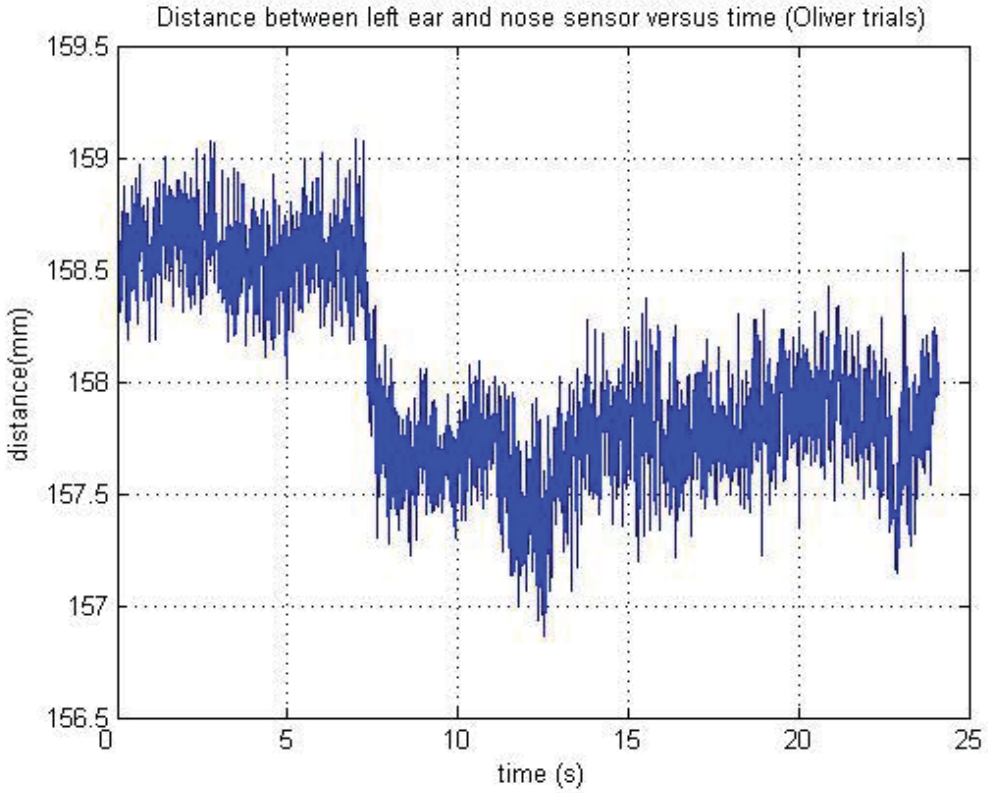

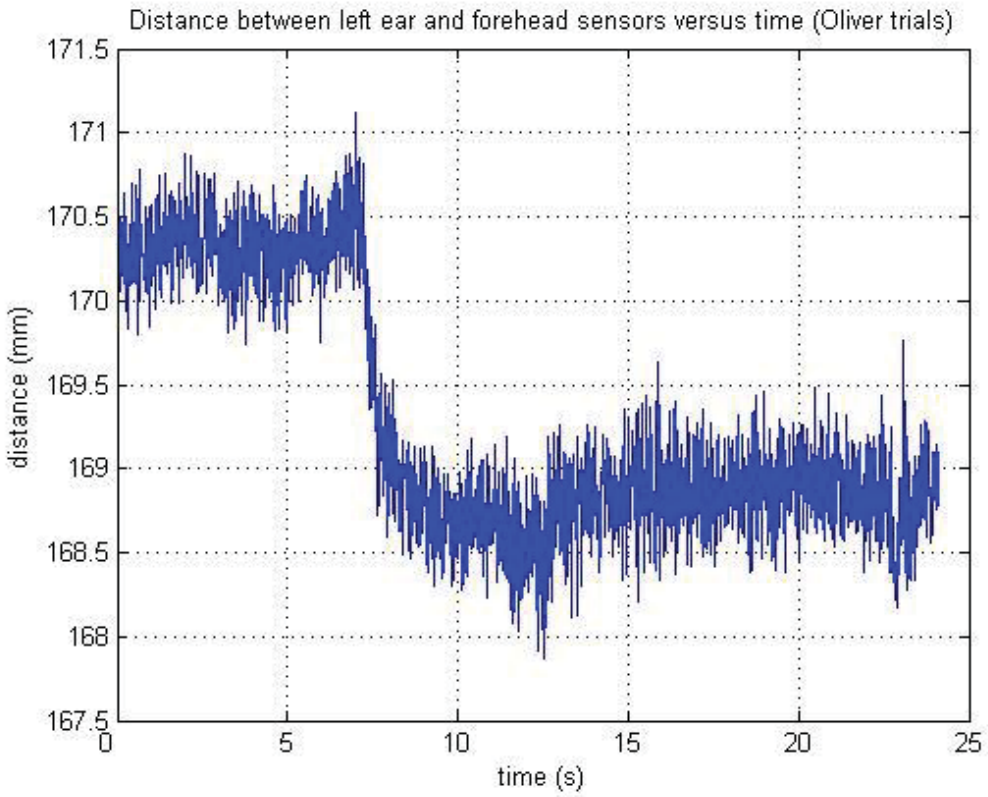

Appendix E Figure 2.

Respective ranges of the above graphs are:

1.7274mm

1.8472mm

0.8360mm

1.8912mm

2.2237mm

3.2455mm

It can be seen errors up to 3.2mm between fixed sensors for this trial.

Before head correction the ranges were:

1.3023mm

1.6227mm

0.8382mm

1.7817mm

2.0642mm

2.8642mm

Trial18

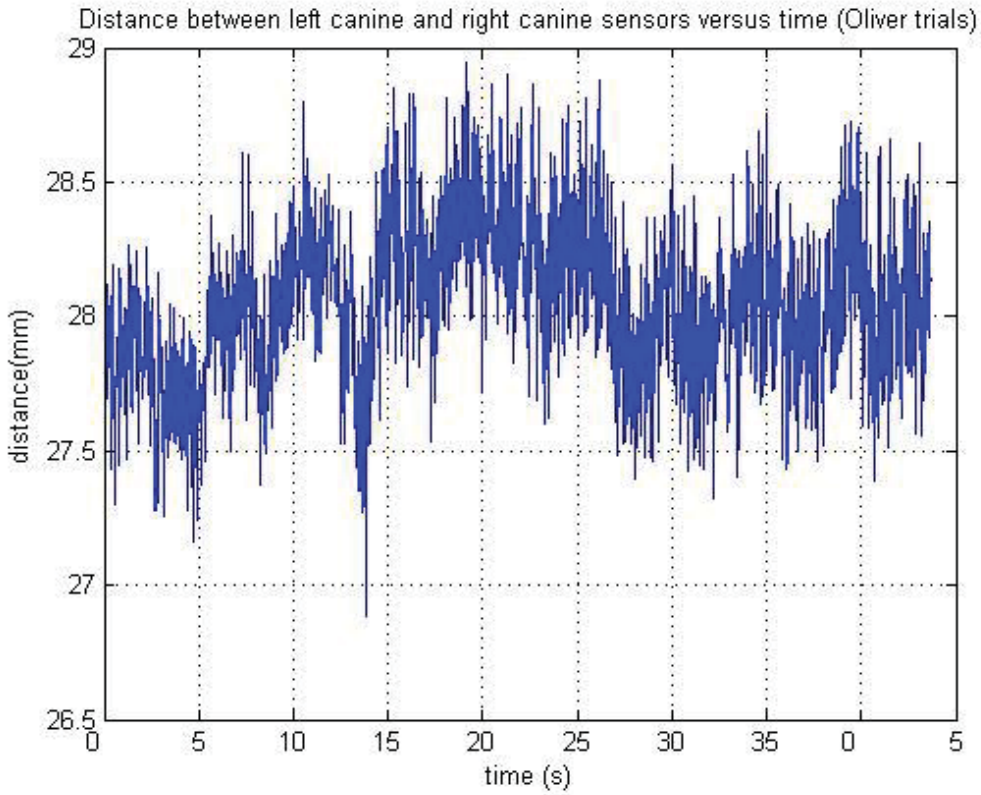
Distance between left canine and right canine sensors versus time (Oliver trials)
distance(mm)
time (s)
29
28.5
28
27.5
27
26.5
0
5
10
15
20
25
30
35
0
5

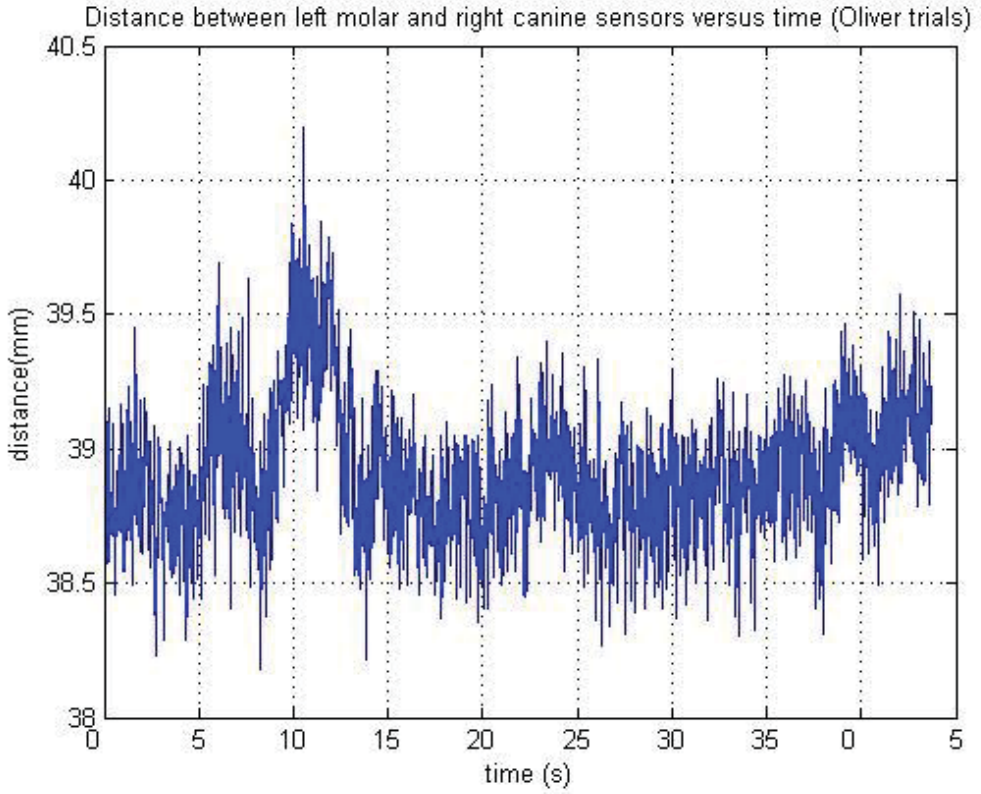
Distance between left molar and right canine sensors versus time (Oliver trials)
distance(mm)
time (s)
40.5
40
39.5
39
38.5
38
0
5
10
15
20
25
30
35
0
5

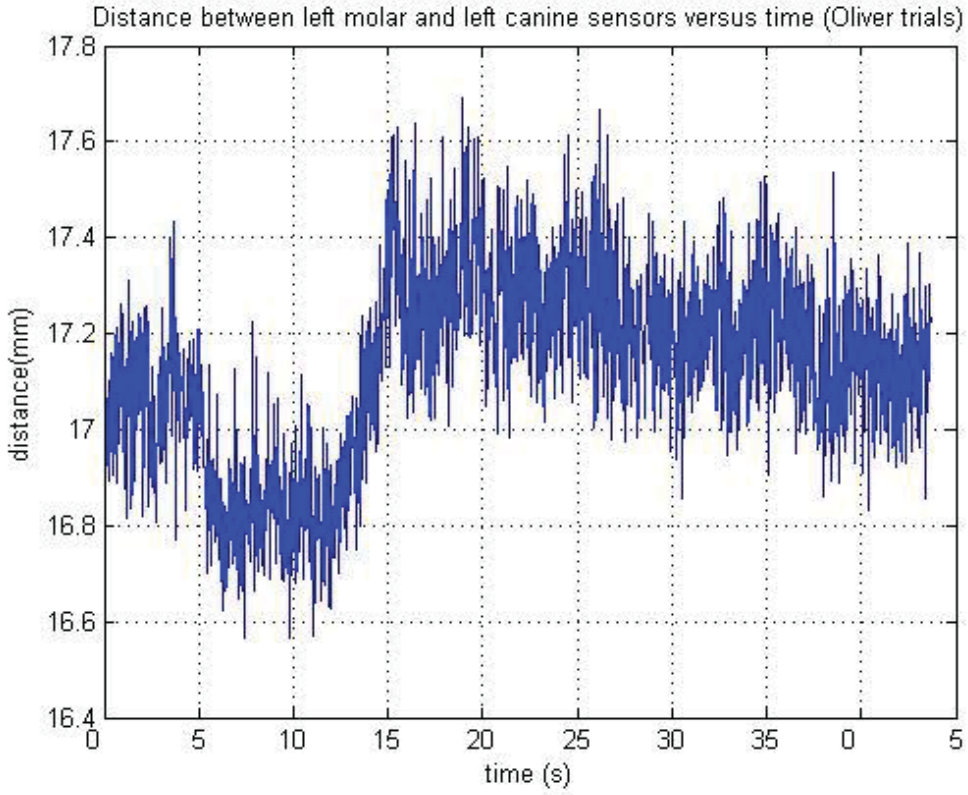
Distance between left molar and left canine sensors versus time (Oliver trials)
distance(mm)
time (s)
17.8
17.6
17.4
17.2
17
16.8
16.6
16.4
0
5
10
15
20
25
30
35
0
5

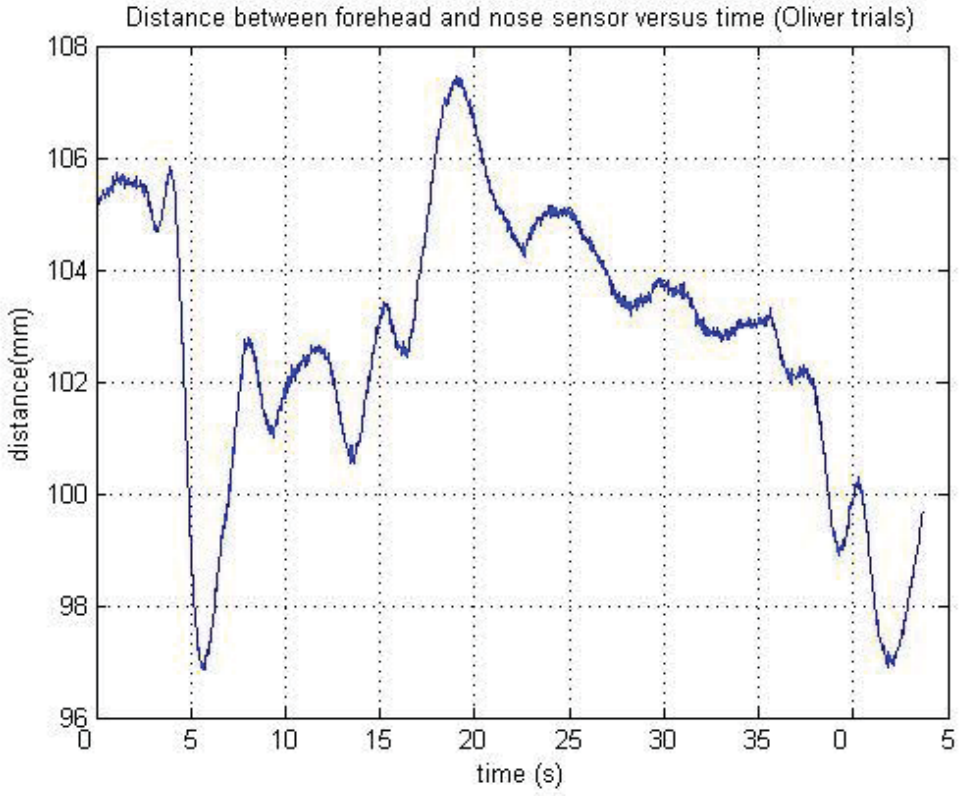
Distance between forehead and nose sensor versus time (Oliver trials)
distance(mm)
time (s)
108
106
104
102
100
98
96
0
5
10
15
20
25
30
35
0
5

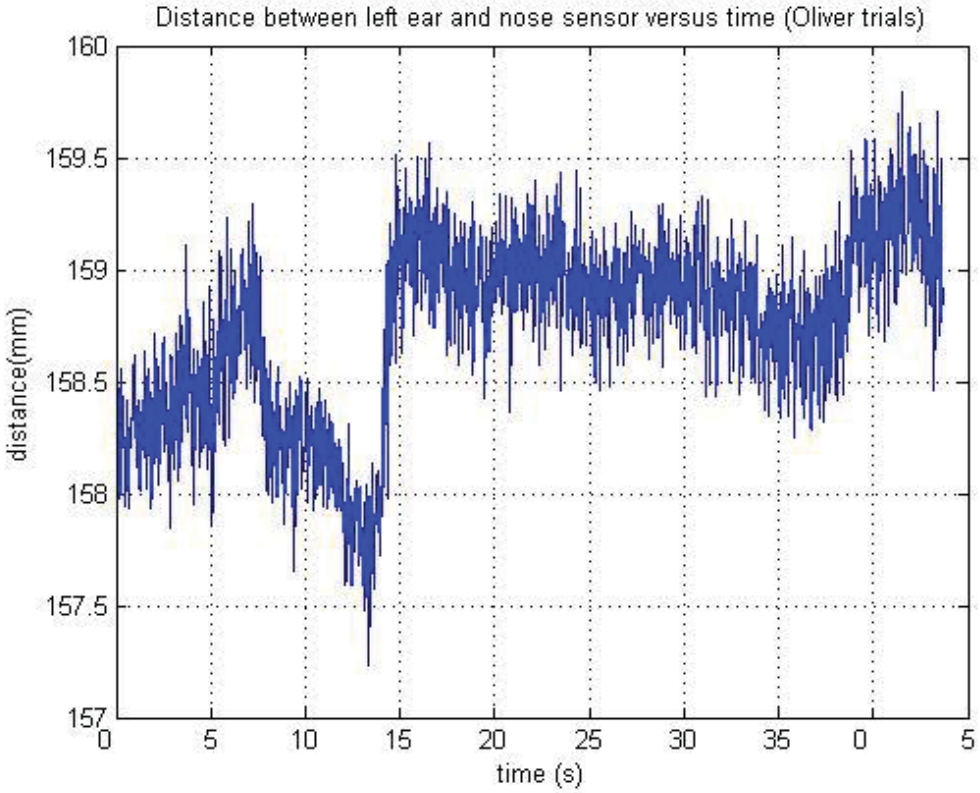

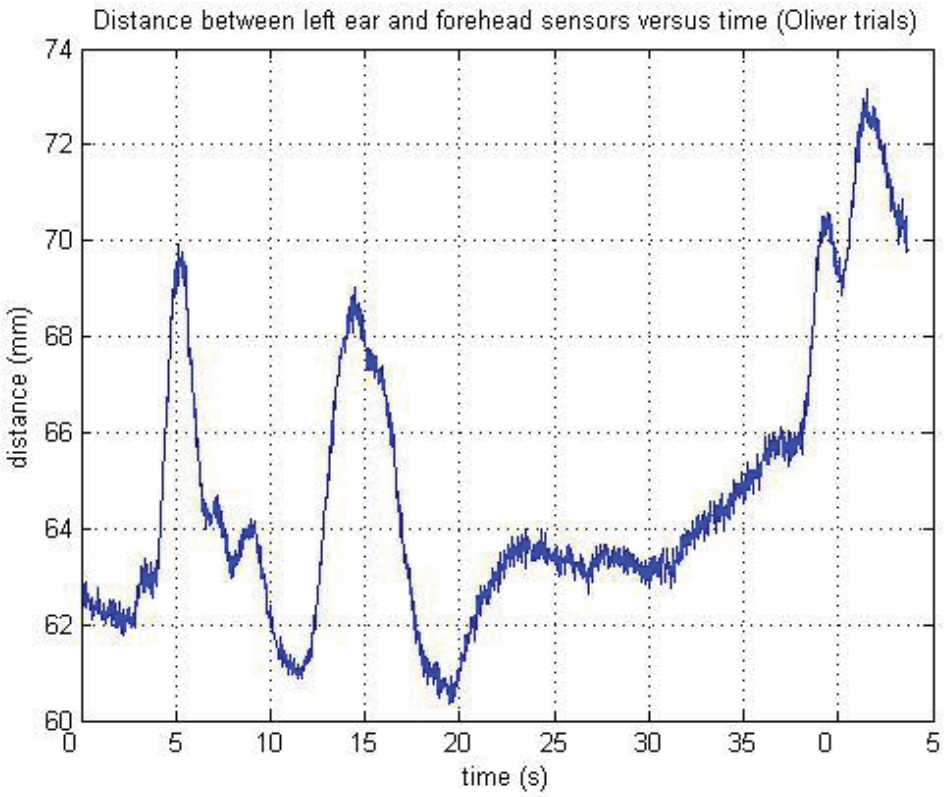

Appendix E Figure 3.

Respective ranges of the above graphs are:

2.0576mm

2.0190mm

1.1274mm

10.5822mm

2.5599mm

12.8144mm

The two large distances over 10mm may be due to a poorly fixed sensor. Movements of up to 2mm are seen between other sensors.

Before head correction the ranges were:

1.5628mm

1.7727mm

0.9674mm

10.5590mm

1.8387mm

12.2304mm

The ranges are of similar magnitude.

- MIKES TRIALS:

Mikes trials used 2 reference sensors placed behind the left and right ear, and 2 teeth sensors on left and right canine. His trials involved chewing a 4g piece of muesli.

Mike_trial1.

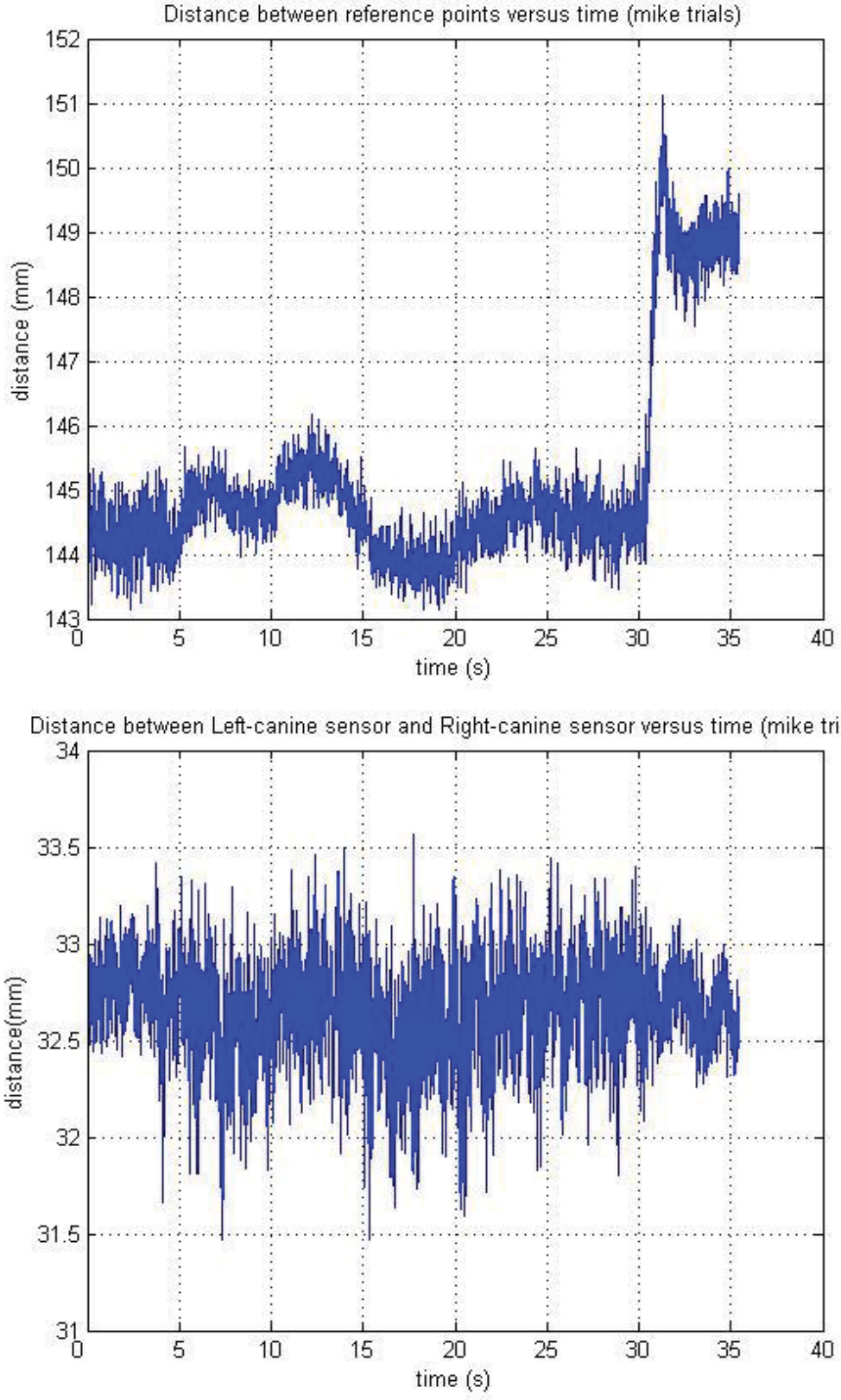

Appendix E Figure 4.

Respective ranges for the above graphs are:

7.9905mm

2.0926mm

A systematic error such as loose sensor, is likely to have caused the 7.99mm distance between reference points.

The same distances for the same trials before head movement correction had the following ranges:

7.9894mm

2.0853mm

Similar to post head movement corrected.

Trial mike3

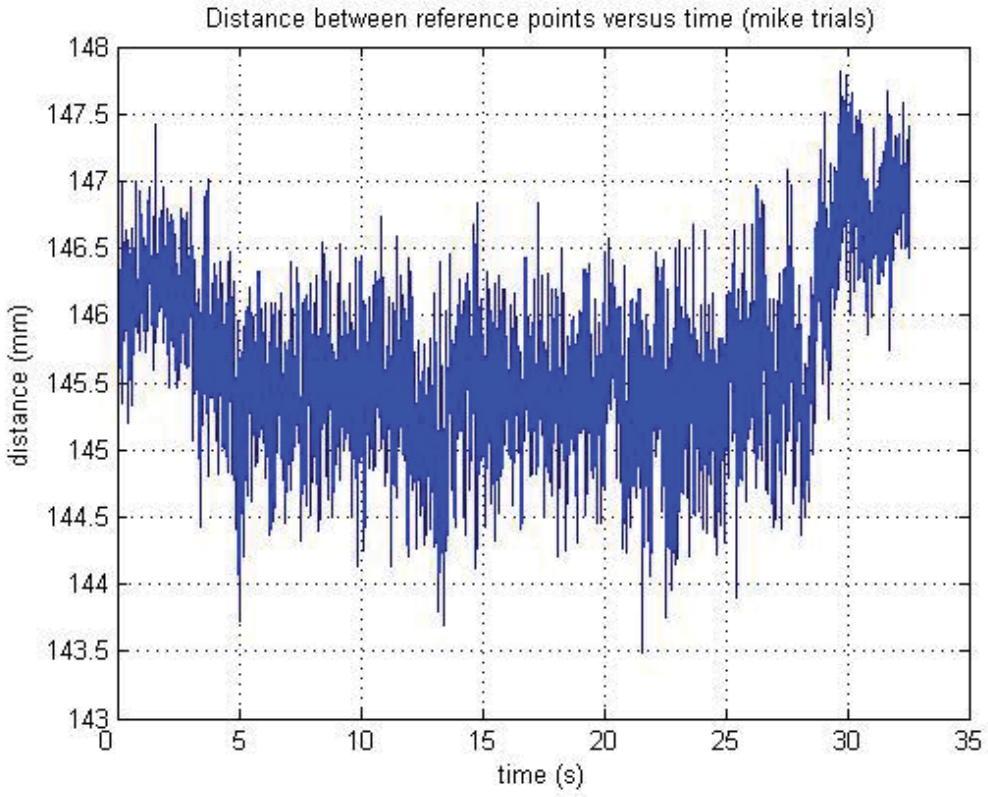

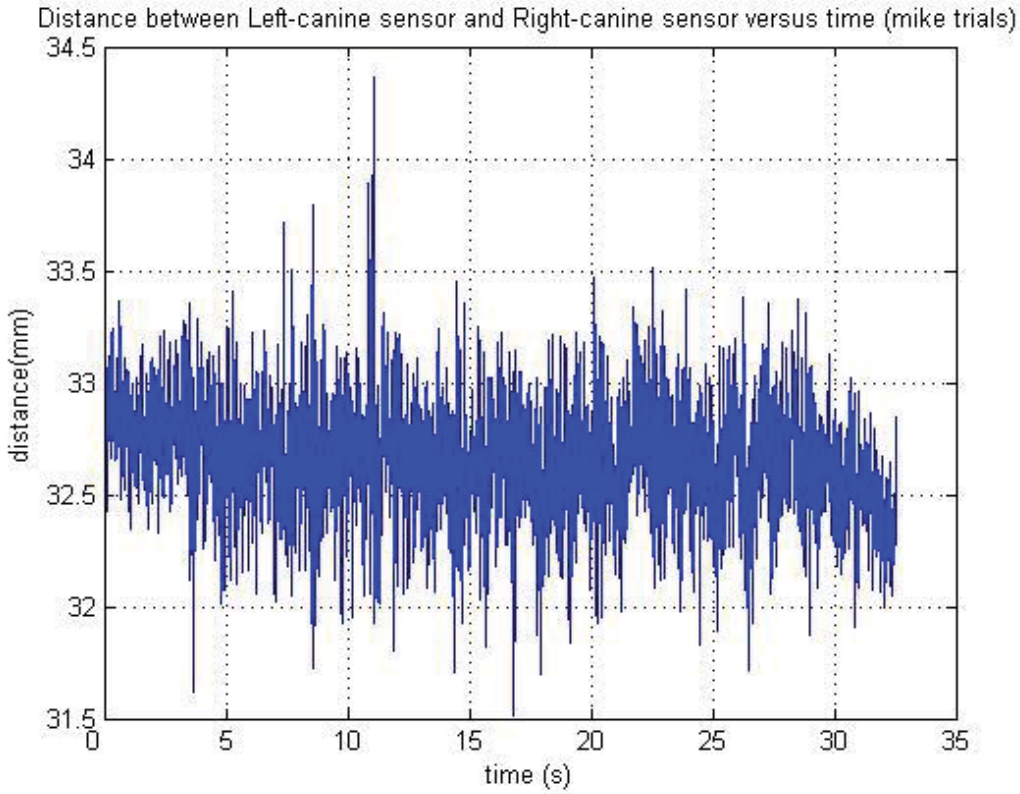

Appendix E Figure 5.

Ranges of the above graphs respectively:

4.3255mm

2.8483mm

Before head movement correction ranges were:

4.3282mm

2.8725mm

Trial mike 9:

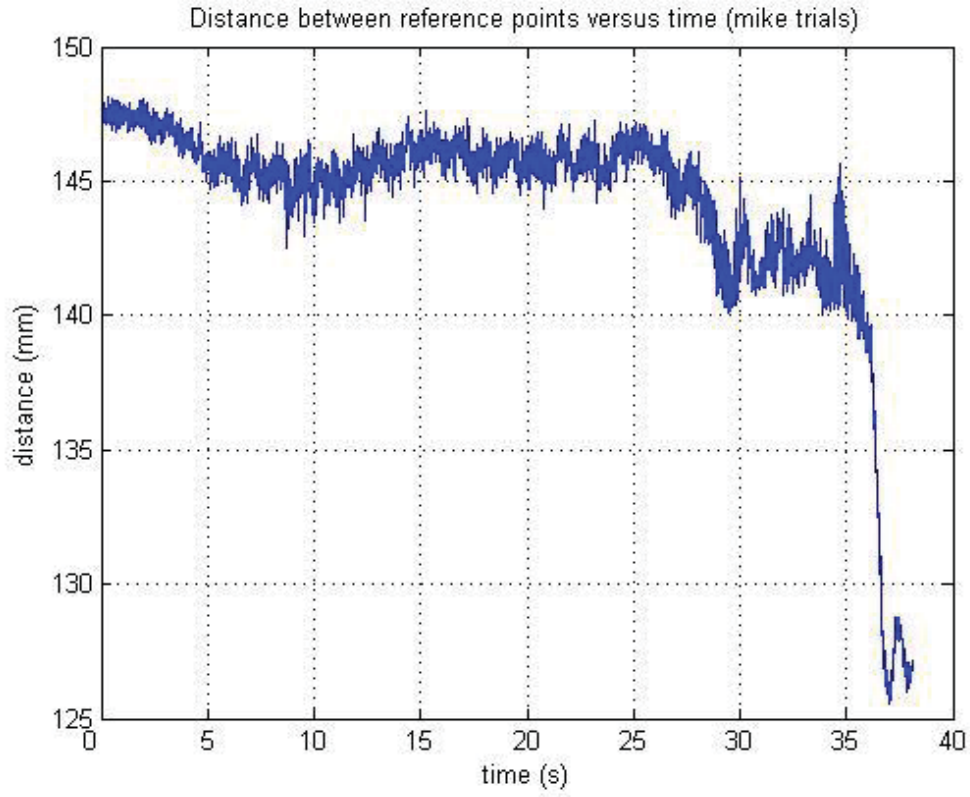

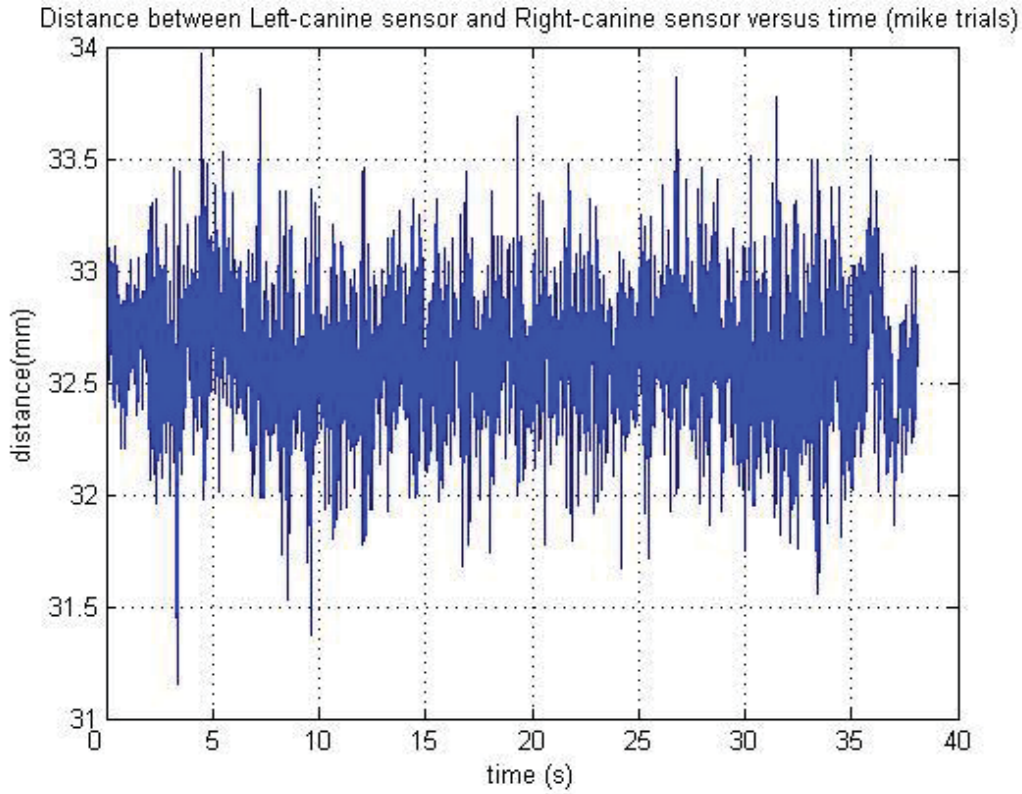

Appendix E Figure 6.

Respective ranges of above graphs:

22.6244mm

2.8214mm

A systematic error is likely to be responsible for the 22mm error.

Before head movement correction:

22.6215mm

2.8169mm

- PETERS TRIALS:

Peter's trials involved placement of 2 reference sensors behind the ears, and 3 teeth sensors located on right-lower incisor point, left premolar, and right premolar. The trials used muesli for the chewing.

Trail Peter2:

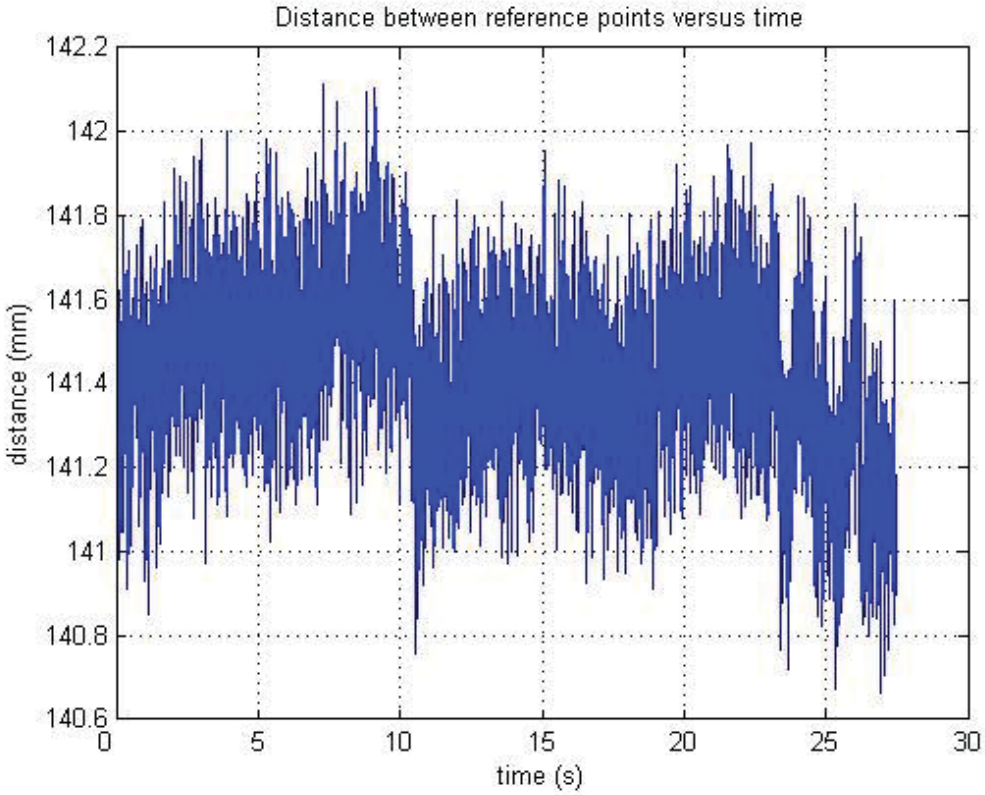

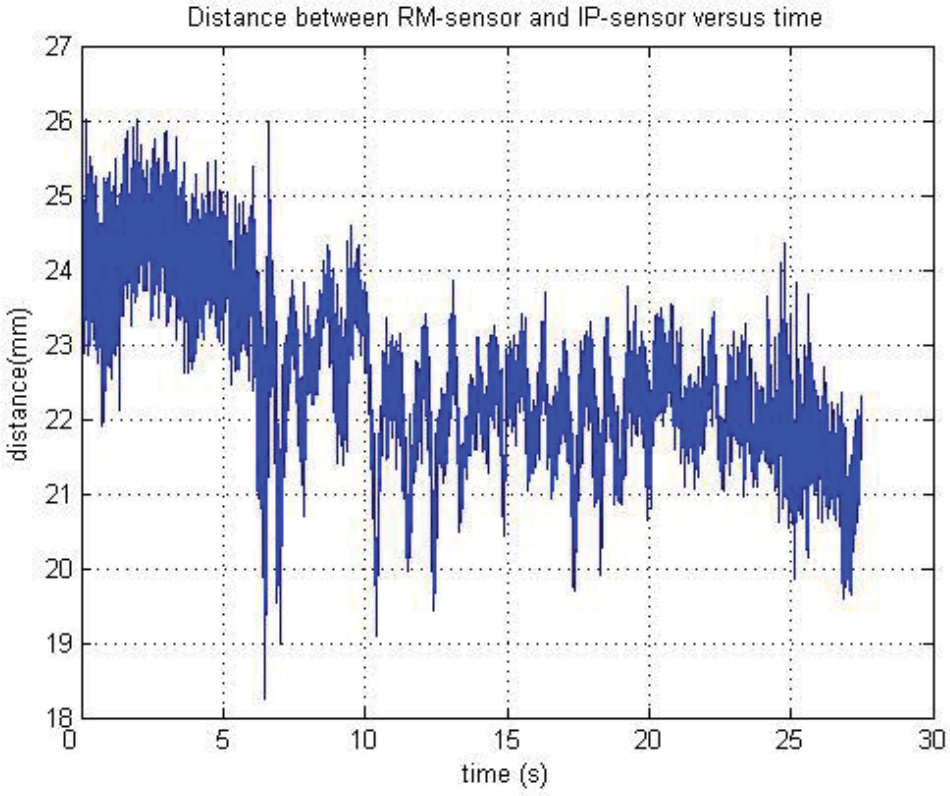

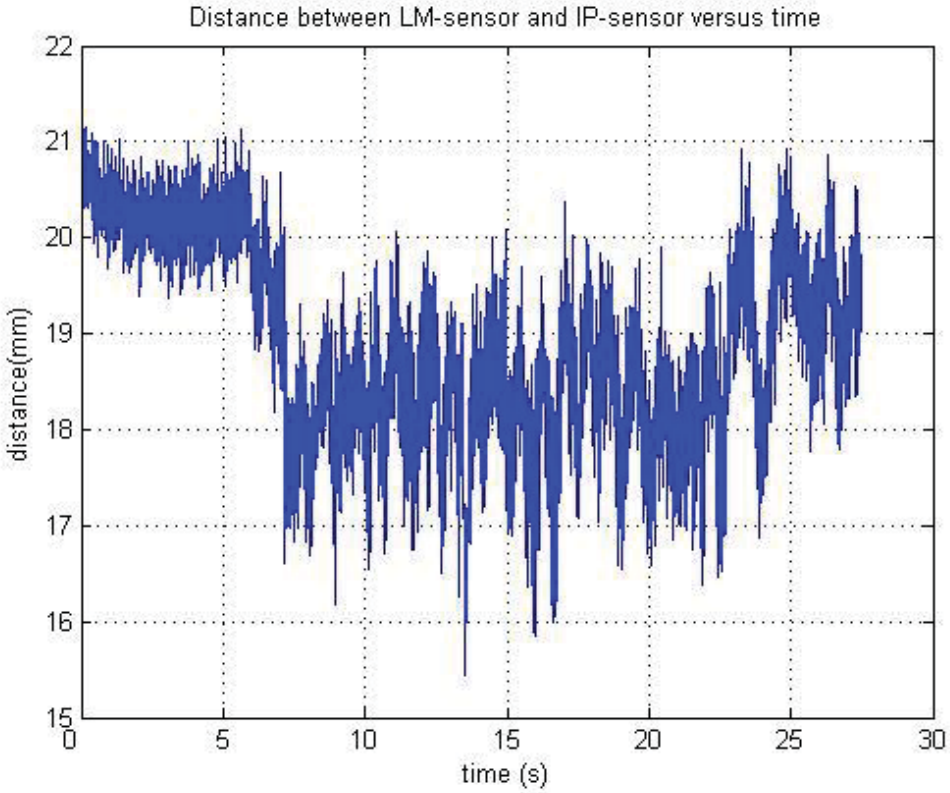

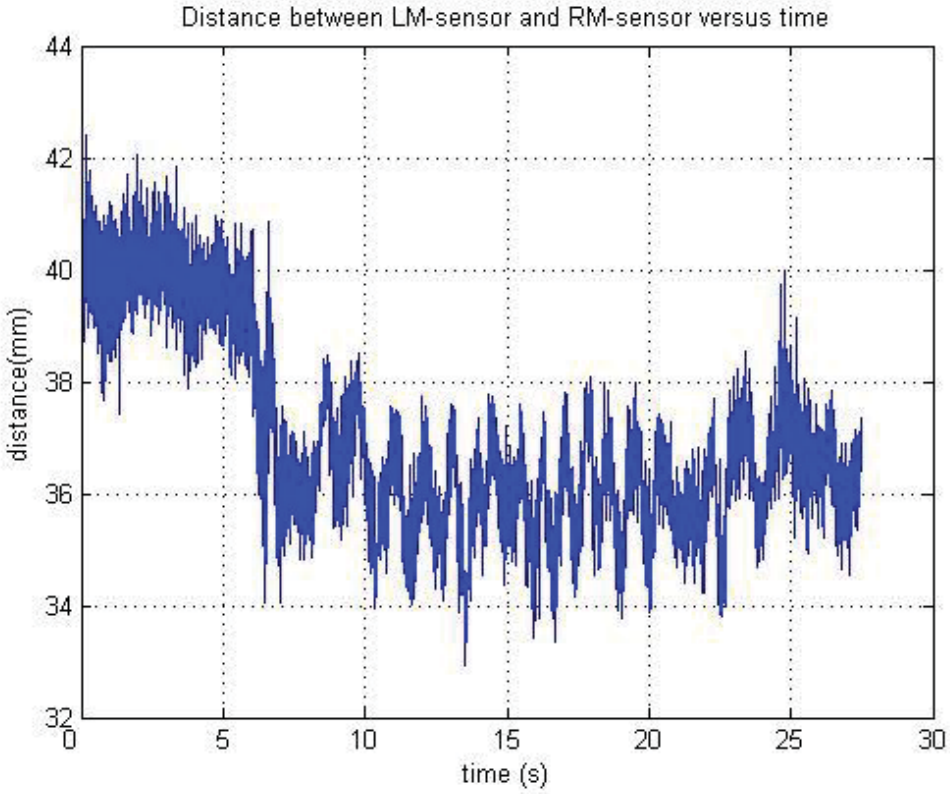

Appendix E Figure 7.

Respective ranges of the above graphs:

1.4528mm

8.2649mm

5.7798mm

9.7722mm

The reference sensor distance measurement appears fair compared to other trials, however there is a lot of movement between sensors located on teeth.

Before head correction the ranges were:

1.4454mm

8.2798mm

5.7898mm

9.7750mm

Trial Peter4:

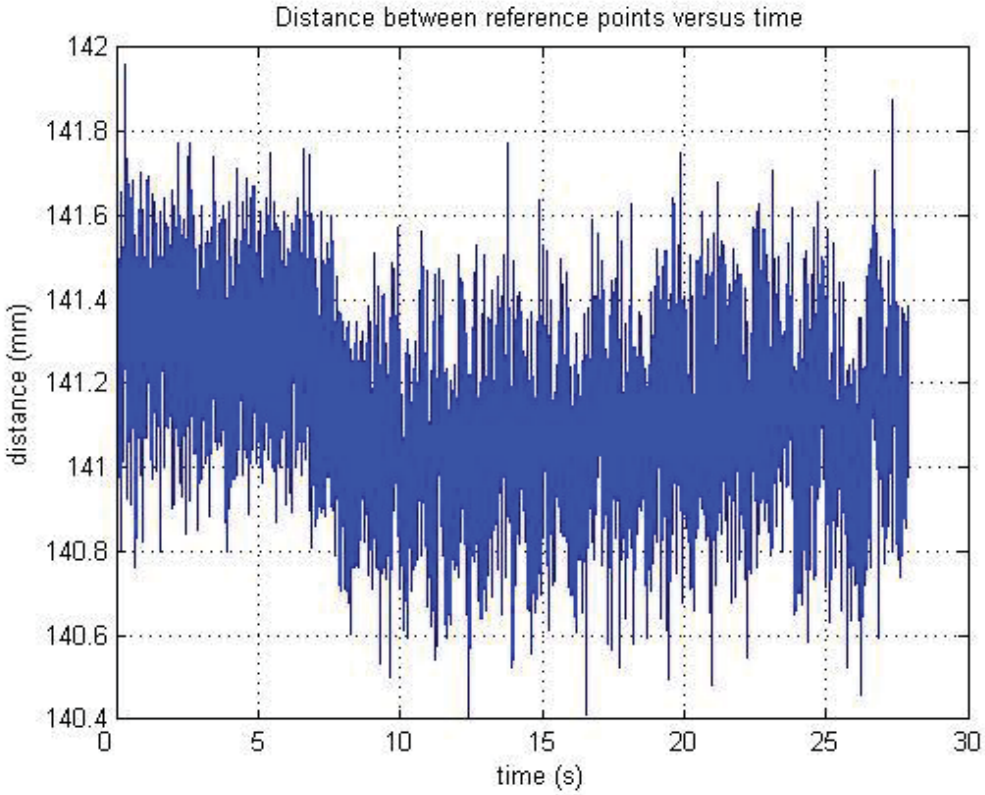

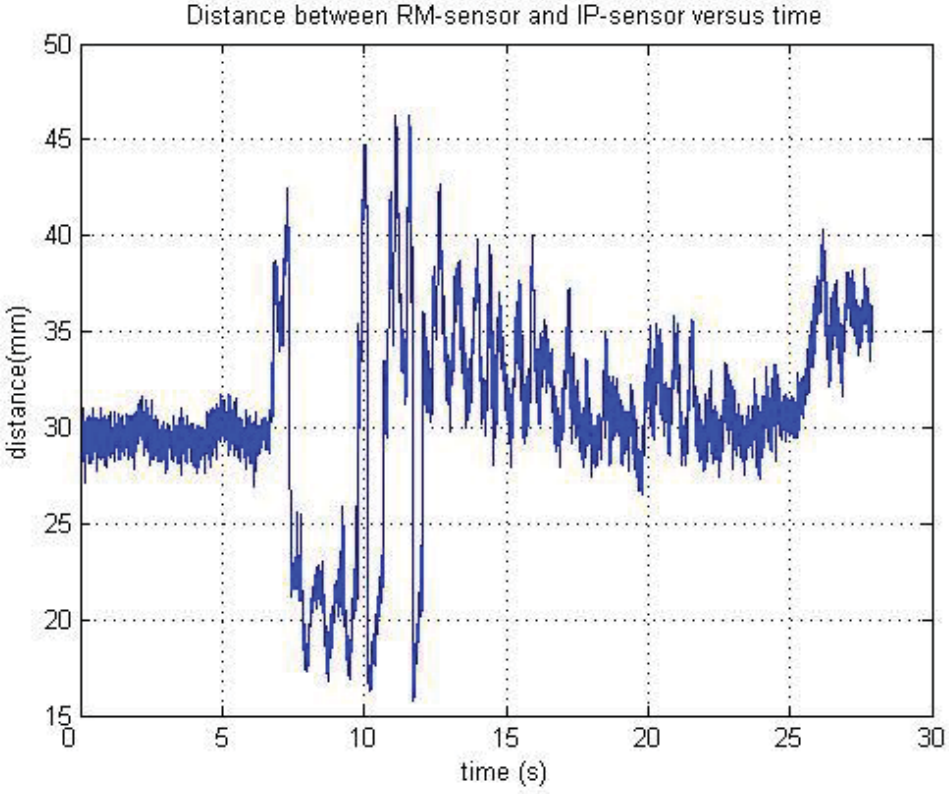

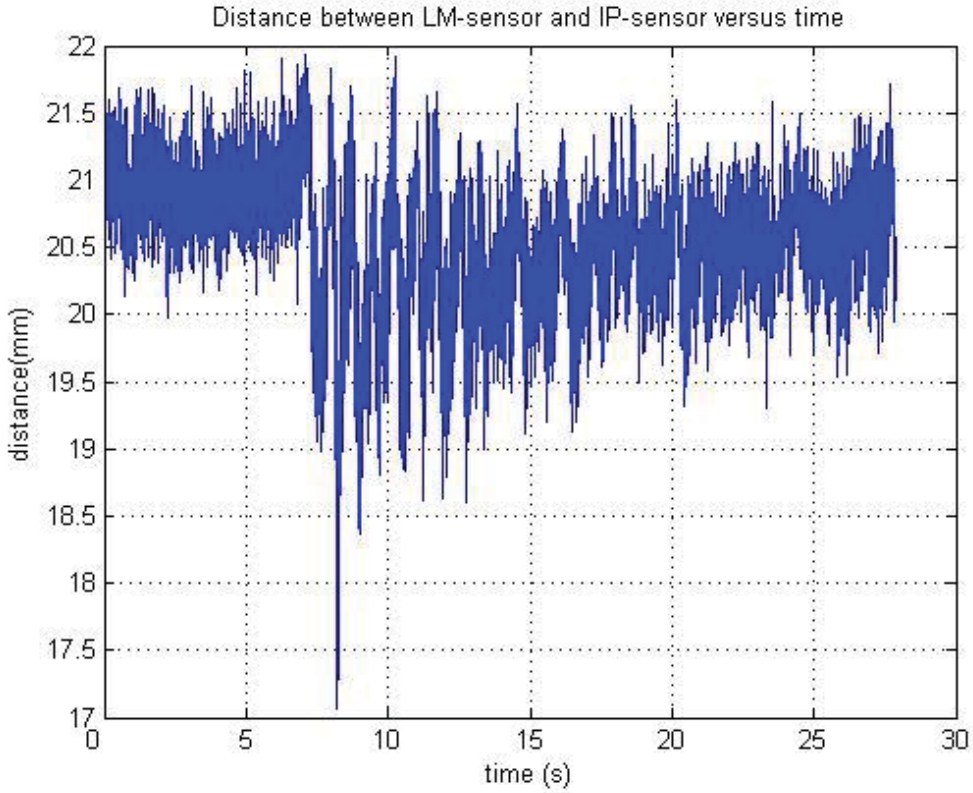

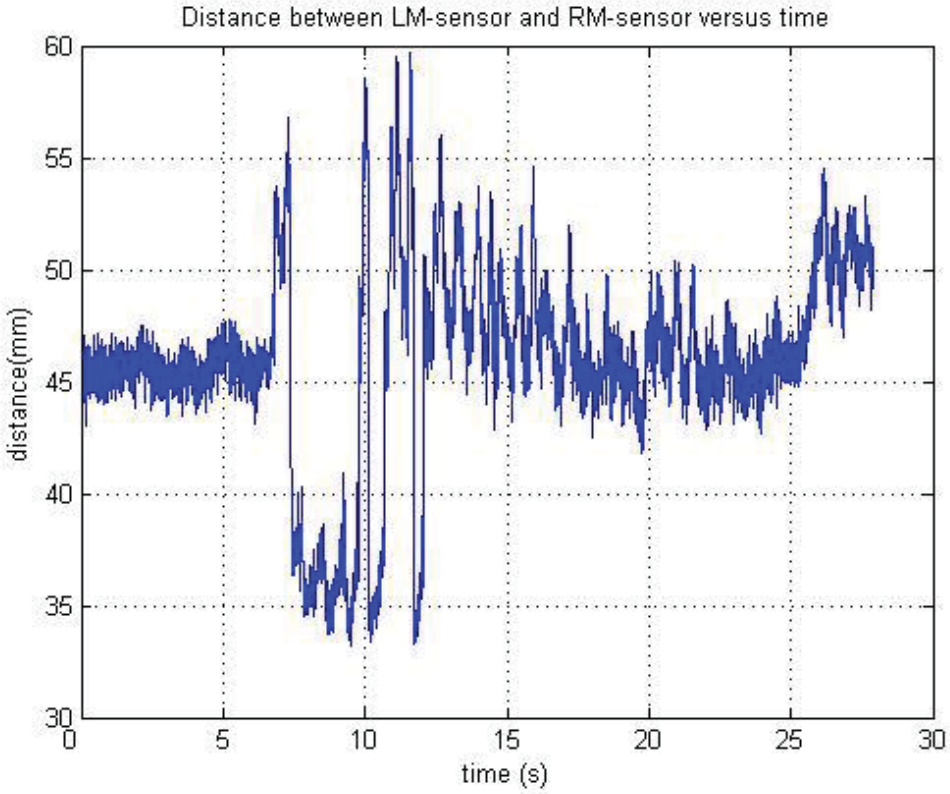

Appendix E Figure 8.

Ranges of graphs respectively:

1.5555mm

30.4820mm

4.8706mm

26.4681mm

Teeth sensors have a large degree of relative movement, possibly due to systematic error. The reference sensors maintain a fairly constant spacing.

Before head movement correction:

1.5604mm

30.4757mm

4.8714mm

26.4741mm

Comparable to post correction ranges.

Trial Peter6:

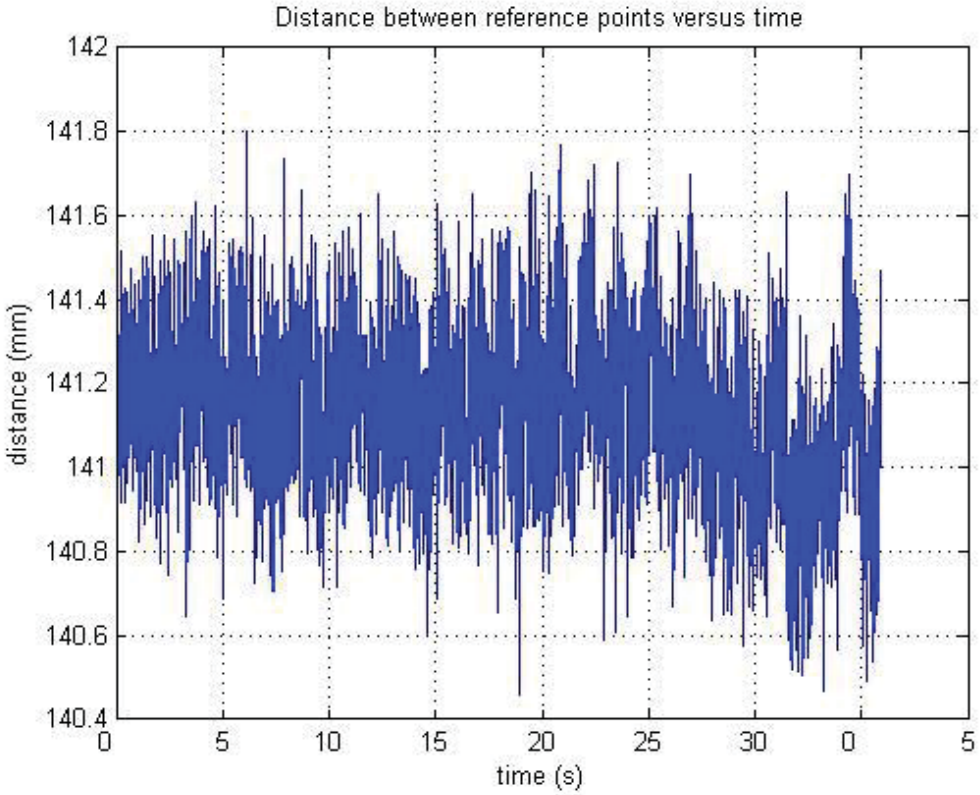

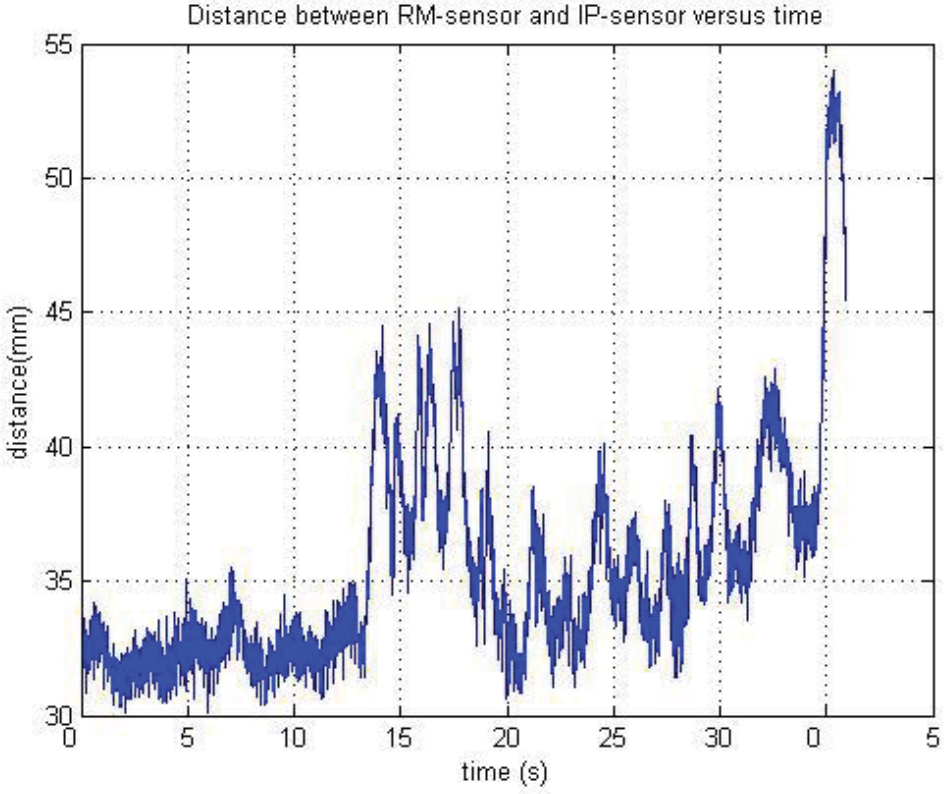

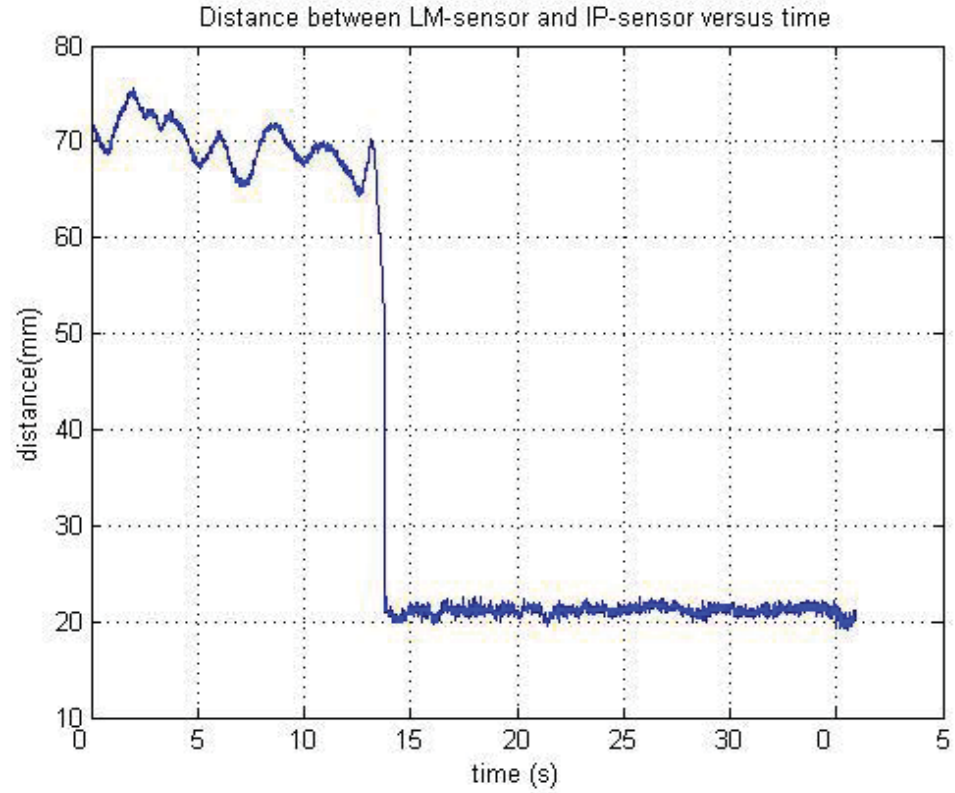

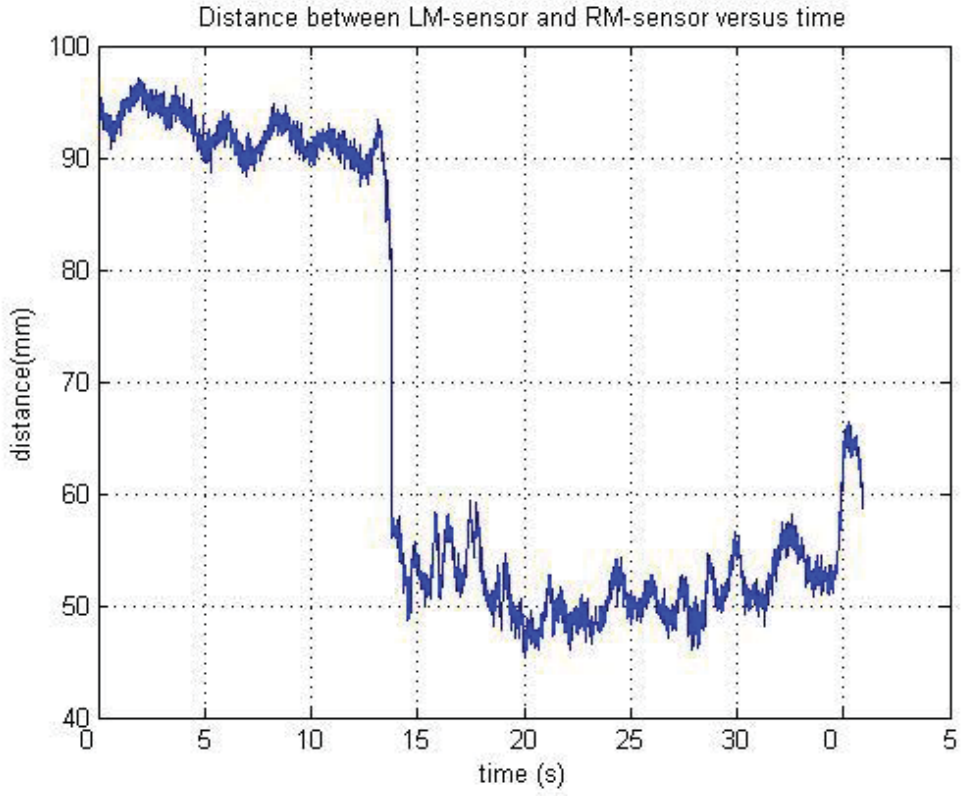

Appendix E Figure 9.

Ranges respectively:

1.3451mm

23.9419mm

56.3835mm

51.7662mm

Reference sensors are fine, but teeth sensors have large movements, not likely to simply be a loose sensor as magnitude is large.

Before head movement correction, the ranges were:

1.3392mm

23.9464mm

56.3817mm

51.7739mm

Discussion:

From the above graphs it is reasonable to assume around 2mm difference in sensor point distances given the absence of systematic error or other influences that have caused much larger differences.

2mm range would be equivalent to a random error of +/-1mm for each data point, and this error should be incorporated into every calculation involving the data.

The more serious systematic error is not able to be corrected as there is no documentation of the cause or any way to calibrate. Data should be checked before hand for systematic error and discarded if present.

The head movement correction process does not appear to have an influence on the accuracy of the final data.

2. Analyse of corrected head movement

- Software with articulograph called ‘normpos.exe’ creates a normalization pattern for reference sensors which corrects all data points for head movement.
- No indication given to the degree of correction expected or means given to verify head-movement correction has been successfully performed.

Objective:

Find degree to which head movement has been corrected and assess if satisfactory for our purposes.

Method:

Take a selection of trials and plot reference sensor movements after head movement correction has been performed. Compare to movements of sensors on the teeth.

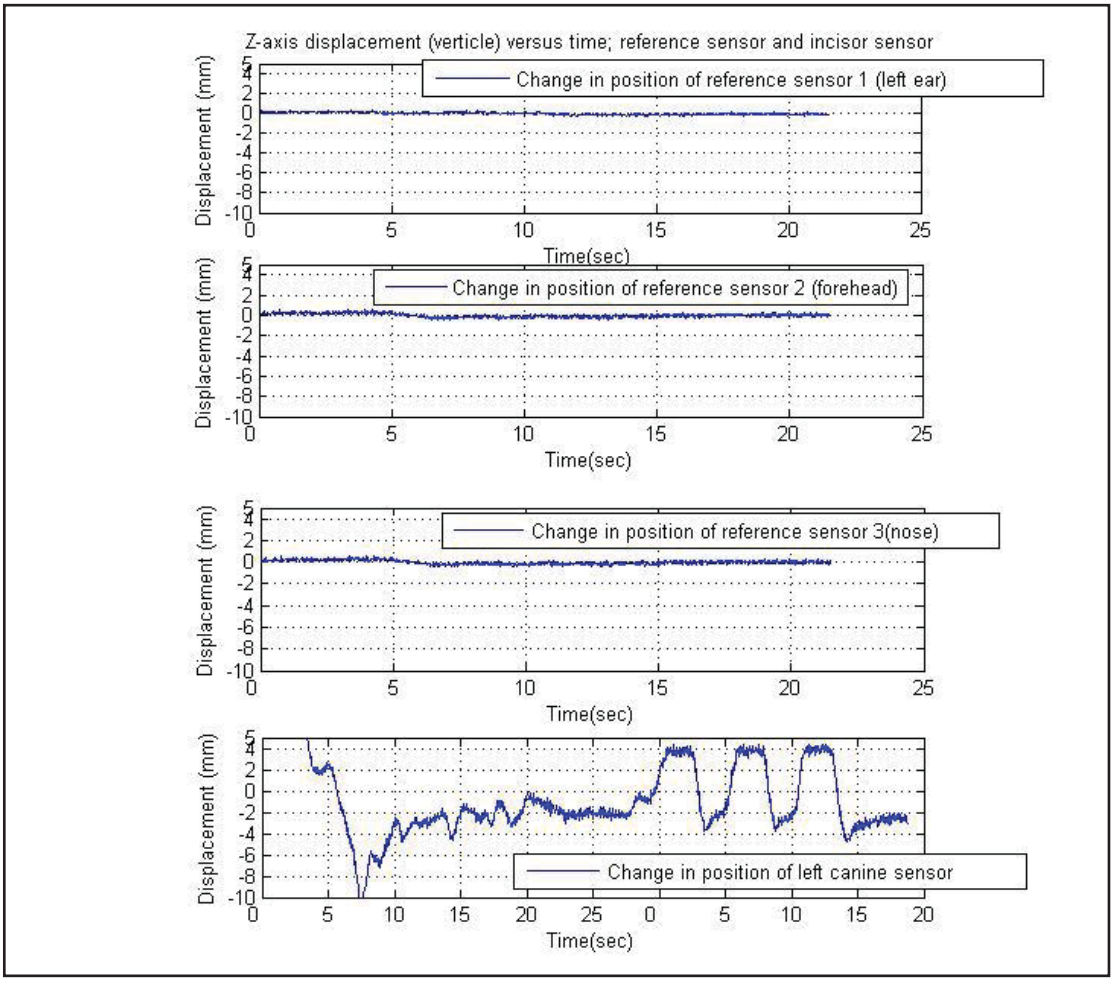
Z-axis displacement (verticle) versus time; reference sensor and incisor sensor
Change in position of reference sensor 1 (left ear)
Displacement (mm)
Time(sec)
Change in position of reference sensor 2 (forehead)
Displacement (mm)
Time(sec)
Change in position of reference sensor 3(nose)
Displacement (mm)
Time(sec)
Change in position of left canine sensor
Displacement (mm)
Time(sec)

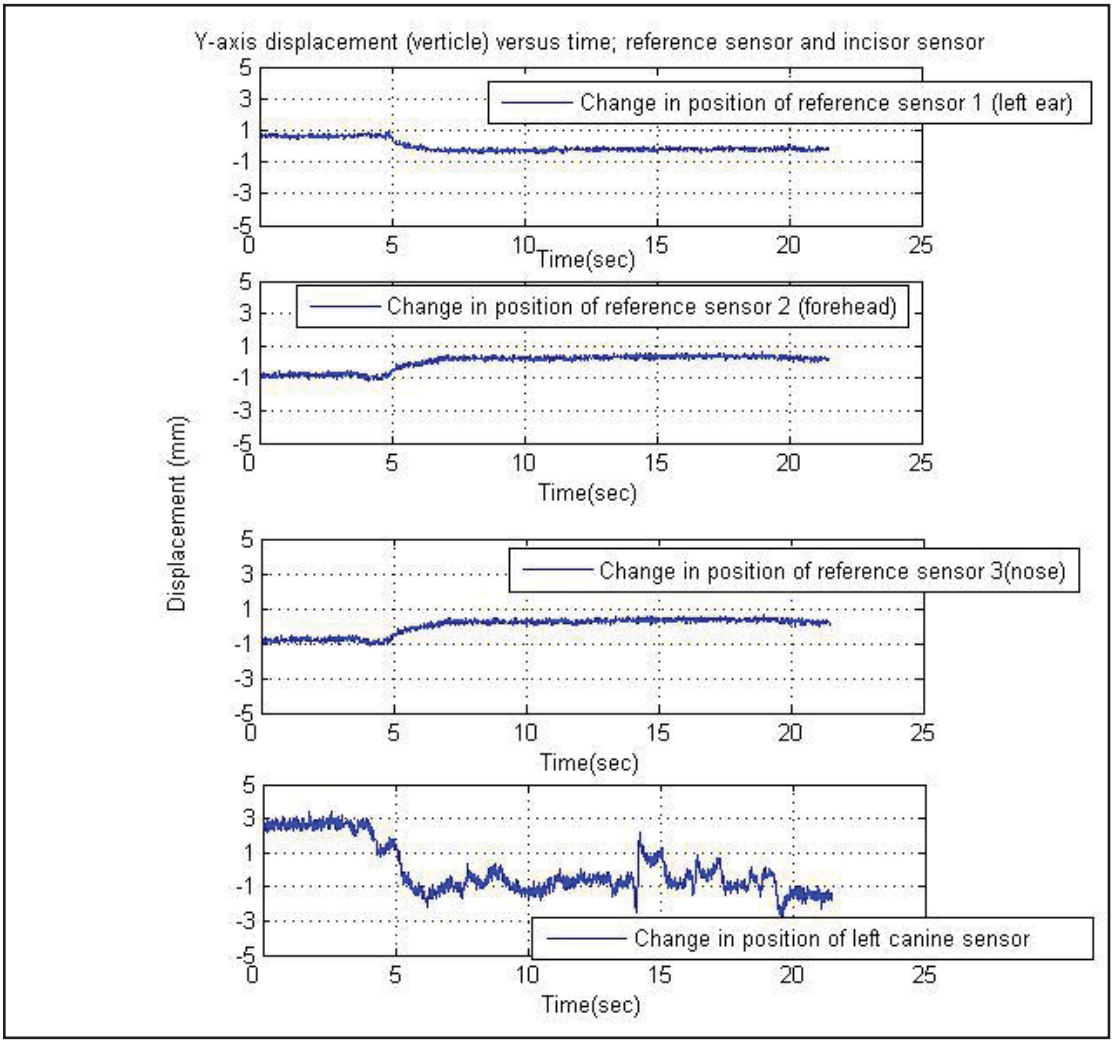
Y-axis displacement (verticle) versus time; reference sensor and incisor sensor
Change in position of reference sensor 1 (left ear)
Change in position of reference sensor 2 (forehead)
Change in position of reference sensor 3(nose)
Change in position of left canine sensor
Displacement (mm)
Time(sec)

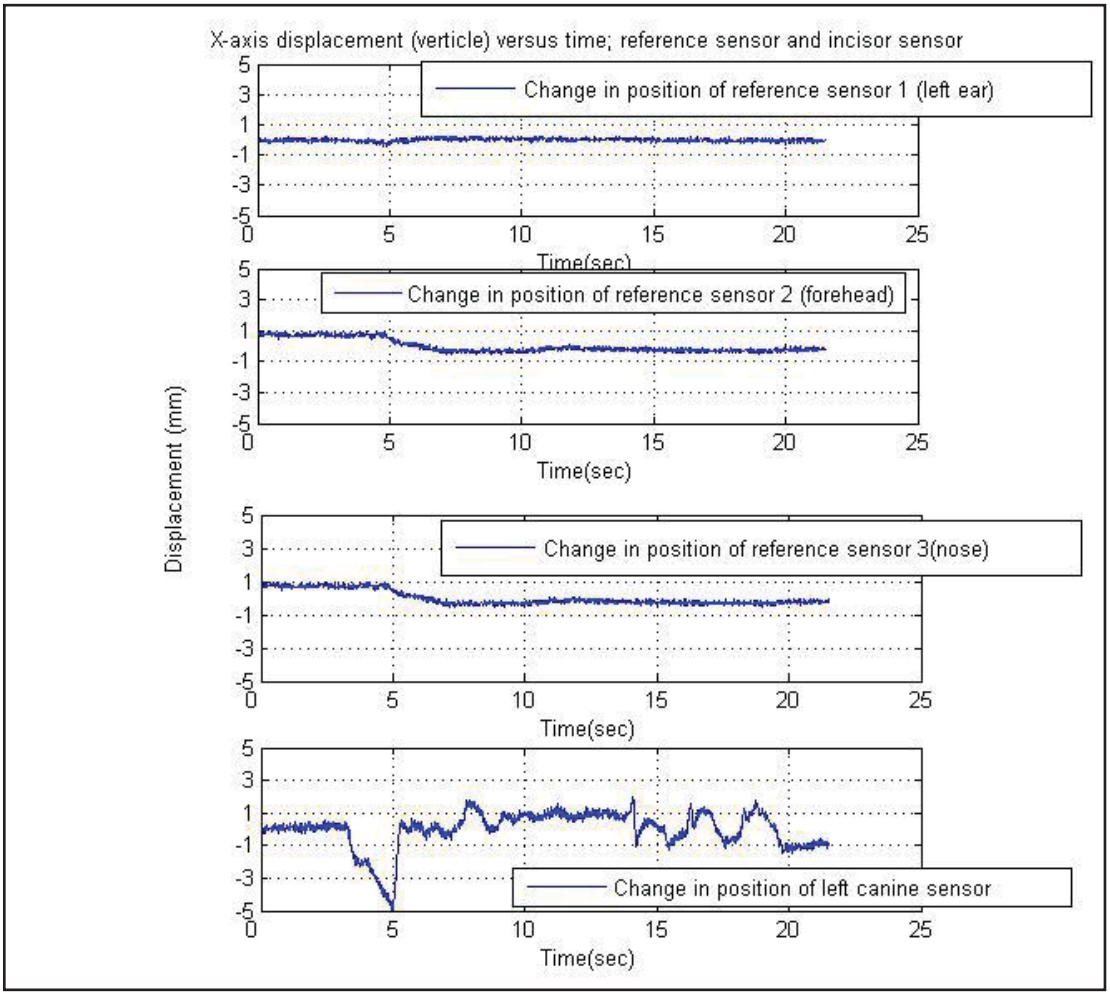
X-axis displacement (verticle) versus time; reference sensor and incisor sensor
Change in position of reference sensor 1 (left ear)
Change in position of reference sensor 2 (forehead)
Change in position of reference sensor 3(nose)
Change in position of left canine sensor
Displacement (mm)
Time(sec)

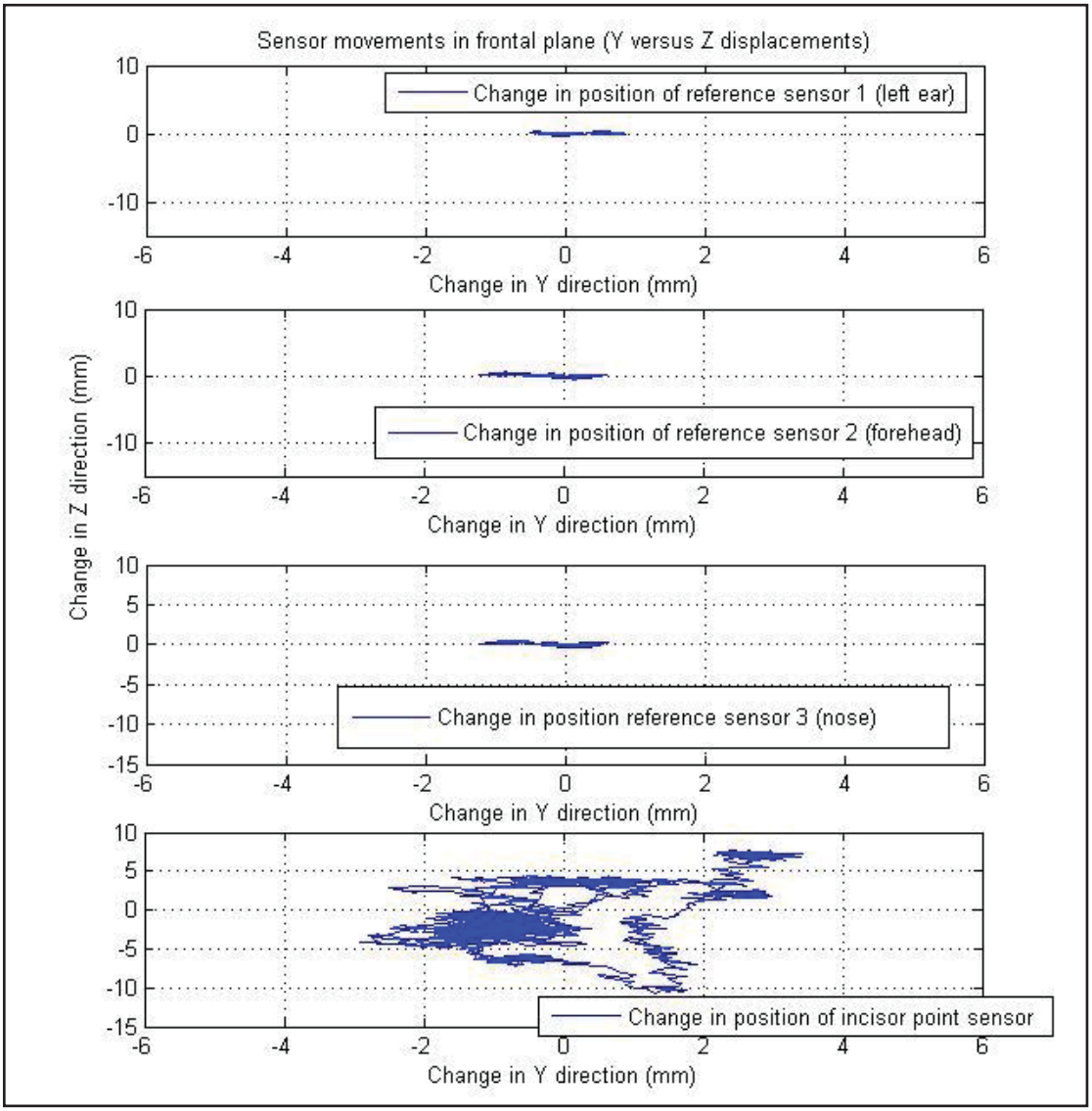
Sensor movements in frontal plane (Y versus Z displacements)
Change in position of reference sensor 1 (left ear)
Change in position of reference sensor 2 (forehead)
Change in position reference sensor 3 (nose)
Change in position of incisor point sensor
Change in Y direction (mm)
Change in Z direction (mm)

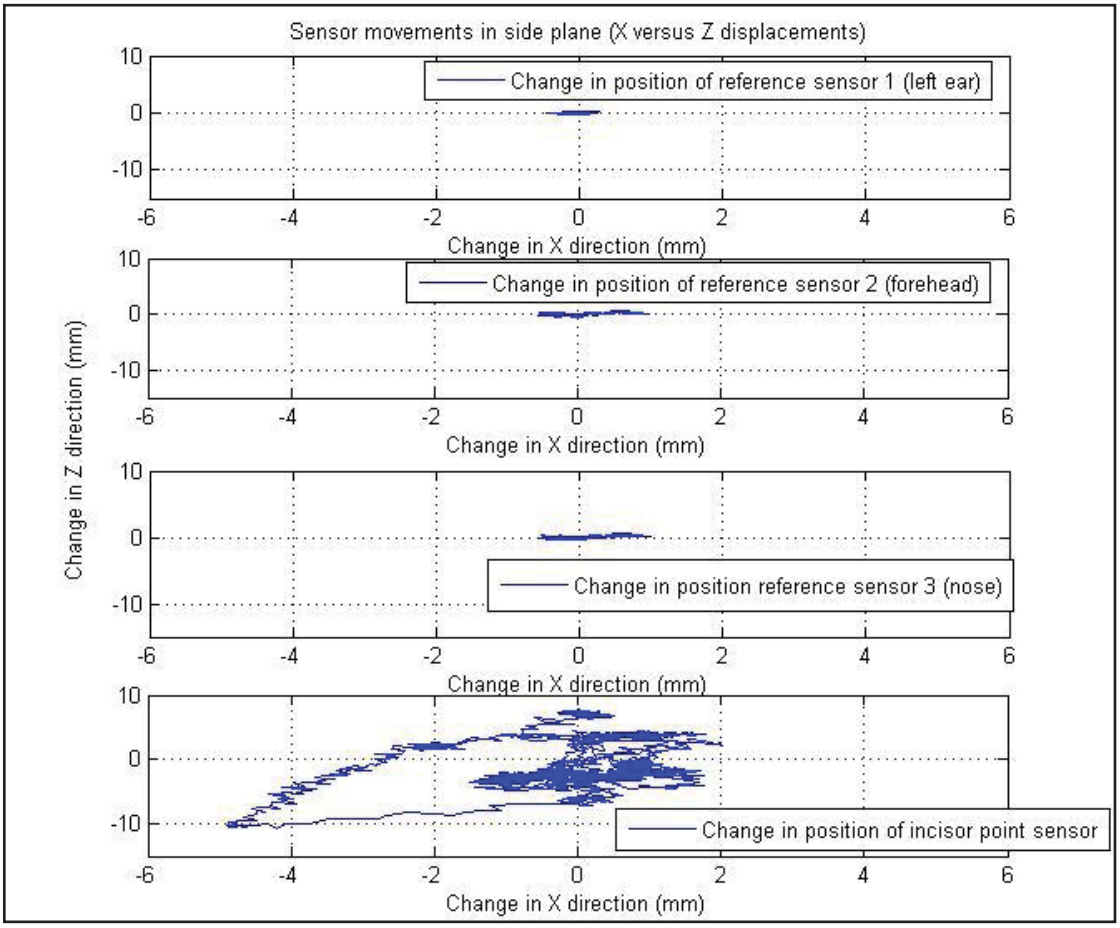
Sensor movements in side plane (X versus Z displacements)
Change in position of reference sensor 1 (left ear)
Change in position of reference sensor 2 (forehead)
Change in position reference sensor 3 (nose)
Change in position of incisor point sensor
Change in Z direction (mm)
Change in X direction (mm)
10
0
-10
-6
-4
-2
0
2
4
6

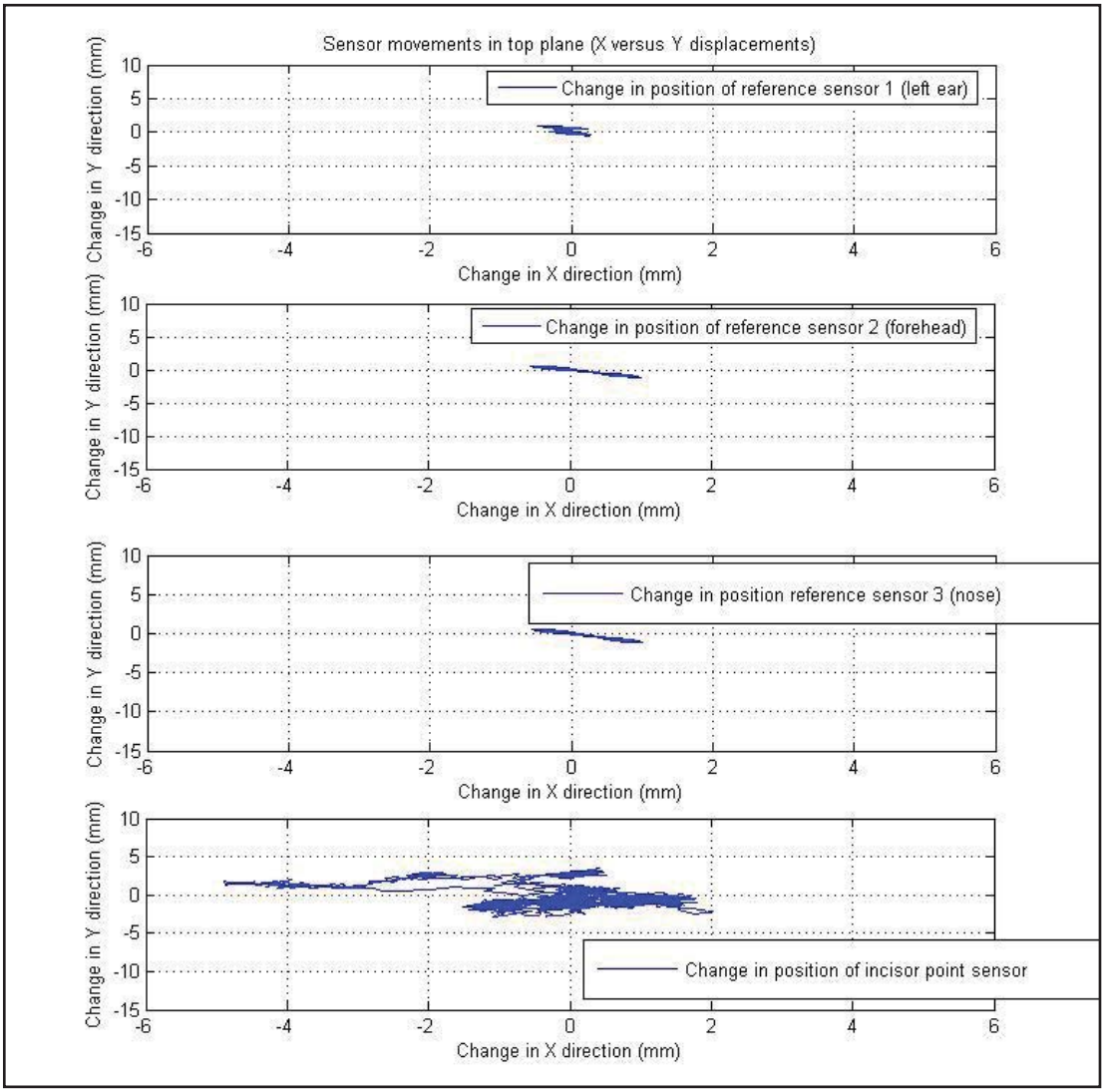

Appendix E Figure 10.

From the graphs it can be seen there is movement in the reference sensors, particularly in the X and Y directions. The movement is however within the +/-1mm error estimated in the previous section.